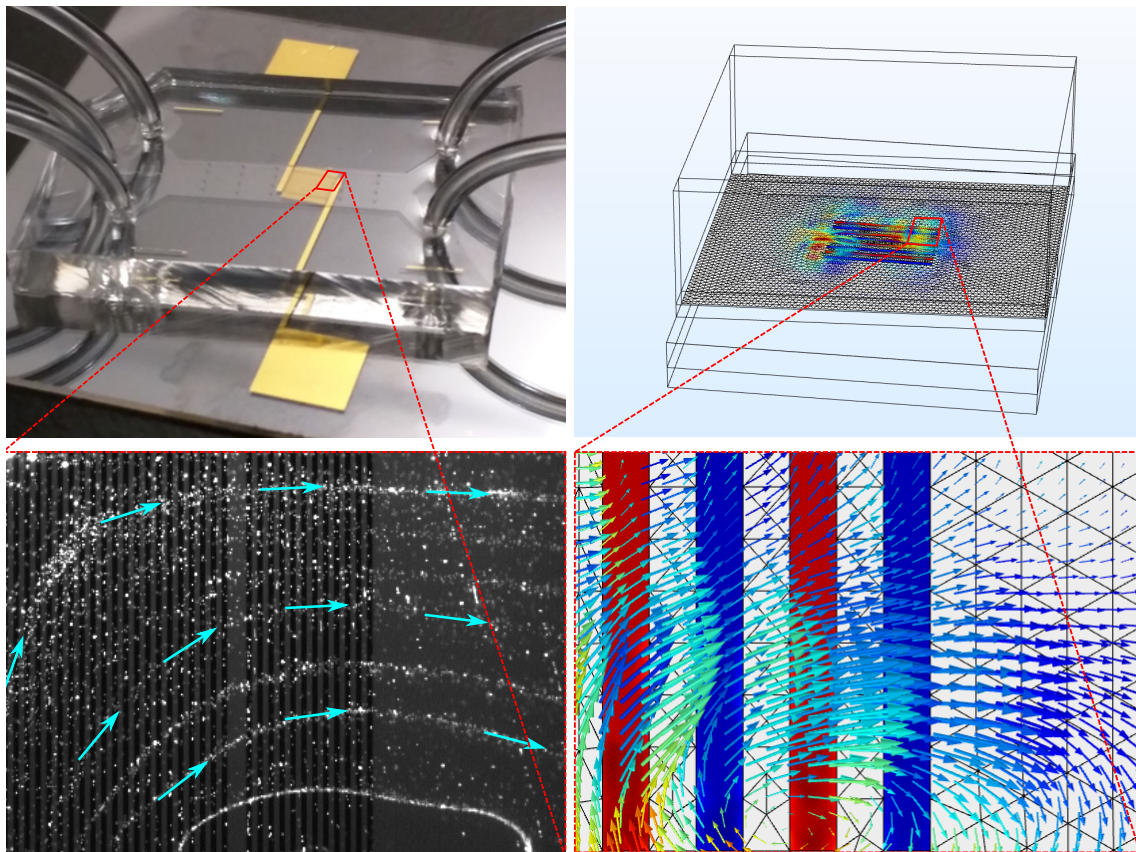


Nils Refstrup Skov

## Modeling of complex acoustofluidic devices



PhD thesis  
Kongens Lyngby, 28 June 2019

Advisor: Professor Henrik Bruus

**Cover illustration: —**

*Experimentally observed particle tracks, showing in-plane streaming rolls and in-plane streaming rolls numerically predicted in a 3D simulation. Photographs courtesy of P. Sehgal.*

Copyright © 2019 Nils Refstrup Skov. All Rights Reserved.  
Typeset using L<sup>A</sup>T<sub>E</sub>X.

Department of Physics  
Technical University of Denmark  
DTU Physics Building 309, DK-2800 Kongens Lyngby, Denmark  
<http://www.fysik.dtu.dk/microfluidics>







# Abstract

Acoustofluidics is the interdisciplinary combined field of ultrasound acoustics and microfluidics. The interplay between acoustic standing pressure- and velocity waves and the laminar channel flows in microchips enable reproducible and controllable manipulation of the position of suspended cells and particles as small as on the nanometer-scale.

Acoustofluidics is an emerging field and the bulk of the theoretical foundation experimentalists rely on when designing new devices is based on idealized systems and approximated two-dimensional numerical models. These create a good understanding of systems and can explain most experimentally observed phenomena.

As the acoustofluidic community grows the channel designs grow in amount and complexity. Hence, a move away from idealized and approximated systems towards more complete, three-dimensional numerical models may be necessary. That is the topic of this thesis.

In this thesis we document the gradual development of a numerical model intended to accurately model complex acoustofluidic microdevices. The model grows from a simple two-dimensional model containing few elements to a three-dimensional model capable of modeling microdevices to scale.

Along the development we verify the model predictions using analytical and experimental results. Additionally, we use it to draw out knowledge about the rapidly oscillating acoustic fields that are not readily measured experimentally, thus gaining insight in the physical phenomena happening in the devices. Finally, we use the predictive powers of the model as a design tool to improve on existing microdevices and even creating an entirely new one.



# Resumé

Akustofluidik er det videnskabelige krydsfelt mellem ultralydsakustik og mikrofluidik. Samspillet mellem stående tryk- og hastighedsbølger fra akustikken og mikrofluidikkens laminare strømninger i kanaler i mikrochips, gør det muligt at reproducerbart og kontrollerbart manipulere med positionen af partikler og celler, i nogle tilfælde helt ned på nanoskala.

Med et udspring i 1990'erne er akustofluidik stadig et ungt felt, og en stor del af det primære teoretiske grundlag eksperimenter læner sig op ad, når de designer nye mikrochips, bygger i høj grad på idealiserede systemer og tilnærmede todimensionelle numeriske modeller. Disse skaber en god forståelse for systemer og kan forklare de fleste fænomener der bliver observeret eksperimentelt.

I takt med at akustofluidik bliver mere populært vokser mængden af forskellige typer kanaler, samtidig med at kompleksiteten af mange chipdesign øges. Her kan det blive nødvendigt at bevæge sig væk fra idealiserede systemer og tilnærmelser i retning mod mere komplette, tredimensionelle numeriske modeller, hvilket er emnet for denne afhandling.

I denne afhandling dokumenterer vi den gradvise udvikling af en numerisk model, med henblik på retvisende at kunne modellere komplekse akustofluidiske mikrosystemer. Modellen går fra at være en simpel todimensionel model med få komponenter til at være en tredimensionel model, der kan modellere mikrochips i størrelsesforholdet én-til-én.

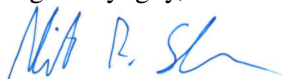
Undervejs i udviklingen verificerer vi modellens forudsigelser ved hjælp af analytiske og eksperimentelle resultater. Vi bruger den i tillæg til at trække informationer ud fra systemer om de hurtigt oscillerende akustiske felter, hvilket svært lader sig gøre eksperimentelt. Vi bruger dette til at få mere indsigt i de fysiske fænomener der foregår i de modellerede systemer. Slutteligt bruger vi modellens forudsigende kræfter som et designværktøj til at forbedre på eksisterende mikrochipdesign og endda skabe en helt ny.



# Preface

This thesis is submitted in candidacy for the degree of Doctor of Philosophy (PhD) from the Technical University of Denmark (DTU). The work was carried out in the Department of Physics, Section of Biophysics and Fluids, in the Theoretical Microfluidics Group led by Professor Henrik Bruus, during the three year period from 15 June 2016 to 14 June 2019. The project included 4 research stays scattered across the PhD from August 2016 to December 2018 in the group of Professor Martin Wiklund at Kungliga Tekniska Högskola, Stockholm, Sweden. Additionally, the PhD included 1 stay of six weeks duration in the group of professor Brian Kirby at Cornell University, Ithaca, New York. The project was funded by a Nordic 5 Tech scholarship from DTU.

Kongens Lyngby, June 2019



Nils Refstrup Skov



# Acknowledgements

I owe a great deal of thanks to many people for helping me along my 3 years as a PhD candidate, but I would like make particular mention of a few.

First and foremost, I would like to thank my supervisor Henrik Bruus, for inspiring me with his infectious enthusiasm for everything physics-related and his great thoroughness. It is impossible to work alongside him without his motivation and drive rubbing off on you.

I also owe many thanks to my collaboration partners Prof. Brian J. Kirby and Prateek Sehgal at Cornell University, for welcoming me to Ithaca on my external stay in the spring of 2018. I thoroughly enjoyed our collaboration and my stay with you.

On the same note I must warmly thank Prof. Martin Wiklund, Karl Olofsson, and Björn Hammarström at KTH Stockholm, for welcoming me on my several short stays in Stockholm. You made Stockholm a home away from home whenever I visited and made me feel as a visiting friend rather than a collaborator.

A special thanks and present members of the Theoretical MicroFluidics group at DTU is also in order. Particularly Jonas T. Karlsen and Mikkel W.H. Ley for showing me the ropes, when I first started and my office buddy Jacob S. Bach for many great discussions on physics and many other things. Thank you also to Wei Qiu, Rayisa Moiseyenko, Fabio Garofalo, Andre G. Steckel, Jonas H. Jørgensen and Bjørn G. Winckelmann for their contributions to making TMF a great working environment.

Furthermore, I am grateful for my friends from high school, for helping me unwind and maintain a good work-social life balance, and my friends from university for making my study years fly by.

I would also like to thank my parents Inger and Jens and my siblings Signe, Thomas, and Pil for nurturing my curiosity, my will to always find out more and my passion for boardgames. I firmly believe the latter and my career path are correlated.

Lastly, and most importantly I would like to thank my wonderful fiancée Helga for her endless support and warmth, and my son Ask for his unfailing ability to make me smile regardless of what else is going on. The thought of them has been my drive and motivation numerous times.





# Contents

<b>Abstract</b>	<b>v</b>
<b>Resumé</b>	<b>vii</b>
<b>Preface</b>	<b>ix</b>
<b>Acknowledgements</b>	<b>xi</b>
<b>Contents</b>	<b>xiii</b>
<b>List of publications</b>	<b>xvii</b>
<b>List of Figures</b>	<b>xix</b>
<b>List of Tables</b>	<b>xxi</b>
<b>List of symbols</b>	<b>xxiii</b>
<b>1 Introduction</b>	<b>1</b>
1.1 Acoustofluidics . . . . .	1
1.2 Acoustophoresis . . . . .	2
1.3 Acoustofluidic devices . . . . .	3
1.4 Numeric modeling and motivation . . . . .	4
1.5 Structure of the thesis . . . . .	6
<b>2 Governing equations of acoustofluidics</b>	<b>9</b>
2.1 Fluid dynamics . . . . .	9
2.2 Solid mechanics . . . . .	10
2.3 Electrostatics . . . . .	14
2.4 Piezoelectric coupling . . . . .	15
2.5 Perturbation theory . . . . .	15
2.6 Boundary conditions . . . . .	19
2.7 Acoustophoretic motion and energy measures . . . . .	21
2.8 Hard-wall fluid acoustic eigenmodes . . . . .	23
2.9 List of assumptions . . . . .	24

2.10	Concluding remarks . . . . .	24
<b>3</b>	<b>Numerical modeling in COMSOL</b>	<b>25</b>
3.1	Weak form of a general linear differential equation . . . . .	25
3.2	Continuity equations in weak form . . . . .	26
3.3	COMSOL Multiphysics . . . . .	28
3.4	High performance cluster computing . . . . .	31
3.5	Convergence analysis . . . . .	32
3.6	Material parameters and Bond matrices . . . . .	33
3.7	Model reductions . . . . .	34
3.8	Concluding remarks . . . . .	35
<b>4</b>	<b>2D Model of a bounded fluid domain</b>	<b>37</b>
4.1	Motivation . . . . .	37
4.2	Model systems . . . . .	38
4.3	Key results and observations . . . . .	42
4.4	Concluding remarks . . . . .	45
	Paper I. Published in Micromachines . . . . .	48
<b>5</b>	<b>Modeling a full device in 3D</b>	<b>63</b>
5.1	Motivation . . . . .	63
5.2	Model system . . . . .	64
5.3	Key results and observations . . . . .	68
5.4	Concluding remarks . . . . .	71
	Paper II. Published in in AIMS Mathematics . . . . .	74
<b>6</b>	<b>Analysis of a complex 3D SAW system</b>	<b>87</b>
6.1	Motivation . . . . .	87
6.2	Model system . . . . .	88
6.3	Key results and observations . . . . .	93
6.4	Concluding remarks . . . . .	101
	Paper III. Submitted to Phys. Rev. Applied . . . . .	103
<b>7</b>	<b>A wall-free multiwell system</b>	<b>119</b>
7.1	Motivation . . . . .	119
7.2	Model system . . . . .	120
7.3	Key results and observations . . . . .	121
7.4	Concluding remarks . . . . .	125
<b>8</b>	<b>Conclusion and Outlook</b>	<b>129</b>
8.1	Conclusion . . . . .	129
8.2	Outlook . . . . .	130
<b>A</b>	<b>Abstract submitted for Acoustofluidics 2019</b>	<b>133</b>

---

<b>B</b>	<b>Notes on the governing equations and notation</b>	<b>137</b>
<b>C</b>	<b>Material parameters for 128° Y-X cut LiNbO<sub>3</sub></b>	<b>139</b>
	<b>Bibliography</b>	<b>141</b>



# List of publications

## Peer-reviewed journal papers

- I. N.R. Skov and H. Bruus, *Modeling of microdevices for SAW-based acoustophoresis - a study of boundary conditions*, *Micromachines* **7**, 182 (2016). Enclosed in Chapter 4, Ref. [1].
- II. N.R. Skov, J. S. Bach, B. G. Winckelmann, and H. Bruus, *3D Modeling of acoustofluidics in a liquid-filled cavity including streaming, viscous boundary layers, surrounding solids, and a piezoelectric transducer*, *AIMS Mathematics* **3**, (2018) . Enclosed in Chapter 5, Ref. [2].
- III. N.R. Skov, P. Sehgal, B. J. Kirby, and H. Bruus *Three-Dimensional Numerical Modeling of Surface Acoustic Wave Devices: Acoustophoresis of Microparticles including Streaming*, submitted to *Phys. Rev. Appl.* Enclosed in Chapter 6, Ref. [3].

## Peer-reviewed conference contributions

1. N. R. Skov, B. Hammarström, M. Wiklund, and H. Bruus, *A wall-free acoustic multi-well system for particle trapping*, Proc. Acoustofluidics 2019 Conference, 26-28 August 2019, Enschede, Neterlands, **poster presentation**. Remark: To be presented by H. Bruus on my behalf. Abstract enclosed in Chapter 7. .
2. N. R. Skov, and H. Bruus, *SAW-induced BAW*, Proc. Acoustofluidics 2018 Conference, 29-31 August 2018, Lille, France, **poster presentation**.
3. N. R. Skov, and H. Bruus, *Steps towards full-system solid-fluid interaction models*, Proc. Acoustofluidics 2017 Conference, 28-29 August 2017, San Diego, CA, USA, **oral presentation**.
4. N. R. Skov, and H. Bruus, *Hard and lossy wall boundary conditions in microscale acoustofluidic devices*, Proc. Acoustofluidics 2016 Conference, 22-23 September 2016, Kgs. Lyngby, DK, **poster presentation**.

## Other conference contributions

5. N.R. Skov and H. Bruus, *Acoustophoresis in polymer devices*, The Swedish Center for Acoustofluidics and Cell Separation (SWECACS) meeting, 19 December 2017, Lund, Sweden, **oral presentation**. Remark: presented along with H. Bruus.

6. N.R. Skov and H. Bruus, *Device-level numeric modelling*, 8th Summer School Complex Motion in Fluids, 24-29 September 2017, Cambridge, UK, **poster presentation**.
7. N.R. Skov and H. Bruus, *Modeling SAW-driven acoustofluidic devices*, 7th Summer School Complex Motion in Fluids, 19-24 August 2016, Twente, Netherlands, **poster presentation**.

# List of Figures

1.1	Acoustophoresis and streaming driving mechanisms. . . . .	3
1.2	Physical device and numerical model . . . . .	5
2.1	Wave propagation in isotropic versus anisotropic media. . . . .	12
2.2	Non-coinciding material and global coordinate systems. . . . .	13
2.3	Constitutive relations visualized . . . . .	16
3.1	Flow-chart of the COMSOL programming process . . . . .	29
3.2	Meshes for acoustics in various materials . . . . .	30
3.3	Solving time over degrees of freedom . . . . .	31
3.4	Convergence analysis plot . . . . .	32
4.1	The four two-dimensional (2D) numeric models investigated . . . . .	38
4.2	Full model F2 with PML . . . . .	40
4.3	Model validation . . . . .	41
4.4	Hard-wall condition versus Pyrex walls at resonance . . . . .	42
4.5	Hard-wall condition versus Pyrex walls at an off-resonance frequency . . . . .	43
4.6	Lossy-wall condition versus PDMS walls . . . . .	44
4.7	The acoustic fields of F2 bounded by PML . . . . .	45
5.1	Piezo-silicon-glass device sketch and cross-section . . . . .	64
5.2	Test rod and silicon speed of sound directionality . . . . .	66
5.3	PIV measurements and model calculations . . . . .	69
5.4	Boundary- and bulk-driven streaming balance . . . . .	71
5.5	Circular acoustophoresis . . . . .	72
6.1	The experimental device and the numeric model . . . . .	88
6.2	128 ° Y-X cut lithium niobate wafer orientation . . . . .	90
6.3	IDT principle sketch and the submerged electrode approximation, . . . . .	92
6.4	Measured and calculated electrical impedances. . . . .	94
6.5	PDMS and Pyrex as acoustic resonators . . . . .	95
6.6	The effect of Bragg reflectors . . . . .	97
6.7	Acoustophoresis in the devices D1 and D2 . . . . .	98
6.8	3D model and acoustophoresis . . . . .	100

7.1	Physical device and numeric model . . . . .	120
7.2	Similarities between radiation potential and transducer motion . . . . .	122
7.3	Observed and predicted particle focusing patterns . . . . .	123
7.4	Focusing insensitivity to cavity dimensions. . . . .	124
7.5	Lead zirconium titanate and aluminum nitride comparison . . . . .	126



# List of Tables

2.1	List of assumptions made in the numeric model . . . . .	24
3.1	Generalized fluxes and source terms of the governing equations of Chapter 2. . .	27
3.2	Acoustic wavelengths, mesh elements and degrees of freedom . . . . .	30
4.1	Key parameters of the numeric model in paper I . . . . .	40
5.1	The device and numerical model dimensions. . . . .	64
6.1	Dimensions of the numeric 2D and 3D models. Adapted from [3]. . . . .	89
7.1	Dimensions of the final device design. . . . .	121



# List of symbols

Symbol	Description	Unit
$p$	Fluid pressure	Pa
$v_i/\mathbf{v}$	Fluid velocity vector	$\text{m s}^{-1}$
$u_i/\mathbf{u}$	Solid displacement vector	m
$\phi$	Electric potential	V
$\rho$	Mass density	$\text{kg m}^{-3}$
$\eta$	Dynamic viscosity	Pa s
$\eta^b$	Bulk viscosity	Pa s
$\sigma_{ik}/\boldsymbol{\sigma}$	Stress tensor	$\text{N m}^{-2}$
$\gamma_{ik}$	Strain rate tensor	$\text{s}^{-1}$
$c_0$	Isentropic fluid sound velocity	$\text{m s}^{-1}$
$\kappa_f = 1/\rho_0 c_0^2$	Isentropic compressibility	$\text{Pa}^{-1}$
$\epsilon_{ik}/\boldsymbol{\epsilon}$	Strain tensor	
$c_L$	Longitudinal/compressional wave speed	$\text{m s}^{-1}$
$c_T$	Transverse/shear wave speed	$\text{m s}^{-1}$
$C_{iklm}/\mathbf{C}$	Elasticity tensor	Pa
$\epsilon_0$	Relative permittivity tensor	
$\tilde{\epsilon}_{ik}/\tilde{\boldsymbol{\epsilon}}$	Permittivity of vacuum	$\text{F m}^{-1}$
$e_{ijk}/\mathbf{e}$	Electromechanical coupling tensor	$\text{C m}^{-2}$
$E_i/\mathbf{E}$	Electric field vector	$\text{V m}^{-1}$
$D_i/\mathbf{D}$	Electric displacement vector	$\text{C m}^{-2}$
$P_i/\mathbf{P}$	Polarization density vector	$\text{C m}^{-2}$
$q$	Unit charge	C
$p_i$	Dipole moment vector	Cm
$Z^{\text{ac}}$	Acoustic impedance	Rayl
$\tilde{Z}^{\text{ac}}$	Acoustic impedance ratio	
$Z^{\text{el}}$	Electrical impedance	$\Omega$

Symbol	Description	Unit
$t$	Time	s
$f$	Frequency	Hz
$\omega = 2\pi f$	Angular frequency	$s^{-1}$
$\lambda$	Wavelength	m
$k_0 = \omega/c$	Undamped wavenumber	$m^{-1}$
$\delta = \sqrt{2\eta/\rho_f\omega}$	Viscous boundary layer length	m
$\Gamma = \left(\frac{4}{3}\eta_f + \eta_f^b\right)\omega\kappa_f$	Viscous damping factor	
$\Gamma_s$	Solid damping factor	
$k_{\text{PML}}$	PML damping factor	
$a$	Particle radius	m
$f_0$	Monopole scattering coefficient	
$f_1$	Dipole scattering coefficient	
$E_{\text{ac}}$	Average acoustic energy density	$J m^{-3}$
$U_{\text{m}}$	Average strain energy density	$J m^{-3}$
$U_{\text{e}}$	Average electric energy density	$J m^{-3}$
$\partial_t$	Partial derivative with respect to time	$s^{-1}$
$\partial_i$	Partial derivative with respect to quantity $i$	$i^{-1}$
$\delta_{ik}$	Kronecker delta	-
$\epsilon_{ijm}$	Levi-Civita symbol	$i^{-1}$
$\nabla$	Gradient vector operator	$m^{-1}$
$\nabla \cdot$	Divergence scalar operator	$m^{-1}$
$(x, y, z)$	Global Cartesian coordinates	m
$(X, Y, Z)$	Material Cartesian coordinates	m
$e_i/\mathbf{e}_k$	Unit vector in the $k$ -direction	
$n_i/\mathbf{n}$	Surface normal vector	
$i = \sqrt{-1}$	Imaginary unit	
$e$	Base of the natural logarithm, $\ln(e) = 1$	
$\langle \square \rangle$	Time average of $\square$	
$\langle \square, \triangle \rangle$	Inner product $\square$ of and $\triangle$ - only Chapter 3	
$ \square $	Absolute value of $\square$	
$\square^*$	Complex conjugate of $\square$	
$\square^0$	Surface field of $\square$	
$\square_1$	Harmonic, first-order field of $\square$	
$\square_2$	Steady, second-order field of $\square$	
$\text{Re}[\square]$	Real part of $\square$	
$\text{Im}[\square]$	Imaginary part of $\square$	
$\square_i$	Three-component index notation	
$\square_\alpha$	Six-component Voigt notation	
$\square_{\parallel}$	Parallel quantity	
$\square^f$	Quantity defined for fluid	
$\square^s$	Quantity defined for elastic solid	
$\square^{\text{pz}}$	Quantity defined for piezoelectric solid	

---

Abbreviation or chemical formula	Word or phrase
2D	Two-dimensional
3D	Three-dimensional
AlN	Aluminum nitride
BAW	Bulk acoustic wave
DOF	Degrees of freedom
HPC	High performance cluster
IDT	Interdigitated transducer
LiNbO <sub>3</sub>	Lithium niobate
PDE	Partial differential equation
PDMS	Polydimethylsiloxane rubber
PML	Perfectly matched layers
Pyrex	Borosilicate glass
PZT	Lead zirconate titanate
SAW	Surface acoustic wave

---



# Chapter 1

## Introduction

To put this thesis and its contribution to the scientific community in perspective, we here bring a cursory introduction to the scientific field of *acoustofluidics* in terms of its comparable fields and its over these advantages. We describe the driving forces of so-called acoustophoresis, which is particle migration due to acoustics. We then discuss examples of devices in which acoustophoresis is achieved. This leads us to the concept and benefits of numeric modeling in acoustofluidics, which is the topic of this thesis.

### 1.1 Acoustofluidics

Acoustofluidics is a branch of the greater field of microfluidics; a field dealing with fluid flows on the micro-scale, typically achieved in microchannels where one or more dimensions are on the sub-millimeter scale. Microfluidics is a multidisciplinary field. The design and manufacture of devices contains elements of solid and fluid mechanics, surface chemistry, materials science, microfabrication and electrical engineering. The applications on the other hand are most commonly biological or biotechnological, with examples being tissue engineering [5], rare cell isolation [6, 7, 8] and diagnostics [9, 10, 11]. The small dimensions of microfluidic devices cause inertial effects to diminish compared to surface effects, which is illustrated by the low Reynolds numbers found in most microfluidic devices. Therefore the fluid flows in microfluidic devices are often laminar and thus highly deterministic.

In the absence of turbulence in a fluid, suspended particles or cells can be manipulated with a high precision and repeatability in a multitude of manners. This may be done passively using sedimentation or the buoyancy of particles [12], effects of fluid inertia [13, 14], cell deformability [15], or actively by applying an external field. Examples of this include, uniform [16, 17] and non-uniform [18, 19] electric fields, magnetic fields [20], laser beams [21], and thermal gradients [22]. In the present work, however, we exclusively deal with *acoustophoresis*, which is the motion of particles in suspension due to externally applied harmonic acoustic fields establishing traveling and standing ultrasonic fields in fluids.

## 1.2 Acoustophoresis

Particle manipulation using acoustophoresis is particularly suitable for biological applications as ultrasound does not impair the viability or proliferation of cells [23, 24]. Furthermore, acoustophoresis requires no labeling of cells because it relies on the contrast in acoustic properties of suspensions and suspended matter giving it inherent selectivity.

The driving mechanism behind acoustophoresis is the interaction of harmonically oscillating acoustic fields giving rise to two forces acting on particles, namely the directly induced *acoustic radiation force*  $F_i^{\text{rad}}$ , and the indirect *streaming drag force*  $F_i^{\text{drag}}$  caused by acoustically induced, circulating, streaming flow rolls.

### 1.2.1 The acoustic radiation force

A wave with wavelength  $\lambda$  propagating through a continuum will scatter at any non-uniformity it encounters. In acoustics the non-uniformity is in the mass density or compressibility and may be due to inhomogeneities in the fluid properties [25]. More often though the scatterers are particles or cells with radius  $a$  suspended in the propagation medium, which due to their small size compared to the acoustic wavelength ( $a \ll \lambda$ ) act as point scatterers.

When scattering, waves impart momentum to the scatterers and exert a net force over an oscillation period due to the interplay of the time-harmonic acoustic fields. The force is exerted over the entire volume of the scatterer and accordingly scales with the particle radius cubed  $a^3$ . This effect was described already in 1934 by King [26]

### 1.2.2 The streaming drag force

In acoustofluidic devices driven under resonance conditions the fluid velocity is far greater than the wall velocity. To connect the two, the fluid must transition over a thin region called the viscous boundary layer. In devices driven at MHz this layer has a thickness on or below the micrometer-scale, which leads to large velocity gradients and thus shear stresses.

These stresses will over a few thousands of cycles [27]<sup>1</sup> build up a steady boundary-driven streaming velocity field, as sketched in in Fig. 1.1(a). The phenomenon was described for circulating rolls in air over Chladni plates by Lord Rayleigh in 1884 [28].

An additional mechanism driving streaming fields is the dissipation of traveling acoustic waves. As they propagate, they impart momentum into the propagation medium in a steady fashion, as described by Eckart in 1948 [29]. We illustrate the principle in Fig. 1.1(c).

Regardless of the driving force, the induced circulating streaming fields have low Reynolds numbers. Therefore, a particle suspended in such a flow will experience a drag following Stokes' law, scaling with the particle radius  $a$  and streaming velocity  $v_{i,2}$ .

---

<sup>1</sup>Note, that a few thousand cycles occurs within a single millisecond when the applied acoustic field is in the MHz-regime.



### 1.2.3 Force balance

The  $a^2$  scaling of the ratio between the radiation force and the streaming drag force creates three regimes of particle motion with no sharp division, as sketched in Fig. 1.1(b). The regimes are based on particle radius, with a device-geometry- and material-dependent critical radius indicating the tipping point from radiation dominated to streaming dominated as theoretically predicted [30] and experimentally observed [31].

(i) Sufficiently large particles experience negligible drag, and migrate almost exclusively due to the radiation force. As the radiation force is time-invariant, all particles will come rest at some point, based on their initial position.

(ii) Intermediate particles experience radiation and drag forces on the same order of magnitude, and the governing cause of migration can be very specific to certain parts of a device. These particles, may end up in a region with a dominant radiation force and be captured or may follow along distorted versions of streaming rolls indefinitely. Again, this is dependent of the initial position of the particle.

(iii) Very small particles will exclusively follow the patterns of the streaming rolls. As the rolls form closed loops, particles mainly undergoing streaming acoustophoresis will follow their loops indefinitely.

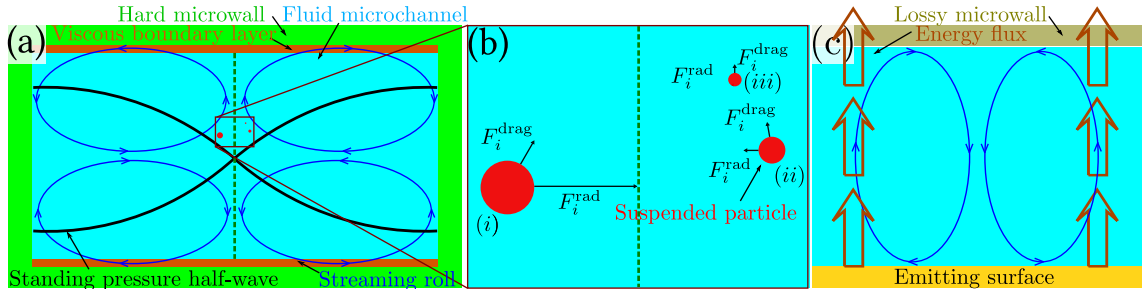


**Figure 1.1:** Streaming driving mechanisms and acoustophoresis. (a) Classical boundary-driven streaming rolls induced by the shear stress in the thin viscous boundary layer in a hard-walled systems actuated at resonance. (b) The balance of forces for three particle sizes; (i) A large particle with radius  $a$ , dominated by the acoustic radiation force  $F_i^{\text{rad}}$  and negligible drag force. (ii) A particle of radius  $\frac{a}{2}$ .  $F_i^{\text{rad}}$  here is 8 times lower than for (i), and of even magnitude as the drag force  $F_i^{\text{drag}}$ . The two forces even out, and the motion is a mixture of the two forces. (iii) A particle of radius  $\frac{a}{4}$ .  $F_i^{\text{rad}}$  here is 64 times lower than for (i), and only  $\frac{1}{16}$  of  $F_i^{\text{drag}}$ . The motion here is completely dominated by the drag force. (c) Streaming induced by inhomogeneous dissipation in the bulk fluid domain. Waves emitted from a surface and absorbed on another cause a local upwards energy flux dissipating into the fluid, establishing a circulating flow.

## 1.3 Acoustofluidic devices

All acoustofluidic devices rely on the aforementioned balance of forces. In some devices the rolling motion caused by streaming fields may be desired as in mixing [32, 33], which is a hurdle

in laminar flows as it is governed solely by diffusion.

In this thesis we focus mainly on devices with a focus on trapping and concentrating particles or cells. The majority of these consist of some combination of an electrode-patterned piezoelectric transducer – in which alternating potentials create mechanical waves – a fluid microchannel or cavity with suspended cells or particles, and an encasing material, usually glass, silicon or a polymer. In these the streaming drag often counteracts the focusing of the radiation force. Hence, it is of interest to find means of either suppressing the streaming [25], or creating streaming combined force landscapes where streaming does not counteract the radiation force, as experimentally realized in [3].

Depending on the actuation method of the piezoelectric material, devices can be categorized into bulk acoustic wave (BAW) and surface acoustic wave (SAW) devices, an example of which is shown in Fig. 1.2. To achieve good separation of particles and high energies for moderate power inputs, the bulk of acoustofluidic devices rely on acoustic fluid resonances, although designing for whole-system resonances is also a viable approach [34]. In either case, the working frequency of acoustofluidic devices are usually well above the highest audible frequency of 20 kHz. BAW devices typically have working frequencies of a few to several MHz to excite fluid cavities on the order of a few hundred micrometers, while SAW devices can have actuation frequencies in the tens of MHz to excite resonances in the piezoelectric substrate.

BAW devices are actuated through a grounded and a charged electrode attached to either side of a slab of piezoelectric ceramic, causing waves to travel through the entirety of the transducer. As the microchannels in BAW are often capillary tubes or a hard material with a cavity, and transducers can be bought ready-made, BAW microchips require simpler facilities to fabricate and are cheap relative to SAW devices.

In SAW microchips, actuation is achieved through a set of interdigitated, alternating charged and grounded electrodes etched onto a piezoelectric wafer. Therefore, waves are formed at the surface of the piezoelectric substrate and propagate along the it while being evanescent in the depth of the material, effectively localizing up to 95 % of the energy on the substrate surface [35]. This is reflected in device designs, as the microchannel is more frequently in contact with the piezoelectric material in SAW devices than in their BAW counterparts. Because SAW devices rely on patterning electrodes onto a piezoelectric substrate using soft lithography rather than purchasing ready-made transducers, SAW devices can have more intricate designs. This comes, however, at a cost as SAW devices require a more expensive class of piezoelectric ceramics and have more cumbersome fabrication processes.

For both categories of devices designs come in a range of complexities, both in terms of production and interaction of elements. While the majority of focusing devices feature long straight extrusions of a two-dimensional cross-section [36, 37, 38, 39, 40] more complex three-dimensional designs are also abundant in the literature [41, 42, 43, 44, 45].

## 1.4 Numeric modeling and motivation

To paraphrase Muller *et al.*[46], experimental work, theoretical analysis, and numeric models are symbiotic in understanding and improving acoustofluidic devices. In this work we primarily focus on the numerical modeling part of acoustofluidics, but collaborate closely with experimentalists

and employ analytical solutions whenever possible.

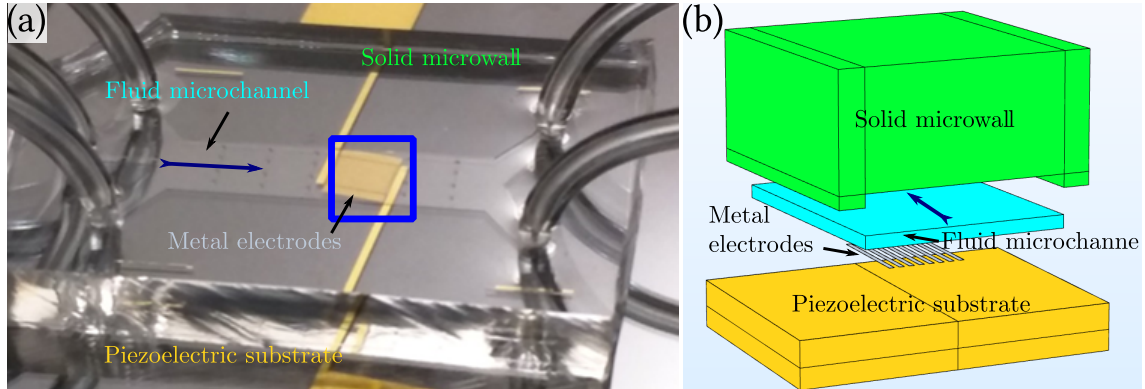


**Figure 1.2:** Physical device and numerical model. (a) The physical surface acoustic wave device used in Chapter 6. Image courtesy of P. Sehgal. (b) Exploded view of a numerical counterpart to the device in (a), rotated  $90^\circ$ . The device is too heavy to compute in its entirety and the numerical model is therefore scaled down representing only portion of the blue box marked in (a) and slightly idealized, but the main components remain. The blue arrows in (a) and (b) show the flow direction of the microchannel.

A great advantage of numerical modeling is the probing and measuring possibilities. The acoustic pressure for instance is impossible to experimentally measure directly in a non-interfering way, due to the high frequencies and large gradients often involved. In numerical models, however, the temporal and spatial dependence of the acoustic pressure is fully resolved. This is also one of the challenges in verifying models experimentally, as this is typically done through secondary effects such as comparison between the calculated and observed acoustophoretic motion.

The good resolution of the acoustic fields in numeric models make them incredibly useful in building understanding of the inner workings of a system. As a consequence the literature has a multitude of numeric models with different layers of complexity; equivalent circuit modeling of piezos with fluid force coupling [47, 47], fluid-only 2D simulations [30, 48, 49, 50, 51], fluid-only 3D simulations [52, 53, 45], 2D and 3D models of fluid-solid systems with solids modeled as fluids [54, 55], 2D fluid-solid models [56], 2D fluid-solid-piezo models [57], 3D fluid-solid models [58], and most complex of all 3D fluid-solid-piezo models with [59] and without damping [40]. All of these approaches have merit, and a good rule of thumb is to use the simplest possible model for whatever task is at hand, as it will often be the quickest and easiest to use. In Fig. 1.2(a) we exemplify a physical device, that only requires a highly complex numerical model to model its inner workings due to its intricate geometry and anisotropic materials.

An other less used, but equally useful application of numerical models is the optimization of acoustophoretic devices. Numerical models enable the examination of device designs for a vast parameter-space that cannot feasibly be tested by repeated manufacture and experimentation on devices [60, 58].

In the present work we aim to create a model encompassing all effects of an isothermal acoustofluidic device, capable of modeling any design regardless of choice of materials, actuation scheme, and geometry. We do this by iteratively improving upon a model, adding complexity

with each step.

We verify the model as a reliable tool through handshakes with experimental work and comparisons to known analytical solutions whenever possible. Concurrently, we use the model to gain insights into the mechanisms of actual devices, improve upon the design of an existing device and guide the design of an entirely new device.

## 1.5 Structure of the thesis

The main chapters of the thesis are outlined below. The bulk of the work done for this dissertation amounted in the two published papers [1, 2], an manuscript in review [3] and an ongoing project [4].

In chapters 4-6 we provide a 'reader's digest' of papers [1, 2, 3]. We go through the work carried out for each manuscript and present the main results with emphasis on the qualitative parts, and refer readers to the papers for quantitative results. Additionally we include some results that were either omitted from the manuscripts or have been carried out in retrospect. At the end of each of the chapters the manuscripts are included in their entirety, as a reference work for details we do not discuss in the main text.

In chapter 7 we present the current state of the numeric model, present some ongoing work, and discuss future work, and include an abstract submitted to the Acoustofluidics 2019 conference.

**Chapter 1 Introduction** — Introduction to the field of acoustofluidics and cursory review of the current state of the art with regards to numeric modeling.

**Chapter 2 Acoustofluidics background** — The governing equations used in full and effective modeling of isothermal, anisotropic, piezo-driven acoustofluidic devices.

**Chapter 3 Finite element modeling background** — Implementation the of governing equations in weak form using COMSOL Multiphysics. Numerical toolkit to work on large-scale systems and description of the DTU High Performance Cluster (HPC).

**Chapter 4 2D model studies of approximative boundary condition validity.** The initial foray into modeling in a 2D fluid-solid system using approximated boundary conditions for the piezo-electric actuation. A study of widely used approximated boundary conditions for use in future work.

**Chapter 5 Full 3D simulation of a presented bulk acoustic wave device** — The expansion of the numeric model by inclusion of additional physical phenomena. We numerically reproduce previously published experimental results and provide an explanation of observed in-plane streaming rolls.

**Chapter 6 Full 3D model studies of a surface acoustic wave device.** — A study of an acoustofluidic device driven by surface acoustic waves. Reasoning for the design improvements made to a device based on our numeric model predictions. Remarks on acoustophoretic motion reminiscent

of that in bulk acoustic wave devices.

**Chapter 7 Chladni-plate-like motion of piezoelectric substrates.** Description of a novel approach to designing acoustofluidic devices. Reasoning for computational savings based on reduced-domain models.

**Chapter 8 Conclusion and outlook** — Conclusion of the thesis and outlook with suggestions for future research with emphasis on the ongoing research project of Chapter 7.



## Chapter 2

# Governing equations of acoustofluidics

In this chapter we define the governing equations for the fields of fluid dynamics, solid mechanics and electrostatics. This order is chosen to reflect the importance of the fields in calculating device acoustofluidics, and the order in which the fields were implemented in our numeric models. Additionally, we present linearizations of the governing equations derived using perturbation theory. Regarding the notation, we make a distinction between pure physics and numeric implementation. We mark this by using index notation when describing the governing equations. When we linearize the equations using perturbation theory we present the resulting equations in both index and vector notation, as the latter serves as a basis for the numerical implementation described in Chapter 3.

### 2.1 Fluid dynamics

The governing equations in a fluid with mass density  $\rho_f$ , dynamic viscosity  $\eta$ , bulk viscosity  $\eta^b$  are the conservation of mass, Eq. (2.1), and the balance of momentum, Eq. (2.2).

#### 2.1.1 Mass conservation

The total mass of a system must stay constant assuming no relativistic effects or nuclear reactions. Conservation of mass is described by the continuity equation,

$$\partial_t \rho_f = -\partial_i (\rho_f v_i). \quad (2.1)$$

Physically this means that the local rate of change of mass density increases where momentum density converges and decreases where it diverges. While water can be assumed to be incompressible for many fluid mechanics problems that is not the case in acoustofluidics as compressional waves are the very essence of acoustics.

#### 2.1.2 Momentum conservation

For a fluid volume fixed in space, fluid particles within can be accelerated by two effects; By forces acting on the surfaces of the volume and due to the convection of momentum. This is described

by the Navier-Stokes equations,

$$\rho_f \partial_t v_i = \partial_k (\sigma_{ik}^f - \rho_f v_k v_i). \quad (2.2a)$$

Here we have assumed the fluid to be Newtonian with the viscous stress tensor,

$$\sigma_{ik}^f = 2\eta(\gamma_{ik}) - p_f \delta_{ik} + \left( \frac{\eta^b}{\eta} - 2/3 \right) \eta \gamma_{jj} \delta_{ik}, \quad (2.2b)$$

describing the force in direction  $k$  per unit area of surface  $i$ , with  $i, k = 1, 2, 3$ . Here,  $\delta_{ik}$  is the Kronecker delta, and  $\gamma_{ik}$  is the strain rate tensor,

$$\gamma_{ik} = \frac{1}{2} (\partial_i v_k + \partial_k v_i). \quad (2.2c)$$

Strains and stresses can be divided into two categories; (i) *normal strains* acting parallel to the normal of a surface, ( $i = j$ ) and (ii) *shear strains* acting within the plane of a surface ( $i \neq j$ ) In words, Eq. (2.2a) states the rate of change of momentum in a fixed point is equal to the sum of locally acting forces and the local influx of momentum.

## 2.2 Solid mechanics

The displacement field  $\mathbf{u}_s$  in a linearly elastic solid material with mass density  $\rho_s$  is governed by the conservation of momentum and a linear strain-stress constitutive relation.

### 2.2.1 Cauchy momentum equation

The governing equation for solid mechanics is the Cauchy momentum equation, from which the Navier-Stokes equations are also derived. As there is no convection in solid materials the non-linear term disappears leaving,

$$\rho_s \partial_t^2 u_i = \partial_k \sigma_{ik}^s. \quad (2.3a)$$

The stress tensor  $\sigma_{ik}^s$  for small displacements in solids is defined by the linear constitutive relation,

$$\sigma_{ik}^s = C_{iklm} \epsilon_{lm}, \quad (2.3b)$$

where  $\epsilon_{ik}$  is the strain tensor,

$$\epsilon_{ik} = \frac{1}{2} (\partial_i u_k + \partial_k u_i), \quad (2.3c)$$

and  $C_{iklm}$  is the 81-components elasticity tensor. Due to symmetries 60 of these are redundant<sup>1</sup> and thus the highest number of elastic constants in any material is 21. This number is further decreased in varying degrees by materials exhibiting symmetries in their microstructure as discussed in Section 2.2.2, and shown in Fig. 2.3. In words, Eq. (2.3a) states that the product of the mass and acceleration of a solid volume element is equal to the forces acting on its surfaces.

<sup>1</sup>See Section B.1



In isotropic, linearly elastic materials the stress state for a given strain can be uniquely defined using just two elastic constants. In acoustics we typically opt for a definition intuitive for wave propagation problems,

$$\sigma_{ik}^s = 2\rho c_T^2 \epsilon_{ik} + (\rho c_L^2 - 2\rho c_T^2) \epsilon_{jj} \delta_{ik}, \quad (2.3d)$$

where  $c_T$  and  $c_L$  are the transverse and longitudinal speeds of sound respectively. In this form there is a clear analogue to the fluid stress definition Eq. (2.2b), with  $\rho c_T^2$  and  $\rho c_L^2$  being the solid counterpart to the dynamic and bulk viscosities of a fluid.

### 2.2.2 Isotropic and anisotropic materials

Depending on their material class and their microstructure solid materials are either isotropic or anisotropic. Isotropic materials are polycrystalline media, such as cast metals and amorphous materials including glass and some polymers. The disorder in these media lead to material properties that may be directionally dependent on the grain scale, but on the macroscopic scale even out and negate any directional dependence.

In Fig. 2.1(a) isotropy is illustrated by displacement waves propagation outward from a point actuation in  $O$  all having the same wavelength, like surface waves emitted from an object dropped in water. This makes isotropic media easier to work with analytically and numerically, as the physics that take place within them are more intuitive than those in anisotropic materials and material parameters need not be given with respect to a certain coordinate system.

Anisotropic media on the other hand, are crystalline media that have long-range order in their structure. Examples include the commonly used bulk acoustic wave actuator lead zirconate titanate and lithium niobate commonly used in surface acoustic wave devices. The order in these media will favor for instance deformation of the material in one direction over others or a certain direction might have higher electrical conductivity. In Fig. 2.1(b) this is illustrated by the directional dependence of wavelengths of the waves propagation outwards from a point actuation in  $O$ . For  $\theta = 0$  the wavelength and hence propagation velocity is twice that for  $\theta = \pi/2$ . While this is a greatly exaggerated example for illustrative purposes, the difference in normal elasticities<sup>2</sup> for anisotropic materials commonly used in acoustofluidics range from 5 to 35 percent.

The degree, directionality, and the material properties affected by anisotropy in a solid are determined by the crystalline structure. Silicon for instance is mechanically isotropic when polycrystalline due to the random order of grains. In its single-crystalline form, however, it is thermally and optically isotropic but shows directional dependence in its elasticity.

Because of the direction dependence of material parameters, table values for anisotropic media are always given in some orientation relative to the crystalline coordinate system. In Section 2.2.2 we go through the steps necessary to transform known properties from one basis to an other and in Chapter 5 we illustrate the directional dependence of wave propagation velocities in monocrystalline silicon.

<sup>2</sup>The proportionality factors between normal strains and stresses, i.e.  $C_{iikk}$

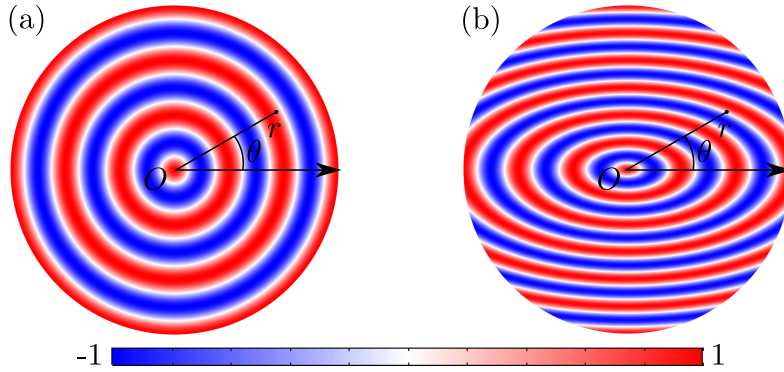


**Figure 2.1:** Illustration of wave propagation in isotropic versus anisotropic media from a point-source emitter. (a) Color plot of displacement waves propagation out from a harmonic point actuation  $u_z = u_0 e^{-i\omega t}$  at  $O = (0, 0)$  in an isotropic medium. (b) Color plot of waves propagation out in an anisotropic medium actuated as in (a).

### Material directionality

When modeling the physics of anisotropic media, we distinguish between two frames of reference that do not necessarily coincide. the material coordinate system  $X, Y, Z$  - for which table values of material properties are given - and the global coordinate system  $x, y, z$  in which the independent variables are defined.

The global coordinate system is arbitrary but usually defined to be convenient to work with, for instance aligned to match the width, depth and height of a device. Fig. 2.2 illustrates a set of non-coinciding material and global coordinate systems for a slab of anisotropic material. Here the material system is defined from the crystalline structure and the global system is defined by the slab's geometry.

A first-order tensor such as the position  $r_i$  is transformed from one coordinate system  $r_k = (x, y, z)$  to another  $r'_j = (X, Y, Z)$  through the transformation tensor  $R_{jk}$

$$r'_j = R_{jk} r_k, \quad (2.4)$$

where the components  $R_{jk}$  are the directional cosines between axis  $x'_k$  and axis  $x_i$ . In general, an  $n$ -order tensor is transformed using  $n$  rotation tensors transforming one index at a time, for instance the elasticity tensor transforms as

$$C'_{iklm} = R_{in} R_{ko} R_{lp} R_{mq} C_{nopq}. \quad (2.5)$$

This is, however, quite tedious numerically. In Section 3.6 we discuss an alternative approach, using the Voigt notation described in the following section.

### 2.2.3 Voigt Notation

When calculating the motion of anisotropic materials it is useful to introduce the Voigt notation. In this notation, the stress and strain tensors defined in Eqs. (2.3d) and (2.3c) are compacted

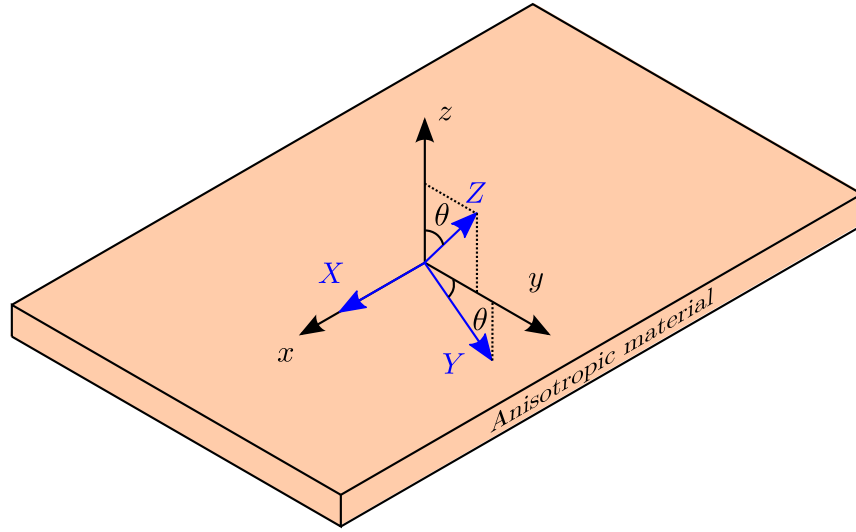


**Figure 2.2:** Sketch illustrating a set of non-coinciding material ( $X, Y, Z$ ) and global ( $x, y, z$ ) coordinate systems. A slice of an anisotropic material is aligned along the global coordinate system, which is at an angle  $\theta$  to the material coordinate system rotated positively around the  $x$ -axis. The  $X$ - and the  $x$ -axes overlap, as do the  $Y, Z$ - and the  $y, z$ -planes. Adapted from [3]

into the vectors  $\epsilon_\alpha$  and  $\sigma_\alpha$ ,  $\alpha = 1, 2, \dots, 6$  by employing the symmetric nature of these tensors  $\sigma_{ik} = \sigma_{ki}$ ,  $\epsilon_{ik} = \epsilon_{ki}$ . For the stress defined in Voigt notation the first three components are the normal stresses and the last three are the shear elements in the order,  $123, 1\bar{2}3, 12\bar{3}$ .

$$\epsilon_\alpha = \begin{pmatrix} \epsilon_1 \\ \epsilon_2 \\ \epsilon_3 \\ \epsilon_4 \\ \epsilon_5 \\ \epsilon_6 \end{pmatrix} = \begin{pmatrix} \epsilon_{11} \\ \epsilon_{22} \\ \epsilon_{33} \\ 2\epsilon_{23} \\ 2\epsilon_{31} \\ 2\epsilon_{12} \end{pmatrix}, \quad \sigma_\alpha = \begin{pmatrix} \sigma_1 \\ \sigma_2 \\ \sigma_3 \\ \sigma_4 \\ \sigma_5 \\ \sigma_6 \end{pmatrix} = \begin{pmatrix} \sigma_{11} \\ \sigma_{22} \\ \sigma_{33} \\ \sigma_{23} \\ \sigma_{31} \\ \sigma_{12} \end{pmatrix}. \quad (2.6)$$

Notice that Voigt shear strain elements are twice the value of those in index notation,  $\epsilon_4 = 2\epsilon_{23}$ , etc. This is by convention to keep the strain energy density  $U \equiv \frac{1}{2}\sigma_\alpha\epsilon_\alpha = \frac{1}{2}\sigma_{ik}\epsilon_{ik}$  invariant of notation<sup>3</sup>, keeping the Voigt notation isometric. One benefit of Voigt notation is the highly compact constitutive relation with no loss of generality,

$$\sigma_\alpha = C_{\alpha\beta}\epsilon_\beta, \quad (2.7)$$

where  $C_{\alpha\beta}$  is the symmetric 6x6 Voigt elasticity tensor. Note that the symmetry of this tensor leaves at most 21 independent components, which fits with the highest possible elastic moduli in anisotropic media. Another benefit is the relative ease of transforming material parameters such as

<sup>3</sup>See Section B

the elasticity tensor from one frame of reference to another. We discuss this further in Section 3.6. With the introduction of  $\sigma_\alpha$  the Cauchy momentum equation in Eq. (2.3a) can be rewritten to

$$\rho \partial_t^2 u_i = \mathcal{V}_{i\alpha} \sigma_\alpha, \quad (2.8)$$

where we have introduced the Voigt index divergence operator,

$$\mathcal{V}_{i\alpha} = \delta_{ik} \delta_{k\alpha} \partial_k + |\epsilon_{ijm}| \partial_m \text{ with } j = \alpha - 3, \quad (2.9)$$

where  $\epsilon_{ijm}$  is the Levi-Civita symbol taking on values of 1 for even permutations of  $i, j, m$ , -1 for odd permutations and 0 if any index is repeated.

## 2.3 Electrostatics

The electric potential  $\phi$  in a linear, anisotropic dielectric material with relative permittivity  $\tilde{\epsilon}_{ik}$  and no free charges  $\rho_f = 0$  is governed by Gauss's law and the constitutive relation of electric fields.

### 2.3.1 Gauss's Law

Due to the absence of free charges in a piezoelectric ceramic Gauss' law simplifies to

$$\partial_i D_i = 0, \quad (2.10)$$

stating that the ingoing and outgoing electric flux are balanced in all points. This is in a sense an electric counterpart of the continuity equation for incompressible fluids. Here, we have defined the electric flux density  $D_i$ ,

$$D_i \equiv \epsilon_0 E_i + P_i^e = \epsilon_0 \tilde{\epsilon}_{ik} E_k, \quad (2.11)$$

where  $\epsilon_0$  is the vacuum permittivity and  $E_k$  is the electric field,

$$E_i = -\partial_i \phi, \quad (2.12)$$

and  $P_i^e$  is the induced polarization density as described below.

### 2.3.2 Electric dipoles

An electric dipole is a pair of equal and opposite charges  $\pm q$  with displacement vectors  $d_i$ . Such a pair has a dipole moment of  $p_i = qd_i$ . On the macroscopic scale a distribution of dipoles lead to a polarization density  $P_i$ ,

$$P_i = \frac{dp_i}{dV}. \quad (2.13)$$

When an dielectric is subjected to an electric field  $E_i$  any pre-existing dipoles will experience a torque tending to align them with the field. Concurrently new dipoles will be induced parallel to the field due to the shift of the positively charged nuclei relative to the electrically charged electron clouds. The resulting electrically induced polarization density is

$$P_i^e = \epsilon_0 \chi_{ik} E_k. \quad (2.14)$$

As we shall see in Section 2.4 an additional polarization can arise from due to electro-mechanical effects.

## 2.4 Piezoelectric coupling

In some anisotropic media the negative and positive ions in the lattice structure move relative to each other when the structure deforms causing dipole moments to appear. On the macroscopic scale this manifests as an added polarization density  $P_i^m$  in the electric flux density due to an applied strain  $\epsilon_\alpha$  due to the so-called piezoelectric effect. In the inverse piezoelectric effect dipoles shift relative to each other when subjected to an external electric field,  $E_i$ , causing a stress contribution  $\sigma_\alpha^e$ .

In the limit of small electric fields and small mechanical strains, the polarization and stress states in piezoelectric materials are superpositions of the mechanically (superscript m) and electrically induced fields (superscript e). Mathematically, this is represented by adding an electromechanical term to each of the auxiliary fields in Eqs. (2.7) and (2.11). The coupling can be expressed in one of several ways. Here we opt to use the so-called *stress-charge* form,

$$D_i = \epsilon_0 E_i + P_i^e + P_i^m = \epsilon_0 \tilde{\epsilon}_{ik} E_k + e_{i\alpha} \epsilon_\alpha, \quad (2.15a)$$

$$\sigma_\alpha = \sigma_\alpha^m + \sigma_\alpha^e = C_{\alpha\beta} \epsilon_\beta - e_{\alpha i} E_i. \quad (2.15b)$$

Here we have introduced the coupling tensor  $e_{i\alpha}$  which is the proportionality factor between the mechanically induced polarization in direction  $i$  and strain component  $\alpha$  in the direct piezoelectric effect, whereas  $e_{\alpha i}$  is the ditto between the electrically induced stress component  $\alpha$  and the electric field in direction  $i$  in the inverse piezoelectric effect.

The resulting constitutive relations for the most general piezoelectric materials can be written on the compact form,

$$\begin{pmatrix} \sigma_1 \\ \sigma_2 \\ \sigma_3 \\ \sigma_4 \\ \sigma_5 \\ \sigma_6 \\ D_x \\ D_y \\ D_z \end{pmatrix} = \begin{pmatrix} C_{11} & C_{12} & C_{13} & C_{14} & C_{15} & C_{16} & -e_{11} & -e_{21} & -e_{31} \\ & C_{22} & C_{23} & C_{24} & C_{25} & C_{26} & -e_{12} & -e_{22} & -e_{32} \\ & & C_{33} & C_{34} & C_{35} & C_{36} & -e_{13} & -e_{23} & -e_{33} \\ & & & C_{44} & C_{45} & C_{46} & -e_{14} & -e_{24} & -e_{34} \\ & & & & C_{55} & C_{56} & -e_{15} & -e_{25} & -e_{35} \\ & & & & & C_{66} & -e_{16} & -e_{26} & -e_{36} \\ & & & & & & \epsilon_{11} & 0 & 0 \\ & & & & & & & \epsilon_{22} & \epsilon_{23} \\ & & & & & & & & \epsilon_{33} \end{pmatrix} \begin{pmatrix} \epsilon_1 \\ \epsilon_2 \\ \epsilon_3 \\ \epsilon_4 \\ \epsilon_5 \\ \epsilon_6 \\ E_x \\ E_y \\ E_z \end{pmatrix}. \quad (2.16)$$

In Fig. 2.3 the amount of non-zero, independent coefficients for the elastic and piezoelectric solids used in this thesis is illustrated.

## 2.5 Perturbation theory

The driving force of the acoustofluidic devices we investigate is an ac potential of frequency  $f$  and angular frequency  $\omega = 2\pi f$  applied across a piezoelectric material through a set of a grounded and a charged electrode. For small potentials the linear response to the actuation are electric and acoustic fields that are directly proportional to the driving voltage and inherit its harmonically oscillating characteristic. Accordingly, the acoustic fields within the device are complex-valued

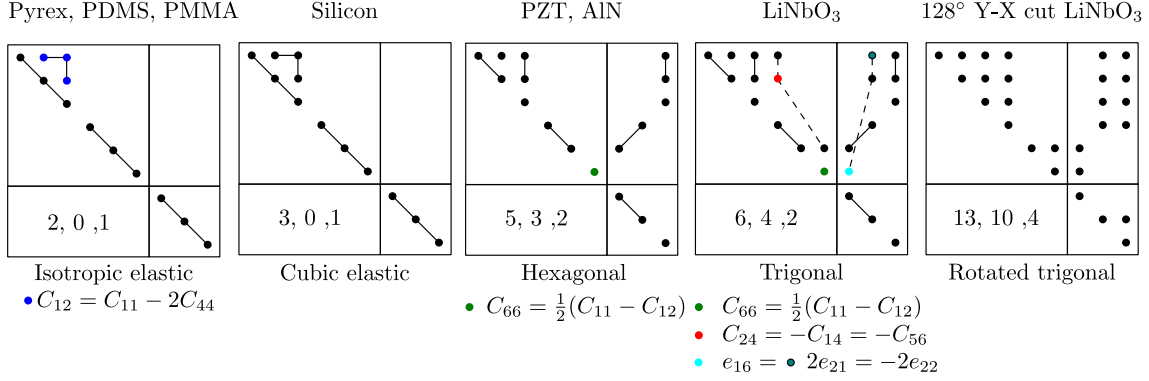


**Figure 2.3:** Visualization of the upper-right, non-zero coefficient in the constitutive relations, of the materials used in this thesis, as shown in Eq. (2.16). Full lines indicate equalities whereas dashed lines indicate relations. and colored circles indicate linear combinations of other coefficients. The numbers indicate the amount of linearly independent elastic, coupling and dielectric coefficients, respectively.

functions  $g(r_i, t) = g_0(r_i)e^{-i\omega t}$ , where  $g_0(r_i)$  is the field amplitude at  $r_i$  and the physical value of the field at time  $t$  can be evaluated as the real part  $g^{\text{phys}}(r_i, t) = \text{Re}[\hat{g}(r_i)e^{-i\omega t}]$ . The harmonically oscillatory nature of the fields simplifies the temporal derivative to  $\partial_t = -i\omega$ .

The fields described above are all small perturbations around a quiescent state, and we employ standard perturbation theory up to second order to linearize the governing equations Eqs. (2.2a), (2.3a), and (2.10). The harmonic fields make up the first-order fields in this perturbation series, which takes on the form

$$u_i(r_i, t) = 0 + u_{i,1}(r_i)e^{-i\omega t} + 0, \quad (2.17a)$$

$$v_i(r_i, t) = 0 + v_{i,1}(r_i)e^{-i\omega t} + v_{i,2}(r_i), \quad (2.17b)$$

$$p(r_i, t) = p_0(r_i) + p_1(r_i)e^{-i\omega t} + p_2(r_i), \quad (2.17c)$$

$$\rho(r_i, t) = \rho_0(r_i) + \rho_1(r_i)e^{-i\omega t} + \rho_2(r_i), \quad (2.17d)$$

$$\phi(r_i, t) = 0 + \phi_1(r_i)e^{-i\omega t} + 0. \quad (2.17e)$$

The second-order fields in the fluid arise from products of first-order fields in the nonlinear governing equations. We are only interested in the steady part of these and let the subscript "2" implicitly mean the time-average of a field,  $g_2(r_i) = \langle g_2(r_i, t) \rangle = \frac{1}{T} \int_0^T g_2(r_i, t) dt$ , where  $T = 2\pi/\omega$  is the period of the harmonic oscillation. We are also only interested in the time-average of second-order products of first-order fields, and let it be implicit that  $\langle g_1(r_i), h_1(r_i) \rangle = \frac{1}{2} \text{Re}[g_1(r_i)h_1(r_i)^*]$ , where the asterisk operator "\*" denotes the conjugate of a complex value.

For brevity we omit the implicit position dependence of all fields and harmonic nature of first-order fields.

### 2.5.1 Full fluid acoustic fields

We introduce the isentropic linear constitutive relation  $p_1 = c_0^2 \rho_1$  – where  $c_0 = (\partial_p / \partial_\rho)^{-1}$  is the isentropic compressional wave speed – and the isentropic compressibility  $\kappa_f = (\rho_0 c_0^2)^{-1}$ . Using these, we insert the perturbation series Eq. (2.17) in the governing fluid equations and collect only first-order terms,

$$-i\omega\kappa_f p_1 = \partial_i v_{i,1} \quad \text{or} \quad \nabla \cdot \mathbf{v}_1 + i\omega\kappa_f p_1 = 0, \quad (2.18)$$

$$-i\omega\rho_0 v_{i,1} = \partial_j \sigma_{ij,1}^f \quad \text{or} \quad \nabla \cdot \boldsymbol{\sigma}_1^f + i\omega\rho_0 \mathbf{v}_1 = \mathbf{0}. \quad (2.19)$$

Here and in the following, the subscript “1” in an auxiliary field ( $\sigma_{ij,1}^f, \epsilon_{\alpha,1}, E_{i,1}, \dots$ ) is used to indicate that it is calculated with first-order dependent values.

### 2.5.2 The Helmholtz equation

Using the stress definition Eq. (2.2b) it can be shown that Eqs. (2.18) and (2.19) can be rewritten to the Helmholtz equation,

$$\partial_i^2 p_1 = -k^2 p_1 \quad \text{or} \quad \nabla \cdot (\nabla p_1) + k^2 p_1 = 0. \quad (2.20)$$

where we have introduced the complex wavenumber  $k = (1 + i\Gamma)\omega/c_0$  with the dimensionless viscous loss factor  $\Gamma = (4/3\eta_f + \eta_f^b)\omega\kappa_f$ . Using the Helmholtz equation reduces the number of unknowns and equations to solve to 1, providing a simpler framework for calculating the acoustic pressure fields in the bulk of a fluid domain. The acoustic velocity is, however, still of interest in acoustic pressure modeling and can be calculated as,

$$v_{i,1} = -i \frac{1 - i\Gamma_f}{\omega\rho_f} \partial_i p_1, \quad \Gamma_f = \left( \frac{4}{3}\eta_f + \eta_f^b \right) \omega\kappa_f. \quad (2.21)$$

Near boundaries the fluid velocity must transition from the bulk solution to the values at the walls, which at resonance is much lower than in the bulk. This occurs over a thin region in the so-called viscous boundary layer of size,

$$\delta_{\text{visc}} = \sqrt{\frac{2\eta}{\rho\omega}} \approx 0.5 \mu\text{m at } 2 \text{ MHz and } 25 \text{ }^\circ\text{C}. \quad (2.22)$$

For devices with dimensions much larger than  $\delta_{\text{visc}}$ , Eq. (2.20) remains a reasonable approximation, when applying the set of boundary conditions developed by Bach and Bruus [61] that analytically accounts for the losses in the boundary layers, see Section 2.6.1.

### 2.5.3 Second-order fields and acoustophoresis

The products of first-order fields in the governing equations give rise to the second-order fields  $v_{i,2}$  and  $p_2$ . These are governed by the time-averaged continuity and Navier-Stokes equations,

$$\partial_i v_{i,2} = 0 \quad \text{or} \quad \nabla \cdot \mathbf{v}_2 = 0, \quad (2.23)$$

$$\rho_0 \partial_i (v_{i,1} v_{j,1}) = \partial_i \sigma_{ik,2}^f \quad \text{or} \quad \nabla \cdot \left( \boldsymbol{\sigma}_2^f - \rho_0 \mathbf{v}_1 \mathbf{v}_1 \right) = \mathbf{0}. \quad (2.24)$$

Here, the subscript “2” denotes the stress tensor calculated using the second-order velocities and pressure.

### 2.5.4 Solid acoustic fields

The governing equations of the solid are completely linear, and the first-order equations are equal to Eq. (2.3a) with  $u_i = u_{i,1}$ ,

$$-\omega^2 \rho_s u_i = \partial_k \sigma_{ik,1}^s \quad \text{or} \quad \nabla \cdot \boldsymbol{\sigma}_1^s + \omega^2 \rho_s \mathbf{u}_1 = \mathbf{0}. \quad (2.25)$$

Note that second-order fields are present in Eq. (2.17a), as a steady displacement field in the solid would correspond to a permanent deformation.

### Acoustic damping in solids

So far we have discussed idealized solids. However, in real devices propagating waves are damped in both fluids and solids. We implement this by the introduction of damping coefficients  $\Gamma$ . Following the analysis by Hahn and Dual [60] we introduce this in the forcing term of Eq. (2.25)

$$\partial_t \rightarrow -i\omega t(1 + i\Gamma_s), \quad (2.26)$$

where  $\Gamma_s$  is the material-dependent damping coefficient. Ideally one would introduce an imaginary part to each stiffness coefficient  $C_{\alpha\beta} = C'_{\alpha\beta} + iC''_{\alpha\beta}$ . These coefficients are, however, exceedingly difficult to measure experimentally and thus we settle with the broadly dampening approach.

### 2.5.5 Gauss's law to first order

As in the solid, no second-order products appear in the governing equations, and the electric potential field is fully described by the harmonically oscillating first-order part.

$$\partial_i D_{i,1} = \rho_{el} \quad \text{or} \quad \nabla \cdot \mathbf{D}_1 - \rho_{el} = 0. \quad (2.27)$$

The potential couples together with the acoustic displacement  $u_i$  due to the interconnectivity between mechanical motion and electric charge in piezoelectric devices.

### 2.5.6 Numerical impedance analysis

The electrical current,  $I$ , running through a piezoelectric device can also be a useful comparison parameter, as we shall see in Chapter 6. In the absence of free charges electrical currents only polarization currents exist. These are attributed to the polarization density  $P_i$ ,

$$P_i = D_i - \varepsilon_0 E_i, \quad (2.28)$$

the temporal derivative of which is the polarization density current  $J_{i,\text{pol}}$

$$J_{i,\text{pol}} = -i\omega P_i. \quad (2.29)$$

The flux of this into the device over the electrode surface  $\partial\Omega_{el}$  yields the electrical current  $I$ ,

$$I = \int_{\partial\Omega_{el}} \mathbf{J}_{\text{pol}} \cdot \mathbf{n} \, dA, \quad (2.30)$$



From the current the electrical impedance  $Z^{\text{el}}$  of the equivalent circuit of a device actuated with a potential  $V_0$  can be calculated,

$$Z^{\text{el}} = \frac{V_0}{I}. \quad (2.31)$$

## 2.6 Boundary conditions

We complete the boundary value problem defined by the bulk domain equations by introducing a set of restraints at select boundaries of the domains.

### 2.6.1 Fluid-solid interfaces

The fluid velocity field couples with the solid displacement field through continuity of the normal velocity, Eq. (2.32a), and stress, Eq. (2.32b). The two-way coupling is achieved by fixing the fluid velocity to the time derivative of the solid displacement, and fixing the solid stress normal to the interface to the ditto of the fluid.

$$n_i \cdot v_{i,1} = n_i \cdot \dot{v}_{i,1}^{\text{s}}, \quad (2.32a)$$

$$n_k \cdot \sigma_{ik,1}^{\text{s}} = n_j \cdot \sigma_{ik,1}^{\text{f}}, \quad (2.32b)$$

where we have defined the velocity of the wall,  $\dot{v}_{i,1}^{\text{s}} = -i\omega u_{i,1}$ .

The same approach can be used when using the Helmholtz equation,

$$\sigma_{ik,1}^{\text{s}} \cdot n_k = -p_1 n_i + ik_{\text{s}} \eta v_{i,1}^{\delta}, \quad (2.33a)$$

$$v_{i,1} \cdot n_i = -i\omega u_1 \cdot n_i + \frac{i}{k_{\text{s}}} \partial_{\parallel} \cdot v_{i,1,\parallel}^{\delta}. \quad (2.33b)$$

Here, the boundary layer velocity  $v_{i,1}^{\delta} = (v_{i,1}^{\text{s}} - v_{i,1})$  is introduced to account for the shearing effects in the viscous boundary layer. The subscript "||" denotes parallel components.

### 2.6.2 Solid-air interfaces

At interfaces between a solid material and the surrounding air a zero-stress condition is applied due to the large impedance ratio between solids and air,

$$n_k \cdot \sigma_{ik,1}^{\text{s}} = 0. \quad (2.34)$$

Even PDMS, which is one of the softest polymers, has an acoustic impedance 3500 times larger than that of air due to the much higher mass density, making the no-stress condition a good approximation for any solid-air interface.

### 2.6.3 Electrode conditions

We assume metal electrodes to be ideal conductors giving them a fixed, homogeneous potential across their entire surface.

$$\phi_1^{\text{ch}} = V_0 \quad , \quad \phi_1^{\text{gr}} = 0, \quad (2.35)$$

We model floating electrodes as having an unknown homogeneous potentials across their surface,

$$\partial_{\parallel} \phi_1^{\text{fe}} = 0, \quad (2.36)$$

The condition fixes the value across the surface to some value  $\phi_1^{\text{fe}}$ , which connected electrodes must take on.

#### 2.6.4 Second-order fluid conditions

The boundary conditions of the second-order fields when using effective pressure modeling are derived and described in detail by Bach and Bruus [61]. We will not go into detail here, but merely reiterate them

$$v_{i,2} = (A_i \cdot e_{\xi,i})e_{\xi,i} + (A_i \cdot e_{\nu,i})e_{\nu,i} + (B_i \cdot e_{\zeta,i})e_{\zeta,i}, \quad (2.37a)$$

$$A_k = \frac{1}{2\omega} \text{Re} \left\{ v_{i,1}^{\delta 0*} \partial_k \left( \frac{1}{2} v_{i,1}^{\delta 0} - i v_{i,1}^s \right) - i v_{i,1}^{s*} \partial_k v_{i,1} \right. \quad (2.37b)$$

$$\left. + \left[ \frac{2-i}{2} \partial_i v_{i,1}^{\delta 0} + i (\partial_k v_{i,1}^s - \partial_{\zeta} v_{\zeta,1}^*) \right] v_{i,1}^{\delta 0} \right\}, \quad (2.37c)$$

$$B_k = \frac{1}{2\omega} \text{Re} \left\{ i v_{i,1}^{0*} \partial_k v_{i,1} \right\}. \quad (2.37d)$$

Here  $e_{\xi,i}$  and  $e_{\nu,i}$  are unit vectors parallel to the surface,  $e_{\zeta,i}$  is the normal vector, and superscript "0" indicates the value defined at the surface, having only a perpendicular component.

#### 2.6.5 Solid approximation conditions

As an alternative to including solid domains surrounding the fluid domain, the fluid-solid interaction can be approximated by one of three boundary conditions depending on the material of the interfacing solid. The soft-wall condition Eq. (2.38b) represents an interface to an infinitely soft materials which cannot sustain stresses, as it states the inviscid stress is zero at the interface. It is typically used to represent fluid-air interfaces.

The hard-wall condition Eq. (2.38a) represents an infinitely hard and dense surface which cannot yield, stating the velocity - and thus displacement - of the wall and the contacting fluid is zero.

Finally the lossy-wall condition Eq. (2.38c) represents an interface reflecting a portion of incoming wave proportional to the acoustic impedance of the interface.

$$n_i \cdot v_i = 0, \quad (2.38a)$$

$$p_1 = 0, \quad (2.38b)$$

$$n_i \cdot \partial_i p_1 = i k \frac{Z^{\text{ac},f}}{Z^{\text{ac},\text{in}}} p_1 = i k_0 \tilde{Z}^{\text{ac}} p_1. \quad (2.38c)$$

Here we have defined the specific acoustic impedances of water  $Z^{\text{ac},f} = c_0 \rho_0$  and the interfacing domain  $Z^{\text{ac},\text{in}} = c_{\text{in}} \rho_{\text{in}}$ , and the impedance ratio  $\tilde{Z} = Z^{\text{ac},f} / Z^{\text{ac},\text{in}}$ . Notice that as  $v_{i,1} \propto \partial_i p_1$  Eqs. (2.38a) and (2.38b) are the limiting cases of Eq. (2.38c) for  $\tilde{Z} \rightarrow 0$  and  $\tilde{Z} \rightarrow \infty$  respectively.

Each of the conditions Eq. (2.38) is coupled with a no-slip condition fixing the fluid tangential velocity to zero.

$$v_{i,1,\parallel} = 0. \quad (2.39)$$

In Chapter 4 we investigate how well Eqs. (2.38a) and (2.38c) approximate various cases of surrounding materials.

### 2.6.6 Surface acoustic wave approximation

The horizontal and vertical displacements of two surface acoustic waves (SAW) traveling towards each other along the  $y$ -axis on an piezoelectric substrate lying in the  $(x, y)$ -plane can be approximated by an analytical solution [62],

$$u_{y,pz} = 0.6u_0e^{-C_d y} \left[ \sin \left( \frac{-2\pi(y - W/2)}{\lambda_{\text{SAW}}} + \omega t \right) + \sin \left( \frac{-2\pi(W/2 - y)}{\lambda_{\text{SAW}}} + \omega t \right) \right], \quad (2.40a)$$

$$u_{z,pz} = -u_0e^{-C_d y} \left[ \cos \left( \frac{-2\pi(y - W/2)}{\lambda_{\text{SAW}}} + \omega t \right) + \cos \left( \frac{-2\pi(W/2 - y)}{\lambda_{\text{SAW}}} + \omega t \right) \right], \quad (2.40b)$$

where  $u_0$  is the max  $z$ -displacement of the substrate,  $C_d$  is a damping coefficient due to contacting solids or liquids,  $W$  is the width of the fluid-domain, and  $\lambda_{\text{SAW}}$  is the SAW wavelength.

To eliminate the piezoelectric substrate in numeric models Eq. (2.40) may be used to approximate the motion of the substrate in a SAW acoustofluidic device.

## 2.7 Acoustophoretic motion and energy measures

We here introduce the concept of particle motion induced by acoustic fields coined acoustophoresis, which is typically aim in acoustofluidic device. We also present three quantities that can be used to measure the energy distribution in a device.

The motion is the superposition of two forces. One is a volume force caused directly by the acoustic waves scattering of particles called the acoustic radiation force  $F_i^{\text{rad}}$ . The other is the streaming drag force  $F_i^{\text{drag}}$  induced indirectly by the circulating streaming field the acoustics build up over a few thousand cycles.

### Acoustic radiation force

The radiation force is the time-averaged force exerted by the scattering of acoustic waves on a particle with radius  $a$ , density  $\rho_p$  and compressibility  $\kappa_p$ , derived using a multipole expansion [63]. For long wavelengths  $\lambda_f \gg a$ , and small thermoviscous boundary layers  $\delta_{\text{visc}} < a$  [64] and express it as the gradient of products of acoustic first-order fields,

$$F_i^{\text{rad}} = -\partial_i U^{\text{rad}}, \quad \text{where} \quad U^{\text{rad}} = \frac{4\pi}{3} a^3 \left( f_0 \frac{1}{4} \kappa_f |p_1|^2 - f_1 \frac{3}{8} \rho_f |v_{j,1} v_{j,1}| \right). \quad (2.41a)$$

The monopole and dipole coefficients for polystyrene beads, which are among the most commonly used test particles, are

$$f_0 = 1 - \frac{\kappa_{\text{ps}}}{\kappa_f} = 0.468, \quad f_1 = \frac{2(\rho_{\text{ps}} - \rho_f)}{2\rho_{\text{ps}} + \rho_f} = 0.034. \quad (2.41b)$$

### Streaming drag

The field  $v_{i,2}$  which by our definition is a steady field, is called the streaming field. A particle with diameter  $a$  suspended in a fluid with a streaming field  $v_{i,2}$  will experience a Stokes drag force,

$$F_i^{\text{drag}} = 6\pi\eta a(v_{i,2} - v_p), \quad (2.42)$$

where  $v_{i,ps}$  is the position-dependent particle velocity.

### Acoustophoretic motion

The motion of particles is simply determined by Newton's second law,

$$\frac{4}{3}\pi a^3 \rho_p \frac{d}{dt} v_p = F_i^{\text{rad}} + F_i^{\text{drag}}. \quad (2.43)$$

To predict the acoustophoretic motion of particles in an acoustofluidic device, we solve Eq. (2.43) using a time-stepping algorithm.

Notice that for biological samples, the monopole and dipole coefficients are often lower than for polystyrene beads as they are acoustically more similar to water than most solids. Accordingly, the radiation force decreases, whereas the streaming drag does not depend on the particle properties only its size. This shifts the balance between the forces, and is part of what makes it difficult to focus biological samples with acoustophoresis.

### Acoustic energy density

As a measure of the energy in the fluid domain we introduce the acoustic energy density,

$$E_{\text{ac}}^{\text{fl}} = \frac{1}{4}\rho_f |v_{i,1} v_{i,1}| + \frac{1}{4}\kappa_f |p_1|^2, \quad (2.44)$$

which is the time-averaged mechanical energy over a single oscillation period  $T$ . When examining the resonant behavior of devices, we plot this as a function of a sweeping parameter - usually the frequency or one or more of the device dimensions. Peaks in such plots indicate fluid resonance conditions, which are the conditions that we typically study the acoustophoresis at.

#### 2.7.1 Strain energy density

In linear elastics the the strain energy density indicates the strain energy stored per volume,

$$U_m = \frac{1}{2} \sigma_{ik,1}^s : \epsilon_{ik,1}^m, \quad (2.45)$$

where the ":"-operator indicates the inner product of two tensors. We use this similarly to the fluid acoustic energy  $E_{\text{ac}}^{\text{fl}}$  as an indicator of resonances of a system. This additional indicator of resonance behavior is useful to determine whether a resonance peak observed for the fluid is also present in the surrounding solid, in which case we call it a system resonance. If not, we call the peak a pure-fluid resonance.

### 2.7.2 Electric energy density

In a linear dielectric the electric energy density is defined as

$$U_e = \frac{1}{2} D_{i,1} \cdot E_{i,1}, \quad (2.46)$$

For piezoelectric materials the total energy density within is defined as the sum of the strain energy density Eq. (2.45) and the negative electric energy,

$$U = U_m - U_e, \quad (2.47)$$

The energy density in the piezoelectric element and in the solid are both secondary to the acoustic fluid density as acoustophoresis only is determined by the latter. However, the acoustic energies in the surrounding solids and the piezoelectric element remain useful to provide an overview the distribution of energy within a system.

While we do not explicitly show resonance plots, we always use them to make sure we investigate the proper frequencies.

## 2.8 Hard-wall fluid acoustic eigenmodes

For a fluid cavity of width  $w$ , length  $l$  and height  $h$  surrounded by hard walls we define the three-index eigenmodes [65] with the pressure distributions

$$p(x, y, z) = p_a \cos\left(n_x \frac{\pi}{l}\right) \cos\left(n_y \frac{\pi}{w}\right) \cos\left(n_z \frac{\pi}{h}\right), \quad (2.48)$$

where  $p_a$  is the pressure magnitude and  $n_x, n_y, n_z = 0, 1, 2, \dots$  are the number of half wavelengths in directions  $x, y, z$ .

In an ideal hard-wall system these eigenmodes are found at the frequencies,

$$f_{n_x, n_y, n_z} = \frac{c_0}{2} \sqrt{\frac{n_x^2}{w^2} + \frac{n_y^2}{l^2} + \frac{n_z^2}{h^2}}. \quad (2.49)$$

In actual systems with hard walls, however, the eigenmodes of Eq. (2.48) are typically observed at slightly lower frequencies than the idealized one, both experimentally and numerically. The mismatch between the frequencies estimated with Eq. (2.49) and the observed ones is due to the walls moving slightly. Thus they do not satisfy the conditions for the ideal case, from which the Eq. (2.49) is derived.

The total pressure field building up near a resonance is in fact a superposition of the pressure field caused by the moving walls and a much larger contribution from idealized pressure field obeying the hard-wall condition. The closer the walls are to the ideal case, the larger the ratio is between the moving-wall contribution and the hard-wall contribution, and vice versa.

## 2.9 List of assumptions

In Table 2.1 we sum up the assumptions made in deriving the governing equations.

**Table 2.1:** List of assumptions made in the numeric model

Assumption	Applied in
Newtonian fluids	Eq. (2.2b)
Negligible body forces	Eq. (2.3a)
Small Linear displacements	Eq. (2.3b)
Negligible free charges in piezoelectric ceramics	Eq. (2.10)
Small acoustic perturbations	Eq. (2.17)
Negligible higher-order fields in perturbation series	Eq. (2.17)
Inviscid bulk fluid	Eq. (2.20)
$\lambda_f \gg a > \delta_{\text{visc}}$	Eq. (2.41)
Spherical particles	Eq. (2.41)
Isotropic solid attenuation	Eq. (2.26)
$Z^{\text{ac},s} \gg Z^{\text{ac},\text{air}}$	Eq. (2.34)
Ideal metal conductors	Eqs. (2.35) and (2.36)
Unyielding walls	Eq. (2.38a)
Partially yielding walls	Eq. (2.38c)
No-slip condition on walls	Eq. (2.38)
Approximated surface acoustic waves	Eq. (2.40)

## 2.10 Concluding remarks

Now that we have defined the governing equations and their linearizations, the boundary conditions and the auxiliary fields the complexity of non-idealized acoustofluidic devices is clear. At the boundary between a piezoelectric domain and a fluid domain, the pressure couples with the solid displacement, which in turn couples with the electric potential. All of these may vary in each of the three dimensions, making an analytical approach very difficult.

Therefore, we now move on to describing a numerical approach to solving the vast boundary value problem formed by the equations of this chapter using the finite element method in the modeling software COMSOL Multiphysics.

## Chapter 3

# Numerical modeling in COMSOL

In this chapter we go through the numerical implementation of the governing equations from the previous chapter. We describe the weak formulations of the governing equations, their implementation in the modeling software COMSOL Multiphysics, and briefly discuss the possibilities of calculating models using high performance cluster (HPC) computing. We then discuss a method for verifying numeric convergence of models, and introduce the concept of Bond matrices. We finish with an overview of possible tools to reduce the computational footprint of models while keeping them true to the physical devices they represent.

In Chapter 2 we used index notation over vector notation for the sake of brevity. As we move away from pure physics and into numerics we use vector notation in this chapter, as it offers a more compact and clearly defined scheme for the purposes described in this chapter, particularly Section 3.6.

### 3.1 Weak form of a general linear differential equation

The weak formulation is a discretized form of the governing equations that only need to be obeyed locally. We consider a general, linear differential equation for the generic scalar field  $g(\mathbf{r})$  of the domain  $\Omega$  with the known source term  $F(\mathbf{r})$ ,

$$\mathcal{T}\{g(\mathbf{r})\} = F(\mathbf{r}). \quad (3.1)$$

The field  $g(\mathbf{r})$  that satisfies the Eq. (3.1) at every point of the domain  $\Omega$  is called the *strong solution*. We define the defect  $d(\mathbf{r})$  as a measure of how well Eq. (3.1) is satisfied at point  $\mathbf{r}$ ,

$$d(\mathbf{r}) \equiv \mathcal{T}\{g(\mathbf{r})\} - F(\mathbf{r}). \quad (3.2)$$

For the strong solution the defect is by definition zero. To create a linear system of equations we introduce the concept of test functions  $\hat{g}$ , by dividing the domain  $\Omega$  into  $N$  slightly overlapping sub-domains each with a corresponding test function  $\hat{g}_n$  for  $n \in [1, N]$ . The field  $g(\mathbf{r})$  can thus be approximated as a linear combination of test functions  $\hat{g}_m$ , each weighted with a corresponding, scalar field coefficient  $c_n$

$$g(\mathbf{r}) \approx \sum_{n=1}^N c_n \hat{g}_n(\mathbf{r}). \quad (3.3)$$

A test function  $\hat{g}_m$  has compact support in sub-domain  $n$ , and takes on values between 0 and 1 determined by a piecewise polynomial of order  $p$ , whereas  $c_n$  make up the unknown weight functions. This resolution of the numeric domain into small elements is called the finite element method.

As a slightly weaker requirement than the strong solution, we demand the defect Eq. (3.2) to be zero within each domain  $n$ . The set of weight functions  $c_n$  satisfying this demand is called the *weak solution*. It can be seen that the limit of the weak solution for infinite domains,  $M \rightarrow \infty$ , is the strong solution, as each sub-domain becomes a point in the domain  $\Omega$ . We state the weak formulation demand by taking the inner product of the field Eq. (3.3) with the defect Eq. (3.2)

$$\langle \hat{g}_m(\mathbf{r}), d(\mathbf{r}) \rangle = 0 \forall m, \quad (3.4)$$

where the inner product of two functions is defined as

$$\langle a(\mathbf{r}), b(\mathbf{r}) \rangle \equiv \int_{\Omega} a(\mathbf{r})b(\mathbf{r})dV. \quad (3.5)$$

Writing out Eq. (3.4), by using the defect definition Eq. (3.2) and the weak field approximation Eq. (3.3) yields

$$\sum_{m=1}^M \left\langle \hat{g}_m(\mathbf{r}), \left( \mathcal{T} \left\{ \sum_{n=1}^N c_n \hat{g}_n(\mathbf{r}) \right\} - F(\mathbf{r}) \right) \right\rangle = 0 \quad \forall m. \quad (3.6)$$

We use that  $\mathcal{T}$  is a linear operator, preserving additivity  $\mathcal{T} \left\{ \sum_{n=1}^N c_n \hat{g}_n(\mathbf{r}) \right\} = \sum_{n=1}^N \mathcal{T} \{ c_n \hat{g}_n(\mathbf{r}) \}$

$$\sum_{m=1}^M \sum_{n=1}^N \left\langle \hat{g}_m(\mathbf{r}), \mathcal{T} \{ \hat{g}_n(\mathbf{r}) \} \right\rangle \sum_{n=1}^N c_n - \sum_{m=1}^M \left\langle \hat{g}_m(\mathbf{r}), F(\mathbf{r}) \right\rangle = 0 \quad \forall m. \quad (3.7)$$

We recognize Eq. (3.7) as a matrix equation

$$\mathbf{K}\mathbf{c} - \mathbf{F} = \mathbf{0}, \quad (3.8)$$

with the stiffness matrix  $\mathbf{K} = \sum_{m=1}^M \sum_{n=1}^N \left\langle \hat{g}_m(\mathbf{r}), \mathcal{T} \{ \hat{g}_n(\mathbf{r}) \} \right\rangle$  derived from the governing equations, field coefficients vector  $\mathbf{c} = \sum_{n=1}^N c_n$ , and forcing term vector  $\mathbf{F} = \sum_{m=1}^M \left\langle \hat{g}_m(\mathbf{r}), F(\mathbf{r}) \right\rangle$ . By solving Eq. (3.8) through straightforward matrix inversions for  $\mathbf{c}$  the weak solution is found;

$$\mathbf{c} = \mathbf{K}^{-1}\mathbf{F}, \quad (3.9)$$

## 3.2 Continuity equations in weak form

We introduced the weak form for a general linear differential equation, but in the following we will assume that the modeled equations can be rewritten to continuity form, Eq. (3.10);

$$\nabla \cdot \boldsymbol{\Sigma} - \mathbf{F} = \mathbf{0}. \quad (3.10)$$



**Table 3.1:** Generalized fluxes and source terms of the governing equations of Chapter 2.

Domain	Equation name	Number	Field	Generalized flux $\Sigma$	Source term $F$
Fluid - full	1st order Fluid mass conservation	(2.18)	$\rho_1$	$\mathbf{v}_1$	$-i\omega\kappa p_1$
Fluid - full	1st order Navier-Stokes	(2.19)	$\mathbf{v}_1$	$\boldsymbol{\sigma}_1^f$	$-i\omega\rho_0\mathbf{v}_1$
Fluid - effective	Helmholtz' equation	(2.20)	$p_1$	$\nabla p_1$	$k^2 p_1$
Fluid - full	2nd order Fluid mass conservation	(2.23)	$\rho_2$	$\rho_0\mathbf{v}_2 + \rho_1\mathbf{v}_1$	0
Fluid - full	2nd order Navier-Stokes	(2.24)	$\mathbf{v}_2$	$\boldsymbol{\sigma}_2^f - \rho_0\mathbf{v}_1\mathbf{v}_1$	0
Solid	Cauchy momentum equation	(2.25)	$\mathbf{u}_1$	$\boldsymbol{\sigma}_1^s$	$\rho\partial_t^2\mathbf{u}_1$
Piezo	Cauchy momentum equation	(2.25)	$\mathbf{u}_1$	$\boldsymbol{\sigma}_1^{pz}$	$\rho\partial_t^2\mathbf{u}_1$
Piezo	Gauss' Law	(2.27)	$\phi_1$	$D_1$	$\rho_{el}$

This holds for each of the governing equations outlined in Chapter 2, with generalized flux  $\Sigma$  and source term  $F$  defined as shown in table Table 3.1.

We let the summations over and spatial dependence of test functions  $\hat{g}$  be implicit for brevity, and insert the continuity form Eq. (3.10) in the defect requirement Eq. (3.4)

$$\int_{\Omega} \hat{g} \nabla \cdot \Sigma - \hat{g} F \, dV = 0. \quad (3.11)$$

We employ the vector calculus identity for products of a scalar and a vector

$$\nabla \cdot (\hat{g} \Sigma) = \Sigma \cdot \nabla \hat{g} + \hat{g} \nabla \cdot \Sigma, \quad (3.12)$$

and Gauss' theorem,

$$\int_{\Omega} \nabla \cdot F \, dV = \int_{\delta\Omega} F \cdot \mathbf{n} \, dA, \quad (3.13)$$

to rewrite Eq. (3.11) to

$$\oint_{\partial\Omega} \hat{g} \mathbf{n} \cdot \Sigma \, dA + \int_{\Omega} -\Sigma \cdot \nabla \hat{g} - \hat{g} F \, dV = 0. \quad (3.14)$$

This moves the spatial derivative from the generalized flux to the piecewise-polynomial test function, for which the derivatives are analytically known. Inserting the appropriate generalized flux and source terms written in Table 3.1 in Eq. (3.14), all the governing equations can be written in weak form.

### 3.2.1 Boundary conditions in weak form

Neumann boundary conditions are used when the flux  $\mathbf{n} \cdot \Sigma$  over a boundary  $\delta\Omega$  is a known function  $\mathbf{h}(\mathbf{r})$ . Implementing them in the weak form is merely a question of inserting the known function in the surface integral of Eq. (3.14).

$$\oint_{\partial\Omega} \hat{g} \mathbf{n} \cdot \Sigma \, dA = \oint_{\partial\Omega} \mathbf{h}(\mathbf{r}) \, dA. \quad (3.15)$$

When no boundary condition is explicitly defined on a surface, the flux is assumed to be zero  $\oint_{\partial\Omega} \hat{g} \mathbf{n} \cdot \Sigma = 0$ .

In Dirichlet conditions, the field value  $g$  along a boundary  $\delta\Omega$  is known to be some value  $j$ . To implement them we introduce the Lagrange multiplier  $\lambda$  that also has a set of test functions, which in the following is implied to be the sum over  $N$ ,

$$\lambda = \sum_{n=1}^N b_n \hat{\lambda}_n, \quad (3.16)$$

and introduce the constraint  $R$

$$R = g - j = 0. \quad (3.17)$$

For the Dirichlet condition to hold, we demand the inner product of the two to be zero

$$\oint_{\delta\Omega} \hat{\lambda}_n R \, dA = 0, \quad (3.18)$$

which is the weak formulation of the Dirichlet condition. We add this to Eq. (3.14) and insert the freely varying Lagrange multiplier  $\lambda$  as the flux

$$\oint_{\delta\Omega} \hat{g} \lambda + \hat{\lambda}_n (g - j) \, dA + \int_{\Omega} -\boldsymbol{\Sigma} \cdot \nabla \hat{g} - \hat{g} \mathbf{F} \, dV = 0. \quad (3.19)$$

Because the test function  $\hat{\lambda}$  only appears in the surface integral Eq. (3.18) is enforced by Eq. (3.19), while the Lagrange multiplier  $\lambda$  takes on the role of the flux  $\mathbf{n} \cdot \boldsymbol{\Sigma}$  and settles to the value that satisfies the weak Dirichlet condition. Eqs. (3.15) and (3.19) are for the cases of Neumann or Dirichlet conditions on all surfaces  $\delta\Omega$ . However, most problems consist of a combination of the two, and the full weak expression for combined problems is

$$\oint_{\delta\Omega_D} \hat{g} \lambda + \hat{\lambda}_n (g - j) \, dA + \oint_{\delta\Omega_N} \hat{g} \mathbf{h}(\mathbf{r}) \, dA + \int_{\Omega} -\boldsymbol{\Sigma} \cdot \nabla \hat{g} - \hat{g} \mathbf{F} \, dV = 0, \quad (3.20)$$

where  $\delta\Omega_D$  are all surfaces with Dirichlet conditions and  $\delta\Omega_N$  are all free surfaces and surfaces with Neumann conditions.

### 3.3 COMSOL Multiphysics

When creating numeric models in COMSOL Multiphysics we manually take care of some parts while the software automatically takes care of the rest:

We draw the devices we wish to model and designate each drawn domain to be one of the four categories listed in Table 3.1, with the corresponding fields. We then define the types and the allowable dimensions of mesh elements for domains, boundaries and points. COMSOL then automatically builds a mesh that meets these the conditions.

We designate a material to each domain, determining the viscosities, mass densities, elasticities, and so on. We then input boundary value problems of the type shown in Eq. (3.20), with the generalized fluxes and source terms of Table 3.1 using the *Weak form PDE module* in COMSOL, and define the order of test functions for each field value. These definitions along with the meshed geometry are used by COMSOL to define the test functions.

Finally, we define the parameters for COMSOL to solve. Typically, this would be a range of frequencies to investigate the resonance behavior of a system. During solving we track this behavior with probes measuring the acoustic energies of the fluid, Eq. (2.44), and the solids, Eq. (2.45), and the electric energies of the piezoelectric element, Eq. (2.46). COMSOL then sets up the system matrix, solves the matrix equation, Eq. (3.8), and outputs the weak solutions  $g^{\text{weak}} = \sum_n^N c_n \hat{g}_n$ , which we post-process to study the system.

In Fig. 3.1 we illustrate the numerical process in COMSOL with a flow-chart including particular steps in the process, the user input, and the final output.

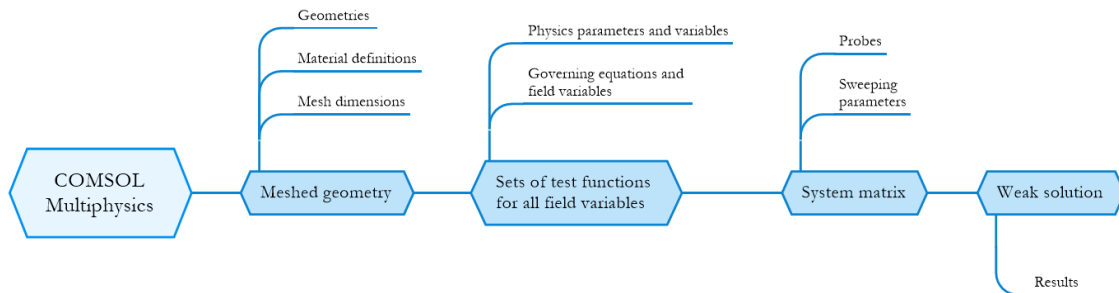


**Figure 3.1:** Flow-chart of the steps involved in creating and studying a numerical model. The hexagons show the principal steps that COMSOL takes care of, while user inputs are shown above the hexagons and the final output is shown below.

### 3.3.1 Model meshing

When meshing devices we obey a rule of thumb stating each wavelength should be resolved by 6 nodes. This helps avoid the masking of spatial frequencies as lower frequencies due to insufficient resolution, known as aliasing.

In acoustic pressure modeling of fluids we apply this rule of thumb to the compressional wavelength not the minute transverse wavelength. In solids, however, we must resolve the shortest of the transverse wavelengths in a system. Hence, a stiff material such as silicon with high speeds of sound and long wavelengths have far less degrees of freedom than a soft material such as PDMS.

In Fig. 3.2 we illustrate the vast difference in the number of mesh elements required to model the acoustic fields at of a  $2 \times 2 \times 2 \text{ mm}^3$  cube for a selection of materials. Note that the numbers listed are the mesh elements needed if using second-order test functions.

The cubes meshed in Fig. 3.2 are all meshed a tetrahedral mesh. This is the default mesh of COMSOL and many other meshing programs as the unevenly spaced distribution of the mesh nodes helps avoid solutions that artificially take the shape of the mesh. Other meshes may be advantageous to use, but require more thought given to the meshing process. In Chapter 6 we use a swept mesh which enables an even spatial mesh resolution.

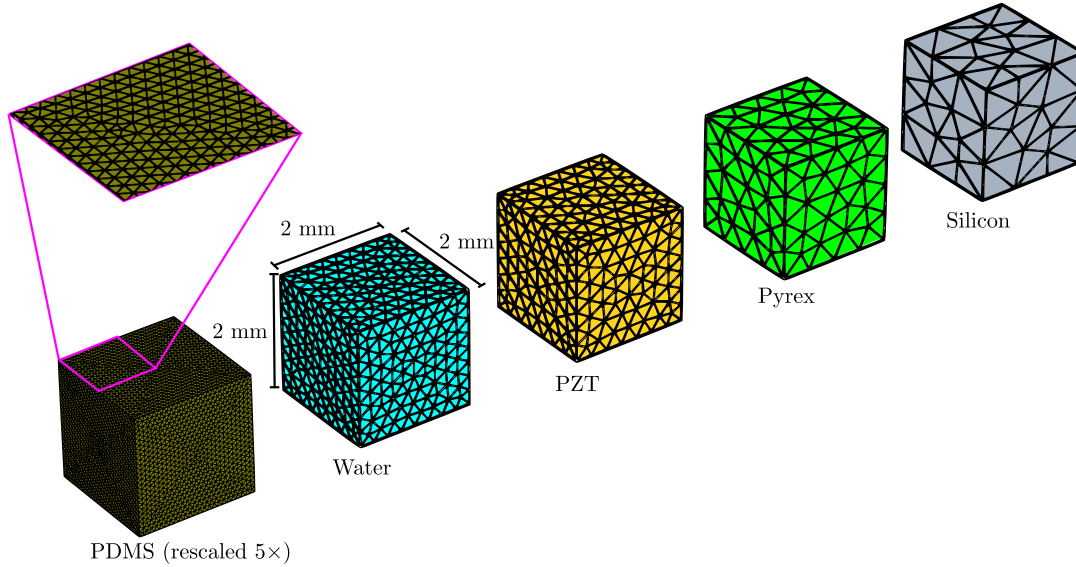


**Figure 3.2:** Triangular meshes needed to resolve the shortest relevant acoustic wavelength at 2 MHz in materials of increasing acoustic impedance. The resolved wavelength and the resulting number of mesh elements is shown for each material. To render it visible the mesh size in PDMS has been increased by a factor of five in the sketch. Also, the resolved wavelength in water is the compressional one corresponding to the mesh required for effective pressure modeling.

### 3.3.2 Number of degrees of freedom

A crucial determinant of the feasibility of calculating a numeric model is the amount of degrees of freedom (DOF) in the system. The DOF is the total amount of computational points COMSOL must define necessary to define all the test functions given the number of domains  $N$  and order  $p$ .

The number of DOF is proportional to the numbers of mesh elements shown in Fig. 3.2, but depends on the acoustic fields present in a material. Water for instance is completely acoustically defined by the scalar pressure field, whereas solids need the velocity vector field to be completely defined. Piezoelectric materials such as lead zirconium titanate (PZT) additionally require the electric potential field adding to the DOF. Thus, the PZT cube of Fig. 3.2 ends up adding more DOF to a problem than the water cube, despite being having fewer mesh elements, as shown in Table 3.2. The table also illustrates why the lossy wall is a popular alternative to modeling PDMS.

**Table 3.2:** Acoustic wavelengths, mesh elements and degrees of freedom required to resolve the acoustics - and in PZT the electric potential - of some of the materials used in this thesis.

	PDMS	Water	PZT	Pyrex	Silicon
Resolved wavelength	50 $\mu\text{m}$	748 $\mu\text{m}$	966 $\mu\text{m}$	1621 $\mu\text{m}$	2618 $\mu\text{m}$
Triangular elements	$29 \times 10^6$	$8 \times 10^3$	$4 \times 10^3$	$8 \times 10^2$	$2 \times 10^2$
number of kDOF	$10^9$ (estimated)	12.2	24.1	4.2	1.3

The number of degrees of freedom determines the size of the stiffness matrix  $\mathbf{K}$  that must be

inverted to solve the matrix equation Eq. (3.8), and thus the memory required to solve a given problem. The scaling between the amount of DOF  $n$  and the time to solve  $t_{\text{solve}}$  a problem is unfortunately a power law. In Fig. 3.3 we show the time  $t_{\text{solve}}$  as a function of the number  $n$ , for an early version of the numeric model described in Chapter 6.

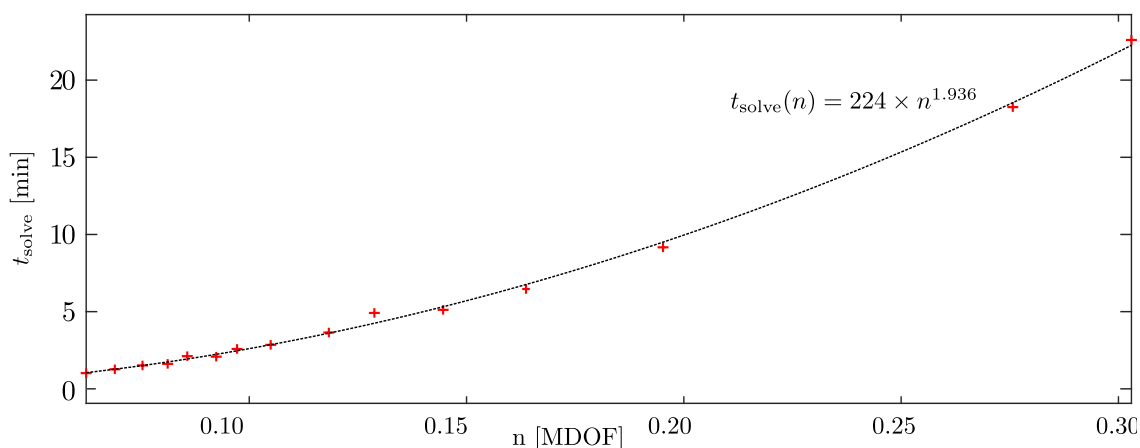


**Figure 3.3:** Line plot of the solution time  $t_{\text{solve}}$  as a function of the amount of degrees of freedom,  $n$ , in the system in millions of degrees of freedom (MDOF), for an early iteration of the model described in Chapter 6. The dotted line is a fitted power function.

Note that the relation plotted in Fig. 3.3 is particular to this device design. This relation is mainly useful for indicate the approximate time requirement if scaling up this particular design. Among other things this has to do with the amount of non-zero elements in the stiffness matrix  $\mathbf{K}$  but a further discussion of this is beyond the scope of this thesis.

### 3.4 High performance cluster computing

We typically aim to keep models solvable on a powerful desktop workstation with 128 GB RAM and 2 3.46 GHz processors. However, some devices are too complex to be represented well by models of this scale. The device in Chapter 6 is a good example of a problem with such a device. It is inherently asymmetric, has large dimensions for an acoustofluidic device, and is run at a high frequency leading to small wavelengths that must be resolved. To compute such models we use the High Performance Cluster (HPC) at DTU [66] that accommodates 100 cores with 25 GB RAM each for computations. The many computational cores enable us to model much larger systems, as the physical memory available to the solver is the limiting factor when running numerical simulations. Using the HPC, we have done simulations on a  $\text{mm}^3$ -sized device run at 49 MHz. This resulted in a model with 4.6 million degrees of freedom, which was solved across 80 nodes of 25 GB RAM in the course of 14 hours. While this is numerically costly and very time-consuming, the simulations illustrated an in-plane streaming pattern that a 2D model could not reproduce. The use of a HPC thus provided otherwise unobtainable, although costly, insight. The device in question is described in Chapter 6.

### 3.5 Convergence analysis

Each combination of a number of sub-domains  $N$  and an order  $p$  of the test functions  $\hat{g}_n$ , gives a unique solution  $g$  to the weak form equation Eq. (3.20). Ideally, the solutions should converge toward the strong solution for increasing  $N$  and  $p$ , as test function  $\hat{g}_n$  approximates the actual field  $g$  increasingly well. To test how well the hypothesis holds we plot the average relative variances  $C(g)$  of calculated fields  $\hat{g}_n$ , as functions of increasing number of elements,

$$C(g) \equiv \frac{\int_{\Omega} (|\hat{g}_n| - |g|)^2 dA}{\int_{\Omega} |g|^2 dA}. \quad (3.21)$$

Here,  $g$  is ideally the analytically known strong solution, but as that is seldom known, we instead use a reference solution, with the largest number  $N$  we can model. If we find that the solutions largely converge to this reference solution, we can conclude that they in general converge well. Fig. 3.4 is an example of what the average relative variance plots as function of mesh generally looks like, for one of the models described in Chapter 4.

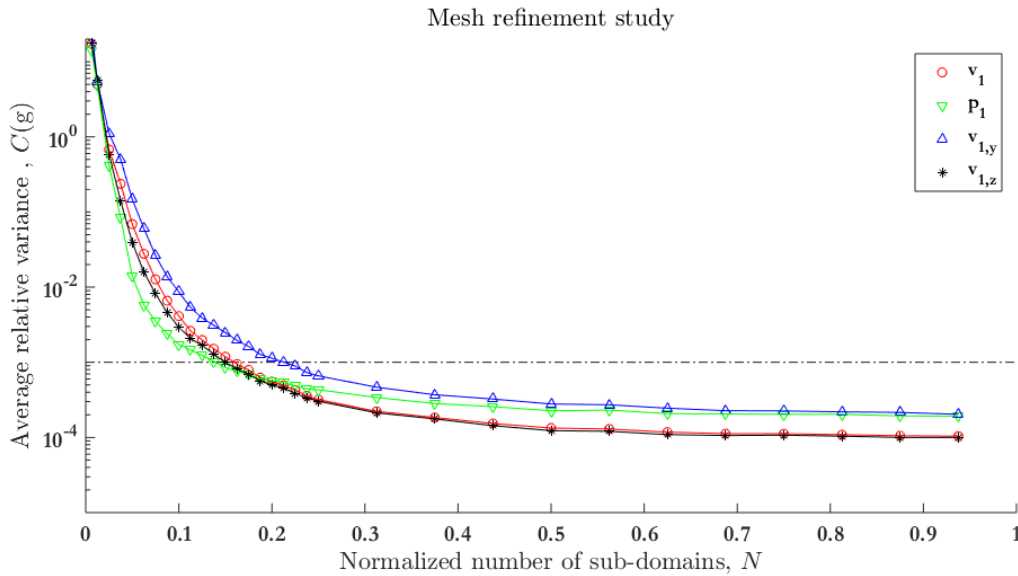


**Figure 3.4:** Line plots of the average relative variance  $C(g)$  for the acoustic fields in a series of simulations with increasing normalized number of sub-domains  $N$ , referenced against the solution with  $N = 1$ . The dotted line indicates an average relative variance of less than  $1 \times 10^{-3}$ . Adapted from [1]

The trend shown in Fig. 3.4 with values of  $C(g)$  well down in the low orders of magnitude and the slopes of the graphs gradually leveling out indicate that the solution has converged. Hence further increases in  $N$  are not warranted as this only adds computational cost without the benefit of better precision. A similar analysis can be carried out, to find orders  $p$  that are good compromises between numeric precision and footprint. Convergence analyses are carried out for the mesh sizes for each of the models in Chapters 4 to 7, but not shown as they are trivial checks.

### 3.6 Material parameters and Bond matrices

In Section 2.2.2 we mention the directional dependence of anisotropic materials, and discuss the transformation of  $n$ -order tensors, using  $n$  transformation matrices  $R_i$ . Numerically this is tedious to implement, so we wish to obtain expressions with fewer terms formulated in vector notation. For a first-order tensor or vector, the transition from index notation to vector notation is straightforward

$$\mathbf{r}' = \mathbf{R}\mathbf{r}, \quad (3.22)$$

where  $\mathbf{R} = R_{ik}$  is the transformation matrix. For the 6-component Voigt stress vector  $\boldsymbol{\sigma}_V = \sigma_\alpha$ , we introduce the  $6 \times 6$  Bond matrices  $\mathbf{M}_\sigma$  and  $\mathbf{M}_\epsilon$ , transforming stress and strain

$$\boldsymbol{\sigma}'_V = \mathbf{M}_\sigma \boldsymbol{\sigma}_V, \quad (3.23)$$

$$\boldsymbol{\epsilon}'_V = \mathbf{M}_\epsilon \boldsymbol{\epsilon}_V, \quad (3.24)$$

Unlike  $\mathbf{R}$ , Bond Matrices are not symmetric, and the inverse of the matrix does not equal the transpose. Also, stress and strain are not transformed using the same matrix, due to the factor 2 in shear elements of the Voigt strain. To derive the form of the Bond-stress-transformation matrix, we consider the transformation of the stress tensor in index notation,

$$\sigma'_{ik} = R_{il}R_{km}\sigma_{lm}. \quad (3.25)$$

By elementwise inspection of Eq. (3.25) we can deduce each element of  $M_{\alpha\beta}$  in terms of the rotation matrix  $R_{ik}$

$$\mathbf{M}_\sigma = \begin{pmatrix} R_{1,1}^2 & R_{1,2}^2 & R_{1,3}^2 & 2R_{1,2}R_{1,3} & 2R_{1,1}R_{1,3} & 2R_{1,1}R_{1,2} \\ R_{2,1}^2 & R_{2,2}^2 & R_{2,3}^2 & 2R_{2,2}R_{2,3} & 2R_{2,1}R_{2,3} & 2R_{2,1}R_{2,2} \\ R_{3,1}^2 & R_{3,2}^2 & R_{3,3}^2 & 2R_{3,2}R_{3,3} & 2R_{3,1}R_{3,3} & 2R_{3,1}R_{3,2} \\ R_{2,1}R_{3,1} & R_{2,2}R_{3,2} & R_{2,3}R_{3,3} & R_{2,2}R_{3,3} + R_{2,3}R_{3,2} & R_{2,3}R_{3,1} + R_{2,1}R_{3,3} & R_{2,1}R_{3,2} + R_{2,2}R_{3,1} \\ R_{1,1}R_{3,1} & R_{1,2}R_{3,2} & R_{1,3}R_{3,3} & R_{1,2}R_{3,3} + R_{1,3}R_{3,2} & R_{1,3}R_{3,1} + R_{1,1}R_{3,3} & R_{1,1}R_{3,2} + R_{1,2}R_{3,1} \\ R_{1,1}R_{2,1} & R_{1,2}R_{2,2} & R_{1,3}R_{2,3} & R_{1,2}R_{2,3} + R_{1,3}R_{2,2} & R_{1,3}R_{2,1} + R_{1,1}R_{2,3} & R_{1,1}R_{2,2} + R_{1,2}R_{2,1} \end{pmatrix}. \quad (3.26)$$

With the Bond-stress-transformation matrix known, the stress state can be found for any rotated coordinate system, where the rotation matrix  $R_i$  is known. Furthermore, we can determine the elasticity, coupling and permittivity tensors of anisotropic materials, using the  $\mathbf{M}_\sigma$ <sup>1</sup>, leading to the following three transformation relations;

$$\mathbf{C}' = \mathbf{M}_\sigma \mathbf{C} \mathbf{M}_\sigma^{-T}, \quad (3.27)$$

$$\mathbf{e}' = \mathbf{R} \mathbf{e} \mathbf{M}_\sigma^T, \quad (3.28)$$

$$\boldsymbol{\epsilon}' = \mathbf{R} \boldsymbol{\epsilon} \mathbf{R}^T. \quad (3.29)$$

<sup>1</sup>The derivations of these are listed in the appendix in Section B.

## 3.7 Model reductions

As mentioned before, numerical modeling is a balance between accurately representing a physical problem and keeping the numerical footprint of the model within a reasonable range. Here we go through some tools that in some cases can reduce model size without compromising the representability of the model, and make note of when they should not be applied.

### 3.7.1 Translational invariance

The bulk of acoustofluidic devices are ideally translationally invariant along the length of the channel. Such devices can be studied in detail using only two-dimensional (2D) models of the cross-section, reducing the footprint enormously. Of course, in physical devices there will always be some variance along the channel due to imperfections in materials or fabrication methods and one often finds that the 2D model is only representative for a portion of the channel [55]. As these imperfections are impossible to fully include in models, cross-sectional 2D studies remain a viable tool for studying channels with long, straight geometries.

### 3.7.2 Symmetries

Many devices inherently contain symmetries or anti-symmetries around points, lines or planes. These can be used to partition the numeric model accordingly while inserting boundary conditions on the cut-lines or planes, reducing the number of degrees of freedom to a fraction of the entire model. For highly symmetric devices, the reduction can be as much as 3/4 of the model, [27, 58]. The conditions should only be used with absolute certainty that the model system is symmetric, as the conditions will introduce always yield a symmetric result. One can thus easily induce unwanted artificial symmetries in numerical simulations by accident.

### 3.7.3 Perfectly matched layers

In computations with inert regions that do not reflect waves traveling into them, perfectly matched layers (PMLs) can reduce the model footprint by absorbing all waves traveling through them. In numeric models they replace part of a domain, usually of larger size than the PML region itself. Mathematically a PML is a region  $\Omega_{\text{PML}}$  with the same material properties as the one it replaces, but with a complex coordinate transformation of spatial derivatives and integral measures inserted in the auxiliary fields, boundary conditions, and the weak formulation governing equations,

$$\partial x_i \rightarrow \partial \tilde{x}_i = \frac{1}{1 + i s(\mathbf{r})} \partial x_i, \quad (3.30a)$$

$$dx_i \rightarrow d\tilde{x}_i = [1 + i s(\mathbf{r})] dx_i. \quad (3.30b)$$

Here  $s(\mathbf{r})$  is a continuous function that has compact support in the PML regions, attains some maximum damping parameter  $k_{\text{PML}}$  at the far perimeter of the PML, is differentiable, and has no slope at the boundary between the PML and the remainder of the model. A second-order polynomial defined only in the PML region fits this well, here shown for the 1D case

$$s(x) = \frac{(x - x_{\text{PML}})^2}{L_{\text{PML}}^2} k_{\text{PML}} \text{ for } x \in \Omega_{\text{PML}}. \quad (3.30c)$$



---

The parameter  $k_{\text{PML}}$  must be tuned to the specific problem; Too high values of  $k_{\text{PML}}$  cause reflections at the interfaces between the physical domains and the PML domains. Too low values on the other hand only partially dampens waves, causing reflections from the PMLs's outer perimeters.

### **3.8 Concluding remarks**

We have now described both the boundary value problem that defines the physics of an acoustofluidic device and how to implement it as a finite element problem in weak form in COMSOL Multiphysics. We are thus ready to create the first iteration of the numerical model that makes up the main result of this thesis. We introduce the first iteration and use it to study the boundary conditions mentioned in Section 2.6.5.



## Chapter 4

# 2D Model of a bounded fluid domain

In this chapter we present the initial stage of the numeric model that will be expanded further in terms of included materials and physical effects in the course of the following chapters. We also present a study of the validity of a set of approximative boundary conditions often used to simplify numeric modeling of acoustofluidic devices, carried out using the model at this point. Specifically we compare how well the fluid acoustics of devices driven by surface acoustic waves with either glass and silicone rubber lids can be modeled using approximate conditions. The majority of the results presented in this paper can also be found in the article journal *Modeling of microdevices for SAW-based acoustophoresis - a study of boundary conditions* by [N. R. Skov](#) and H. Bruus [1] (PDF, DOI:[10.3390/mi7100182](https://doi.org/10.3390/mi7100182)), which is enclosed in full at the end of this chapter. However, the text of this chapter is a reformulation and in some parts extends beyond the paper.

### 4.1 Motivation

To recapitulate Section 1.4 numeric models are a great tool to complement experimental work. Therefore, we wish to establish a numeric model capable of predicting the acoustophoretic behavior of a device with any degree of complexity. To achieve this we start from a simple two-dimensional (2D) model which we iteratively improve upon and compare to current and past experiments as well as to analytical expressions when available to check its validity, as described in this and the following chapters. To ensure the leanest possible model going forward we here investigate whether a particular set of boundary conditions can be used to save on computational costs.

#### 4.1.1 Study of reduced-model system

When making a numeric model it is necessary to strike a balance between confinement and representativity. On one hand the computational cost and complexity of the model must be kept down by using approximations and idealizations whenever possible. On the other hand it is vital that the simplifications do not change the defining characteristics of a problem lest the model no longer be applicable to that certain problem. Here we wish to examine two approximate boundary conditions defined in [65] that are commonly used in acoustofluidics [30, 52, 53, 67, 27, 48, 68, 69]

instead of modeling the solids surrounding the fluid. The boundary conditions in question are the hard-wall and the lossy-wall conditions that are used in reduced models. In these the interactions between the fluid chamber and the surrounding medium is approximated by the boundary conditions without including said medium in the calculations, as described in Section 2.6.5. The hard wall condition emulates the presence of infinitely hard walls reflecting all incoming waves while the lossy wall conditions emulates a partially absorbing material that reflects a portion of incident waves proportional to the acoustic impedance ratio between the fluid and the medium.

## 4.2 Model systems

For each of the boundary conditions we set up two parallel 2D models: the reduced models *R1* and *R2* and the full models *F1* and *F2* shown in Fig. 4.1. The models are considered isothermal and all fluid parameter values are taken at 25 °C. In the reduced models we include a water domain of

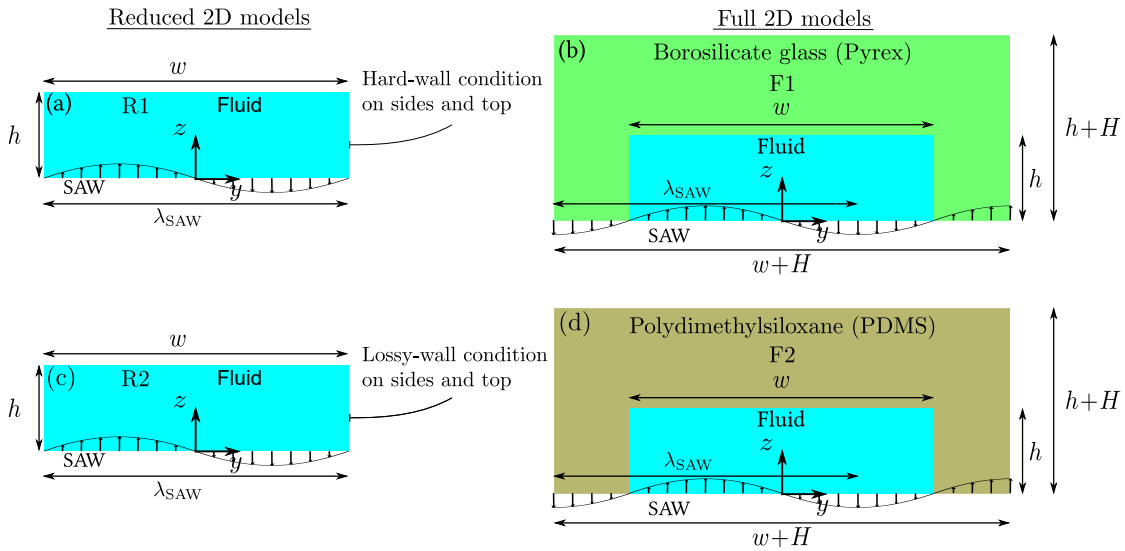


**Figure 4.1:** The four two-dimensional (2D) numeric models investigated. (a) The reduced model, R1, consists solely of a  $w$ -by- $h$  fluid domain bounded by effective boundary conditions on the sides and the top wall approximating solid motion. On the bottom surface an analytic expression for a standing surface acoustic wave field is applied. (b) In the full model, F1, a fluid domain of the same dimension is bounded on the sides and the top wall by an isotropic solid of width  $w + H$  and height  $h + H$ . (c) R2 is like R1 but with the lossy-wall condition. (d) F2 is like F1 but defined in PDMS, . Adapted from [1]

area  $w \times h$  governed by the first-order acoustic fluid equations Eqs. (2.18) and (2.19),

$$\nabla \cdot \mathbf{v}_1 + i\omega\kappa p_1 = 0, \quad (4.1)$$

$$\nabla \cdot \boldsymbol{\sigma}_1^f + i\omega\rho_0 \mathbf{v}_1 = \mathbf{0}. \quad (4.2)$$

On the sides and roof of the microchannel approximate boundary conditions are applied. In R1 we use the hard-wall condition Eq. (2.38a)

$$\mathbf{n} \cdot \mathbf{v}_1 = 0, \quad (4.3a)$$

and in R2 we use the lossy-wall condition Eq. (2.38c),

$$\mathbf{n} \cdot \mathbf{v}_1 = \frac{1}{Z_s^{\text{ac}}} p_1. \quad (4.3b)$$

Ideally, R1 and R2 should yield the same results as the full model simulations in F1 and F2 respectively. The model is driven from the bottom surface by a Dirichlet condition fixing the velocity field  $v_{i,1}$  to the analytical expression of a SAW described in Eq. (2.40),

$$u_{y,pz} = 0.6u_0 e^{-C_d y} \left[ \sin \left( \frac{-2\pi(y - w/2)}{\lambda_{\text{SAW}}} + \omega t \right) + \sin \left( \frac{-2\pi(w/2 - y)}{\lambda_{\text{SAW}}} + \omega t \right) \right], \quad (4.4a)$$

$$u_{z,pz} = -u_0 e^{-C_d y} \left[ \cos \left( \frac{-2\pi(y - w/2)}{\lambda_{\text{SAW}}} + \omega t \right) + \cos \left( \frac{-2\pi(w/2 - y)}{\lambda_{\text{SAW}}} + \omega t \right) \right]. \quad (4.4b)$$

In F1 and F2 the water domain is surrounded on the sides and top by an isotropic solid governed by Cauchy's momentum equation Eq. (2.25)

$$\nabla \cdot \boldsymbol{\sigma}_1^s + \omega^2 \rho_s \mathbf{u}_1 = \mathbf{0}. \quad (4.5)$$

In the full models the analytical SAW actuation is applied along the bottom of the solid and of the fluid. The solid has a height of  $H$  and a width of  $\frac{1}{2}H$  on either side of the fluid, and the two are coupled through the normal velocity and stress continuity conditions Eq. (2.32).

$$\mathbf{n} \cdot \mathbf{v}_1 = -i\omega \mathbf{n} \cdot \mathbf{u}_1, \quad (4.6a)$$

$$\mathbf{n} \cdot \boldsymbol{\sigma}_1^s = \mathbf{n} \cdot \boldsymbol{\sigma}_1^f. \quad (4.6b)$$

On the interface between the surrounding air and the solid, the no-stress condition Eq. (2.34)

$$\mathbf{n} \cdot \boldsymbol{\sigma}_1^s = \mathbf{0} \quad (4.7)$$

is applied. The solid in F1 is borosilicate glass (Pyrex) whereas the solid in F2 is polydimethylsiloxane rubber (PDMS). The thicknesses  $H$  were chosen to range from the size of a thin capillary tube (60  $\mu\text{m}$ ) through microscope slide thickness (600  $\mu\text{m}$ ) up to a bulk slab of glass (1500  $\mu\text{m}$ ).

#### 4.2.1 Perfectly matched layers

The thicknesses we've used in the full PDMS model F2 in the article are all smaller than the 3 mm damping length of PDMS at 6.65 MHz, as it is not feasible to model such large dimensions of PDMS, confer Fig. 3.2. Following the publication of our paper [1], we added perfectly matched layers to F2 as shown in Fig. 4.2, to also represent devices with dimensions larger than the 3-mm

**Table 4.1:** Key parameters of the numeric model presented here. Only model-specific parameters are included. For material parameters we refer to [1].

Quantity	Symbol	Unit	Value
Water width	$w$	$\mu\text{m}$	600
Water height	$h$	$\mu\text{m}$	125
Material thickness	$H$	$\mu\text{m}$	60-1800
SAW wavelength	$\lambda_{\text{SAW}}$	$\mu\text{m}$	600
SAW displacement amplitude	$u_0$	nm	0.1
On-resonance frequency	$f_{\text{res}} = \frac{2w}{c_0}$	MHz	1.24
On-resonance angular frequency	$\omega_{\text{res}} = 2\pi f_{\text{res}}$	Mrad/s	7.79
Off-resonance frequency	$f_{\text{off}}$	MHz	6.65
Off-resonance angular frequency	$\omega_{\text{res}} = 2\pi f_{\text{off}}$	Mrad/s	41.76
PML-domain width	$L_{\text{PML}}$	$\mu\text{m}$	100
PML damping factor	$k_{\text{PML}}$	1	20

damping length. We follow the principle outlined in Section 3.7.3 and add complex transformations Eq. (3.30) of the partial derivatives and integral measures of the model,

$$\partial x_i \rightarrow \partial \tilde{x}_i = \frac{1}{1 + i s(\mathbf{r})} \partial x_i, \quad dx_i \rightarrow d\tilde{x}_i = [1 + i s(\mathbf{r})] dx_i. \quad (4.8)$$

In this model the function  $s(\mathbf{r})$  was chosen to be a sum of two quadratic functions.

$$s(y, z) = \left( \frac{(z - z_{\text{PML}})^2}{L_{\text{PML}}^2} + \frac{(y - y_{\text{PML}})^2}{L_{\text{PML}}^2} \right) k_{\text{PML}} \text{ for } (y, z) \in \Omega_{\text{PML}}. \quad (4.9)$$

Note that the PML was only applied in the model yielding the results shown in Fig. 4.7

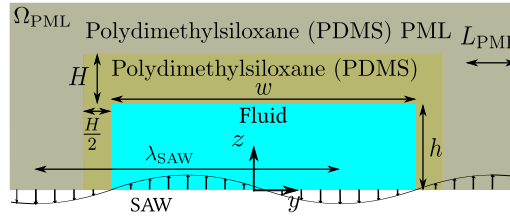


**Figure 4.2:** F2 PML-PDMS model. The full model representing PDMS devices larger than the 3-mm damping length of PDMS at 6.65 MHz. An F2 model with  $H = 100 \mu\text{m}$ , with an added 100- $\mu\text{m}$ -thick layer of PML-PDMS.

## 4.2.2 Model check

We do a convergence analysis and see that the results converge towards a single solution as the mesh is increased as outlined in Section 3.5. To further study the model we check the linear elasticity assumption and compare the calculated acoustic pressure of the fluid in model F1 at the theoretical horizontal half-wave eigenfrequency with the first analytic eigenmode for hard-wall systems.

### Linear elasticity check

The constitutive relation used relies on an assumption of the stresses of the solid being below the elastic limit, which is the cut-off point for the linear relationship between stress and strain. Beyond this point the relation between the two is non-linear. For PDMS a resulting plastic deformation will occur beyond this point while Pyrex will most likely experience a sudden, brittle fracture. PDMS has been reported to exhibit an elastic response up to deformations of 40 %, [70], whereas borosilicate glass has a reported yield strength in the range 22-32 MPa[71], corresponding to a strain of  $3.1\text{-}4.6 \times 10^{-4}$ . The maximum strain in both F1 and F2 is  $8 \times 10^{-7}$ , making linear elasticity a very reasonable assumption under the given actuation conditions.

### Validation against analytical solution

We check the model through comparisons with the known analytical solution for the three-index acoustic eigenmode (0,1,0) with predicted resonance frequency  $f_{0,1,0} = \frac{1}{2}c_0/w = 1.25$  MHz. In Fig. 4.3 we show line plots of the first-order horizontal velocity component magnitude  $|v_{y,1}|$  normalized with the actuation velocity  $-i\omega u_0$  along the horizontal centerline for an analytical expression [65] and for models R1 and F1 with  $H = 4.8h$ .

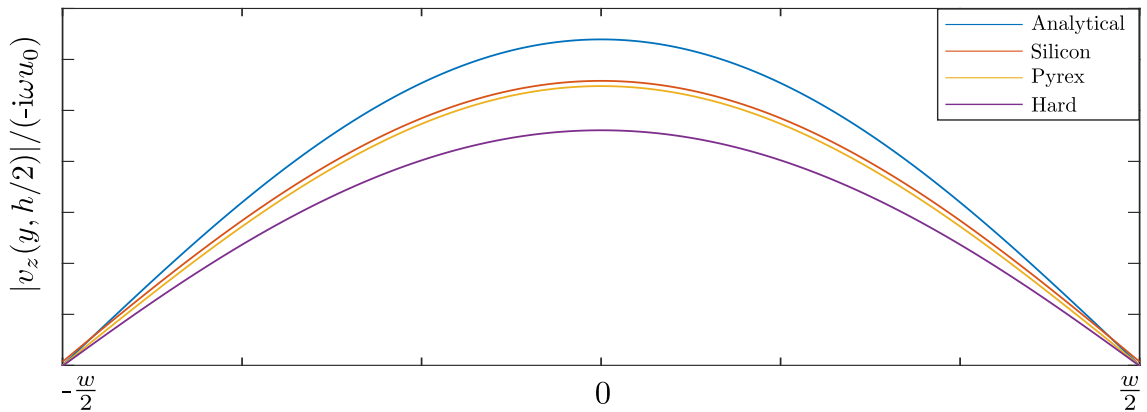


**Figure 4.3:** Model validation through comparison to analytical solution. Line plots of the vertical component of the first-order velocity field  $|v_{y,1}|$  normalized with the actuation velocity  $-i\omega u_0$  in the reduced model, two full models with Pyrex and silicon casing respectively and the analytically predicted one [65] with  $\Gamma = \delta_{\text{visc}}/h = 1.2 \times 10^{-2}$  [72].

From the good agreement of the shapes of the velocity profiles in Fig. 4.3 between both of the models and the analytic 1D shape prediction, we surmise that the numeric model predicts the acoustic fields correctly. From the good agreement between models R1 and F1 we also see a first indication that the hard-wall condition seems to give the same acoustic fields as the modeled Pyrex.

### 4.3 Key results and observations

We compare the first-order acoustic pressure fields predicted by the models R1, F1, R2, and F2, and study line plots of the displacement along the top wall of the channel. From this we hope to infer how well the hard-wall condition replicates the acoustic varying thicknesses of glass on a SAW device, and the lossy-wall for modeling PDMS-bounded fluids. We study the pressure, rather than a more easily observed field such as the radiation force field, because we mainly wish to know how well the reduced and full models agree numerically.

#### 4.3.1 Hard-wall condition

In Fig. 4.4 we plot the surface plots of the first-order acoustic pressure for the models R1 and F1 for three material thicknesses  $H$  at the lowest acoustic hard-wall eigenmode of the water  $f = f_{0,1,0}$ . We also show line plots of the displacement magnitude along the top fluid-solid interface in F1 for three values of  $H$ , normalized with the maximum displacement magnitude of the SAW.

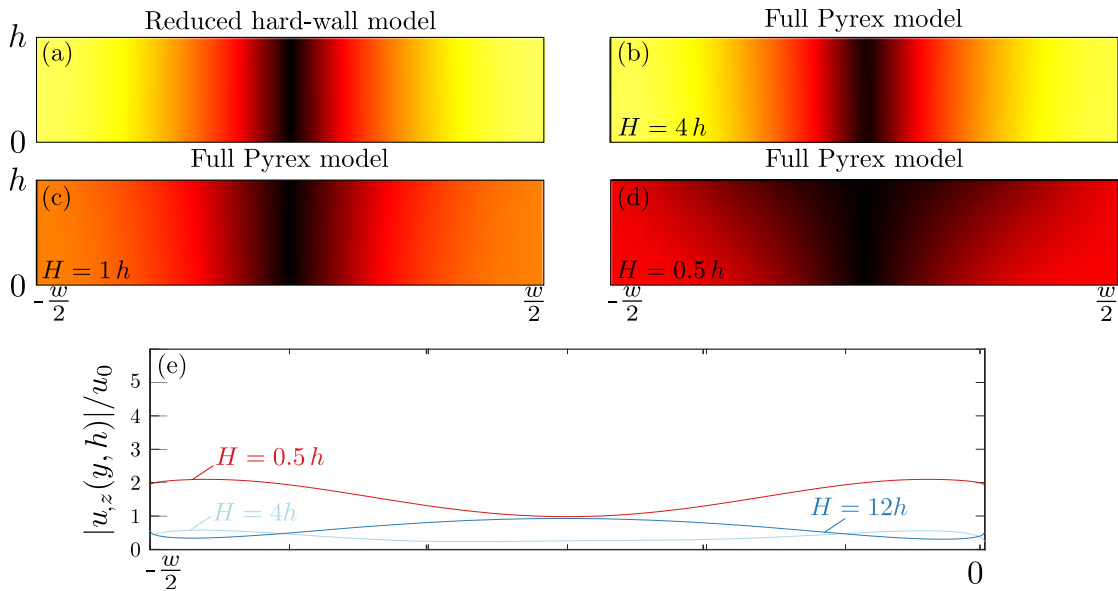


**Figure 4.4:** Hard-wall condition versus Pyrex walls at the lowest hard-wall acoustic eigenmode  $f = f_{0,1,0} = 1.204$  MHz. (a) Color plot of the first-order acoustic pressure  $p_1$  predicted using the reduced hard-wall model, from 0 (black) to 80 kPa (white). (b) As in (a) for the full Pyrex model with thickness  $H = 4h = 600$   $\mu\text{m}$ . (c) As in (b) with  $H = h = 125$   $\mu\text{m}$ . (d) As in (c) with  $H = 0.5h = 60$   $\mu\text{m}$ . (e) Line plots of the vertical displacement component magnitude  $|u_z(y, h)|$  normalized with the actuation displacement  $u_0$  at the top wall  $z = h$  along half the channel width. Adapted from [1]

We see a quite good qualitative agreement between the pressure fields of the reduced model R1 (a) and of the full model F1 for all three thicknesses (b)-(d) shown in Fig. 4.4. The topologies are very similar with a single nodal line at  $y = \frac{1}{2}w$ , and nearly identical fields in (a) and (b). Quantitatively the fields are quite different though, with smaller thicknesses leading to weaker acoustic



pressure fields. Furthermore, as the thickness is decreased, the node broadens slightly at the top, but remains very similar to the reduced model even for the smallest value of  $H$ . This is despite line plot (e) showing that the displacements along the top wall are larger than the driving actuation  $u_0$ , which indicates resonant behavior in either the Pyrex or the water in the vertical direction. Interestingly, the fields are nearly impossible to discern from an acoustophoretic perspective for large particles, as they all predict focusing of particles in the horizontal centre of the device albeit with differing speeds.

In Fig. 4.5 we show the same plots as in Fig. 4.4 but at the off-resonance frequency  $f_{\text{off}} = 6.65$  MHz. We choose this frequency to compare our PDMS simulations to experimental results, and to examine how well the hard-wall condition approximates solid walls in a more general case.

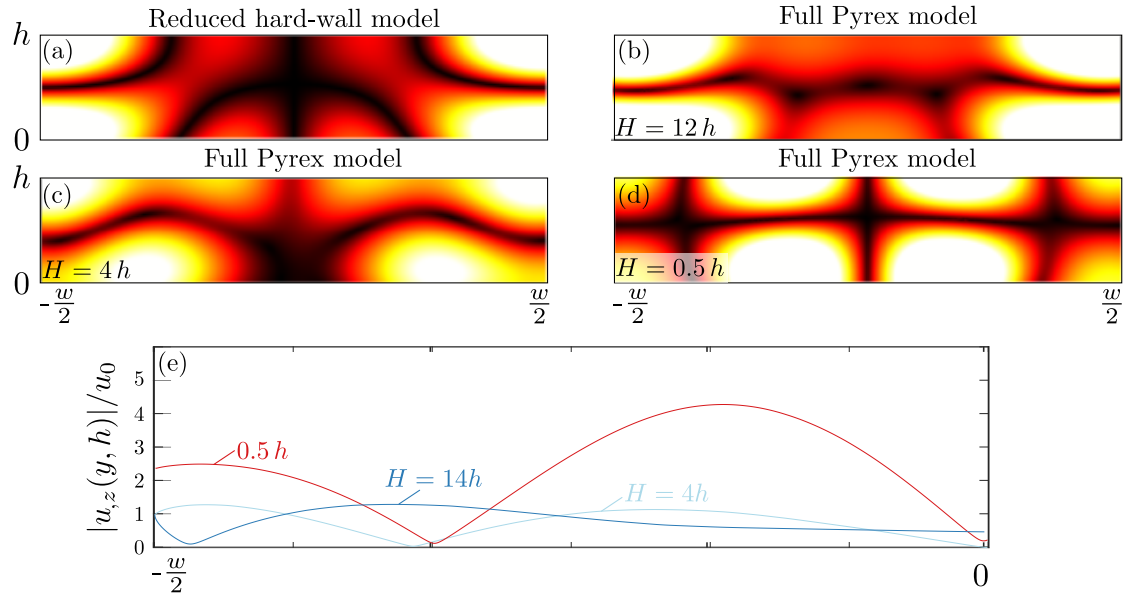


**Figure 4.5:** Hard-wall condition versus Pyrex walls at the off-resonance frequency  $f = f_{\text{off}} = 6.65$  MHz used by [48]. (a) Color plot of the first-order acoustic pressure  $p_1$  predicted using the reduced hard-wall model, from 0 (black) to 40 kPa (white). (b) As in (a) for the full Pyrex model with thickness  $H = 4h = 600$   $\mu\text{m}$ . (c) As in (b) with  $H = 4h = 125$   $\mu\text{m}$ . (d) As in (b) with  $H = 4h = 60$   $\mu\text{m}$ . (e) Line plots of the vertical displacement component magnitude  $|u_z(y, h)|$  normalized with the actuation displacement  $u_0$  at the top wall  $z = h$  along half the channel width. Adapted from [1]

We see in Fig. 4.5 that there are distinct discrepancies between the fields predicted by model R1 (a) and for each thickness in model F1 (b)-(d) when moving away from resonance conditions. For instance the number of pressure anti-nodes in R1 is 6, while it for F1 is 5, 4 and 8 respectively for the heights  $H = 12h$  (b),  $H = 4h$  (c) and  $H = \frac{1}{2}h$  (d). The best match is found for the thickest layer,  $H = 12h$ . This is to be expected as thicker layers of material have greater inertia and are less likely to move, and the hard-wall condition is a stationary wall. With decreasing thickness  $H$  in the full model the discrepancy between the reduced and the full model gradually grows. The only

feature to remain quite similar across all four models is the nodal line approximately at  $z = \frac{1}{2}h$ . For  $H = 60 \mu\text{m}$  the structures in the two pressure fields are markedly different exhibiting the pattern of the  $f_{1,3,0}$  acoustic eigenmode for hard-wall systems, theoretically found at  $f_{1,3,0} = 18.0 \text{ MHz}$ . This is because a vertical resonance builds up in the Pyrex at this combination of thickness and frequency creating a system resonance. The line plots of (e) attest to this, as the line for  $H = 60 \mu\text{m}$  has values exceeding unity indicating a larger displacement at the top of the device than the input.

### 4.3.2 Lossy-wall condition

In Fig. 4.6 we plot the same as in Fig. 4.5, but for R2 and F2. We choose to only show the fields at  $f = f_{\text{off}}$  as the fields at either frequency  $f_{0,1,0}$  or  $f_{\text{off}}$  lead to the same conclusions, due to the inability of PDMS to sustain large fluid pressures. The only similarity of the fields

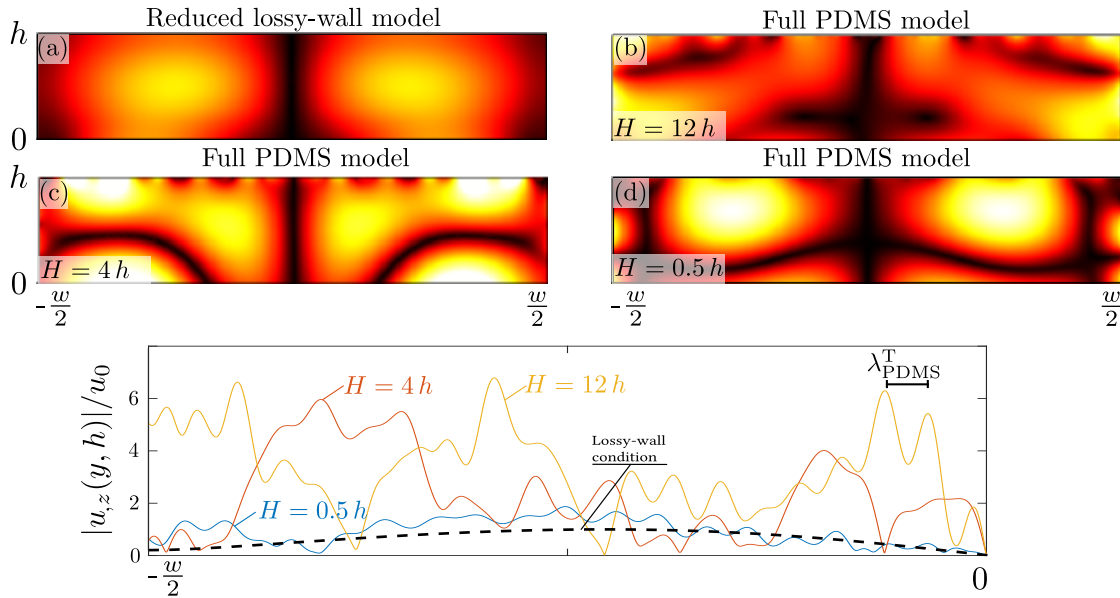


**Figure 4.6:** Lossy-wall condition versus PDMS walls at the frequency  $f_{\text{off}} = 6.65 \text{ MHz}$  (a) Color plot of the first-order acoustic pressure  $p_1$  predicted using the reduced hard-wall model, from 0 (black) to 30 kPa (white). (b) As in (a) for the full Pyrex model with thickness  $H = 4h = 600 \mu\text{m}$ . (c) As in (b) with  $H = 4h = 125 \mu\text{m}$ . (d) As in (b) with  $H = 4h = 60 \mu\text{m}$ . (e) Line plots of the vertical displacement component magnitude  $|u_z(y, h)|$  normalized with the actuation displacement  $u_0$  at the top wall  $z = h$  along half the channel width. Adapted from [1]

in Fig. 4.6 is the nodal line in the horizontal center of the channel, which is likely due to the shape of the SAW actuation. The reduced model yields 2 smooth, elliptic anti-nodes whereas the fields in the full models are more complex shapes with smaller structures. This is mirrored by the normalized vertical displacement plot, where the displacement imposed by the lossy-wall condition is a smooth, half sine wave. The displacements predicted by the full models on the other hand, are far more muddled with a rippling structure. This length between peaks in the plots equals

the transverse wavelength of PDMS at the driving frequency, and can be seen along the edges of the color plots in (b) and (c) as well.

### 4.3.3 Expanding F2 to represent large PDMS devices

We expanded on the full PDMS model F2 to represent devices larger than the 3-mm damping length by adding a PDMS-PML layer around the PDMS as described in Section 4.2.1, and shown in Fig. 4.2.

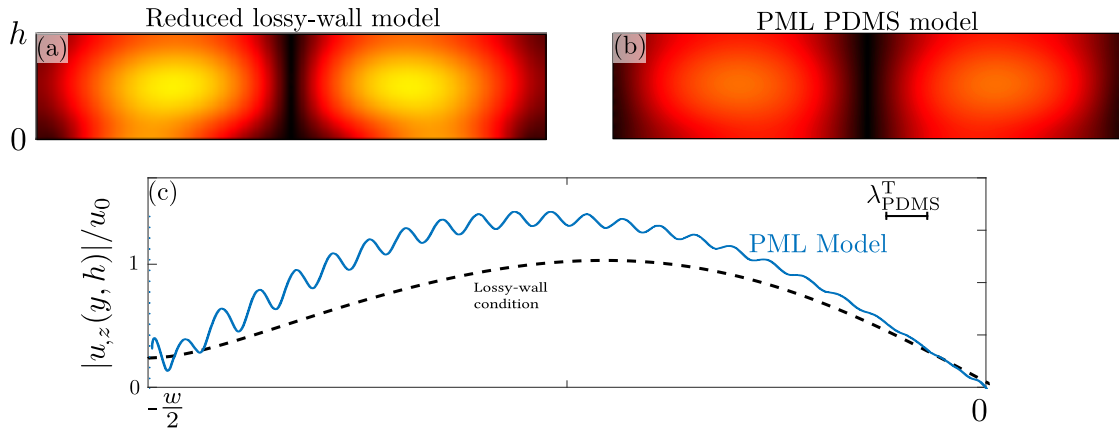


**Figure 4.7:** (a) Color plot of the first-order acoustic pressure  $p_1$  predicted using the reduced lossy-wall model, from 0 (black) to 30 kPa (white). (b) As in (a) for the full PDMS model with an added 100  $\mu\text{m}$ -thick PDMS-PML layer surrounding a 100  $\mu\text{m}$ -thick PDMS layer. (c) Line plots of the vertical displacement component magnitude  $|u_z(y, h)|$  normalized with the actuation displacement  $u_0$  at the top wall  $z = h$  along half the channel width.

In Fig. 4.7 we see that the validity of the reduced lossy-wall model is vastly better for large systems as the PML replicates. Qualitatively the two pressure fields in Fig. 4.7(a) and (b) are very similar with two elliptic pressure nodes evenly spaced around the vertical centerline. However, by comparing the displacement profile lines in Fig. 4.7(c) the omission of the transverse wavelength in the lossy-wall condition is clear particularly when moving away from the center of the channel  $y = 0$ . For the full model ripples can be seen along the displacement profile but not in the lossy wall as there is no way to account for this with the lossy-wall condition. In addition, the fields quantitative match between the line profiles is only good near the edge  $y = -w/2$  and center  $y = 0$  of the channel.

## 4.4 Concluding remarks

From the work presented here, we obtained reduced (R1,R2) and full (F1,F2) numeric model in 2D that represents an idealized version of a long, straight channel actuated by surface acoustic waves in direct contact with the fluid and solid, which is the archetypal design of a SAW device. The full model accounts for fluid-solid interactions between the fluid and an isotropic solid, while

the reduced only approximate it. Both sets of models rely on an analytical approximation for the SAW actuation.

We find that the hard-wall condition does not approximate the motion of the walls very well, as the top wall moves approximately as much as the driving wall and is thus quite far from stationary. However, the resulting pressure fields for all three thicknesses are very similar to the reduced model all the same. This is because we drive the system at a fluid-hard-wall resonance, and each field of the full models is a superposition of the hard-wall eigenmode of the system and a much smaller solution which obeys the velocity boundary conditions applied by the surrounding Pyrex and the SAW. Thus, the hard-wall condition is a reasonable approximation when qualitatively studying the bulk domain of simple eigenmodes of devices with Pyrex walls, but it does not approximate the actual wall motion well.

When moving away from resonance, the bulk pressure field mainly obeys the boundary conditions, with a small contribution from the nearest resonance mode. This exacerbates the poor agreement between the hard-wall motion and thin Pyrex walls. Consequently, the thickness of the surrounding solid becomes the primary cause for differing acoustic fluid fields, since resonances in the solid may play a part as we see in the case with the smallest thickness.

Regardless of frequency and material thickness, the motion of PDMS walls is not approximated well by the lossy-wall condition, and neither is the acoustic fields within for devices smaller than 3 mm. For larger devices, the PML model approximates the acoustic fluid fields relatively well, but not the motion.

The poor agreement between the calculated and approximated motion is partly due to the fact that the lossy-wall condition is based on the partial transmission of incoming planar compressional waves, while completely neglecting the minute transverse wavelength. However, compressional and transverse waves in solids couple together at interfaces so neither should be excluded in assuming the wall motion.

An other aspect that neither approximation takes into account is the actuation of the solid itself. In SAW devices as we study here, the solid is typically bonded directly to the piezoelectric substrate. This means the waves entering the fluid domain from the bottom have already passed under the solid, leaking energy into it and causing motion along the walls.

The takeaway from our comparisons between reduced and full models is that solids should be included in models for them to be as generally applicable as possible as the reduced models in general do not agree well with the full models quantitatively. We note that the discrepancies between reduced (R1) and the full model (F1) in the hard wall case were diminished when the actuation frequency was close to an acoustic fluid eigenfrequency, and when increasing material thickness.

Due to the poor general fit between the approximated case and the full case for interactions between fluids and isotropic solids, we decide to also include the piezoelectric motion in our model going forward. We do this to ensure that we do not apply conditions that are only applicable under certain conditions. This is our basis for moving forward with our numeric model into 3D simulations.

*Modeling of microdevices for SAW-based acoustophoresis - a study of boundary conditions*

**DOI:** [10.3390/mi7100182](https://doi.org/10.3390/mi7100182) .

**Authors:** N.R. Skov and H. Bruus.

**Journal:** Micromachines **7**, 182 (2016).

**Remarks:** While parts of this paper was presented in my MSc thesis [1], the work has been significantly extended for this paper.

Article

# Modeling of Microdevices for SAW-Based Acoustophoresis — A Study of Boundary Conditions

Nils Refstrup Skov and Henrik Bruus \*

Department of Physics, Technical University of Denmark, DTU Physics Building 309, DK-2800 Kongens Lyngby, Denmark; nilsre@fysik.dtu.dk

\* Correspondence: bruus@fysik.dtu.dk; Tel.: +45-4525-3307

Academic Editors: Marc Desmulliez, Anne Bernassau and Baixin Chen

Received: 2 August 2016; Accepted: 23 September 2016; Published: 5 October 2016

**Abstract:** We present a finite-element method modeling of acoustophoretic devices consisting of a single, long, straight, water-filled microchannel surrounded by an elastic wall of either borosilicate glass (pyrex) or the elastomer polydimethylsiloxane (PDMS) and placed on top of a piezoelectric transducer that actuates the device by surface acoustic waves (SAW). We compare the resulting acoustic fields in these full solid-fluid models with those obtained in reduced fluid models comprising of only a water domain with simplified, approximate boundary conditions representing the surrounding solids. The reduced models are found to only approximate the acoustically hard pyrex systems to a limited degree for large wall thicknesses and but not very well for acoustically soft PDMS systems shorter than the PDMS damping length of 3 mm.

**Keywords:** microdevices; acoustofluidics; surface acoustic waves; numeric modeling; hard wall; lossy wall; polydimethylsiloxane (PDMS); borosilicate glass (pyrex)

## 1. Introduction

Separation of particles and cells is important in a wide array of biotechnological applications [1–7]. This has traditionally been carried out by bulk processes including centrifugation, chromatography, and filtration. However, during the last three decades, microfluidic devices have proven to be a valuable alternative [1,7,8], as they allow for lower sample sizes and decentralized preparations of biological samples, increasing the potential for point-of-care testing. Microfluidic methods for separating particles suspended in a medium include passive methods where particle separation is solely determined by the flow and the size or density of particles [2,9–12], and active methods where particles migrate due to the application of various external fields each targeting specific properties for particle sorting [1,3,4,6,13–16]. Acoustophoresis is an active method, where emphasis is on gentle, label-free, precise handling of cells based on their density and compressibility relative to the suspension medium as well as their size [17]. Within biotechnology, acoustophoresis has been used to confine, separate, sort or probe particles such as microvesicles [6,18], cells [1,16,19–22], bacteria [23,24], and biomolecules [25]. Biomedical applications include early detection of circulating tumor cells in blood [26,27] and diagnosis of bloodstream infections [28].

The acoustic fields used in acoustophoresis are mainly one of the following two kinds: (1) bulk acoustic waves (BAW), which are set up in the entire device and used in systems with acoustically hard walls. BAW depend critically on the high acoustic impedance ratio between the walls and the water. In addition, (2) surface acoustic waves (SAW), which are defined by interdigital electrodes on the piezoelectric transducer and propagate along the transducer surface. SAW are nearly independent of the acoustical impedance ratio of the device walls and the microchannel, and this feature makes the SAW technique versatile. SAW can be used both with hard- and soft-walled acoustophoretic devices, often in the generic setup sketched in Figure 1, where the fluid-filled microchannel is encased by a solid

material and is placed directly on top of the piezoelectric substrate to ensure optimal coupling to the SAW induced in the substrate.

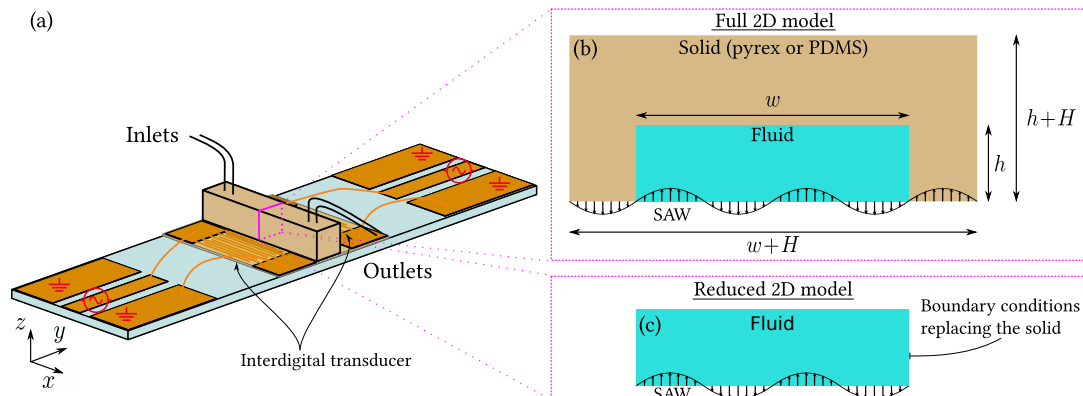


**Figure 1.** (a) Sketch of the generic acoustophoretic device under study. A fluid flows through a long straight microchannel defined by a surrounding solid wall (pyrex or polydimethylsiloxane (PDMS), **light brown**) and placed on top of a piezoelectric substrate (**light blue**). By actuating the interdigital transducers (IDTs, **dark brown**) placed on either side of the device, surface acoustic waves (SAW) propagate along the surface of the substrate, and when timed properly they form a standing wave; (b) Sketch in the transverse  $yz$  cross-section of the full 2D model consisting of a solid domain with wall thickness  $H$  and a fluid domain of width  $w$  and height  $h$ ; (c) Similar sketch of the reduced 2D model, which consists solely of the fluid domain in (b), but with boundary conditions (hard wall or lossy wall) representing in an approximate manner the surrounding solid.

Because SAW-based acoustophoretic microdevices are very promising as powerful and versatile tools for manipulation of microparticles and cells, numerical modeling of them is important, both for improved understanding of the acoustofluidic conditions within the devices and to guide proper device design. In the literature, such modeling has been performed in numerous ways. For many common elastic materials, the dynamics of the walls are straightforward to compute fully through the usual Cauchy model of their displacement fields  $\mathbf{u}$  and stress tensors  $\boldsymbol{\sigma}$ . The coupling to the acoustic pressure  $p$  and velocity  $\mathbf{v}$  in the microchannel, described by the Navier–Stokes equation, is handled by the continuity conditions  $\mathbf{n} \cdot \boldsymbol{\sigma}_s = \mathbf{n} \cdot \boldsymbol{\sigma}_f$  and  $\partial_t \mathbf{u} = \mathbf{v}$  of the stress and velocity fields. This full model is discussed in detail in Section 4. For acoustically hard walls, such as borosilicate glass (pyrex) with a high impedance ratio ( $\tilde{Z} = 8.4$ ) relative to water, the full model is often replaced by a reduced model (exact for  $\tilde{Z} = \infty$ ) with less demanding numerics, where only the fluid domain in the microchannel is treated, and where the elastic walls are replaced by the so-called hard-wall boundary condition demanding zero acoustic velocity at the boundary of the fluid domain [29–31]. For rubber-like polymers such as the often used PDMS, the full device modeling is more challenging. For large strains (above 40 %), a representation of the underlying macromolecular network of polymer chains is necessary [32], while for the moderate strains appearing in typical acoustophoretic devices, standard linear elasticity suffices [33,34]. Some authors argue that the low ratio of the transverse to longitudinal speed of sound justifies a fluid-like model of PDMS based on a scalar Helmholtz equation [30,35]. Furthermore, since the acoustic impedance ratio  $\tilde{Z} = 0.7$  between PDMS and water is nearly unity, the full model has in the literature been replaced by a reduced model, consisting of only the fluid domain with the so-called lossy-wall boundary condition representing in an approximate manner the acoustically soft PDMS walls [16,36,37].

The main aim of this paper is to investigate to which extent the numerically less demanding hard- and lossy-wall reduced models compare with the full models for SAW-based acoustofluidic devices. In the full models, we study the two generic cases of acoustically hard pyrex walls and acoustically soft PDMS walls, both treated as linear elastic materials. In the reduced models, the pyrex



and PDMS walls are represented by hard-wall and lossy-wall boundary conditions, respectively. In all the models, the fluid (water) is treated as a Newtonian fluid governed by the continuity equation and the Navier–Stokes equation. Our main result is that, for pyrex walls, the reduced model approximates the full model reasonably well for sufficiently thick walls, but fails for thin walls, while for PDMS walls, the lossy-wall boundary condition fails regardless of the wall thickness.

## 2. Results: Comparing the Full and Reduced 2D Models

In the following, we present our results for the numerical simulations of the acoustic fields in the reduced and full models with SAW actuation, and we compare the two cases. As the microchannels are long and straight along the  $x$ -direction, we assume translational invariance along  $x$  and restrict the calculational domain to the two-dimensional (2D) cross section in the  $yz$  plane. The full model consists of coupled fluid and solid domains, whereas the reduced model consists of a single fluid domain with boundary conditions that in an approximate manner represent the walls. The principle of our model approach is illustrated in Figure 1, while the models are described in detail in Section 4.

### 2.1. Pyrex Devices: Full Model and Reduced Hard-Wall Model

We consider first the full model of a pyrex microdevice, in which a rectangular water-filled channel of width  $w$  and height  $h$  is encased by a pyrex wall of height  $h + H$  and width  $w + H$  (see Figure 1b). We simulate the case of actuating the system both at the horizontal standing half-wave resonance in the water  $f_{\text{res}} = c_0/2w = 1.24$  MHz often exploited in experiments, and at the off-resonance frequency  $f_{\text{off}} = 6.65$  MHz chosen to facilitate comparisons with the literature [36]. An example of a full-model result for the velocity field  $-i\omega\mathbf{u}$  and relative volume change  $|\nabla \cdot \mathbf{u}_s|$  in the pyrex as well as  $v_f$  and  $p_f$  in the water, is shown in Figure 2a,c.

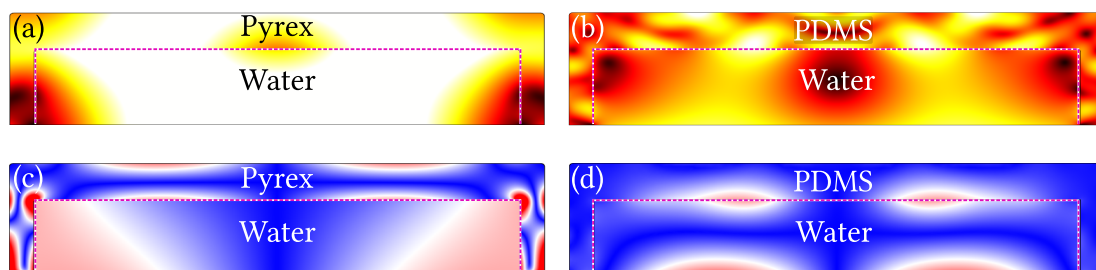


**Figure 2.** Examples of full model results for  $h = 125 \mu\text{m}$ ,  $w = 600 \mu\text{m}$ , and  $H = 60 \mu\text{m}$  (see Figure 1b). (a) Color plot from 0 mm/s (black) to 2.0 mm/s (white) of the velocity field  $|-i\omega\mathbf{u}_s|$  in the pyrex and  $|v_f|$  in the water obtained in a full-model simulation of a pyrex SAW device actuated at the on-resonance frequency  $f_{\text{res}} = 1.24$  MHz; (b) The same as in (a) but for a full-model PDMS SAW device. The dashed magenta line indicates the solid-fluid interface; (c) Color plot from 0 (dark blue) to  $8 \times 10^{-7}$  (dark red) of the amplitude of the relative volume change  $|\nabla \cdot \mathbf{u}_s|$  in the Pyrex and the rescaled pressure  $|p_f| / (\frac{1}{5}K_{\text{pyrex}})$  in the fluid, of the full model from (a), where  $K_{\text{pyrex}}$  is the bulk modulus of Pyrex; (d) The same as (c) but for the full model from (b) and the rescaled pressure  $|p_f| / K_{\text{PDMS}}$  using the bulk modulus  $K_{\text{PDMS}}$  of PDMS.

We then investigate to which extent the full model can be approximated by the reduced hard-wall model often used in the literature [29,38], where only the water domain is considered, while the pyrex walls are represented by the hard-wall condition. In Figure 3, we show for both off-resonance (left column) and on-resonance (right column) actuation, a qualitative comparison between the reduced and the full model, with wall thickness  $H$  ranging from 60 to 1800  $\mu\text{m}$ . Considering the resulting amplitudes  $|p_f|$  of first-order pressure field  $p_f$  in the water domain, we note that, for off-resonance actuation at the frequency  $f_{\text{off}}$ , the full model with thick walls  $H = 1500 \mu\text{m}$  has some features in common with the reduced model.



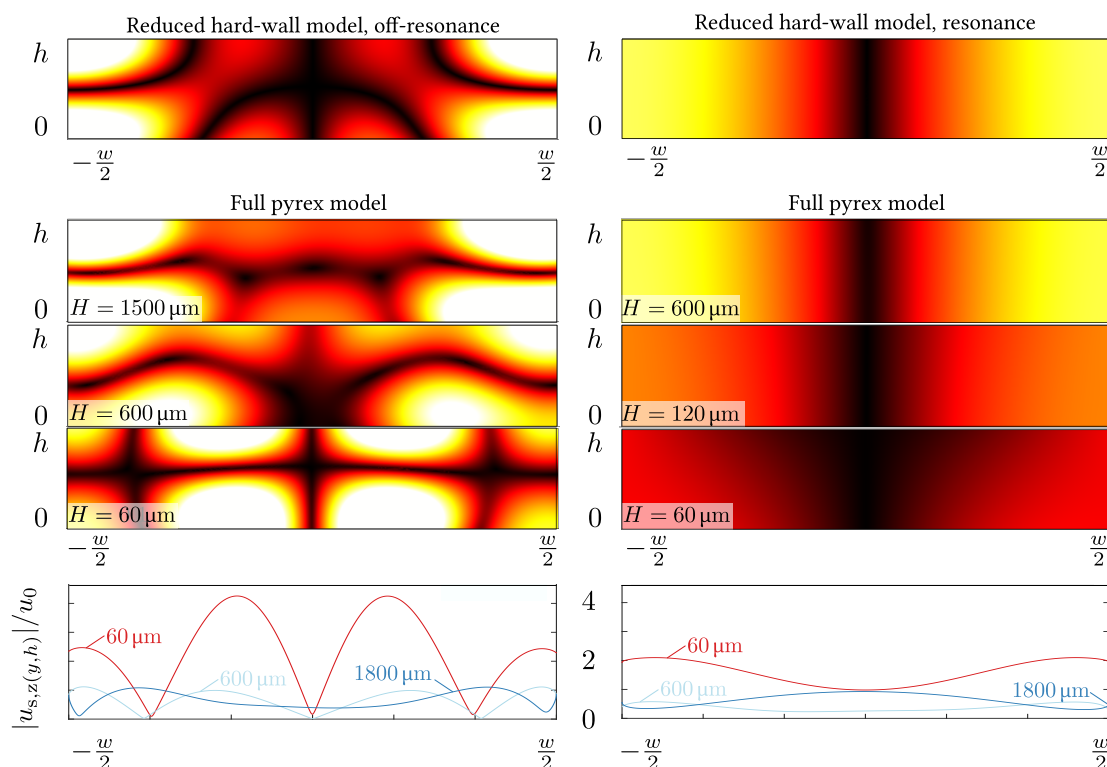


**Figure 3.** Left column: color plots from 0 kPa (black) to 40 kPa (white) at the off-resonance frequency  $f_{\text{off}} = 6.65$  MHz of the amplitude  $|p_f|$  of the first-order pressure field  $p_f$  in the fluid domain of the reduced hard-wall model and the full pyrex model Figure 1a, but with  $H = 60, 600,$  and  $1500 \mu\text{m}$ . The surrounding pyrex is not shown. Right column: the same as to the left, but at the on-resonance actuation frequency  $f = 1.24$  MHz and with the color plots ranging from 0 kPa (black) to 80 kPa (white). Bottom row: off- and on-resonance line plots of the amplitude  $|u_{s,z}(y,h)|$  of the vertical displacement along the top fluid-solid interface at  $z = h$  normalized by the amplitude  $u_0$  of the SAW actuation displacement for wall thickness  $H = 60, 600,$  and  $1500 \mu\text{m}$ .

There are pressure anti-nodes in the corners and an almost horizontal pressure node close to the horizontal centerline. For decreasing wall thickness  $H$  in the full model, the pressure field changes qualitatively, as the pressure anti-nodes detach from the side walls and shift towards the center of the fluid domain. When actuated on resonance at the frequency  $f_{\text{res}}$ , for wall thicknesses as low as  $H = 120 \mu\text{m}$ , the full-model pressure is nearly indistinguishable from that of the hard-wall reduced model, namely a cosine function with vertical pressure anti-nodal lines along the side walls and a vertical pressure nodal line in the center. For the smallest wall thickness  $H = 60 \mu\text{m}$ , the iso-bars in the full model tilt relative to vertical. In summary, the correspondence between the full and the reduced model is overall better for on-resonance actuation, but for a large wall thickness, the reduced hard-wall model describes the full pyrex model reasonably well. Table 1 shows the values of the thickness-to-wavelength ratios  $H/\lambda$ .

Finally, in the bottom row of Figure 3, we investigate for the full pyrex model model the displacement at the upper boundary in units of the imposed displacement amplitude  $u_0$  at the SAW-actuated lower boundary. If the hard-wall condition of the reduced model is good, this displacement should be very small. However, from the figures it is clearly seen that for the thin wall  $H = 60 \mu\text{m}$ , the upper-wall displacement is significant, with an amplitude of  $4u_0$  at  $f_{\text{off}}$  and  $2u_0$  at  $f_{\text{res}}$ . As the wall thickness  $H$  increases, the upper-wall displacement amplitudes decreases towards  $u_0$ . Again, this reflects that the reduced hard-wall model is in fair agreement with the full model for a large wall thickness  $H$ , and it is better on resonance, where the specific values at the boundaries are

less important as the pressure field is dominated by the pressure eigenmode that does in fact fulfill the hard-wall condition (see Section 3.2).

**Table 1.** The ratio  $H/\lambda$  for various values of the material thickness  $H$  and the different acoustic wavelengths  $\lambda$  present in the system at the two frequencies  $f_{\text{res}}$  and  $f_{\text{off}}$ .

$f_{\text{res}} = 1.24 \text{ MHz}$					$f_{\text{off}} = 6.65 \text{ MHz}$				
$\lambda$ ( $\mu\text{m}$ )	$H$ ( $\mu\text{m}$ )				$\lambda$ ( $\mu\text{m}$ )	$H$ ( $\mu\text{m}$ )			
	60	600	1500			60	600	1500	
$\lambda^{\text{SAW}}$	600	0.100	1.000	2.500	$\lambda^{\text{SAW}}$	600	0.100	1.000	2.500
$\lambda^{\text{wa}}$	1200	0.050	0.500	1.250	$\lambda^{\text{wa}}$	225	0.267	2.667	6.667
$\lambda_{\text{T}}^{\text{pyrex}}$	2745	0.022	0.219	0.546	$\lambda_{\text{T}}^{\text{pyrex}}$	515	0.117	1.165	2.913
$\lambda_{\text{L}}^{\text{pyrex}}$	4483	0.013	0.134	0.335	$\lambda_{\text{L}}^{\text{pyrex}}$	841	0.071	0.713	1.784
$\lambda_{\text{T}}^{\text{PDMS}}$	80	0.750	7.500	18.750	$\lambda_{\text{T}}^{\text{PDMS}}$	15	4.000	40.000	100.000
$\lambda_{\text{L}}^{\text{PDMS}}$	826	0.073	0.726	1.816	$\lambda_{\text{L}}^{\text{PDMS}}$	155	0.387	3.871	9.677

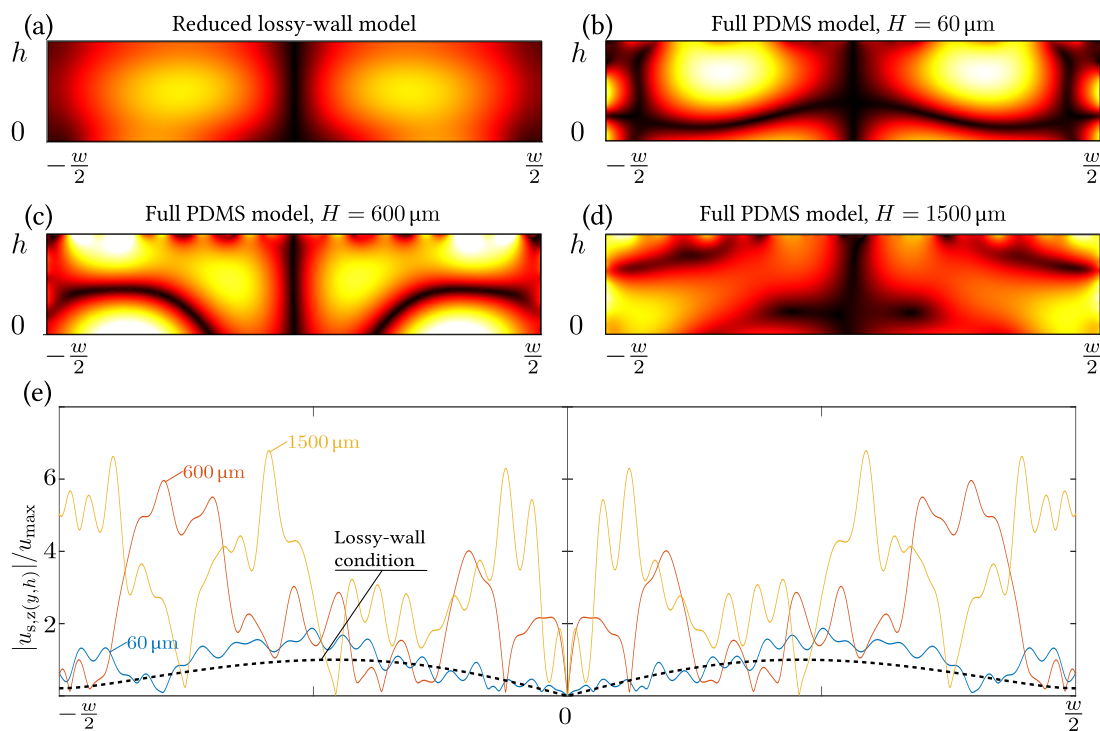


**Figure 4.** Color plot from 0 kPa (black) to 30 kPa (white) at  $f_{\text{off}} = 6.65 \text{ MHz}$  of the amplitude  $|p_f|$  of the first-order pressure field  $p_f$  in the fluid domain of (a) the reduced lossy-wall model and (b–d) the full PDMS model with wall thickness  $H = 60, 180, \text{ and } 1500 \mu\text{m}$ . The surrounding PDMS is not shown; (e) line plots of the normalized amplitude  $|u_{s,z}(y,h)|/u_{\text{max}}$  of the vertical displacement along the upper fluid-solid interface at  $z = h$  in the full model (full colored lines) with  $H = 60, 600, \text{ and } 1500 \mu\text{m}$  and in the reduced lossy-wall model (dashed black line). The normalization unit  $u_{\text{max}}$  is the maximum amplitude found in the reduced lossy-wall model.

### 2.2. PDMS Devices: Full Model and Reduced Lossy-Wall Model

We then move on to show the same comparisons, but where the full model has PDMS walls, and the reduced model has the lossy-wall boundary condition, which takes deformation in the

normal direction of the wall into account. The reduced lossy-wall model for PDMS, actuated at the off-resonance frequency  $f_{\text{off}} = 6.65$  MHz, is exactly the one used by Nama et al. [36]. Given the low impedance ratio  $\tilde{Z} = 0.7$  between PDMS and water, there is no resonance. Results for the full PDMS model are shown in Figure 2b,d at  $f_{\text{res}} = 1.24$  MHz, and results at  $f_{\text{off}} = 6.65$  MHz for the reduced lossy-wall model, and the full PDMS model is shown in Figure 4 with plots similar to the ones in the left column of Figure 3 for the reduced hard-wall model and the full pyrex model.

Initially, we compare in Figure 4a–d the amplitude  $|p_f|$  of the first-order pressure field  $p_f$  of the reduced lossy-wall model with that of the full PDMS model for the wall thickness  $H$  varying from 60 to 1500  $\mu\text{m}$ . Due to the lossy-wall boundary condition (Equation (14)), the ellipsoidal pressure anti-nodes in Figure 4a traverse the fluid domain upwards during one oscillation cycle. This is in stark contrast to the pressure structures of the full PDMS model in Figure 4b–d, which are stationary due to the free stress condition (Equation (12)) imposed on the exterior of the PDMS. Moreover, the pressure structure of the reduced lossy-wall model consists of only two pressure antinodes, which is much simpler than the multi-node structure of the full PDMS model. In fact, the only common feature in the pressure fields is the appearance of a well-defined pressure node along the vertical centerline.

The poor qualitative agreement between the pressure field in the reduced lossy-wall model and in the full PDMS model is further supported in Figure 4e, where the upper-wall displacement amplitudes of the models are shown. We introduce the unit  $u_{\text{max}}$  as the maximum displacement along the upper-wall in the reduced lossy-wall model, and note that the lossy-wall condition imposes a broad single-node sinusoidal velocity amplitude of unity magnitude, while each of the four full model cases ( $H = 60, 600,$  and  $1500 \mu\text{m}$ ) shows a rippled, multi-peaked displacement amplitude of relative magnitudes ranging from 2 to 6. The ripples are caused by the small wavelength (15  $\mu\text{m}$ ) of the transverse waves in PDMS at the given frequency (see Table 1).

### 3. Discussion

#### 3.1. Physical Limitations of the Hard-Wall Condition

As illustrated in Figure 3, there are clear discrepancies between the fields obtained by the reduced hard-wall model and those found using the full pyrex models. This can likely be attributed to two factors in particular: the finite stiffness and density of pyrex, and the non-local SAW actuation imposed along the bottom edge in the model.

The hard-wall condition is physically correct for an infinitely stiff and dense wall, which does not undergo any deformation or motion regardless of the stress exerted by the fluid. A hard wall thus reflects all acoustic energy incident on it back into the fluid. However, pyrex has a finite stiffness and density, and it will thus deform and allow for a partial transmittance of acoustic energy from the fluid. This aspect is part of the full pyrex model, but not of the reduced hard-wall model.

The specific SAW actuation is also different in the full and the reduced model. The microdevice rests on top of the piezoelectric substrate, so in the full model, the standing SAW along the surface of the piezoelectric substrate (typically lithium niobate) will transmit significant amounts of acoustic energy directly into both the pyrex wall and the water, but only the latter is taken into account in the reduced hard-wall model. The coupling between lithium niobate and pyrex is strong since the direction-dependent elastic stiffness coefficients of lithium niobate lies in the range from 53 to 200 GPa [39] and the Young's modulus of pyrex of 64 GPa lies in the same range [40]. Consequently, the interface between the pyrex wall and the water will move under the combined action of the acoustic fields loaded into the pyrex and the water, respectively.

**Table 2.** List of parameters used for geometry, materials, and surface acoustic waves (SAW) in the numerical model. The values for the damping parameters  $\Gamma$  are from Reference [41].

Quantity	Symbol	Unit	Pyrex [40]	Polydimethylsiloxane (PDMS) [42,43]	Water [44]	SAW [36]
Width	$\frac{1}{2}H$ or $w$	$\mu\text{m}$	30–900	30–750	600	-
Height	$H$ or $h$	$\mu\text{m}$	60–1800	60–1500	125	-
Density	$\rho_f$ or $\rho_s$	$\text{kg}\cdot\text{m}^{-3}$	2230	1070	997	-
Bulk modulus	$K_f$ or $K_s$	GPa	38.46	1.12	2.23	-
Longitudinal sound speed	$c_L$ or $c_0$	$\text{m}\cdot\text{s}^{-1}$	5591	1030	1496	-
Transversal sound speed	$c_T$	$\text{m}\cdot\text{s}^{-1}$	3424	100	-	-
Damping coefficient	$\Gamma_f$ or $\Gamma_s$	1	0.001	0.001	0.002	0
Acoustic impedance ratio	$\tilde{Z} = \frac{\rho_s c_L}{\rho_f c_0}$	1	8.4	0.7	1	-
SAW wavelength	$\lambda^{\text{SAW}}$	$\mu\text{m}$	-	-	-	600
SAW displacement amplitude	$u_0$	nm	-	-	-	0.1
SAW on-resonance frequency	$f_{\text{res}} = \frac{2w}{c_0}$	MHz	-	-	-	1.24
SAW off-resonance frequency	$f_{\text{off}}$	MHz	-	-	-	6.65

### 3.2. Acoustic Eigenmodes

Due to the high impedance ratio  $\tilde{Z} = 8.4$  for pyrex relative to water (see Table 2), it is possible in the full pyrex model to excite a resonance in the device at the frequency  $f_{\text{res}} = 2w/c_0 = 1.24$  MHz, which is close to the ideal standing half-wave pressure eigenmode of the reduced hard-wall system. At this resonance frequency, the pressure amplitude  $|p_f|$  in the water is several times larger than the pressure amplitude  $\rho_f c_0 \omega u_0$  set by the imposed SAW displacement, and the resonance field mainly depends on the frequency and not significantly on the detailed actuation along the boundary [29]. The full pyrex model and the reduced hard-wall model are therefore expected to be in good agreement at  $f_{\text{res}}$ , as is verified by the right column in Figure 3.

In contrast, at off-resonance frequencies, such as  $f_{\text{off}} = 6.65$  MHz in the left column of Figure 3, the detailed actuation does matter. The lower left panel of Figure 3 is an example of this, as it highlights an aspect that restricts the validity of the reduced hard-wall model. For the full model with 60- $\mu\text{m}$ -thick pyrex walls, the maximum displacement along the top boundary of the water domain is approximately four times larger than the displacement amplitude  $u_0$  of the imposed SAW boundary condition on the bottom boundary of the water domain. This indicates that the system is actuated close to a structural acoustic eigenmode of the pyrex. An amplification is also seen in the lower right panel of Figure 3 although to a smaller degree. This amplification of boundary displacements brought about by the existence of structural eigenmodes is not taken into account in the reduced hard-wall model.

### 3.3. Physical Limitations of the Lossy-Wall Condition

The comparison between the reduced lossy-wall model and the full PDMS model in Figure 4 shows a clear mismatch. The most important reasons for this are that the lossy-wall model neglects the actuation of both the solid and fluid domain, and that it neglects the transverse motion of the PDMS along the PDMS-water interface.

As for the hard-wall model, the lossy-wall model neglects the strong direct transfer of acoustic energy from the SAW to the PDMS wall, and the implications are the same: the lossy-wall model underestimates the deformation and motion of the PDMS-water boundaries due to this. Moreover, due to the low impedance ratio  $\tilde{Z} = 0.7$ , there are no strong resonances in the water domain like the one at  $f_{\text{res}}$  for which the detailed boundary conditions do not matter.

In contrast to the reduced hard-wall model, some aspects of the deformation and motion of the PDMS-water boundaries are taken into account in the reduced lossy-wall model, as it includes the partial reflection and absorption waves from the water domain with perpendicular incidence on the PDMS wall. While this approach would be a good description of a planar or weakly curving interface between two fluids, where all the acoustic excitation takes place in one of the fluids, it is of limited

use in the present system, for three reasons: (1) as discussed above, the acoustic energy is injected by the SAW into both the water and the PDMS domain; (2) the PDMS-water boundary is not planar, but consists of three linear segments joined at right angles; and (3) PDMS is not a fluid, but supports shear waves, which are neglected in the reduced lossy-wall model. These three aspects are all part of the full PDMS model, in which PDMS is described as a linear elastic material supporting both longitudinal and transverse waves.

### 3.4. Modeling PDMS as a Linear Elastic

When modeling large strains above 0.4 in PDMS, non-linear effects are commonly included using hyperelasticity models in the form of a constitutive relation for the stress and strain for which the elastic moduli depends on the stress instead of being constant. For small strains below 0.4, PDMS becomes a usual linear elastic material [45–49]. The magnitude of the strain in terms of the relative volume change  $|\nabla \cdot \mathbf{u}_s|$  is shown for our system in Figure 2c,d for  $H = 60 \mu\text{m}$ . The maximum value of  $|\nabla \cdot \mathbf{u}_s|$  for PDMS is seen to be  $5.59 \times 10^{-6}$ , which justifies the use of linear elastics as the governing equations of the PDMS walls in our system. Similarly for pyrex, where the maximum value for  $|\nabla \cdot \mathbf{u}_s|$  is  $8.51 \times 10^{-7}$ . The use of linear elasticity is further validated in the literature, where linear elastic models of PDMS yield results comparable to those found when using more complex approaches, such as a Mooney–Rivlin constitutive model [33], a neo–Hookian approach [34], and a Maxwell–Wiechert model [50].

Further simplifications based on neglecting the transverse motion of PDMS, such as modeling it as a fluid [30,35] and applying the lossy wall conditions [36], are not advised, since PDMS does have a non-zero transverse bulk modulus and does support transverse sound waves [42,48,49].

As characterization results for PDMS are scarce in the literature, we had to combine the material parameters found in References [42,43] in our simulations.

## 4. Materials and Methods

Our modeling is based on the generic device design [4,14] illustrated in Figure 1. The device consists of a long, straight, fluid-filled microchannel surrounded by an elastic solid wall on the sides and top. The microchannel and walls rest on a piezoelectric substrate, along which a standing SAW is imposed as a boundary condition. We assume translational invariance along the axial  $x$  direction, and only model the transverse  $yz$  plane. We implement 2D numerical models in COMSOL Multiphysics 5.2 (COMSOL, Stockholm, Sweden) [51] using the parameters listed in Table 2. All acoustic fields are treated using an Eulerian description, and they have a harmonic time-dependence of the form  $\mathbf{u}_s(y, z) e^{-i\omega t}$ , such that  $\partial_t$  becomes  $-i\omega$ , where  $i = \sqrt{-1}$ , while  $\omega = 2\pi f$  is the angular frequency and  $f$  the frequency of the imposed SAW. For simplicity, we often suppress the spatial and temporal variable and write a field simply as  $\mathbf{u}_s$ . Finally, following Hahn and Dual [41], we introduce damping in the fluid and the solid using the complex-valued frequency  $(1 - i\Gamma_m)\omega$ , where  $\Gamma_m$  is the damping coefficient in the medium with the values listed in Table 2. For simplicity, we used  $\Gamma_s = 0.001$  for both pyrex and PDMS, however this implies a damping length for PDMS longer than the 3 mm given in [36], so our model is only valid for PDMS devices with walls thinner than 3 mm.

In total, four models are set up, all with the imposed SAW as a boundary condition representing the actual piezoelectric lithium niobate substrate: (1) the full pyrex model, Figure 5a, where the solid wall is modeled as a linearly elastic material with the parameters of pyrex, while the fluid is modeled as water; (2) the reduced hard-wall model, Figure 5b, where only the water is modeled, while hard-wall boundary conditions replace the pyrex wall; (3) the full PDMS model, Figure 5a, which is the full pyrex model in which the pyrex parameters are replaced by PDMS parameters; and (4) the reduced hard-wall model, Figure 5b, where only the water is modeled, while lossy-wall boundary conditions replace the PDMS wall.

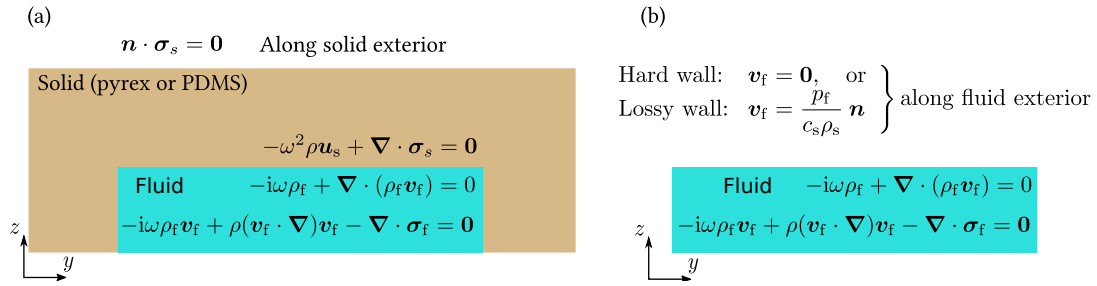


**Figure 5.** Sketches of the models used in the study. (a) The full model with a solid domain (pyrex or PDMS) and a fluid domain (water); and (b) the reduced model with only a fluid domain with boundary conditions (hard or lossy) representing the surrounding solid (pyrex or PDMS, respectively).

#### 4.1. Governing Equations

The unperturbed fluid at constant temperature  $T = 298$  K in the fluid domain is characterized by its density  $\rho_0$ , viscosity  $\eta_0$ , and speed of sound  $c_0$ . The governing equations for the acoustic pressure  $p_f$ , density  $\rho_f$ , and velocity  $v_f$  are the usual mass and momentum equations. The constitutive equation between the acoustic pressure  $p_f$  and density  $\rho_f$  is the usual linear expression,  $p_f = c_0^2 \rho_f$ . Neglecting external body forces on the fluid, while applying perturbation theory [38] and inserting the harmonic time-dependence, the governing equations and the constitutive equation are linearized to the following first-order expressions:

$$i(1 - i\Gamma_f)\omega p_f = \rho_0 c_0^2 \nabla \cdot v_f \quad (1)$$

$$-\rho_0 i(1 - i\Gamma_f)\omega v_f = \nabla \cdot \sigma_f \quad (2)$$

$$\sigma_f = -p_f \mathbf{I} + \eta_0 [\nabla v_f + (\nabla v_f)^T] + \beta \eta_0 \nabla (\nabla \cdot v_f) \mathbf{I} \quad (3)$$

where we have introduced the Cauchy stress tensor  $\sigma_f$ , and where superscript "T" denotes tensor transpose,  $\beta$  is the bulk-to-shear viscosity ratio, and  $\mathbf{I}$  is the unit tensor. With appropriate boundary conditions, the first-order acoustic fields  $p_f$ ,  $\rho_f$ , and  $v_f$ , can be fully determined by Equations 1–3. The specific model-dependent boundary conditions are presented and discussed in Sections 1 and 4.2.

The dynamics in the solid of unperturbed density  $\rho_s$  is described by linear elastics through the momentum equation in terms of the displacement field  $u_s$  and the solid stress tensor  $\sigma_s$ . The constitutive equation relating displacement and stress is defined using the longitudinal  $c_{L,s}$  and transverse  $c_{T,s}$  speeds of sound of the given solid:

$$-\rho_s (1 - i\Gamma_s)^2 \omega^2 u_s = \nabla \cdot \sigma_s \quad (4)$$

$$\sigma_s = \rho_s \left[ c_{T,s}^2 (\nabla u_s + \nabla u_s^T) + (c_{L,s}^2 - 2c_{T,s}^2) (\nabla \cdot u_s) \mathbf{I} \right] \quad (5)$$

#### 4.2. Boundary Conditions

For simplicity, the full dynamics of the piezoelectric substrate is not modeled. Instead, the standing SAW is implemented by prescribing displacements  $u_{pz} = (u_{y,pz}, u_{z,pz})$  in the  $y$ - and  $z$ -directions, respectively, on the bottom boundary of our domain using the following analytical expression from the literature [36,52], where the damping coefficient of  $116 \text{ m}^{-1}$  has been neglected given the small dimensions ( $< 0.002$  m) of the microfluidic device [36]:

$$u_{y,pz} = 0.6u_0 \left\{ \sin \left[ k \left( \frac{1}{2}w - y \right) + \omega t \right] + \sin \left[ k \left( y - \frac{1}{2}w \right) + \omega t \right] \right\} \quad (6)$$

$$u_{z,pz} = -u_0 \left\{ \cos \left[ k \left( \frac{1}{2}w - y \right) + \omega t \right] + \cos \left[ k \left( y - \frac{1}{2}w \right) + \omega t \right] \right\} \quad (7)$$



$$v_f = -i\omega u_{pz} \quad \text{imposed on the fluid at the fluid-SAW interface,} \quad (8)$$

$$u_s = u_{pz} \quad \text{imposed on the solid at the solid-SAW interface,} \quad (9)$$

where  $k = 2\pi/\lambda$  is the wavenumber and  $u_0$  the displacement amplitude of the SAW.

In the full models, a no-stress condition for  $\sigma$  is applied along the exterior boundary of the solid. On the interior fluid-solid boundaries, continuity of the stress is implemented as a boundary condition on  $\sigma_s$  in the solid domain imposed by the fluid stress  $\sigma_f$ , while continuity of the velocity is implemented as a boundary condition on  $v_f$  in the fluid domain imposed by the solid velocity  $-i\omega u_s$ . Along the free surfaces of the solid, a no-stress condition is applied:

$$n_s \cdot \sigma_s = n_s \cdot \sigma_f \quad \text{imposed on the solid at the fluid-solid interface,} \quad (10)$$

$$v_f = -i\omega u_s \quad \text{imposed on the fluid at the fluid-solid interface,} \quad (11)$$

$$n_s \cdot \sigma_s = \mathbf{0} \quad \text{imposed on the solid at exterior boundaries.} \quad (12)$$

We have also performed simulations, where the stress-free condition Equation (12) on the exterior boundaries is changed into a lossy-wall conditions involving high acoustic impedance ratios (PDMS/air 3600 and pyrex/air 41000). As expected, the resulting fields are almost unchanged: we observe the same morphology, and, quantitatively, the average value pressure field in the water domain exhibits relative changes less than  $4 \times 10^{-5}$ , hence we employ the simpler Equation (12).

In the reduced models, boundary conditions are imposed on the fluid to represent the surrounding material. Stiff and heavy materials such as pyrex are represented by the hard-wall (no motion) condition at the boundary of the fluid domain. Soft and less heavy materials such as PDMS are represented by the lossy-wall condition for partial acoustic transmittance perpendicular to the boundary of the fluid domain. For both conditions, a no-slip condition is applied on the tangential velocity component. The specific expression implemented in COMSOL are:

$$v_f = \mathbf{0} \quad \text{boundary condition representing hard walls,} \quad (13)$$

$$v_f = \frac{p_f}{c_s \rho_s} \mathbf{n} \quad \text{boundary condition representing lossy walls.} \quad (14)$$

### 4.3. Numerical Implementation and Validation

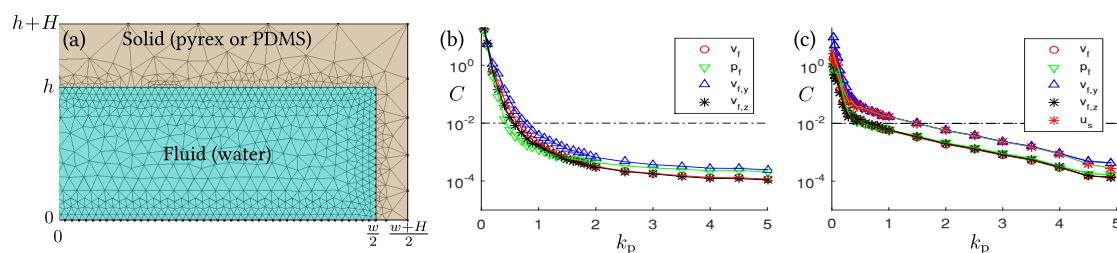


**Figure 6.** (a) The mesh implemented in COMSOL 5.2 (COMSOL, Stockholm, Sweden), here shown in a coarse version for illustrative purposes with the small value  $k_p = 0.1$  for the mesh parameter; (b) For each of the fields  $p_f$ ,  $v_f$ ,  $v_{f,y}$ , and  $v_{f,z}$ , the relative mesh convergence parameter  $C$  is plotted versus mesh parameter  $k_p$  for the reduced lossy-wall model. The dashed line represents  $C = 0.01$ ; (c) The same as in (b) but for the water domain in the full PDMS model with the inclusion of the field  $u_s$ .

We follow our previous work [29,53], and implement the governing equations in weak form in the commercial software COMSOL Multiphysics 5.2 [51]. To fully resolve the thin acoustic boundary layer of width  $\delta$ ,

$$\delta = \sqrt{\frac{2\eta_0}{\rho_0\omega}} = 0.21 \mu\text{m} \text{ at } \omega = 2\pi \times 6.5 \text{ MHz} \quad (15)$$

in the water domain near its edges, the maximum mesh size  $h_{\text{edge}}$  at the solid-fluid boundary is much smaller than that in the bulk called  $h_{\text{bulk}}$ . Both of these are controlled by the mesh parameter  $k_p$ ,

$$h_{\text{edge}} = \frac{1}{k_p} \delta \quad h_{\text{bulk}} = 50h_{\text{edge}} \quad \text{with } k_p = 1 \text{ in the main runs.} \quad (16)$$

The coarse mesh with  $k_p = 0.1$  is shown in Figure 6a. In our largest (full) models using  $k_p = 1$ , the implementation resulted in  $8.1 \times 10^6$  degrees of freedom and a computational time of 30 min on a standard PC work station. The implementation of the model in the fluid domain has been validated both numerically and experimentally in our previous work [29,53]. The solid domain implementation was validated by calculating resonance modes for a long rectangular cantilever, clamped at one end and free at the other, and comparing them successfully against analytically known results. Finally, for both the full and the reduced models, we performed a mesh convergence analysis using the relative mesh convergence parameter  $C(g)$  for a given field  $g(y, z)$  as introduced in Reference [29]:

$$C(g) = \sqrt{\frac{\int_{\Omega} (g - g_{\text{ref}})^2 dydz}{\int_{\Omega} (g_{\text{ref}})^2 dydz}} \quad (17)$$

Here,  $g_{\text{ref}}$  is the solution obtained with the finest possible mesh resolution, in our case the one with mesh parameter  $k_p = 5$ . For all fields, our mesh analysis revealed that satisfactory convergence was obtained with the mesh parameter set to  $k_p = 1$ . For this value, the relative mesh convergence parameter was both small,  $C \approx 0.01$ , and exhibited an exponential asymptotic behavior,  $C \simeq e^{-k_p}$ , as a function of the mesh parameter  $k_p$  (for two examples, see Figure 6b,c).

## 5. Conclusions

A numerical method has been presented for 2D full modeling of a generic SAW microdevice consisting of a long, straight, fluid-filled microchannel encased in a elastic wall and resting on a piezoelectric substrate in which a low-MHz-frequency standing SAW is imposed. We have also presented reduced models consisting only of the fluid domain, where boundary conditions are used as simplified representations of the elastic wall. An acoustically hard wall, such as pyrex, is represented by a hard-wall boundary condition, while an acoustically soft wall, such as PDMS, is represented by a lossy-wall boundary condition. Our results show that the full pyrex model is approximated fairly well for thick pyrex walls using the hard-wall model, when the SAW is actuated on a frequency corresponding to a resonance frequency of the water domain, but less well for thinner walls at resonance and for any wall thickness off resonance. The reduced lossy-wall model was found to poorly approximate the full PDMS model for walls thinner than the 3-mm PDMS damping length, especially regarding the resulting running pressure waves in the reduced lossy-wall model in contrast the standing waves in the full PDMS model.

Modeling of acoustofluidic devices should thus be performed in full to take into account all effects relating to the elastic walls defining the microchannel. At higher frequencies or higher acoustic power levels, even the full model presented here must be extended to take into account thermoviscous effects in the form of increased heating and temperature-depending effects [44,54]. Finally, to obtain quantitatively better results for the pressure fields driving acoustophoresis in the water domain, the piezoelectric substrate should be included in future simulations. Hopefully, such an analysis will be of interest to experimentalists, who in turn may provide improved experimental data to validate the model. Moreover, with such an extended model including the dynamics of the piezoelectric substrate,



a study could be carried out for other actuation conditions than the ones studied here, such as bulk acoustic wave actuation, for which more experimental results exist.

**Author Contributions:** N.R.S and H.B. contributed equally to the work.

**Conflicts of Interest:** The authors declare no conflict of interest.

## Abbreviations

The following abbreviations are used in this manuscript:

Pyrex	Borosilicate glass
PDMS	Polydimethylsiloxane
SAW	Surface acoustic wave
BAW	Bulk acoustic wave
IDT	Interdigital transducer

## Bibliography

- Petersson, F.; Åberg, L.; Sward-Nilsson, A.M.; Laurell, T. Free flow acoustophoresis: Microfluidic-based mode of particle and cell separation. *Anal. Chem.* **2007**, *79*, 5117–5123.
- Amini, H.; Lee, W.; Di Carlo, D. Inertial microfluidic physics. *Lab Chip* **2014**, *14*, 2739–2761.
- Shi, J.; Huang, H.; Stratton, Z.; Huang, Y.; Huang, T.J. Continuous particle separation in a microfluidic channel via standing surface acoustic waves (SSAW). *Lab Chip* **2009**, *9*, 3354–3359.
- Shi, J.; Yazdi, S.; Lin, S.C.S.; Ding, X.; Chiang, I.K.; Sharp, K.; Huang, T.J. Three-dimensional continuous particle focusing in a microfluidic channel via standing surface acoustic waves (SSAW). *Lab Chip* **2011**, *11*, 2319–2324.
- Chen, Y.; Nawaz, A.A.; Zhao, Y.; Huang, P.H.; McCoy, J.P.; Levine, S.J.; Wang, L.; Huang, T.J. Standing surface acoustic wave (SSAW)-based microfluidic cytometer. *Lab Chip* **2014**, *14*, 916–923.
- Lee, K.; Shao, H.; Weissleder, R.; Lee, H. Acoustic purification of extracellular microvesicles. *ACS Nano* **2015**, *9*, 2321–2327.
- Liga, A.; Vliegthart, A.D.B.; Oosthuyzen, W.; Dear, J.W.; Kersaudy-Kerhoas, M. Exosome isolation: A microfluidic road-map. *Lab Chip* **2015**, *15*, 2388–2394.
- Pamme, N. Continuous flow separations in microfluidic devices. *Lab Chip* **2007**, *7*, 1644.
- Sethu, P.; Sin, A.; Toner, M. Microfluidic diffusive filter for apheresis (leukapheresis). *Lab Chip* **2006**, *6*, 83–89.
- Huh, D.; Bahng, J.H.; Ling, Y.; Wei, H.H.; Kripfgans, O.D.; Fowlkes, J.B.; Grothberg, J.B.; Takayama, S. Gravity-driven microfluidic particle sorting device with hydrodynamic separation amplification. *Anal. Chem.* **2007**, *79*, 1369–1376.
- Sugiyama, D.; Teshima, Y.; Yamanaka, K.; Briones-Nagata, M.P.; Maeki, M.; Yamashita, K.; Takahashi, M.; Miyazaki, M. Simple density-based particle separation in a microfluidic chip. *Anal. Methods* **2014**, *6*, 308–311.
- Zhang, J.; Yan, S.; Yuan, D.; Alici, G.; Nguyen, N.T.; Warkiani, M.E.; Li, W. Fundamentals and applications of inertial microfluidics: A review. *Lab Chip* **2016**, *16*, 10–34.
- Pamme, N.; Wilhelm, C. Continuous sorting of magnetic cells via on-chip free-flow magnetophoresis. *Lab Chip* **2006**, *6*, 974–980.
- Guldiken, R.; Jo, M.C.; Gallant, N.D.; Demirci, U.; Zhe, J. Sheathless size-based acoustic particle separation. *Sensors* **2012**, *12*, 905–922.
- Travagliati, M.; Shilton, R.; Beltram, F.; Cecchini, M. Fabrication, Operation and flow visualization in surface-acoustic-wave-driven acoustic-counterflow microfluidics. *J. Vis. Exp.* **2013**, *78*, e50524.
- Guo, F.; Mao, Z.; Chen, Y.; Xie, Z.; Lata, J.P.; Li, P.; Ren, L.; Liu, J.; Yang, J.; Dao, M.; et al. Three-dimensional manipulation of single cells using surface acoustic waves. *Proc. Natl. Acad. Sci. USA* **2016**, *113*, 1522–1527.
- Bruus, H.; Dual, J.; Hawkes, J.; Hill, M.; Laurell, T.; Nilsson, J.; Radel, S.; Sadhal, S.; Wiklund, M. Forthcoming lab on a chip tutorial series on acoustofluidics: Acoustofluidics-exploiting ultrasonic standing

- wave forces and acoustic streaming in microfluidic systems for cell and particle manipulation. *Lab Chip* **2011**, *11*, 3579–3580.
18. Evander, M.; Gidlof, O.; Olde, B.; Erlinge, D.; Laurell, T. Non-contact acoustic capture of microparticles from small plasma volumes. *Lab Chip* **2015**, *15*, 2588–2596.
  19. Wiklund, M. Acoustofluidics 12: Biocompatibility and cell viability in microfluidic acoustic resonators. *Lab Chip* **2012**, *12*, 2018–2028.
  20. Collins, D.J.; Morahan, B.; Garcia-Bustos, J.; Doerig, C.; Plebanski, M.; Neild, A. Two-dimensional single-cell patterning with one cell per well driven by surface acoustic waves. *Nat. Commun.* **2015**, *6*, 8686.
  21. Ahmed, D.; Ozcelik, A.; Bojanala, N.; Nama, N.; Upadhyay, A.; Chen, Y.; Hanna-Rose, W.; Huang, T.J. Rotational manipulation of single cells and organisms using acoustic waves. *Nat. Commun.* **2016**, *7*, 11085.
  22. Augustsson, P.; Karlsen, J.T.; Su, H.W.; Bruus, H.; Voldman, J. Iso-acoustic focusing of cells for size-insensitive acousto-mechanical phenotyping. *Nat. Commun.* **2016**, *7*, 11556.
  23. Hammarström, B.; Laurell, T.; Nilsson, J. Seed particle enabled acoustic trapping of bacteria and nanoparticles in continuous flow systems. *Lab Chip* **2012**, *12*, 4296–4304.
  24. Carugo, D.; Octon, T.; Messaoudi, W.; Fisher, A.L.; Carboni, M.; Harris, N.R.; Hill, M.; Glynne-Jones, P. A thin-reflector microfluidic resonator for continuous-flow concentration of microorganisms: A new approach to water quality analysis using acoustofluidics. *Lab Chip* **2014**, *14*, 3830–3842.
  25. Sitters, G.; Kamsma, D.; Thalhhammer, G.; Ritsch-Martel, M.; Peterman, E.J.G.; Wuite, G.J.L. Acoustic force spectroscopy. *Nat. Meth.* **2015**, *12*, 47–50.
  26. Augustsson, P.; Magnusson, C.; Nordin, M.; Lilja, H.; Laurell, T. Microfluidic, label-free enrichment of prostate cancer cells in blood based on acoustophoresis. *Anal. Chem.* **2012**, *84*, 7954–7962.
  27. Li, P.; Mao, Z.; Peng, Z.; Zhou, L.; Chen, Y.; Huang, P.H.; Truica, C.I.; Drabick, J.J.; El-Deiry, W.S.; Dao, M.; et al. Acoustic separation of circulating tumor cells. *Proc. Natl. Acad. Sci. USA* **2015**, *112*, 4970–4975.
  28. Hammarström, B.; Nilson, B.; Laurell, T.; Nilsson, J.; Ekström, S. Acoustic trapping for bacteria identification in positive blood cultures with MALDI-TOF MS. *Anal. Chem.* **2014**, *86*, 10560–10567.
  29. Muller, P.B.; Barnkob, R.; Jensen, M.J.H.; Bruus, H. A numerical study of microparticle acoustophoresis driven by acoustic radiation forces and streaming-induced drag forces. *Lab Chip* **2012**, *12*, 4617–4627.
  30. Leibacher, I.; Schatzer, S.; Dual, J. Impedance matched channel walls in acoustofluidic systems. *Lab Chip* **2014**, *14*, 463–470.
  31. Muller, P.B.; Bruus, H. Theoretical study of time-dependent, ultrasound-induced acoustic streaming in microchannels. *Phys. Rev. E* **2015**, *92*, 063018.
  32. Arruda, E.M.; Boyce, M.C. A three-dimensional constitutive model for the large stretch behavior of rubber elastic materials. *J. Mech. Phys. Solids* **1993**, *41*, 389–412.
  33. Yu, Y.S.; Zhao, Y.P. Deformation of PDMS membrane and microcantilever by a water droplet: Comparison between Mooney–Rivlin and linear elastic constitutive models. *J. Colloid Interface Sci.* **2009**, *332*, 467–476.
  34. Bourbaba, H.; Achaiba, C.B.; Mohamed, B. Mechanical behavior of polymeric membrane: Comparison between PDMS and PMMA for micro fluidic application. *Energy Procedia* **2013**, *36*, 231–237.
  35. Darinskii, A.N.; Weihnacht, M.; Schmidt, H. Computation of the pressure field generated by surface acoustic waves in microchannels. *Lab Chip* **2016**, *16*, 2701–2709.
  36. Nama, N.; Barnkob, R.; Mao, Z.; Kähler, C.J.; Costanzo, F.; Huang, T.J. Numerical study of acoustophoretic motion of particles in a PDMS microchannel driven by surface acoustic waves. *Lab Chip* **2015**, *15*, 2700–2709.
  37. Mao, Z.; Xie, Y.; Guo, F.; Ren, L.; Huang, P.H.; Chen, Y.; Rufo, J.; Costanzo, F.; Huang, T.J. Experimental and numerical studies on standing surface acoustic wave microfluidics. *Lab Chip* **2016**, *16*, 515–524.
  38. Bruus, H. Acoustofluidics 2: Perturbation theory and ultrasound resonance modes. *Lab Chip* **2012**, *12*, 20–28.
  39. Weis, R.; Gaylord, T. Lithium niobate: Summary of physical properties and crystal structure. *Appl. Phys. A* **1985**, *37*, 191–203.
  40. Narottam, P.; Bansal, N.P.; Bansal, R.H.D. *Handbook of Glass Properties*; Elsevier LTD: Amsterdam, The Netherlands, 1986.
  41. Hahn, P.; Dual, J. A numerically efficient damping model for acoustic resonances in microfluidic cavities. *Phys. Fluids* **2015**, *27*, 062005.

42. Madsen, E.L. Ultrasonic shear wave properties of soft tissues and tissuelike materials. *J. Acoust. Soc. Am.* **1983**, *74*, 1346–1355.
43. Zell, K.; Sperl, J.I.; Vogel, M.W.; Niessner, R.; Haisch, C. Acoustical properties of selected tissue phantom materials for ultrasound imaging. *Phys. Med. Biol.* **2007**, *52*, N475.
44. Muller, P.B.; Bruus, H. Numerical study of thermoviscous effects in ultrasound-induced acoustic streaming in microchannels. *Phys. Rev. E* **2014**, *90*, 043016.
45. Kim, D.H.; Song, J.; Choi, W.M.; Kim, H.S.; Kim, R.H.; Liu, Z.; Huang, Y.Y.; Hwang, K.C.; Zhang, Y.W.; Rogers, J.A. Materials and noncoplanar mesh designs for integrated circuits with linear elastic responses to extreme mechanical deformations. *Proc. Natl. Acad. Sci. USA* **2008**, *105*, 18675–18680.
46. Schneider, F.; Fellner, T.; Wilde, J.; Wallrabe, U. Mechanical properties of silicones for MEMS. *J. Micromech. Microeng.* **2008**, *18*, 065008.
47. Hohne, D.N.; Younger, J.G.; Solomon, M.J. Flexible microfluidic device for mechanical property characterization of soft viscoelastic solids Such as bacterial biofilms. *Langmuir* **2009**, *25*, 7743–7751.
48. Still, T.; Oudich, M.; Auerhammer, G.K.; Vlassopoulos, D.; Djafari-Rouhani, B.; Fytas, G.; Sheng, P. Soft silicone rubber in phononic structures: Correct elastic moduli. *Phys. Rev. B* **2013**, *88*, 094102.
49. Johnston, I.D.; McCluskey, D.K.; Tan, C.K.L.; Tracey, M.C. Mechanical characterization of bulk Sylgard 184 for microfluidics and microengineering. *J. Micromech. Microeng.* **2014**, *24*, 035017.
50. Lin, I.K.; Ou, K.S.; Liao, Y.M.; Liu, Y.; Chen, K.S.; Zhang, X. Viscoelastic characterization and modeling of polymer transducers for biological applications. *J. Microelectromech. Syst.* **2009**, *18*, 1087–1099.
51. COMSOL Multiphysics, version 5.2. Available online: [www.comsol.com](http://www.comsol.com) (accessed on 25 September 2015).
52. Köster, D. Numerical simulation of acoustic streaming on surface acoustic wave-driven biochips. *SIAM J. Sci. Comput.* **2007**, *29*, 2352–2380.
53. Muller, P.B.; Rossi, M.; Marin, A.G.; Barnkob, R.; Augustsson, P.; Laurell, T.; Kähler, C.J.; Bruus, H. Ultrasound-induced acoustophoretic motion of microparticles in three dimensions. *Phys. Rev. E* **2013**, *88*, 023006.
54. Ha, B.H.; Lee, K.S.; Destgeer, G.; Park, J.; Choung, J.S.; Jung, J.H.; Shin, J.H.; Sung, H.J. Acoustothermal heating of polydimethylsiloxane microfluidic system. *Sci. Rep.* **2015**, *5*, 11851.



© 2016 by the authors; licensee MDPI, Basel, Switzerland. This article is an open access article distributed under the terms and conditions of the Creative Commons Attribution (CC-BY) license (<http://creativecommons.org/licenses/by/4.0/>).



## Chapter 5

# Modeling a full device in 3D

In this chapter we will describe improvements made to the numeric fluid-solid full models F1 & F2 described in Chapter 4, to more accurately represent complex acoustofluidic devices. We check our implementation of anisotropic materials against analytical solutions, compare the model against previously published experimental results [54], and comment on the particular steady streaming field that arises in the device due to its geometry. As in Chapter 4, parts of the improvements and results presented here are described in more detail in the journal article *3D modeling of acoustofluidics in a liquid-filled cavity including streaming, viscous boundary layers, surrounding solids, and a piezoelectric transducer* by [N. R. Skov](#), J. S. Bach, B. G. Winckelmann, and H. Bruus [3] (PDF, DOI:10.3934/Math.2019.1.99), enclosed in full at the end of this chapter. Other parts of this chapter have not been presented before, and the entirety of the text is a reformulation from the article.

### 5.1 Motivation

Based on the conclusion in Section 4.4 we will expand our model to include piezoelectric motion. Additionally, we wish to make our model more generally applicable by moving beyond isotropic materials and introducing anisotropic linear elastics and piezoelectric materials to the model. As a last improvement, we move from 2D to 3D modeling, in an effort to include the entire device in our numeric model. This requires the implementation of effective pressure modeling, as full fluid modeling is not feasible in 3D due to the minute thickness of the viscous boundary layer.

#### 5.1.1 Reproducing published experimental results

To verify that the new additions to our model give reliable acoustophoretic predictions we expand on the fluid-solid model described in Chapter 5, to model the acoustofluidic device used by Hagsäter *et al.* [54] sketched in Fig. 5.1(a). In addition to providing an experimental handshake for our model, it also opens for the possibility of a studying the particular  $6 \times 6$  streaming velocity pattern observed in this device. This was previously done by Lei *et al.* [53], using a reduced fluid-only 3D numeric model with which they concluded that the streaming was boundary-driven. Analysis in [109] of an idealized version of the device however, indicated that this particular streaming may

be bulk-driven, which we investigate with our model.

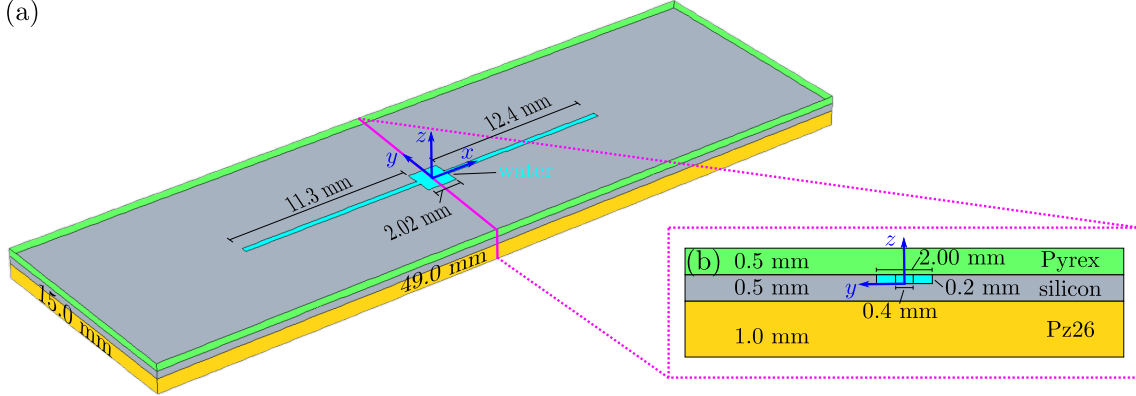


**Figure 5.1:** Sketch and cross-section of the device. (a) Sketch of the device, with the Pyrex lid rendered invisible. The channel is perfectly centered in the  $x$ -direction. (b) Cross-section of the line marked in magenta.

**Table 5.1:** The device and numerical model dimensions.

Domain	Length ( $x$ ) [mm]	Width ( $y$ ) [mm]	Height ( $z$ ) [mm]
Pz26	49	15	1.0
Silicon	49	15	0.5
Pyrex	49	15	0.5
Cavity	2	2.02	0.2
Channel 1	11.3	0.4	0.2
Channel 2	11.3	0.4	0.2

## 5.2 Model system

The device, shown in Fig. 5.1 consists of a microchannel etched into a slab of mono-crystalline silicon, - hereon implied by 'silicon'. Positioned 0.55mm / 2.3 % off from the middle of the channel is a fluid cavity with a nearly quadratic cross-section, with the length of the cavity being 0.02mm / 1.0 % longer than its width, possibly due to a manufacturing error. A Pyrex glass lid of equal surface area as the silicon slab with inlet and outlet holes at the ends of the microchannel covers the silicon and the fluid domain. The system is actuated by a rectangular piece of lead zirconium titanate (PZT) glued to the bottom of the silicon. Our numeric model, outlined in Fig. 5.1(a), is a 1:1 model of the physical device, where we have assumed the PZT to be Pz26 and to have the same cross-sectional area as the silicon slab and height, since neither the exact type or the actual dimensions are not reported. See Fig. 5.1 and Table 5.1 for the exact dimensions.

The new additions over the previously described model are, (i) one linearly elastic and one piezoelectric anisotropic material, (ii) the physics of piezoelectricity, (iii) effective acoustic pressure modeling in the fluid including the streaming field, (iv) particle tracking calculations and (v) the third dimension in the numeric model.

### 5.2.1 Anisotropic materials

The linear elastics used in the device are Pyrex glass, silicon and PZT. Pyrex is an isotropic material and was already included in the model from previously, while silicon and PZT both are anisotropic materials, with general stress constitutive relations.

Silicon is of the cubic crystal class and requires 3 elastic moduli to fully determine the stress state. PZT is of the tetragonal crystal and has 5 independent elastic moduli, 2 constants of permittivity and 3 coupling constants, as it is also piezoelectric.

We include the new stress definitions in our model, using the Voigt notation described in Section 2.2.3. For silicons the stress is purely mechanic Eq. (5.1a), while it in the PZT is electromechanic Eq. (5.1b),

$$\boldsymbol{\sigma}_V = \mathbf{C}\boldsymbol{\epsilon}_V, \quad (5.1a)$$

$$\boldsymbol{\sigma}_V = \mathbf{C}\boldsymbol{\epsilon}_V - \mathbf{e}^T \mathbf{E}. \quad (5.1b)$$

The increased complexity also increases the probability of human errors and typos. To verify that we implement the new materials properly, we make a simple test system that can be compared with analytical values. We choose to do so for silicon where the speed of sound as a function of material orientation is analytically known. Hence, we use these as grounds for validating our implementation of Voigt notation.

#### Analytical speeds from the Christoffel equation

The propagation speed of a plane wave in a solid depends on the propagation direction expressed by wavenumber  $k_i$ . For a given direction the propagation speed  $c$  and wave polarizations  $p_i = \frac{u_i}{\sqrt{u_j u_j}}$  can be found as the eigenmodes of the Christoffel equation [110]

$$\left[ \rho_s c^2 \delta_{ik} - C_{ijkl} n_j n_l \right] u_k = 0 \quad (5.2)$$

We solve Eq. (5.2) for a wave propagating in the  $x, y$ -plane with  $k_i = (\cos(\theta), \sin(\theta), 0)$ , and find a solution for each of the three principal polarizations. The wave polarized along the propagating direction is called the longitudinal wave and has the speed  $c_{L,x}^{\text{ana}}$ . The waves polarized in  $y$  and  $z$  are the transverse waves and have propagation speeds  $c_{T,y}^{\text{ana}}$  and  $c_{T,z}^{\text{ana}}$ , which we wish to compare to numerically found values.

#### Numerical velocities based on a quasi-1D model system

The model we use for comparison is a rod of silicon shown in Fig. 5.2(a). The rod lies along the  $x$ -axis from  $x = 0$  to  $x = L_{\text{PML}}$ , has a quadratic cross-section of width  $w$ . From  $x = L$  to  $x = L_{\text{PML}}$  is a PML-silicon region with the same cross-section. The crystal  $X$ -axis is rotated positively an angle of  $\theta$  around the global  $z$ -axis, using the Bond matrices described in Section 3.6. Along the  $y$ - and  $z$ -facing rod surfaces, symmetry conditions are applied to mimic an infinitely thick domain, making the model quasi-one-dimensional. Therefore, any actuation applied at the surface  $x = 0$  propagates unperturbed along the rod until the PML region where it is fully absorbed. This

allows us to investigate the propagation of traveling waves of any polarization in silicon for any given rotation about the  $z$ -axis.

We make a series of simulations with varying  $\theta$  in which we apply a wave with one of the three principal polarizations: the longitudinal  $x$ -polarized wave and the transverse  $y$ - and  $z$ -polarized waves. For each wave polarization, we measure the wavelength  $\lambda$  and use it to calculate the corresponding propagation speed from the single-frequency dispersion relation  $c = \lambda f$ . The speeds of sound are  $c_{L,x}^{\text{num}}$ ,  $c_{T,y}^{\text{num}}$  and  $c_{T,z}^{\text{num}}$  respectively. In Fig. 5.2(b) we show a velocity surface of the analytically and numerically obtained values as functions of  $\theta$ . We see that the analytically

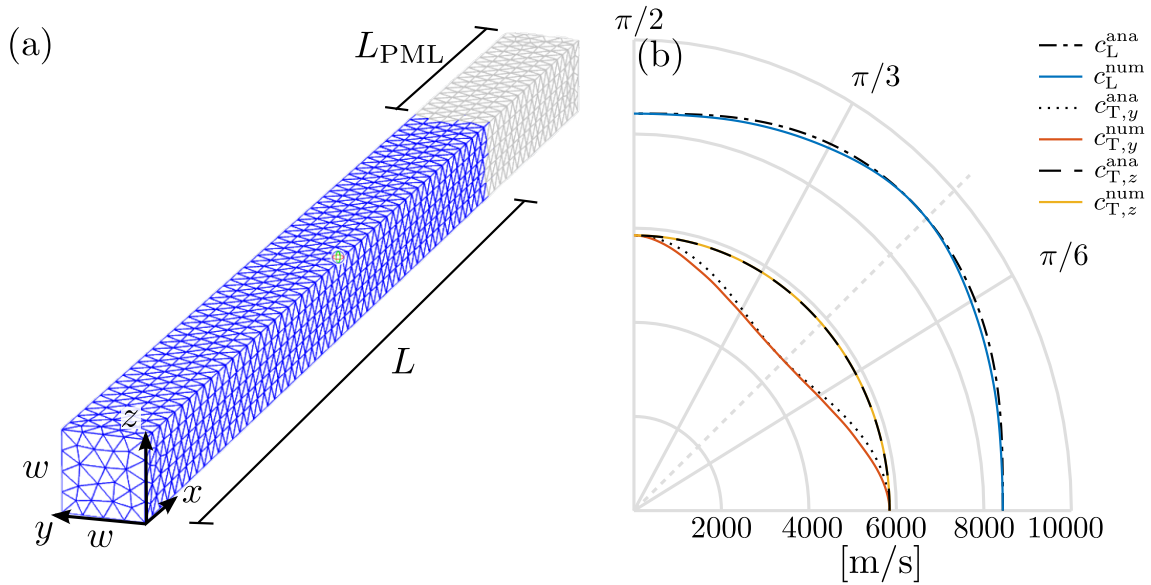


**Figure 5.2:** (a) The numeric model of a rod, used to measure wavelengths of waves polarized along principal axes. The blue mesh shows the silicon domain, and the gray mesh shows the silicon-PML domain. (b) Velocity surface in the  $x, y$ -plane, showing speed of sound for the three principal wave polarizations as a function of rotation angle  $\theta$  around the  $z$ -axis. We plot only a quarter of the surface diagram, since cubic crystals have symmetry planes in between principal axes, illustrated by the dashed line at  $\pi/4$ .

and numerically velocity surfaces agree quite well, particularly for the  $z$ -polarized wave, where the two are identical. This is to be expected, as the rotation is about the  $z$ -axis. Therefore the stiffness determining the speed of sound for the  $z$ -polarized wave does not change.

For the other two surfaces, the maximum deviations are 1.1% and 2.7% respectively indicating that we have properly implemented the anisotropic material and Bond matrices in our model. Note that a rotation about either of the principal axes yields the same result due to silicon being a cubic crystal. This is not the case for crystal classes with fewer symmetries such as PZT.

## 5.2.2 Piezoelectricity

We include the piezoelectric effect in the PZT transducer to exactly model the actuation of the fluid domain. For this we implement Gauss's law, Eq. (2.27), for a harmonically oscillating potential



$\phi_1$  in our model.

$$\nabla \cdot \mathbf{D}_1 = 0. \quad (5.3)$$

The electric density flux here is calculated in the PZT using Eq. (2.15)

$$\mathbf{D}_1 = \varepsilon_0 \tilde{\mathbf{e}} \mathbf{E}_1 + \mathbf{e} \varepsilon_{V,1}, \quad (5.4)$$

We model the PZT as having a charged top surface and a grounded bottom surface implemented as described in Eq. (2.35),

$$\phi_1^{\text{ch}} = V_0 \text{ at top charged surface} \quad , \quad \phi_1^{\text{gr}} = 0 \text{ at bottom grounded surface.} \quad (5.5)$$

### 5.2.3 Effective acoustic pressure modeling and streaming calculations

We replace the first-order fluid mass and momentum conservation equations with effective acoustic pressure modeling and compute the pressure using Eq. (2.20)

$$\nabla \cdot (\nabla p_1) - k^2 p_1 = 0, \quad (5.6)$$

where the fluid velocity is defined as in Eq. (2.21)

$$\mathbf{v} = -i \frac{1 - i\Gamma_f}{\omega \rho_f} \nabla p_1, \quad \Gamma_f = \left( \frac{4}{3} \eta_f + \eta_f^b \right) \omega \kappa_f. \quad (5.7)$$

We employ the theory for effective boundary conditions Eq. (2.33) developed by Bach and Bruus in [61]

$$\boldsymbol{\sigma}_1^s \cdot \mathbf{n} = -p_1 \mathbf{n} - ik_s \eta_f (\mathbf{v}_{sl} - \mathbf{v}_1) \quad \text{Fluid-controlled stress continuity,} \quad (5.8a)$$

$$\mathbf{v}_1 \cdot \mathbf{n} = \mathbf{v}^s \cdot \mathbf{n} - \frac{i}{k_s} \nabla_{\parallel} \cdot (\mathbf{v}_{sl} - \mathbf{v}_1)_{\parallel} \quad \text{Solid-controlled velocity continuity.} \quad (5.8b)$$

We also introduce the streaming field  $\mathbf{v}_2$  to the model. We calculate this using particular forms of Eqs. (2.23) and (2.24) that emphasizes the energy-flux density vector  $\langle \mathbf{S}_{ac} \rangle = \langle p_1 \mathbf{v}_1 \rangle$

$$\nabla \cdot \mathbf{v}_2 = 0, \quad (5.9)$$

$$\nabla \cdot \left[ - (p_2 - \langle L_{ac} \rangle) \mathbf{I} + \eta_f \nabla \mathbf{v}_2 \right] + \frac{\Gamma \omega}{c_f^2} \langle \mathbf{S}_{ac} \rangle = \mathbf{0}. \quad (5.10)$$

Here we use a form of the effective boundary conditions on the streaming velocity specifically for devices driven at resonance [61],

$$\mathbf{n} \cdot \mathbf{v}_2^{\text{bc}} = 0, \quad (\mathbf{1} - \mathbf{n}\mathbf{n}) \cdot \mathbf{v}_2 = -\frac{1}{8\omega} \nabla_{\parallel} \|\mathbf{v}_1\|^2 - \text{Re} \left[ \left( \frac{2 - i}{4\omega} \nabla_{\parallel} \cdot \mathbf{v}_1^* + \frac{i}{2\omega} \partial_{\perp} v_{1\perp}^* \right) \mathbf{v}_{1\parallel} \right]. \quad (5.11)$$

Implementing effective fluid acoustics reduces the number of DOF in the system drastically, as the vector velocity field and scalar pressure field is reduced by a single scalar pressure field. Additionally, the theory analytically solves the fluid motion within the micrometer-sized viscous boundary layer that has to be spatially resolved by at least 7 nodes in the full model. Implementing the effective pressure modeling reduces the number of DOF enough that we can model the device in its entirety, which would otherwise not be feasible.

### 5.2.4 Particle trajectories

To predict the acoustophoretic motion of a set of fictitious particles distributed across the cavity we iteratively solve Newton's second law Eq. (2.43)

$$4/3\pi a^3 \rho_{\text{ps}} \frac{d}{dt} \mathbf{v}_{\text{ps}}(\mathbf{r}, t) = \mathbf{F}^{\text{rad}} + \mathbf{F}^{\text{drag}}, \quad (5.12)$$

with the streaming drag  $\mathbf{F}^{\text{drag}}$  defined as

$$\mathbf{F}^{\text{drag}} = 6\pi\eta a (\mathbf{v}_2(\mathbf{r}) - \mathbf{v}_{\text{ps}}(\mathbf{r}, t)) \quad (5.13)$$

and the acoustic radiation force  $\mathbf{F}^{\text{drag}}$  defined as a gradient force

$$\mathbf{F}^{\text{rad}} = -\nabla U^{\text{rad}}, \quad \text{where} \quad U^{\text{rad}} = \frac{4\pi}{3} a^3 \left( f_0 \frac{1}{4} \kappa_f |p_1|^2 - f_1 \frac{3}{8} \rho_f |\mathbf{v}_1|^2 \right). \quad (5.14a)$$

Here the monopole  $f_0$  and dipole  $f_1$  coefficients are defined for polystyrene beads as

$$f_0 = 1 - \frac{\kappa_{\text{ps}}}{\kappa_f} = 0.468, \quad f_1 = \frac{2(\rho_{\text{ps}} - \rho_f)}{2\rho_{\text{ps}} + \rho_f} = 0.034. \quad (5.14b)$$

### 5.2.5 Three-dimensional modeling

Moving from two to three dimensions is trivial with regards to the numerics. It is merely a question of adding terms for the third dimensions in the auxiliary fields and the governing equations. For instance the Laplacian of the pressure in Eq. (5.6) has three terms instead of two in 3D simulations.

The most significant factor when adding a dimension is in the meshing, because mesh elements also gain dimensions and any changes in the mesh element size are lifted to the power of the dimensions of the model. For instance, reducing a mesh element length to half its original size results in twice as many elements in a 1D model, four times as many in a 2D model and 8 times as many in 3D model. Hence, much more care must be taken to reduce the mesh as much as possible, while obeying the 6-nodes-per-wavelength rule of thumb. To minimize the number of DOF in the model, we define mesh element sizes for each of the domains PZT, silicon, fluid and Pyrex, corresponding to 6 elements per wavelength in the material. In the solids, this is chosen to be the shortest wavelength, while it in the fluid is the compressional wave.

## 5.3 Key results and observations

We compare our numeric model to the experimental results of Ref. [54], through the observed and calculated acoustophoretic motion of beads suspended in the fluid cavity, when running the device at a frequency near the two hard-wall eigenmodes  $f_{3,0,0} \approx f_{0,3,0} = 2.45$  MHz of the fluid cavity. Note that the modes are only approximately equal due to the 1.0% deviation in the two side lengths. Furthermore, we study the cause of the  $6 \times 6$ -streaming pattern in the system by tuning the relative strength of the bulk forcing term to the velocity imposed on the streaming field by the boundary conditions.

### 5.3.1 Handshake with experimental observations

In Fig. 5.3(a1) and (a2), we show experimental particle image velocimetry (PIV) measurements in the initial stages of acoustophoresis briefly after ultrasound is turned on for large and small particles plotted on a background of a micrograph of the cavity. In (b1) we compare the traces of (a1) to the calculated acoustic radiation potential  $U^{\text{rad}}$  and the acoustic radiation force  $F^{\text{rad}}$ . In (b2) on the other hand we compare the acoustic streaming velocity  $v_2$  to the motion of (a2).

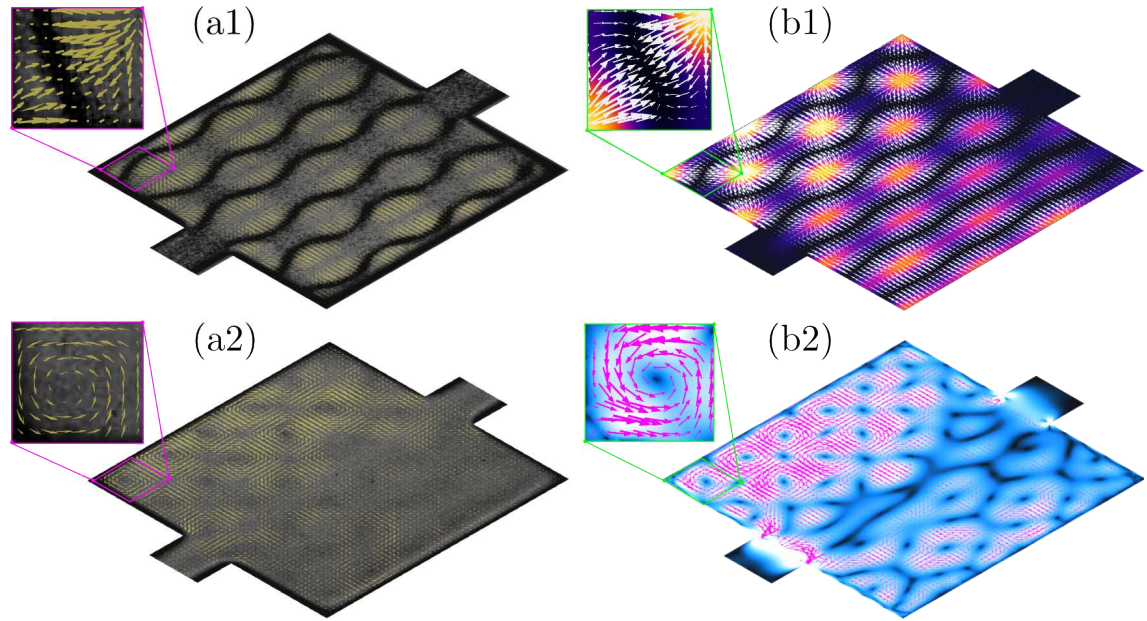


**Figure 5.3:** The experimentally observed and numerically predicted second-order fields. (a1) Arrow plot of particle image velocimetry measurements of 5  $\mu\text{m}$  polystyrene beads, 1 ms after an ac potential with frequency  $f = 2.17$  MHz is applied across the PZT. The arrow plot's background is a micrograph of the cavity after the beads have settled. The silicon chip is gray, while particle agglomerations are black. (a2) Same as in (a1) but for 1  $\mu\text{m}$  beads. Here the micrograph shows no particles continuously following closed loops. (b1) Contour of the radiation potential at the vertical center-plane of the cavity with superimposed arrows showing the direction of the radiation force  $F^{\text{rad}}$ , for the applied frequency  $f = 2.166$  MHz. (b2) Surface plot of the streaming velocity  $v_2$  magnitude, with superimposed arrows showing the direction, for the applied frequency  $f = 2.163$  MHz. From Ref. [2]

Given the size of the particles in (a1) we expect the acoustophoretic motion to be purely dominated by the radiation force  $F^{\text{rad}}$  that scales with  $a^3$ . Thus, the acoustic force calculated in (b1) should correspond to the measured particle tracks in (a1), if our numeric model holds. Similarly, the small particles in (a2) should be purely dominated by the streaming drag due to the  $a^2$ -scaling of the force ratio. Therefore, we expect that our calculated  $v_2$  field in (b2) should be similar to the particle traces in (a2).

In both cases we see that there is a good agreement between the numerically predicted field and the particle traces and thus between the calculated and experimentally inferred forces. In (a1)

and (b1) we see a structure of 6 bands in which the radiation force focuses particles. The particular pattern is due to fluid eigenmodes  $f_{0,3,0}$  and  $f_{3,0,0}$  degenerating slightly due to the quadratic shape of the cavity. The slight deviation from a purely quadratic cross-section and the channel in- and outlet break the symmetry, however, leading to two neighboring resonance peaks. Each of these are a mixture of the two modes. The plotted one is dominated by  $f_{3,0,0}$  but contains parts of  $f_{0,3,0}$ , causing the particular pattern observed. The neighboring peak, shows the opposite case, as it is dominated by the  $f_{0,3,0}$  mode.

Regarding (a2) and (b2) we observe that the observed streaming field is parallel to the transducer, and has  $6 \times 6$  rolls, rather than the 4 vertical rolls per wavelength one would expect from classical, boundary-driven, Rayleigh streaming. We also note that the 36 rolls have large variations in their intensity – a trait shared with the experimental data. Hagsäter *et al.*[54] make specific mention of this phenomenon with the statement “*If the frequency is shifted slightly in the vicinity of 2.17 MHz, the same vortex pattern will still be visible, but the strength distribution between the vortices will be altered*”. We observe this high frequency-sensitivity of the streaming field in our model simulations, possibly caused by the cavity’s broken symmetry. In Fig. 5.3 we chose the 2.163 MHz frequency for (b2) as this gave the best agreement with (a2), and it is reasonable to believe that the frequency was not kept fixed between the experiments with large and small particles.

Due to the lack of reported values regarding the exact design of the chip and of the driving voltage quantitative comparisons are difficult to carry out. We merely note that with an estimated driving voltage of 1 V, and a Pz26 slab covering the entire bottom surface of the silicon, our predicted particle velocities are very similar to those reported.

### 5.3.2 Streaming driving force

In Fig. 5.4 we plot sets of particle trajectories calculated using our model. In (a) we show particle paths and final positions of radiation-force-dominated particles. In (b) we show the initial paths and instantaneous positions of small particles when using an exaggerated bulk driving force in the streaming field, while we in (c) plot the same with no bulk force.

In Fig. 5.4(a) we see the large particles forming 6 bands parallel to the inlet, mirroring the field of Fig. 5.3(a1) as the radiation force completely dominates the motion of particles of this size. More interestingly, we note in Fig. 5.4(b) that as we amplify the  $\langle S_{ac} \rangle$ -term, the small particles follow the  $6 \times 6$  pattern in a large portion of the cavity cross-section, as a consequence of the bulk driving force being larger relative to the driving boundary conditions. When we conversely eliminate the bulk driving altogether in (c) we see that the particle motion is no longer rotating, but much more similar to that of the large particles.

### 5.3.3 Large-particle acoustophoresis for a circular cavity

As an additional verification of the model we reshape the cavity to a 1-mm-radius circle as is also shown in Ref. [54]. We calculate the radiation potential and plot it against the measured motion of large particles in Fig. 5.5.

The studied cross-section is circular apart from the connecting channel, so a good approximate solution to the pressure distribution may be given by the modified Bessel function of the first kind

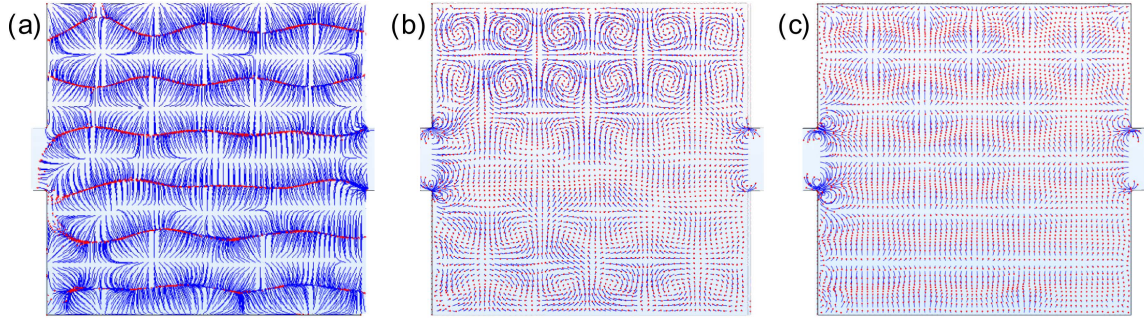


**Figure 5.4:** Particle traces for radiation force and streaming drag. (a) Particle paths (blue) and positions (red) for a homogeneous  $60 \times 60$  initial grid of  $5 \mu\text{m}$ -diameter-polystyrene beads in the mid-height of the cavity  $1.5 \text{ s}$  after applying the ac potential with  $V_0 = 1 \text{ V}$  and  $f = 2.166 \text{ MHz}$ . (b) The same as in (a) but for  $1\text{-}\mu\text{m}$ -diameter beads,  $f = 2.163 \text{ MHz}$ , and with a prefactor of 4 on the  $\langle S_{ac} \rangle$  term in Eq. (5.10) (c) As in (c) but with a prefactor of 0. From Ref. [2].

$p(r, \theta) \approx J_n(r) \cos(n\theta)$ , where  $n$  is an integer. Accordingly, the radiation potential can be approximated  $U^{\text{rad}} \approx p(r, \theta)^2 \approx J_n(r)^2 \cos(n\theta)$ . To compare this simple analytical estimate to our calculated one, we overlay the prediction radiation potential with contour lines of  $J_n(r)^2 \cos(n\theta)$ , for  $r = 0$  at the center of the cavity and  $\theta = 0$  aligned with the  $y$ -axis.

We see from Fig. 5.5(a) and (b) that the numeric model once again is in good agreement with the observed particle motion, and that the relative deviation between the observed and calculated frequencies is merely  $0.5 \%$ . From the overlaid contour plot in Fig. 5.5(b), we see that the acoustic radiation potential is also quite well approximated by the squared Bessel with a rotational dependence,  $J_1(r)^2 \cos(\theta)$ .

## 5.4 Concluding remarks

We have expanded on our 2D model from previously with five new features, allowing us to model the most important aspects of an isothermal acoustofluidic devices. We have modeled a previously presented device and compared our calculated acoustic fields with their experimental findings.

We found a good agreement between our numerically predicted and their experimentally observed acoustophoretic motion. We have also found that for the circular cross-sections in Ref. [54], the acoustophoresis of large particles can be approximated even simpler by using Bessel functions.

By amplifying the  $\langle S_{ac} \rangle$ -term of Eq. (5.10) in Fig. 5.4(b), we are effectively increasing the amount of energy transferred from the acoustic waves into net motion of the fluid, which is one of the two driving mechanisms for the streaming field, the other being the shear effects at boundaries. Vice versa, by nullifying it the streaming is only driven by the boundaries. We thus tip the scales in favor of the streaming being dominated by bulk forces or boundary driven in Fig. 5.4(b) and (c) respectively.

Hence, we infer that the driving mechanism of the streaming observed in Ref. [54] must be bulk-driven, as increasing relative strength of the bulk-term increases the agreement with experi-



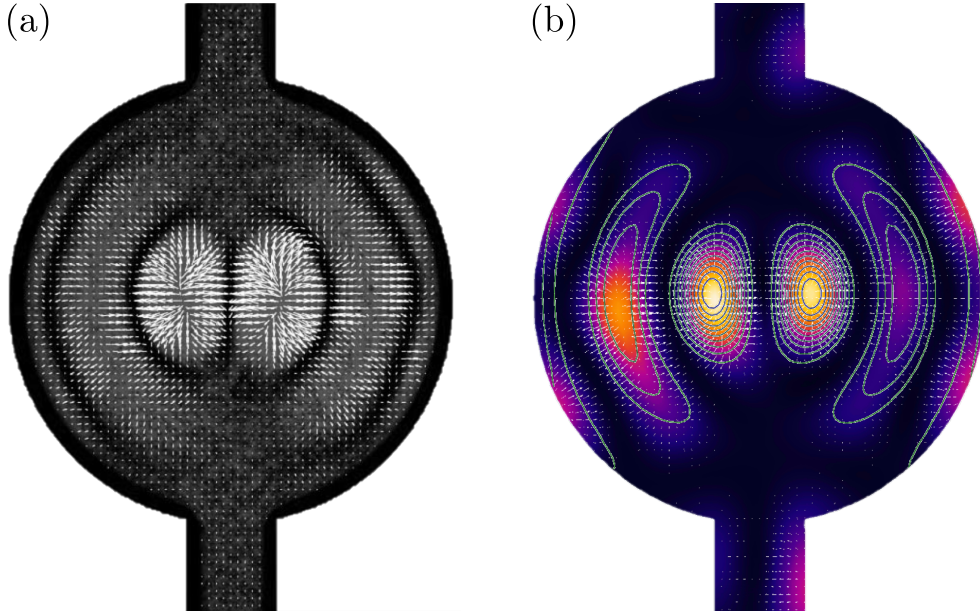


**Figure 5.5:** (a) Arrow plot of particle image velocimetry measurements of 5  $\mu\text{m}$  polystyrene beads, 1 ms after an ac potential with frequency  $f = 1.936$  MHz is applied across the PZT. The nearly-quadratic cavity of the device has here been replaced by a 1-mm-radius circular one. The arrow plot's background is a micrograph of the cavity after the beads have settled. The silicon chip is gray, while particle agglomerations are black. Adapted from Ref. [54]. (b) Contour of the radiation potential at the vertical center-plane of the cavity with superimposed arrows showing the direction of the radiation force  $\mathbf{F}^{\text{rad}}$ , for the applied frequency  $f = 1.925$  MHz. The overlaid contour lines indicate the square of the analytical solution  $U^{\text{rad}} \approx J_1(r)^2 \cos(\theta)$ , centered in the middle of the circular cavity.

ments, while eliminating it completely decreases it. This is despite the common knowledge that Eckart-streaming is primarily observed in larger systems.

Lei *et al.*[53] also noted the possibility of the Eckart bulk force driving the streaming pattern, but omitted the effect in their work. In their model they did observe the  $6 \times 6$  pattern driven by the boundaries, but only in 2 small regions away from the vertical center of the cavity, in which the particles are present. We on the other hand observed the reported streaming patterns in 80 % of the cavity height, with the deviations located at the 10 % each at the floor and ceiling of the cavity. Note that this was even observed with no prefactor on the  $\langle \mathcal{S}_{\text{ac}} \rangle$ -term. We merely used it to make the effect clearer.

With our 3D model including piezoelectric effect, anisotropy and effective pressure acoustics verified by past experiments, we feel confident in applying it to new areas. Therefore, we now move on to modeling of the novel device described by Sehgal and Kirby [44] with the intention to explain the working of the device and improve upon the design.

*3D modeling of acoustofluidics in a liquid-filled cavity including streaming, viscous boundary layers, surrounding solids, and a piezoelectric transducer*

**DOI:** [10.3934/Math.2019.1.99](https://doi.org/10.3934/Math.2019.1.99).

**Authors:** N. R. Skov, J. S. Bach, B. G. Winckelmann, and H. Bruus.

**Journal:** AIMS Mathematics **3**, 11556 (2019).



---

*Research article*

## **3D modeling of acoustofluidics in a liquid-filled cavity including streaming, viscous boundary layers, surrounding solids, and a piezoelectric transducer**

**Nils R. Skov, Jacob S. Bach, Bjørn G. Winckelmann and Henrik Bruus\***

Department of Physics, Technical University of Denmark, DTU Physics Building 309, DK-2800 Kongens Lyngby, Denmark

\* **Correspondence:** Email: [bruus@fysik.dtu.dk](mailto:bruus@fysik.dtu.dk); Tel: +4545253307.

**Abstract:** We present a full 3D numerical simulation of the acoustic streaming observed in full-image micro-particle velocimetry by Hagsäter *et al.*, Lab Chip **7**, 1336 (2007) in a 2 mm by 2 mm by 0.2 mm microcavity embedded in a 49 mm by 15 mm by 2 mm chip excited by 2-MHz ultrasound. The model takes into account the piezo-electric transducer, the silicon base with the water-filled cavity, the viscous boundary layers in the water, and the Pyrex lid. The model predicts well the experimental results.

**Keywords:** microscale acoustofluidics; acoustic streaming; numerical simulation; 3D modeling

**Mathematics Subject Classification:** 42B37, 65M60, 70J35, 74F10

---

### **1. Introduction and definition of the model system**

For the past 15 years, ultrasound-based microscale acoustofluidic devices have successfully and in increasing numbers been used in the fields of biology, environmental and forensic sciences, and clinical diagnostics [1–5]. However, it remains a challenge to model and optimize a given device including all relevant acoustofluidic aspects. Steadily, good progress is being made towards this goal. Examples of recent advances in modeling include work in two dimensions (2D) by Muller and Bruus [6, 7] on thermoviscous and transient effects of acoustic pressure, radiation force, and streaming in the fluid domain, and work by Nama *et al.* [8] on acoustophoresis induced by a given surface acoustic wave in a fluid domain capped by a PDMS lid. Examples of 3D modeling include work by Lei *et al.* [9, 10] on boundary-layer induced streaming in fluid domains with hard wall and outgoing plane-wave boundary conditions, work by Gralinski *et al.* [11] on the acoustic pressure fields in circular capillaries including the fluid and glass domains and excited by a given wall vibration, a model later extended by Ley and Bruus [12] to take into account absorption and outgoing waves, and work by Hahn and Dual [13] on the acoustic pressure and acoustic radiation force in the fluid domain including the surrounding transducer, silicon and glass domains, as well as bulk, boundary-layer, and thermal dissipation.



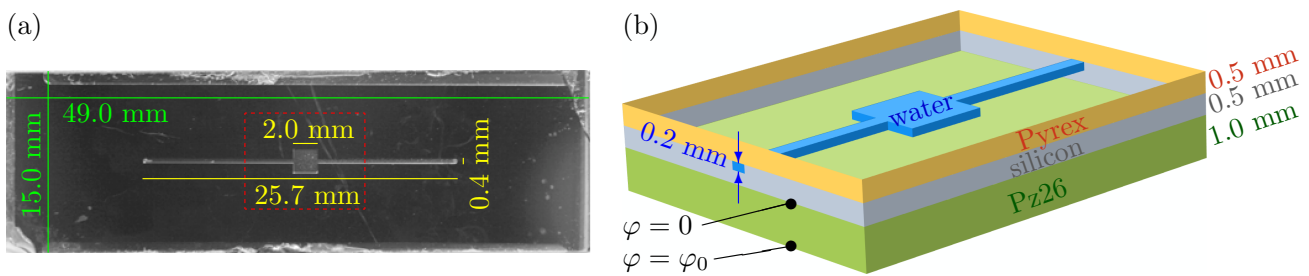


**Figure 1.** (a) Top-view photograph of the original transducer-silicon-glass device studied in 2007 by Hagsäter *et al.* [16]. (b) A cut-open 3D sketch of the device in the red-dashed area of panel (a) showing the Pz26 piezo-electric transducer (green), the silicon base (gray), the water-filled cavity (blue) in the top of the silicon base, and the Pyrex lid (orange).

**Table 1.** The length, width, and height  $L \times W \times H$  (in mm) of the six rectangular elements in the acoustofluidic device model of Figure 1(b): The piezoelectric transducer (pz), the silicon base (si), the Pyrex lid (py), the main cavity (ca), and the two inlet channels (c1) and (c2).

Pz26	Silicon	Pyrex	Cavity	Channel 1	Channel 2
$L_{pz} \times W_{pz} \times H_{pz}$	$L_{si} \times W_{si} \times H_{si}$	$L_{py} \times W_{py} \times H_{py}$	$L_{ca} \times W_{ca} \times H_{ca}$	$L_{c1} \times W_{c1} \times H_{c1}$	$L_{c2} \times W_{c2} \times H_{c2}$
$49 \times 15 \times 1.0$	$49 \times 15 \times 0.5$	$49 \times 15 \times 0.5$	$2.02 \times 2 \times 0.2$	$11.3 \times 0.4 \times 0.2$	$12.4 \times 0.4 \times 0.2$

In this paper, we present a 3D model and its implementation in the commercial software COMSOL Multiphysics [14] of a prototypical acoustofluidic silicon-glass-based device that takes into account the following physical aspects: the piezo-electric transducer driving the system, the silicon base that contains the acoustic cavity, the fluid with bulk- and boundary-layer-driven streaming, the Pyrex lid, and a dilute microparticle suspension filling the cavity. This work represents a synthesis of our previous modeling of streaming in 2D [6], acoustic fields in 3D [12], and boundary-layer analysis [15] enabling effective-model computation of streaming in 3D, and it combines and extends the 3D streaming study in the fluid domain by Lei *et al.* [10] and the 3D study of acoustics in the coupled transducer-solid-fluid system by Hahn and Dual [13]. To test the presented coupled 3D model, we have, as Lei *et al.* [10], chosen to model the system studied experimentally by Hagsäter *et al.* in 2007 [16] and shown in Figure 1. It consists of a rectangular 0.5-mm high silicon base, into the surface of which is etched a shallow square-shaped cavity with two inlet channels attached. The cavity is sealed with a 0.5-mm high Pyrex lid that exactly covers the silicon base. At the bottom of the silicon base is attached a 1-mm high rectangular Pz26 piezo-electric transducer. All three solid layers are 49 mm long and 15 mm wide. The nearly-square cavity is 2.02 mm long and 2 mm wide and has attached two inlet channels both 0.4 mm wide, but of unequal lengths 11.3 mm and 12.4 mm, respectively. The channels and cavity are 0.2 mm deep. A sketch of the model device is shown in Figure 1, and its geometrical parameters are summarized in Table 1. The transducer is grounded at the top and driven by an ac voltage  $\tilde{\varphi}$  of amplitude  $\varphi_0 = 1$  V and a frequency around 2.2 MHz applied to its bottom surface.

## 2. Theoretical background

We summarize the coupled equations of motion for a system driven by a time-harmonic electric potential,  $\tilde{\varphi} = \varphi_0 e^{-i\omega t}$  applied to selected boundaries of a piezo-electric Pz26 ceramic. Here, tilde denotes a field with harmonic time dependency,  $\omega$  is the angular frequency in the low MHz range, and “i” is the imaginary unit. This harmonic boundary condition excites the time-harmonic fields: the electric potential  $\tilde{\varphi}(\mathbf{r}, t)$  in the Pz26 ceramic, the displacement  $\tilde{\mathbf{u}}(\mathbf{r}, t)$  in the solids, and the acoustic pressure  $\tilde{p}_1(\mathbf{r}, t)$  in the water,

$$\tilde{\varphi}(\mathbf{r}, t) = \varphi(\mathbf{r}) e^{-i\omega t}, \quad \tilde{\mathbf{u}}(\mathbf{r}, t) = \mathbf{u}(\mathbf{r}) e^{-i\omega t}, \quad \tilde{p}_1(\mathbf{r}, t) = p_1(\mathbf{r}) e^{-i\omega t}. \quad (2.1)$$

In our simulation, we first solve the linear equations of the amplitude fields  $\varphi(\mathbf{r})$ ,  $\mathbf{u}(\mathbf{r})$ , and  $p_1(\mathbf{r})$ . Then, based on time-averaged products (over one oscillation period) of these fields, we compute the nonlinear acoustic radiation force  $\mathbf{F}^{\text{rad}}$  and the steady-state acoustic streaming velocity  $\mathbf{v}_2(\mathbf{r})$ .

### 2.1. Linear acoustics in the fluid

In the fluid (water) of density  $\rho_{\text{fl}}$ , sound speed  $c_{\text{fl}}$ , dynamic viscosity  $\eta_{\text{fl}}$ , and bulk viscosity  $\eta_{\text{fl}}^{\text{b}}$ , we model the acoustic pressure  $p_1$  as in Ref. [12],

$$\nabla^2 p_1 = -\frac{\omega^2}{c_{\text{fl}}^2} (1 + i\Gamma_{\text{fl}}) p_1, \quad \mathbf{v}_1 = -i \frac{1 - i\Gamma_{\text{fl}}}{\omega \rho_{\text{fl}}} \nabla p_1, \quad \Gamma_{\text{fl}} = \left( \frac{4}{3} \eta_{\text{fl}} + \eta_{\text{fl}}^{\text{b}} \right) \omega \kappa_{\text{fl}}. \quad (2.2)$$

Here,  $\mathbf{v}_1$  is the acoustic velocity which is proportional to the pressure gradient  $\nabla p_1$ , while  $\Gamma_{\text{fl}} \ll 1$  is a weak absorption coefficient, and  $\kappa_{\text{fl}} = (\rho_{\text{fl}} c_{\text{fl}}^2)^{-1}$  is the isentropic compressibility of the fluid, see Table 2 for parameter values. The time-averaged acoustic energy density  $E_{\text{ac}}^{\text{fl}}$  in the fluid domain is the sum of the time-averaged (over one oscillation period) kinetic and compressional energy densities,

$$E_{\text{ac}}^{\text{fl}} = \frac{1}{4} \rho_{\text{fl}} |\mathbf{v}_1|^2 + \frac{1}{4} \kappa_{\text{fl}} |p_1|^2. \quad (2.3)$$

**Table 2.** Material parameters at 25 °C for isotropic Pyrex borosilicate glass [17], cubic-symmetric silicon [18], and water [6]. Note that  $c_{12} = c_{11} - 2c_{44}$  for isotropic solids.

Parameter	Pyrex	Si	Unit	Parameter	Water	Unit
Mass density	$\rho_{\text{sl}}$ 2230	2329	kg m <sup>-3</sup>	Mass density	$\rho_{\text{fl}}$ 997.05	kg m <sup>-3</sup>
Elastic modulus	$c_{11}$ 69.72	165.7	GPa	Sound speed	$c_{\text{fl}}$ 1496.7	m s <sup>-1</sup>
Elastic modulus	$c_{44}$ 26.15	79.6	GPa	Dyn. viscosity	$\eta_{\text{fl}}$ 2.485	mPa s
Elastic modulus	$c_{12}$ 17.43	63.9	GPa	Bulk viscosity	$\eta_{\text{fl}}^{\text{b}}$ 0.890	mPa s
Damping coeff.	$\Gamma_{\text{sl}}$ 0.0004	0.0000	1	Damping coeff.	$\Gamma_{\text{fl}}$ 0.00002	1
–	–	–	–	Compressibility	$\kappa_{\text{fl}}$ 452	TPa <sup>-1</sup>

### 2.2. Linear elastic motion of the solids

In the solid materials, each with a given density  $\rho_{\text{sl}}$ , we model the displacement field  $\mathbf{u}$  using the equation of motion given by [12]

$$-\rho_{\text{sl}} \omega^2 (1 + i\Gamma_{\text{sl}}) \mathbf{u} = \nabla \cdot \boldsymbol{\sigma}, \quad (2.4)$$

where  $\Gamma_{sl} \ll 1$  is a weak damping coefficient. Here,  $\sigma$  is the stress tensor, which is coupled to  $u$  through a stress-strain relation depending on the material-dependent elastic moduli. The time-averaged acoustic energy density in the solids is given by the sum of kinetic and elastic contributions,

$$E_{ac}^{sl} = \frac{1}{4} \rho_{sl} \omega^2 |u|^2 + \frac{1}{4} \text{Re}[(\nabla u) : \sigma^*], \quad (2.5)$$

where "Re" denotes the real value and "\*" the complex conjugate of a complex number, respectively.

### 2.3. Stress-strain coupling in elastic solids

For a crystal with either cubic or isotropic symmetry, the relation between the stress tensor  $\sigma_{ij}$  and strain components  $\frac{1}{2}(\partial_i u_j + \partial_j u_i)$  is given in the compact Voigt representation as [19]

$$\begin{pmatrix} \sigma_{xx} \\ \sigma_{yy} \\ \sigma_{zz} \\ \sigma_{yz} \\ \sigma_{xz} \\ \sigma_{xy} \end{pmatrix} = \begin{pmatrix} c_{11} & c_{12} & c_{12} & 0 & 0 & 0 \\ c_{12} & c_{11} & c_{12} & 0 & 0 & 0 \\ c_{12} & c_{12} & c_{11} & 0 & 0 & 0 \\ 0 & 0 & 0 & c_{44} & 0 & 0 \\ 0 & 0 & 0 & 0 & c_{44} & 0 \\ 0 & 0 & 0 & 0 & 0 & c_{44} \end{pmatrix} \begin{pmatrix} \partial_x u_x \\ \partial_y u_y \\ \partial_z u_z \\ \partial_y u_z + \partial_z u_y \\ \partial_x u_z + \partial_z u_x \\ \partial_x u_y + \partial_y u_x \end{pmatrix}, \quad \text{for Pyrex and silicon.} \quad (2.6)$$

Here,  $c_{ij}$  are the elastic moduli which are listed for Pyrex and silicon in Table 2.

### 2.4. Stress-strain coupling in piezoelectric ceramics

Lead-zirconate-titanate (PZT) ceramics are piezoelectric below their Curie temperature, which typically is 200 – 400 °C. Using Cartesian coordinates and the Voigt notation for a PZT ceramic, the mechanical stress tensor  $\sigma_{ij}$  and electric displacement field  $D_i$  are coupled to the mechanical strain components  $\frac{1}{2}(\partial_i u_j + \partial_j u_i)$  and the electrical potential  $\varphi$  through the relation [19]

$$\begin{pmatrix} \sigma_{xx} \\ \sigma_{yy} \\ \sigma_{zz} \\ \sigma_{yz} \\ \sigma_{xz} \\ \sigma_{xy} \\ D_x \\ D_y \\ D_z \end{pmatrix} = \begin{pmatrix} c_{11} & c_{12} & c_{13} & 0 & 0 & 0 & 0 & 0 & -e_{31} \\ c_{12} & c_{11} & c_{13} & 0 & 0 & 0 & 0 & 0 & -e_{31} \\ c_{13} & c_{13} & c_{33} & 0 & 0 & 0 & 0 & 0 & -e_{33} \\ 0 & 0 & 0 & c_{44} & 0 & 0 & 0 & -e_{15} & 0 \\ 0 & 0 & 0 & 0 & c_{44} & 0 & -e_{15} & 0 & 0 \\ 0 & 0 & 0 & 0 & 0 & c_{66} & 0 & 0 & 0 \\ 0 & 0 & 0 & 0 & e_{15} & 0 & \epsilon_{11} & 0 & 0 \\ 0 & 0 & 0 & e_{15} & 0 & 0 & 0 & \epsilon_{11} & 0 \\ e_{31} & e_{31} & e_{33} & 0 & 0 & 0 & 0 & 0 & \epsilon_{33} \end{pmatrix} \begin{pmatrix} \partial_x u_x \\ \partial_y u_y \\ \partial_z u_z \\ \partial_y u_z + \partial_z u_y \\ \partial_x u_z + \partial_z u_x \\ \partial_x u_y + \partial_y u_x \\ -\partial_x \varphi \\ -\partial_y \varphi \\ -\partial_z \varphi \end{pmatrix}, \quad \text{for Pz26.} \quad (2.7)$$

The values of the material parameters for the PZT ceramic Pz26 are listed in Table 3. Due to the high electric permittivity of Pz26, we only model the electric potential  $\varphi$  in the transducer, and since we assume no free charges here and only low-MHz frequencies,  $\varphi$  must satisfy the quasi-static equation,

$$\nabla \cdot D = 0, \quad \text{for Pz26.} \quad (2.8)$$

**Table 3.** Material parameters of Ferroperm Ceramic Pz26 from Meggitt A/S [20]. Isotropy in the  $x$ - $y$  plane implies  $c_{66} = \frac{1}{2}(c_{11} - c_{12})$ . The damping coefficient is  $\Gamma_{sl} = 0.02$  [13].

Parameter	Value	Parameter	Value	Parameter	Value
$\rho_{sl}$	7700 kg/m <sup>3</sup>	$\varepsilon_{11}$	828 $\varepsilon_0$	$\varepsilon_{33}$	700 $\varepsilon_0$
$c_{11}$	168 GPa	$c_{33}$	123 GPa	$e_{31}$	-2.8 C/m <sup>2</sup>
$c_{12}$	110 GPa	$c_{44}$	30.1 GPa	$e_{33}$	14.7 C/m <sup>2</sup>
$c_{13}$	99.9 GPa	$c_{66}$	29.0 GPa	$e_{15}$	9.86 C/m <sup>2</sup>

### 2.5. Boundary conditions and boundary layers in the fluid at the fluid-solid interfaces

The applied boundary conditions are the usual ones, namely that (1) the stress and the velocity fields are continuous across all fluid-solid and solid-solid interfaces, (2) the stress is zero on all outer boundaries facing the air, (3) the piezoelectric ceramic is driven by a given electric potential at specified surfaces that represent the presence of infinitely thin, massless electrodes, and (4) there are no free charges on the surface of the ceramic. The influence ( $A \leftarrow B$ ) on domain A from domain B with the surface normal  $\mathbf{n}$  pointing away from A, is given by

$$\text{Pz26 domain} \leftarrow \text{ground electrode, top:} \quad \varphi = 0, \quad (2.9a)$$

$$\text{Pz26 domain} \leftarrow \text{phase electrode, bottom:} \quad \varphi = \varphi_0, \quad (2.9b)$$

$$\text{Pz26 and solid domain} \leftarrow \text{air:} \quad \boldsymbol{\sigma} \cdot \mathbf{n} = \mathbf{0} \quad \text{and} \quad \mathbf{n} \cdot \mathbf{D} = 0, \quad (2.9c)$$

$$\text{Solid domain} \leftarrow \text{fluid:} \quad \boldsymbol{\sigma} \cdot \mathbf{n} = -p_1 \mathbf{n} + ik_s \eta_{fl} (\mathbf{v}_{sl} - \mathbf{v}_1), \quad (2.9d)$$

$$\text{Fluid domain} \leftarrow \text{solid:} \quad \mathbf{v}_1 \cdot \mathbf{n} = \mathbf{v}_{sl} \cdot \mathbf{n} + \frac{1}{k_s} \nabla_{\parallel} \cdot (\mathbf{v}_{sl} - \mathbf{v}_1)_{\parallel}. \quad (2.9e)$$

While the overall structure of these boundary conditions is the usual continuity in stress and velocity, the details of Eqs. (2.9d) and (2.9e) are not conventional. They are the boundary conditions for the surface stress  $\boldsymbol{\sigma} \cdot \mathbf{n}$  of Eq. (2.4) and the acoustic velocity  $\mathbf{v}_1$  of Eq. (2.2) (proportional to the gradient of the acoustic pressure  $p_1$ ) derived by Bach and Bruus using their recent effective pressure-acoustics theory [15]. In this theory, the viscous boundary layer of thickness  $\delta = \sqrt{2\eta_{fl}/(\rho_{fl}\omega)}$  ( $\approx 0.35 \mu\text{m}$  at 2.3 MHz) has been taken into account analytically. As a result, terms appear in Eqs. (2.9d) and (2.9e) that involve the shear-wave number  $k_s = (1+i)\delta^{-1}$  as well as the tangential divergence of the tangential component of the difference between the solid-wall velocity  $\mathbf{v}_{sl} = -i\omega\mathbf{u}$  and the acoustic velocity  $\mathbf{v}_1$  at the fluid-solid interface. This boundary condition also takes into account the large dissipation in the boundary layers, which leads to an effective damping coefficient  $\Gamma_{fl}^{\text{eff}} \approx \frac{\delta}{H} \approx 0.002$ , the ratio of the boundary layer width  $\delta$  to the device height  $H$  [6, 13, 15]. Remarkably, this boundary-layer dissipation dominates dissipation in the fluid domain, because  $\Gamma_{fl} \ll \Gamma_{fl}^{\text{eff}} \ll 1$ .

### 2.6. The acoustic streaming

The acoustic streaming is the time-averaged (over one oscillation period), steady fluid velocity  $\mathbf{v}_2$  that is induced by the acoustic fields. In our recent analysis [15], we have shown that the governing equation of  $\mathbf{v}_2$  corresponds to a steady-state, incompressible Stokes flow with a body force in the bulk due to the time-averaged acoustic dissipation proportional to  $\Gamma_{fl}$ . Further, at fluid-solid interfaces, the slip velocity  $\mathbf{v}_2^{\text{bc}}$  takes into account both the motion of the surrounding elastic solid and the Reynolds

stress induced in viscous boundary layer in the fluid,

$$\nabla \cdot \mathbf{v}_2 = 0, \quad \eta_{\text{fl}} \nabla^2 \mathbf{v}_2 = \nabla p_2 - \frac{\Gamma_{\text{fl}} \omega}{2c_{\text{fl}}^2} \text{Re}[p_1^* \mathbf{v}_1], \quad \mathbf{v}_2 = \mathbf{v}_2^{\text{bc}}, \quad \text{at fluid-solid interfaces,} \quad (2.10a)$$

$$\mathbf{n} \cdot \mathbf{v}_2^{\text{bc}} = 0, \quad (\mathbf{1} - \mathbf{n}\mathbf{n}) \cdot \mathbf{v}_2^{\text{bc}} = -\frac{1}{8\omega} \nabla_{\parallel} |\mathbf{v}_{1\parallel}|^2 - \text{Re} \left[ \left( \frac{2-i}{4\omega} \nabla_{\parallel} \cdot \mathbf{v}_{1\parallel}^* + \frac{i}{2\omega} \partial_{\perp} v_{1\perp}^* \right) \mathbf{v}_{1\parallel} \right]. \quad (2.10b)$$

Here, we have used a special case of the slip velocity  $\mathbf{v}_2^{\text{bc}}$ , which is only valid near acoustic resonance, where the magnitude  $|\mathbf{v}_1|$  of the acoustic velocity in the bulk is much larger than  $\omega |\mathbf{u}_{\text{sl}}^{\text{bc}}|$  of the walls.

### 2.7. The acoustic radiation force and streaming drag force on suspended microparticles

The response of primary interest in acoustofluidic applications, is the acoustic radiation force  $\mathbf{F}^{\text{rad}}$  and the Stokes drag from the acoustic streaming  $\mathbf{v}_2$  acting on suspended microparticles. In this work, we consider 1- and 5- $\mu\text{m}$ -diameter spherical polystyrene "Styron 666" (ps) particles with density  $\rho_{\text{ps}}$  and compressibility  $\kappa_{\text{ps}}$ . For such large microparticle suspended in water of density  $\rho_{\text{fl}}$  and compressibility  $\kappa_{\text{fl}}$ , thermoviscous boundary layers can be neglected, and the monopole and dipole acoustic scattering coefficients  $f_0$  and  $f_1$  are real numbers given by [21],

$$f_0 = 1 - \frac{\kappa_{\text{ps}}}{\kappa_{\text{fl}}} = 0.468, \quad f_1 = \frac{2(\rho_{\text{ps}} - \rho_{\text{fl}})}{2\rho_{\text{ps}} + \rho_{\text{fl}}} = 0.034. \quad (2.11a)$$

Given an acoustic pressure  $p_1$  and velocity  $\mathbf{v}_1$ , a single suspended microparticle of radius  $a$ , experience an acoustic radiation force  $\mathbf{F}^{\text{rad}}$ , which, since  $f_0$  and  $f_1$  are real, is given by the potential  $U^{\text{rad}}$  [22],

$$\mathbf{F}^{\text{rad}} = -\nabla U^{\text{rad}}, \quad \text{where} \quad U^{\text{rad}} = \frac{4\pi}{3} a^3 \left( f_0 \frac{1}{4} \kappa_{\text{fl}} |p_1|^2 - f_1 \frac{3}{8} \rho_{\text{fl}} |\mathbf{v}_1|^2 \right). \quad (2.11b)$$

The microparticle is also influenced by a Stokes drag force  $\mathbf{F}^{\text{drag}} = 6\pi\eta_{\text{fl}}a(\mathbf{v}_2 - \mathbf{v}_{\text{ps}})$ , where  $\mathbf{v}_2$  and  $\mathbf{v}_{\text{ps}}$  is the streaming velocity and the polystyrene particle velocity at the particle position  $\mathbf{r}_{\text{ps}}(t)$ , respectively. In the experiments, the streaming and particle velocities are smaller than  $v_0 = 1$  mm/s, which for a 5- $\mu\text{m}$ -diameter particle corresponds to a small particle-Reynolds number  $\frac{1}{\rho_{\text{fl}}}\eta_{\text{fl}}av_0 = 0.6$ . Consequently, we can ignore the inertial effects and express the particle velocity for a particle at position  $\mathbf{r}$  from the force balance  $\mathbf{F}^{\text{rad}} + \mathbf{F}^{\text{drag}} = \mathbf{0}$ , between the acoustic radiation force and streaming drag force,

$$\mathbf{v}_{\text{ps}}(\mathbf{r}) = \mathbf{v}_2(\mathbf{r}) + \frac{1}{6\pi\eta_{\text{fl}}a} \mathbf{F}^{\text{rad}}(\mathbf{r}). \quad (2.12)$$

The particle trajectory  $\mathbf{r}_{\text{ps}}(t)$  is then determined by straightforward time integration of  $\frac{d}{dt}\mathbf{r}_{\text{ps}} = \mathbf{v}_{\text{ps}}(\mathbf{r}_{\text{ps}})$ .

### 2.8. Numerical implementation

Following the procedure described in Ref. [12], including mesh convergence tests, the coupled field equations (2.2) and (2.4) for the fluid pressure  $p_1$  and elastic-solid displacement  $\mathbf{u}$  are implemented directly in the finite-element-method software Comsol Multiphysics 5.3a [14] using the weak form interface "PDE Weak Form". A COMSOL script with a PDE-weak-form implementation

of acoustofluidics is available as supplemental material in Ref. [7]. Here, we extend the model of Ref. [12] by including the transducer with the piezoelectric stress-strain coupling Eq. (2.6) and implementing the governing equation (2.8) for the electric potential  $\varphi$  in weak form. Similarly, the boundary conditions Eq. (2.9) are implemented in weak form. Specifically, the effective-model boundary conditions are implemented as “*Weak Contributions*” as follows. The stress condition Eq. (2.9d) is given by the weak contribution

$$\begin{aligned} & \text{test}(uX) * (-p1 * nX + i * ks * etaf1 * (vs1X - v1X)) \\ & + \text{test}(uY) * (-p1 * nY + i * ks * etaf1 * (vs1Y - v1Y)) \\ & + \text{test}(uZ) * (-p1 * nZ + i * ks * etaf1 * (vs1Z - v1Z)), \end{aligned} \quad (2.13)$$

where  $\mathbf{n} = (nX, nY, nZ)$  is the normal vector away from the solid domain, and  $\text{test}(uX)$  is the finite-element test function corresponding to the  $x$ -component  $u_x$  of the solid displacement field  $\mathbf{u}$ , and similar for  $y$  and  $z$ . The velocity condition Eq. (2.9e) is given by the weak contribution

$$\begin{aligned} & i * \omega * \rho_{\text{fl}} / (1 - i * \Gamma_{\text{fl}}) * \text{test}(p1) * (vs1X * nX + vs1Y * nY + vs1Z * nZ \\ & + i / ks * (\text{dtang}(vs1X - v1X, x) + \text{dtang}(vs1Y - v1Y, y) + \text{dtang}(vs1Z - v1Z, z))), \end{aligned} \quad (2.14)$$

where  $\mathbf{n} = (nX, nY, nZ)$  now is the normal vector away from the fluid,  $\text{test}(p1)$  is the test function for  $p_1$ , and  $\text{dtang}$  is the tangent-plane derivative operator available in COMSOL, see Ref. [15].

In a second step, we implement Eq. (2.10) for the acoustic streaming  $\mathbf{v}_2$  in weak form. Specifically, the effective-model slip velocity condition are implemented as a “*Dirichlet Boundary Condition*” as follows. We use the outward normal vector  $(nX, nY, nZ)$  as before and also the two perpendicular tangent vectors  $(t1X, t1Y, t1Z)$  and  $(t2X, t2Y, t2Z)$ , and write the  $x$ -component  $v2_{bcX}$  of  $\mathbf{v}_2^{\text{bc}}$  as,

$$v2_{bcX} = (t1X * AX + t1Y * AY + t1Z * AZ) * t1X + (t2X * AX + t2Y * AY + t2Z * AZ) * t2X, \quad (2.15)$$

and similarly for the  $y$  and  $z$  components. Here,  $(AX, AY, AZ)$  is a vector defined in terms of the tangent-plane derivative  $\nabla_{\parallel}$  and the parallel velocity  $\mathbf{v}_{\parallel} = (v1_{\text{par}X}, v1_{\text{par}Y}, v1_{\text{par}Z})$  with the  $x$ -component  $v1_{\text{par}X} = (\mathbf{v}_1 \cdot \mathbf{t}_1) t_{1x} + (\mathbf{v}_1 \cdot \mathbf{t}_2) t_{2x}$ , as follows,

$$AX = -1/8/\omega * (\text{dtang}(S1, x) + \text{realdot}((4 + 2 * i)/4 * S2 - 4 * i * S3, v1_{\text{par}X})), \quad (2.16a)$$

$$AY = -1/8/\omega * (\text{dtang}(S1, y) + \text{realdot}((4 + 2 * i)/4 * S2 - 4 * i * S3, v1_{\text{par}Y})), \quad (2.16b)$$

$$AZ = -1/8/\omega * (\text{dtang}(S1, z) + \text{realdot}((4 + 2 * i)/4 * S2 - 4 * i * S3, v1_{\text{par}Z})), \quad (2.16c)$$

$$S1 = \text{abs}(v1_{\text{par}X})^2 + \text{abs}(v1_{\text{par}Y})^2 + \text{abs}(v1_{\text{par}Z})^2, \quad (2.16d)$$

$$S2 = \text{dtang}(v1_{\text{par}X}, x) + \text{dtang}(v1_{\text{par}Y}, y) + \text{dtang}(v1_{\text{par}Z}, z), \quad (2.16e)$$

$$S3 = i * \omega / \rho_{\text{fl}} / c_{\text{fl}}^2 * p1 - S2. \quad (2.16f)$$

Finally, the acoustic radiation force  $\mathbf{F}^{\text{rad}}$  acting on the particles is calculated from Eq. (2.11) using the acoustic pressure  $p_1$  and velocity  $\mathbf{v}_1$ , and subsequently in a third step, following Ref. [23], we compute the particle trajectories  $\mathbf{r}_{\text{ps}}(t)$  from the time-integration of Eq. (2.12).

We optimize the mesh to obtain higher resolution in the water-filled cavity, where we need to calculate numerical derivatives of the resulting fields to compute the streaming and radiation forces, and less in the surrounding solids and in the transducer. We ensure having at least six nodal points per

wave length in all domains, which for the second-order test function we use, corresponds to maximum mesh sizes of 0.52 mm, 0.59 mm, 0.50 mm, and 0.22 mm in the domains of Pz26, silicon, Pyrex, and water, respectively. The final implementation of the model contains 1.1 and 0.4 million degrees of freedom for the first- and second-order fields, respectively. On our workstation, a Dell Inc Precision T7500 Intel Xeon CPU X5690 at 3.47 GHz with 128 GB RAM and 2 CPU cores, the model requires 45 GB RAM and takes 18 min per frequency. When running frequency sweeps of up to 70 frequency values, we used the DTU high-performance computer cluster requiring 464 GB RAM and 11 min per frequency.

### 3. Results for the transducer-glass-silicon acoustofluidic device

We apply the 3D model of Section 2 to the transducer-glass-silicon acoustofluidic device by Hagsäter *et al.* [16], shown in Figure 1 and using the parameter values listed in Tables 1, 2, and 3. In Figure 2 we compare the experimental results from Ref. [16] with our model simulations.

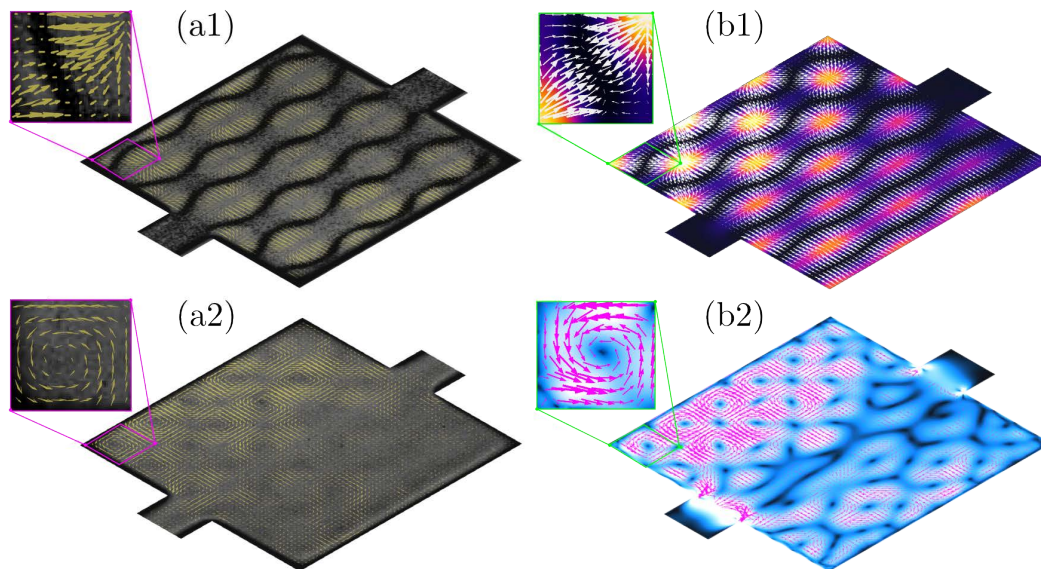


**Figure 2.** (a1) Micro-PIV measurements adapted from Ref. [16] of the particle velocity  $v_{ps}$  after 1 ms (yellow arrows, maximum 200  $\mu\text{m/s}$ ) superimposed on a micrograph of the final positions (black curved bands) of 5- $\mu\text{m}$ -diameter polystyrene particles in water with a standing ultrasound wave at 2.17 MHz. (a2) Same as panel (a1), but for 1- $\mu\text{m}$ -diameter polystyrene particles moving in a 6-by-6 flow-roll pattern without specific final positions. (b1) Numerical 3D COMSOL modeling with actuation voltage  $\varphi_0 = 1$  V of the acoustic potential  $U^{\text{rad}}$  from 0 fJ (black) to 7 fJ (orange) and the velocity (yellow arrows, maximum 170  $\mu\text{m/s}$ ) after 1 ms of 5- $\mu\text{m}$ -diameter polystyrene particles in the horizontal center plane of the water-filled cavity at the resonance  $f = 2.166$  MHz. (b2) Numerical modeling at the same conditions as in panel (b1), but at the slightly lower frequency 2.163 MHz, of the particle velocity  $v_{ps}$  (magenta vectors) and its magnitude  $v_{ps}$  from 0 (black) to 200  $\mu\text{m/s}$  (white) of 1- $\mu\text{m}$ -diameter polystyrene particles.

In Figure 2(a1) we show the measured micro-particle image velocimetry (micro-PIV) results obtained on a large number of 5- $\mu\text{m}$ -diameter tracer particles at an excitation frequency of 2.17 MHz. The yellow arrows indicate the velocity of the tracer particles 1 ms after the ultrasound has been turned on, and the black bands are the tracer particles focused at the minimum of the acoustic potential  $U^{\text{rad}}$  after a couple of seconds of ultrasound actuation. A clear pattern of 3 wavelengths in each direction is observed. Similarly, in Figure 2(a2) is shown the micro-PIV results for the smaller 1- $\mu\text{m}$ -diameter tracer particles. It is seen that these particles, in contrast to the larger particles, are not focused but keep moving in a 6-by-6 flow-roll pattern. This result from Ref. [16] is remarkable, as the conventional Rayleigh streaming pattern [6, 7, 23] has four streaming rolls per wavelength oriented in the vertical plane, but here is only seen two rolls per wavelength, and they are oriented in the horizontal plane.

In Figure 2(b1) and (b2) we see that our model predicts the observed acoustofluidics response qualitatively for both the larger and the smaller tracer particles at a resonance frequency slightly below 2.17 MHz. Even the uneven local amplitudes of the particle velocity  $v_{\text{ps}}$  in the 6-by-6 flow-roll pattern, which shifts around as the frequency is changed a few kHz, is in accordance with the observations. In Ref. [16] it is mentioned that “*If the frequency is shifted slightly in the vicinity of 2.17 MHz, the same vortex pattern will still be visible, but the strength distribution between the vortices will be altered.*”. We have chosen the 3-kHz lower frequency in Figure 2(b2) compared to (b1) to obtain a streaming pattern similar to the observed one for the small 5- $\mu\text{m}$ -diameter particles.

Quantitatively, we find the following. The acoustic resonance is located at 2.166 MHz, only 0.2 % lower than the experimental value of 2.17 MHz. This good agreement should not be over emphasized, as we had to assume a certain length and width of the Pz26 transducer, because its actual size was not reported in Ref. [16]. Another source of error is that we have not modeled the coupling gel used in the experiment between the Pz26 transducer and the silicon base. The actual actuation voltage in the experiment has not been reported, so we have chosen  $\varphi_0 = 1$  V, well within the range of the 20 V peak-to-peak function generator mentioned in Ref. [16], as it results in velocities  $v_{\text{ps}} \approx 170$   $\mu\text{m/s}$  for the large 5- $\mu\text{m}$ -diameter, in agreement with the 200  $\mu\text{m/s}$  reported in the experiment.

In Figure 3 we show another result that is in agreement with the experimental observations, namely the particle trajectories  $r_{\text{ps}}(t)$  for suspensions of tracer particles of different size. The larger 5- $\mu\text{m}$ -diameter particles are focused along the bottom of the troughs in the acoustic potential  $U^{\text{rad}}$ , shown in Figure 2(b1), after a short time  $\frac{1}{12}(2 \text{ mm})/(170 \mu\text{m/s}) \approx 1$  s, forming the red wavy bands in Figure 3(a) very similar to the observed black bands in Figure 2(a1). In contrast, the smaller 1- $\mu\text{m}$ -diameter particles are caught by the 6-by-6 streaming vortex pattern and swirl around without being focused, at least within the first 1.5 s as shown in Figure 3(b), in full agreement with the experimental observation shown in Figure 2(a2).

#### 4. Discussion

Our full 3D numerical model, which takes into account the piezo-electric transducer, the silicon base with the water-filled cavity, the viscous boundary layers in the water, and the Pyrex lid, has been tested qualitatively and quantitatively by comparing the results for the acoustic radiation force, for the streaming velocity, and for the trajectories of tracer particles of two different sizes with the decade-old experimental results presented by Hagsäter *et al.* [16]. Remarkably, as predicted by Bach



and Bruus [15], we find that the characteristic horizontal 6-by-6 flow-roll pattern of the small 1- $\mu\text{m}$ -diameter particles is caused by the so-called Eckart bulk force, the term in (2.10a) proportional to the acoustic energy flux density or intensity  $\mathcal{S}_{\text{ac}} = \frac{1}{2}\text{Re}[p_1^*v_1]$ . In our simulations this pattern occupies 80 % of the cavity volume stretching from 0.1 to 0.9 in units of the channel height  $H_{\text{ca}}$  and looks as the one in the midplane at  $0.5 H_{\text{ca}}$  shown in Figs. 2(b2) and 3(b). Lei *et al.* [10] also pointed out that  $\mathcal{S}_{\text{ac}}$  could lead to the horizontal 6-by-6 flow-roll pattern in their 3D-fluid-domain model with hard-wall and outgoing-plane-wave boundary conditions of the same device. In their model, the Eckart bulk force was neglected, and the horizontal-flow-roll producing term  $\mathcal{S}_{\text{ac}}$  appears only as part of their limiting-velocity boundary condition. As the remaining curl-free part of the boundary condition is dominating, they found the horizontal 6-by-6 flow-roll pattern to be confined to narrow regions around the two horizontal planes at 0.2 and 0.8  $H_{\text{ca}}$  and absent in the center plane at  $0.5 H_{\text{ca}}$ , the focal plane in the experimental studies. As our slip-velocity condition (2.10b) also contains  $\mathcal{S}_{\text{ac}}$ , see Eq. (62a) in Ref. [15], we do reproduce their findings, when we suppress the Eckart bulk force in Eq. (2.10b). This is illustrated in Figure 3(c), where we show that the flow-roll behavior is suppressed in the center plane and replaced by a clear divergent behavior.

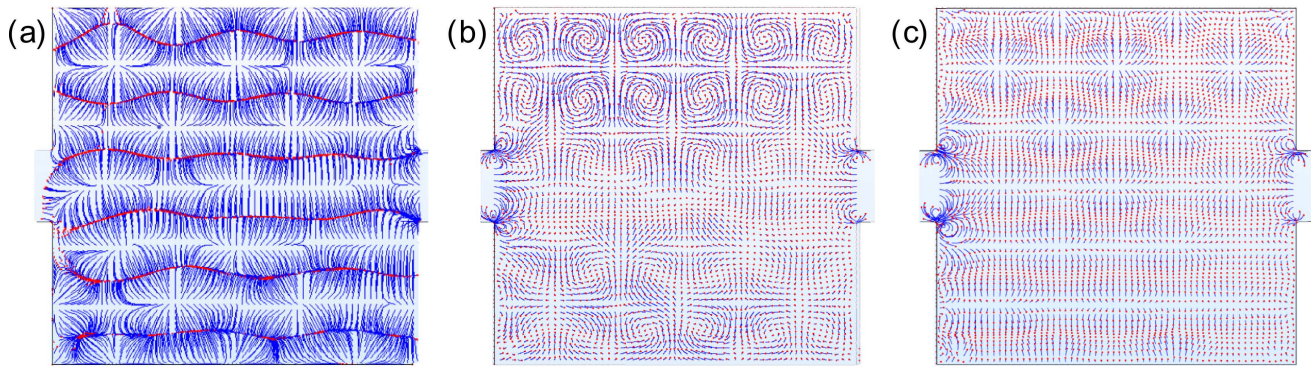


**Figure 3.** Numerical 3D COMSOL modeling of the trajectories  $r_{\text{ps}}(t)$  (blue tracks) of 3600 polystyrene particles of radius  $a$  corresponding to the cases shown in Figure 2(b1) and (b2). The particles start from  $60 \times 60$  regular quadratic grid points in the horizontal center plane of the cavity at  $t = 0$  s when the ultrasound field is turned on, and their positions after 1.5 s are represented by red points. (a)  $a = 2.5 \mu\text{m}$  at  $f = 2.166$  MHz. (b)  $a = 0.5 \mu\text{m}$  at  $f = 2.163$  MHz with the Eckart bulk force in Eq. (2.10a) increased by a factor 4. (c) Same as panel (b) but without the Eckart bulk force in Eq. (2.10a).

In agreement with Lei *et al.* [10], we find that although the determination of the first-order pressure  $p_1$  and the acoustic potential  $U^{\text{rad}}$  is fairly robust, the computation of the streaming velocity  $v_2$  from the Stokes equation (2.10a) is sensitive to the exact value of the frequency and of the detailed shape of the fluid solid interface. In Ref. [24] we have shown in a simplified 3D-rectangular-fluid-domain model that the rotation of the acoustic intensity changes an order of magnitude when the aspect ratio  $L_{\text{ca}}/W_{\text{ca}}$  changes 1 %. In this study we have increased the Eckart bulk force in Eq. (2.10a) by a factor of 4 in order to make the rotating 6x6 pattern dominate clearly over the Rayleigh streaming in the center plane. This amplification may reflect that the chosen aspect ratio  $L_{\text{ca}}/W_{\text{ca}} = 1.01$  was not

exactly the one realized in the experiment, an effect which should be studied further in experiments and simulations.

Our numerical study indicate that although the cavity in the Hagsäter device has a size of only three acoustic wavelengths, the existence of in-plane flow rolls may be controlled by the Eckart bulk force. This conclusion runs contrary to the conventional wisdom that the Eckart bulk force is only important in systems of a size, which greatly exceeds the acoustic wave length. This phenomenon deserves a much closer study in future work.

While our model takes many of the central aspects of acoustofluidics into account, it can still be improved. One possible improvement would be to include the influence of heating on the material parameters as in Ref. [6]. One big challenge in this respect is to determine the material parameters of the solids, which may be temperature and frequency dependent. Another difficult task is to model the coupling between the transducer and the chip, which in experiments typically are coupled using coupling gels or other ill-characterized adhesives. The last point we would like to raise is use of the simple Stokes drag law on the suspended particles in the cavity. Clearly, this model may be improved by including particle-wall effects and particle-particle interactions. However, as direct simulations of both of these effects are very memory consuming their implementation would require effective models.

## 5. Conclusion

We have described the implementation of a full 3D modeling of an acoustofluidic device taking into account the viscous boundary layers and acoustic streaming in the fluid, the vibrations of the solid material, and the piezoelectricity in the transducer. As such, our simulation is in many ways close to a realistic device, which is also reflected in the agreement between the simulation and the experiment shown in Figs. 2 and 3. Our model has correctly predicted the unusual streaming pattern observed in the device at the 2.17-Mz resonance: a horizontal 6-by-6 flow-roll pattern in 80 % of the cavity volume, a pattern much different from the conventional 12-by-2 Rayleigh streaming pattern in the vertical plane. Moreover, our model has revealed the surprising importance of the Eckart bulk force in an acoustic cavity with a size comparable to the acoustic wavelength. In future work, we must analyze the sensitivity of the streaming velocity and improve our understanding of the amplitude of the Eckart bulk force.

By introducing the model, we have demonstrated that simulations can be used to obtain detailed information about the performance of an acoustofluidic device in 3D. Such simulations are likely to be useful for studies of the basic physics of acoustofluidics as well as for engineering purposes, such as improving existing microscale acoustofluidic devices. However, To fully exploit such modeling, more accurate determination is needed of the acoustic parameters of the actual transducers, elastic walls, and particle suspensions employed in a given experiment.

## Acknowledgments

H. Bruus was supported by the *BioWings* project funded by the European Union's Horizon 2020 *Future and Emerging Technologies* (FET) programme, grant No. 801267.

---

## Conflict of interest

All authors declare no conflicts of interest in this paper.

## References

1. A. Lenshof, C. Magnusson and T. Laurell, *Acoustofluidics 8: Applications in acoustophoresis in continuous flow microsystems*, *Lab Chip*, **12** (2012), 1210–1223.
2. M. Gedge and M. Hill, *Acoustofluidics 17: Surface acoustic wave devices for particle manipulation*, *Lab Chip*, **12** (2012), 2998–3007.
3. E. K. Sackmann, A. L. Fulton and D. J. Beebe, *The present and future role of microfluidics in biomedical research*, *Nature*, **507** (2014), 181–189.
4. T. Laurell and A. Lenshof, *Microscale Acoustofluidics*, Cambridge: Royal Society of Chemistry, 2015.
5. M. Antfolk and T. Laurell, *Continuous flow microfluidic separation and processing of rare cells and bioparticles found in blood - a review*, *Anal. Chim. Acta*, **965** (2017), 9–35.
6. P. B. Muller and H. Bruus, *Numerical study of thermoviscous effects in ultrasound-induced acoustic streaming in microchannels*, *Phys. Rev. E*, **90** (2014), 043016.
7. P. B. Muller and H. Bruus, *Theoretical study of time-dependent, ultrasound-induced acoustic streaming in microchannels*, *Phys. Rev. E*, **92** (2015), 063018.
8. N. Nama, R. Barnkob, Z. Mao, et al. *Numerical study of acoustophoretic motion of particles in a PDMS microchannel driven by surface acoustic waves*, *Lab Chip*, **15** (2015), 2700–2709.
9. J. Lei, P. Glynne-Jones and M. Hill, *Acoustic streaming in the transducer plane in ultrasonic particle manipulation devices*, *Lab Chip*, **13** (2013), 2133–2143.
10. J. Lei, P. Glynne-Jones and M. Hill, *Numerical simulation of 3D boundary-driven acoustic streaming in microfluidic devices*, *Lab Chip*, **3** (2014), 532–541.
11. I. Gralinski, S. Raymond, T. Alan, et al. *Continuous flow ultrasonic particle trapping in a glass capillary*, *J. Appl. Phys.*, **115** (2014), 054505.
12. M. W. H. Ley and H. Bruus, *Three-dimensional numerical modeling of acoustic trapping in glass capillaries*, *Phys. Rev. Appl.*, **8** (2017), 024020.
13. P. Hahn and J. Dual, *A numerically efficient damping model for acoustic resonances in microfluidic cavities*, *Phys. Fluids*, **27** (2015), 062005.
14. COMSOL Multiphysics 53a, 2017. Available from: [www.comsol.com](http://www.comsol.com).
15. J. S. Bach and H. Bruus, *Theory of pressure acoustics with viscous boundary layers and streaming in curved elastic cavities*, *J. Acoust. Soc. Am.*, **144** (2018), 766–784.
16. S. M. Hagsäter, T. G. Jensen, H. Bruus, et al. *Acoustic resonances in microfluidic chips: full-image micro-PIV experiments and numerical simulations*, *Lab Chip*, **7** (2007), 1336–1344.
17. CORNING, *Glass Silicon Constraint Substrates*, Houghton Park C-8, Corning, NY 14831, USA, accessed 23 October 2018. Available from: [http://www.valleydesign.com/Datasheets/Corning\\_Pyrex\\_7740.pdf](http://www.valleydesign.com/Datasheets/Corning_Pyrex_7740.pdf).

18. M. A. Hopcroft, W. D. Nix and T. W. Kenny, *What is the Young's modulus of silicon*, IEEEASME Journal of Microelectromechanical Systems, **19** (2010), 229–238.
19. J. Dual and D. Möller, *Acoustofluidics 4: Piezoelectricity and Application to the Excitation of Acoustic Fields for Ultrasonic Particle Manipulation*, Lab Chip, **12** (2012), 506–514.
20. Meggit A/S, *Ferroperm Matdat 2017*, Porthusvej 4, DK-3490 Kvistgaard, Denmark, accessed 23 October 2018. Available from:  
<https://www.meggittferroperm.com/materials/>.
21. J. T. Karlsen and H. Bruus, *Forces acting on a small particle in an acoustical field in a thermoviscous fluid*, Phys. Rev. E, **92** (2015), 043010.
22. M. Settnes and H. Bruus, *Forces acting on a small particle in an acoustical field in a viscous fluid*, Phys. Rev. E, **85** (2012), 016327.
23. P. B. Muller, R. Barnkob, M. J. H. Jensen, et al. *A numerical study of microparticle acoustophoresis driven by acoustic radiation forces and streaming-induced drag forces*, Lab Chip, **12** (2012), 4617–4627.
24. J. S. Bach and H. Bruus, *Different origins of acoustic streaming at resonance*, Proceedings of Meeting on Acoustics 21ISNA, **34** (2018), 022005.



AIMS Press

© 2019 the Author(s), licensee AIMS Press. This is an open access article distributed under the terms of the Creative Commons Attribution License (<http://creativecommons.org/licenses/by/4.0>)

## Chapter 6

# Analysis of a complex 3D SAW system

In this chapter we will describe slight improvements made to the iteration of the numeric model described in Chapter 5, by adding to the material library and solving it in 3D on DTU's high performance cluster [66]. We now apply the model to the SAW device described by Sehgal and Kirby [44] to study its inner workings and improve upon its design. Once again this chapter has a large overlap with the enclosed manuscript for a journal article *3D modeling of acoustofluidics in a liquid-filled cavity including streaming, viscous boundary layers, surrounding solids, and a piezoelectric transducer* by N. R. Skov, P. Sehgal, B. J. Kirby, and H. Bruus submitted to Physical Review Applied [3] (<sup>1</sup>PDF), enclosed in full at the end of this chapter.

### 6.1 Motivation

The numeric model is now at a point where it can model a BAW device with dimensions on the centimeter-scale one-to-one, and give results that agree well with experimentally observed acoustophoretic motion. To further expand on our model, we move on to model a SAW device that has shown promise in separating microparticles on the nanometer-scale [44] to understand and improve upon it. To model the device we add a new material, a new set of boundary conditions, a virtual impedance measurement, and antisymmetry lines.

#### 6.1.1 Improving on an existing design

As mentioned in Chapter 1 the aim of acoustofluidic devices is almost always the manipulation of suspended particles or cells in some way. One interesting aspect is the concentration of so-called exosomes that are sub-micron-sized extracellular vesicles showing potential in diagnostics [111]. Given their small size in blood they are difficult to isolate even in acoustofluidic devices due to the force balance tipping in favor of streaming dominated motion. Conventional methods of separation include bulk centrifuge, which requires large bulk samples, takes several hours to achieve, and has a yield of 5% to 25% [77].

Some focusing of small particles has been successful in BAW devices using streaming effects [112] or seed particles [38] and in SAW devices using vortices [113]. However, these methods

---

<sup>1</sup>FiXme: Fix link.

have little in the way of selectivity and capture cells of all sizes.

A novel SAW device designed by Collins *et al.*[114] achieved a good separation of 300 nm particles from 500 nm particles. Sehgal and Kirby [44] improved upon this design and achieved separation between 100 nm and 300 nm particles. We reshape our numeric model to study the device in Ref. [44], and improve upon its design. Based on our analysis a new device was made showing improved particle focusing.

## 6.2 Model system

The model system is shown in Fig. 6.1(a). It consists of a lithium niobate substrate with a bi-directional parallel-finger interdigitated transducer (IDT) electrode patterned on its top. The IDT has a resonant frequency determined by the electrode periodicity  $\lambda_{\text{SAW}}$  and the surface wave velocity  $v_{\text{SAW}}$ , as  $f_{\text{res}}^{\text{SAW}} = v_{\text{SAW}}/\lambda_{\text{SAW}} = 49.94$  MHz, see Section 6.2.2. When an ac potential is applied across the IDT electrodes the IDT emits vertically polarized surface waves with a plane wave front parallel to the finger pairs. On both of the emitting sides of the IDT a set of Bragg reflector electrodes are patterned to reflect outgoing surface waves back towards the IDT.

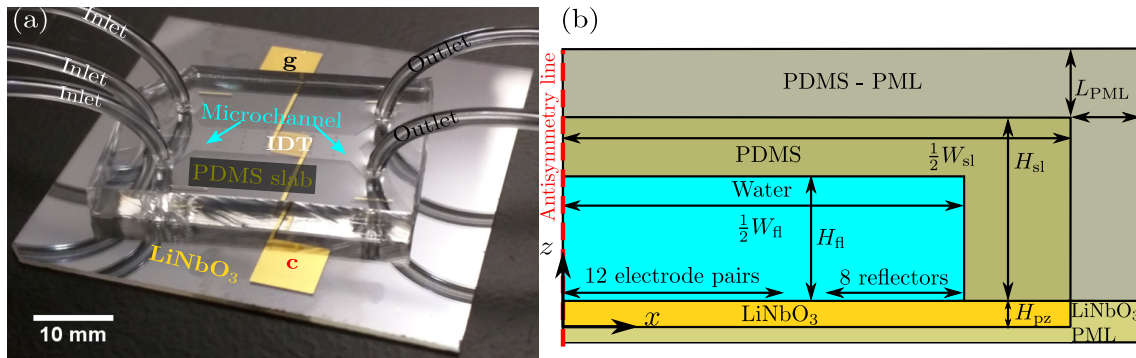


**Figure 6.1:** The model system used. (a) The experimental device of [44]. A microchannel defined in a slab of PDMS rests on a lithium niobate substrate. The substrate is patterned with an interdigitated transducer electrode bounded by Bragg reflector electrodes on both emitting sides Image from Prateek Sehgal. (b) The 2D numeric model initially studied. The outermost Lithium niobate and PDMS is replaced by PML domains to reduce the computational cost. Additionally, half of the domain is omitted by using symmetry conditions on the vertical centerline. Image courtesy of P. Sehgalx

Bonded to the top of the substrate is a large PDMS with a microchannel defined in it. A portion of the microchannel covers the entirety of the IDT-reflector configuration and makes a 10 % angle with the electrode fingers and a 80 % angle with the outgoing waves of the IDT. Fluid is fed to the channel through 2 buffer inlets and a particle inlet trifurcating upstream of the portion of the channel covering the IDT. Downstream of the IDT the water leaves the chip in two separate outlets. Particles having migrated to one side of the channel is thus collected in one outlet, whereas particles who have not migrated are collected at the other. See Fig. 6.1(b) and Table 6.1 for dimensions of the models.



Whereas we have successfully performed full-scale simulations of a device in Chapter 5, we are now dealing with a computationally much heavier problem. This is due to the high actuation frequency range of the device. We therefore set up a 2D version of the model as shown in Fig. 6.1(b) for doing frequency sweeps and a 3D model for calculations at select frequencies determined using the 2D models. The 2D model shown in Fig. 6.1 accounts for the piezoelectric coupling in lithium niobate and the fluid-structure interactions between the fluid and both solids. The 2D model reintroduces PML from Chapter 4 due to the exceedingly high damping in PDMS and contains an antisymmetry line as mentioned in Section 3.7.2. Note that the 2D representation here is not strictly representative for any portion of the channel as the IDT makes a 10% angle with the channel walls. However, as the device does not rely on setting up a resonance in the width of the channel, the 2D approximation is still in good agreement with experimental results. The

In addition to the model shown in Fig. 6.1(b) we set up a similar 2D model but encased in Pyrex instead, as this should intuitively increase the intensity of the acoustic fields in the device by decreasing the energy dissipating in the solid lid due to two effects; Pyrex has a higher acoustic impedance ratio with water and thus reflects a larger portion of energy back into the fluid domain. Additionally it has a lower damping factor  $\Gamma_s$ . Therefore a portion of the energy that is transmitted into the Pyrex from the fluid is reflected at the Pyrex-air interface and will be transmitted back into the fluid. In the following we denote the PDMS-lid model representing the device from Ref. [44] *D1* and the model of the new design with a Pyrex lid *D2*.

To model the SAW device, we expand further on the numeric model, by including 128° cut YX-lithium niobate, antisymmetry conditions, and a virtual probe for numerically calculating the electrical impedance of the device.

**Table 6.1:** Dimensions of the numeric 2D and 3D models. Adapted from [3]

Parameter	Symbol	2D (D1)	2D (D2)	3D	Unit
Device depth ( $y$ )	$L_{sl}$	-	-	1200	$\mu\text{m}$
Solid height ( $z$ )	$H_{sl}$	300	500	500	$\mu\text{m}$
Solid width ( $x$ )	$W_{sl}$	200	200	80	$\mu\text{m}$
Solid material	-	PDMS	Pyrex	Pyrex	-
Channel height	$H_{fl}$	50	50	50	$\mu\text{m}$
Channel width	$W_{fl}$	3500	3500	900	$\mu\text{m}$
Piezo height	$H_{pz}$	300	300	300	$\mu\text{m}$
PML length	$L_{PML}$	80	80	80	$\mu\text{m}$
PML domains	$\Omega_{PML}$	Piezo and PDMS	Piezo	Piezo	-
No. of electrode pairs	$n_{el}$	24	24	4	-
No. of reflectors	$n_{rf}$	6	6/0	0	-

### 6.2.1 128° Y-X cut lithium niobate

The piezoelectric substrate in the device is the commonly used 128° Y-X cut lithium niobate due to its good piezoelectric coupling [115]. The material parameters for this cut are not measured experimentally so we calculate them from the unrotated values collected by Weis [98]. Tan *et al.* [116] did calculate and report values for 128° Y-X cut lithium niobate but the values they find are not

in accordance with ours. Therefore we shortly account for our method for determining the rotated material properties here.

The wafers are made by slicing mono-crystalline lithium niobate at a  $128^\circ$  angle relative to the crystal  $XY$ -plane. The outward facing normal to the top surfaces of wafers thus make a  $128^\circ$  angle with the crystal  $Y$ -axis and a  $128 - 90 = 38^\circ$  angle with the crystal  $Z$ -axis [115], illustrated in Fig. 6.2.

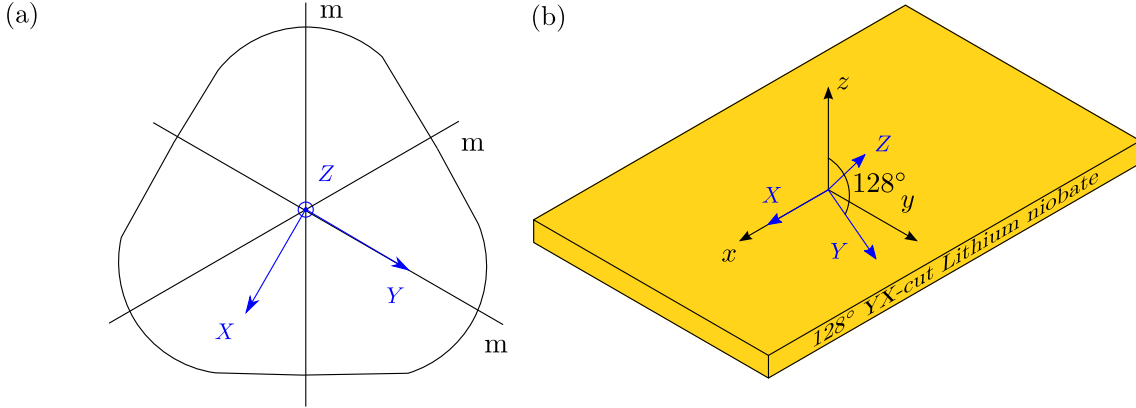


**Figure 6.2:** (a) The material coordinate system of mono-crystalline lithium niobate relative to the 3 mirror planes. The growth direction is the  $Z$ -axis. (b)  $128^\circ$  Y-X cut lithium niobate wafer and the global coordinate system  $x, y, z$  relative to the material coordinate system  $X, Y, Z$ . Adapted from [3]

We define the rotation matrix,

$$\mathbf{R}_x(\theta) = \begin{pmatrix} 1 & 0 & 0 \\ 0 & \cos(\theta) & \sin(\theta) \\ 0 & -\sin(\theta) & \cos(\theta) \end{pmatrix}, \quad (6.1)$$

$$(6.2)$$

and the resulting Bond-stress-transformation matrix

$$\mathbf{M}_\sigma = \begin{pmatrix} 1 & 0 & 0 & 0 & 0 & 0 \\ 0 & \cos(\theta)^2 & \sin(\theta)^2 & 2 \cos(\theta) \sin(\theta) & 0 & 0 \\ 0 & \sin(\theta)^2 & \cos(\theta)^2 & -2 \cos(\theta) \sin(\theta) & 0 & 0 \\ 0 & -\cos(\theta) \sin(\theta) & \cos(\theta) \sin(\theta) & \cos(\theta)^2 - \sin(\theta)^2 & 0 & 0 \\ 0 & 0 & 0 & 0 & \cos(\theta) & \sin(\theta) \\ 0 & 0 & 0 & 0 & -\sin(\theta) & \cos(\theta) \end{pmatrix}, \quad (6.3)$$

as described in Section 3.6 and use them to calculate the elasticity tensor  $\mathbf{C}'$ , coupling tensor  $\mathbf{e}'$  and permittivity tensor  $\boldsymbol{\varepsilon}'$  of the  $128^\circ$  Y-X cut lithium niobate using the three relations

$$\mathbf{C}' = \mathbf{M}_\sigma \mathbf{C} \mathbf{M}_\sigma^{-T}, \quad (6.4)$$

$$\mathbf{e}' = \mathbf{R} \mathbf{e} \mathbf{M}_\sigma^T, \quad (6.5)$$

$$\boldsymbol{\varepsilon}' = \mathbf{R} \boldsymbol{\varepsilon} \mathbf{R}^T. \quad (6.6)$$



In Chapter C the calculated material parameters for 128 ° Y-X cut lithium niobate are listed.

### 6.2.2 IDT -, reflector - and submerged electrodes

The principle of the interdigitated transducer is sketched in Fig. 6.3(a) for an IDT consisting of 2 finger pairs, neighboring a single Bragg reflector array consisting of 4 reflector fingers. By applying alternating charge and ground on electrodes, waves with a wavelength  $\lambda_{\text{SAW}}$  are formed at each finger pair.

By matching the time of flight for formed waves with the periodicity of the actuation potential, a resonance can be built up over the array of fingers. Ideally this effect should be enhanced by the Bragg reflector electrodes. Each finger should partially reflect waves back over the IDT array in phase with the newly formed outgoing waves.

#### Reflector electrode conditions

The Bragg reflectors are electrically shorted at the ends. This cannot be captured by a 2D model as we capture the cross-section indicated by the dashed purple line in Fig. 6.3. We work around it using a constraint and a Dirichlet boundary conditions. The unknown, floating potential  $\phi_1^{\text{fe}}$  of the reflector finger closest to the IDT is fixed by the condition Eq. (2.36)

$$\partial_{\parallel} \phi_1^{\text{fe}} = 0. \quad (6.7)$$

The potential given by Eq. (6.7) is then applied as a Dirichlet condition on the remaining fingers of the Bragg reflector,

$$\phi_1^{\text{br}} = \phi_1^{\text{fe}} \quad (6.8)$$

#### Submerged electrode modeling

To reduce the numeric inaccuracy caused by the sharp edges and simplify the meshing, we model the electrodes as being submerged. In the actual device the electrodes protrude  $H_{\text{el}} = 400$  nm into the fluid as shown in Fig. 6.3(b), but we instead model them as being deposited 400 nm into the substrate Fig. 6.3(b). This change is negligible with regards to the propagation of SAW in the substrate and the bulk acoustic pressure in the height, but is crucial in eliminating the numerical singularities caused by sharp edges.

### 6.2.3 Virtual impedance analyzer

As an additional measure of numerical agreement with experiments we compare the magnitude  $|Z^{\text{el}}|$  and phase  $\psi$  of the physically measured complex electrical impedance  $Z^{\text{el}}$  with our numerically calculated ones. The electrical impedance is defined as the ratio of the driving voltage  $V_0$  to the current  $I$  running through the device

$$Z^{\text{el}} = |Z^{\text{el}}| e^{-i\psi} = \frac{V_0}{I}, \quad (6.9)$$

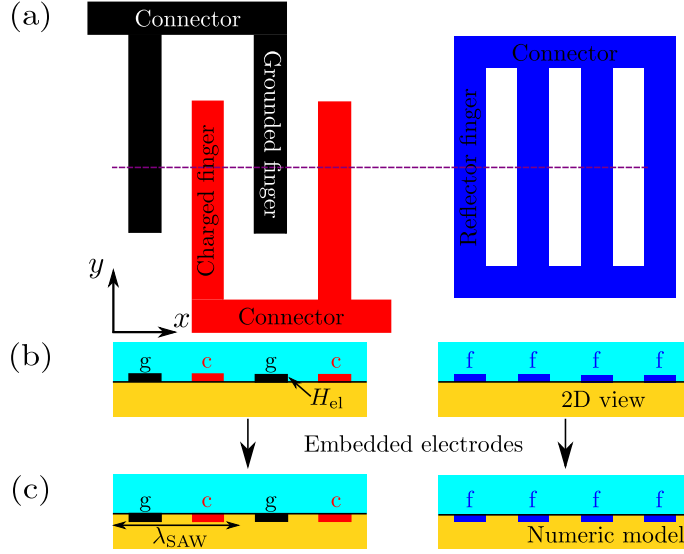


**Figure 6.3:** (a) Top-view sketch of the parallel-finger bi-directional IDT and Bragg reflector designs. (b) Side-view sketch of the actual positions of grounded (black), charged (red) and reflector (blue) electrodes. (c) Side-view sketch of the modeled positions of electrodes.

We compute the numerical electrical impedance by combining Eqs. (2.28)-(2.30) of Section 2.5.6 into a single expression which we integrate over the charged electrodes with surface  $\partial\Omega_{ch}$

$$I = \int_{\partial\Omega_{ch}} -i\omega(\mathbf{D} - \varepsilon_0\mathbf{E}) \cdot \mathbf{n} \, dA, \quad (6.10)$$

We use this value to compute the electrical impedance of the equivalent circuit of our device

$$|Z^{el}| = \left| \frac{V_0}{I} \right|, \quad \psi = \arg \left( \frac{V_0}{I} \right). \quad (6.11)$$

#### 6.2.4 2D Antisymmetry conditions

In our 2D models, we employ antisymmetry conditions along a vertical line passing the center of the IDT. The conditions are and their causes are;

$$\partial_x u_x = 0 \quad x\text{-polarized displacement antinode in the middle of electrode fingers,} \quad (6.12a)$$

$$u_z = 0 \quad z\text{-polarized displacement nodes in the middle of electrode fingers,} \quad (6.12b)$$

$$\phi = \frac{1}{2}V_0 \quad \text{Average potential of a charged and a grounded electrode,} \quad (6.12c)$$

$$p_1 = 0 \quad \text{Pressure nodes in the middle of electrode fingers.} \quad (6.12d)$$

We verify that these conditions hold by running a single simulation for a full 2D device and compare the resulting fields in the full simulation to those obtained using the symmetry condition.

To compare the two solutions we define the maximum relative deviation

$$\underline{g} = \frac{\max(g - g_{\text{ref}})}{\max(g_{\text{ref}})} \quad (6.13)$$

For the first-order fields, using the full solution as reference solution  $g_{\text{ref}}$  we find  $\underline{\phi}_1 = 5.5 \times 10^{-4}$ ,  $\underline{v}_{x,1} = 1.7 \times 10^{-3}$ ,  $\underline{v}_{z,1} = 1.2 \times 10^{-3}$ , and  $\underline{p}_1 = 6 \times 10^{-3}$ , showing good numerical agreement between the full-width model and the symmetry-condition model.

Implementing the above conditions in the 2D simulation cut the degrees of freedom from 1.28 million to 0.64 million and reduced the computation time for solving a single frequency from 360 seconds to 48 seconds on a regular work station.

### 6.2.5 3D modeling using the high performance cluster computing

Relative to the model in Chapter 5 the frequency used here is  $\sim 25$  times higher, and thus the wavelength is 25 times smaller. Accordingly a fixed-dimension domain would require  $25^3 = 15625$  times as many mesh elements to model at this frequency. Hence, to model the device in 3D it was necessary to utilize the high performance cluster (HPC) at DTU mentioned in Section 3.4 [66].

Even so it was necessary to scale down the 3D model to feasibly compute it with the cores available to us, and solely model the Pyrex-lid device. Therefore we created a model with only 4 electrode pairs, and no Bragg reflectors due to their small effect on the acoustic fields. We model the IDT in an idealized fashion as an array of parallel lines with no connector electrodes. Even with these reductions the model has 4.4 million degrees of freedom and took 14 hours to compute across 80 computational nodes of 25 GB RAM each.

## 6.3 Key results and observations

First off we compare our numeric model to the physical device through the electrical impedance before moving to acoustic fields. We compare the experimentally observed acoustophoretic motion in the channel cross-section to the one we predict numerically in our 2D models. We additionally compare observed the acoustophoretic motion parallel to the substrate to a large-scale 3D simulation of the improved device design for a single frequency.

### 6.3.1 Electrical response

We initially study the agreement of the electrical response between the device from [44], and D1. In Fig. 6.4 we show the magnitude  $|Z^{\text{el}}|$  and phase  $\psi$  of the complex electrical impedance  $Z^{\text{el}}$ , measured for the device using an impedance analyzer and calculated as described in Section 6.2.3.

We see in Fig. 6.4 that for both the empty and the filled device our numeric model captures the relative electrical behavior quite well despite being a 2D approximation of a 3D problem. The model captures the overall monotony and approximates the resonance peak frequencies quite well with our calculated resonance frequencies lying within 2.2 % of the measured.

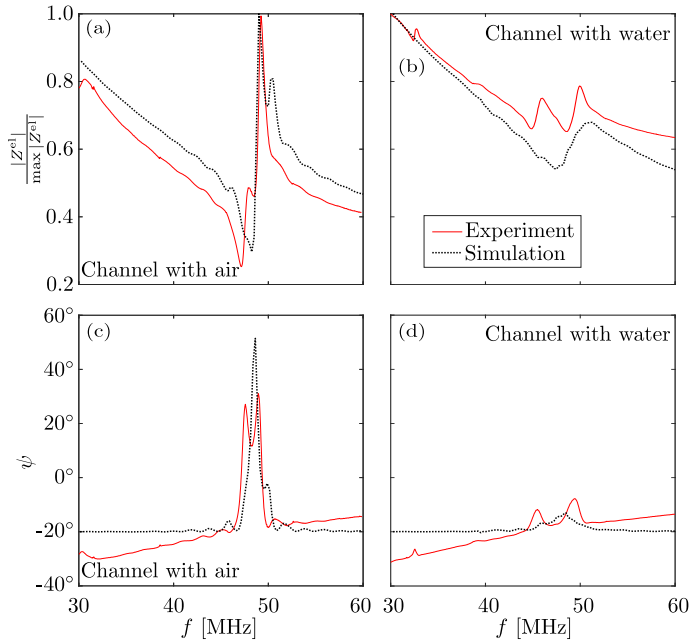


**Figure 6.4:** The normalized magnitude  $|Z^{el}|$  and phase  $\psi$  of the measured (red) and the calculated (black, dotted) electrical impedances for an empty channel and for a channel filled with deionized water. From [3]

The relative magnitudes of the peaks are, however, not fully captured in the model. Furthermore, the measured impedance in has additional minor bulges that do not appear in the simulation. This is to be expected as a 2D approximation of a 3D problem invariably omits some effects.

### 6.3.2 PDMS and Pyrex reflectors

We now compare the two device designs D1 and D2 in terms of their abilities as acoustic resonators. In Fig. 6.5 we plot the  $z$ -component of the displacement along a vertical line passing the center of an IDT electrode finger, at the resonant frequencies of the two devices closest to the SAW resonance frequency,  $f_{\text{res}}^{\text{SAW}}$ ;  $f_{\text{res}}^{\text{D1}} = 47.75$  MHz and  $f_{\text{res}}^{\text{D2}} = 46.50$  MHz. In the fluid the vertical displacement is given by  $u_z = iv_z/\omega$ .

The difference in both acoustic impedance and damping in PDMS and Pyrex are clear from Fig. 6.5. The former can be seen from the small amplitude of the oscillations of waves in the water domain in (a), compared to those in (b). These are small as there is no resonance building up in the system because theoretically only 12 % of the energy of a planar wave impinging the fluid-solid interface are reflected whereas the rest is transmitted. This is in stark contrast to the 78% theoretical reflection at a fluid-Pyrex interface. It can also be seen from the large magnitude of the vertical displacement in the PDMS relative to that in the fluid (97%), as the fluid only carries energy without storing any significant amount. In D2 though, most of the energy is stored in the fluid due to reflections at the interface, and the displacement of the solid relative to the fluid is only 45 %.

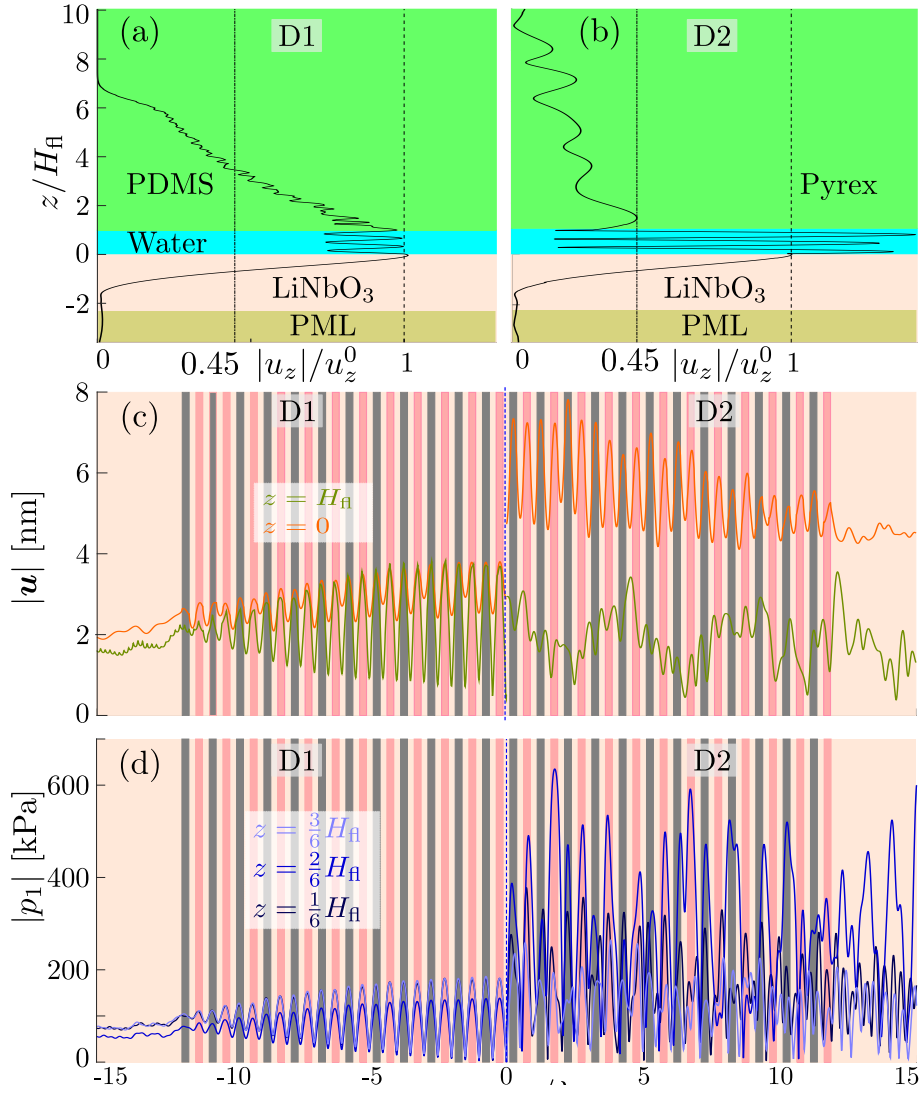


**Figure 6.5:** The acoustic resonator capabilities of PDMS and Pyrex. Line plots of the  $z$ -component of displacement normalized with the maximum value along a vertical line going through the first electrode finger in D1. (b) The same as in (a) but in D2. (c) Line plots of the magnitude of the solid displacement along the floor (orange) and ceiling (green) of the microchannel in the cross-sectional domain in D1 and D2, at  $f_{\text{res}}^{\text{D1}} = 47.75$  MHz and  $f_{\text{res}}^{\text{D2}} = 46.50$  MHz. The black and red vertical lines indicate the position and periodicity of electrode fingers, (red charged, black grounded), and the dashed blue line indicates the center of the IDT array. (d) Line plots of the pressure magnitude  $|p_1|$  along horizontal lines of the cross-sectional domain in D1 and D2. The electrode positions and IDT center are again illustrated with vertical lines. From [3]

The high damping in PDMS is also evident in Fig. 6.5(a) as the waves die out in the PDMS within 7 times the fluid domain height. The exponential decay in the height of the PDMS lid also reveals the traveling nature of the waves. In the Pyrex domain in Fig. 6.5(b) on the other hand, the line plot shows some local minima combined with an overall diminishing absolute value. This indicates a mixture of traveling and standing waves as Pyrex is not loss-free.

In Fig. 6.5(c) we observe a similar trend in the lateral direction of the device. In PDMS the displacement amplitudes gradually decrease when moving along the substrate away from the centerline. This is because each finger pair emits a wave. Accordingly, the outermost finger pair has 23 pairs emitting traveling waves towards it. At the center of the device on the other hand 12 pairs are emitting from both sides. In D2 waves are reflected much more at the fluid-solid and solid-air interfaces leading to a more jumbled displacement field.

Again in Fig. 6.5(d) we see the same behavior in the pressure magnitude. Near the center of the IDT, the wave field appears to be standing and gradually shifts to a traveling wave field away from the center. In D2 on the other hand, the intensity is more homogeneous in the width of the channel and also several times higher. An other important note is the similar magnitudes at all three heights in the fluid in D1, as traveling waves have no pressure nodes. In D2 the pressure magnitudes are two to three times higher than the other two heights at  $z = 2/6H_f$  showing that the pressure has large gradients in the height of the channel.

### 6.3.3 Effect of Bragg reflectors

We study the effects of surrounding the IDT with Bragg reflectors. In telecommunications Bragg reflectors are used in piezoelectric filters to reflect traveling surface acoustic waves [117]. Ideally they should reflect waves emitted from IDTs back and create a standing wave field in this device as well. However, the fluid contacting the piezoelectric substrate in telecommunication devices is usually air, whereas it is water in acoustofluidic, and the effect may not be the same. We study this in Fig. 6.6 by comparing the acoustic pressure field magnitudes  $|p_1|$  for two models with and without Bragg reflectors.

As seen in Fig. 6.6 the fields with and without Bragg reflectors are very similar hinting that the reflectors may not have the anticipated effect. Through closer study differences in the two fields can be seen away from the IDT in Fig. 6.6(c) and (d). However, the region of primary interest with regards to acoustophoresis is the region over the IDT, so the small differences in the pressure field in (c) and (d) are of little concern.

The fields are also quantitatively very similar, albeit with a curious detail. The largest pressure magnitude in the model without reflectors is 1.4 % higher than in the model with. This shows that the Bragg reflectors may even have a slightly adverse effect by causing destructive interference. Nevertheless, we keep them in the model as they are present in the physical device.

### 6.3.4 2D acoustophoresis

From the resonator properties of the two materials we move to investigating the acoustophoretic motion of both small and large particles suspended in either of the devices, as shown in Fig. 6.7. We here choose the resonant SAW frequency as it shows the best acoustophoretic motion despite having lower acoustic energies than the two device resonance  $f_{\text{res}}^{\text{D1}}$  and  $f_{\text{res}}^{\text{D2}}$ .

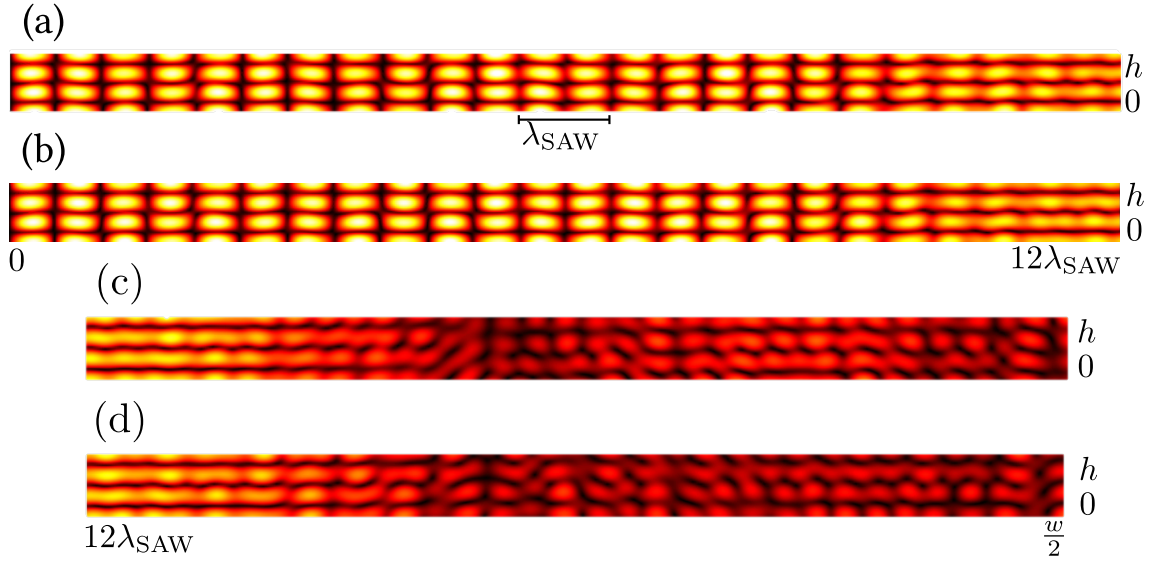


**Figure 6.6:** The effect of Bragg reflectors at a single frequency. (a) and (b) Color plot of the magnitude of the first-order acoustic pressure  $|p_1|$  from 0 (black) to 200 kPa (white), in the fluid over half of the IDT from the center  $x = 0$  to the far edge  $x = 12\lambda_{\text{SAW}}$ , actuated at  $f = 49.9$  MHz and  $V_0 = 1$  V. (a) is for a numeric model without Bragg reflectors and (b) is with. (c) and (d) same as (a) and (b), but from the edge of the IDT  $x = 12\lambda_{\text{SAW}}$  to the edge of the channel  $x = w/2$ .

In Fig. 6.7(a) and (e), we see a clear difference between the focusing of particles in the two devices. In D1 particles tend to focus on the sides of the IDT electrodes when viewed from above, whereas they in In D2 tend to focus on top of electrodes with some outliers lying in between. Additionally the particles in D2 form incoherent bands of agglomerations making a  $45\text{-}55^\circ$  angle with the electrodes that we currently lack an explanation for.

Interestingly, the streaming velocity and radiation force fields in (b) and (f) look quite similar for the two devices at first glance. Particularly the streaming fields show the same tendency of an upwards motion over the electrode, and downwards on the sides. This is caused by the energy-flux density vector  $\langle \mathbf{S}_{\text{ac}} \rangle$  as in Chapter 5, which points vertically up over electrodes and is zero in between. Thus we once again observe streaming driven by bulk forces rather than the classical Rayleigh-streaming in a device with micrometer dimensions.

The radiation force fields, however, are in fact quite different in both shape and intensity. In D1 the regions of low radiation force at  $z = 1/3H_{\text{fl}}$ ,  $z = 2/3H_{\text{fl}}$  are unstable equilibria as the lateral radiation forces point away from the points. Contrarily D2 has three stable equilibria directly over the electrode at  $z = 1/6H_{\text{fl}}$ ,  $z = 3/6H_{\text{fl}}$ ,  $z = 5/6H_{\text{fl}}$  due to the minute lateral forces pointing inwards. An other interesting difference is the position of field features relative to the electrode. In D1 the unstable equilibria are shifted slightly to the side relative to the electrode center, whereas the stable equilibria in D2 are directly over the electrode center.

The differences in shape and intensity in the radiation force field of the two devices are also reflected in the acoustophoretic motion of particles shown in Fig. 6.7. In D1 the 100 nm particles follow the streaming rolls as expected, as the drag force is the dominating term due to the small



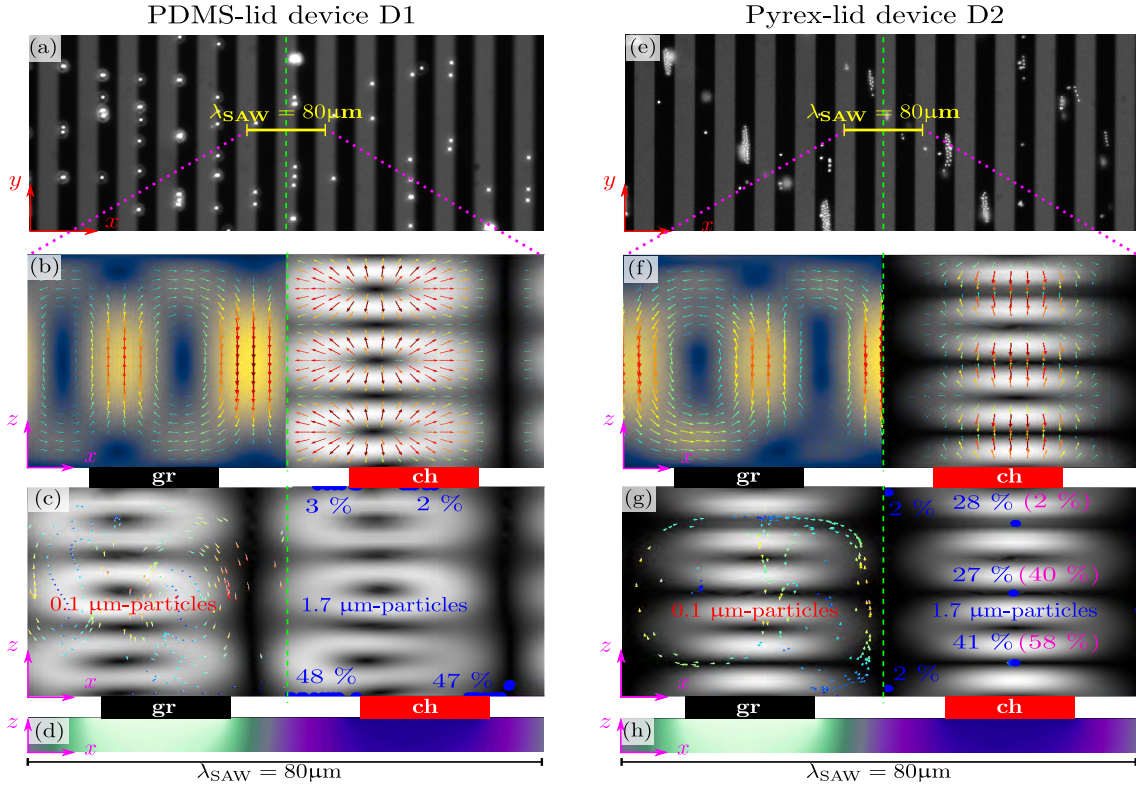


**Figure 6.7:** Acoustophoresis in the devices D1 and D2, at  $f_{\text{res}}^{\text{SAW}} = 49.94 \text{ MHz}$ . (a) Photograph of the microchannel over a central portion of the IDT in D1. The black lines are electrodes, gray lines are the lithium niobate substrate and the white spots are particles. (b) Surface plots of computed acoustic fields in the fluid domain over a unit cell of the IDT. The unit cell of width  $\lambda_{\text{SAW}}$  consists of a charged and a grounded electrode of widths  $1/4\lambda_{\text{SAW}}$  and spacers in-between. The shown fields are a color plot of the streaming velocity field magnitude  $|v_2|$  (left) and a gray-scale plot of the acoustic radiation force magnitude  $|\mathbf{F}^{\text{rad}}|$  (right). The plots are overlaid with arrow plots of the direction of fields. The green dashed line shows the center-line of the unit cell. (c) Color point-plot of particle positions 0.1 after the ultrasound is turned on for small (left) and large (right) particles initially spaced evenly in a  $13 \times 19$  grid across the unit-cell fluid domain. Tails point towards the particle position last time-step. The numbers indicate the percentage of particles settling in each of the 4 shown positions. (d) Color plot of the electric potential in a thin slice of the unit cell's lithium niobate. (e)-(h) as in (a)-(d) but for the Pyrex-lid device D2. Numbers in parenthesis indicate the settling percentages when using the same initial distribution allowed to sediment for 3 minutes before turning on the ultrasound. From [3]



particle diameter. In D2 this is also true, but the particles follow slightly compressed rolls as the radiation force is more powerful relative to the streaming in D2 and thus not negligible.

For the 1700 nm particles, the difference in acoustophoretic motion is even more distinct. The absence of stable equilibria in D1 causes the majority of particles to migrate away from the region above the electrode into the downward portion of the streaming rolls. Eventually they are dragged to where the streaming drag force and radiation force are equally strong and opposite and settle here. The portion of particles that are not pushed out by the radiation force stick to the ceiling of the channel in the same lateral positions as those at the floor.

As an interesting side note, this device clearly has a focusing limit lower than the critical-2-mm diameter reported by Muller *et al.*[30]. Using their formula, we find a critical diameter for polystyrene of

$$a = \sqrt{12 \frac{\Psi}{\Phi} \delta_{\text{visc}}} \approx 130 \text{ nm} \quad (6.14)$$

with the geometry-dependent factor calculated to be  $\Psi = \frac{c_0 |v_2^{\text{bc}}|}{|v_1|^2} \approx 0.4$ , whereas the material-dependent contrast factor  $\Phi = 0.165$ , and the crucial most factor; the viscous-boundary-layer width is  $\delta_{\text{visc}} = \sqrt{\frac{2\eta}{\rho\omega}} = 24 \text{ nm}$ .

In a device with classical Rayleigh streaming separation of particles should be possible down to the critical diameter. However, due to the mostly bulk-driven streaming that is not the case in this device. It is, however, still able to separate 100 and 300 nm particles, so the estimate remains reasonable.

On the subject of particle sizes, the entire regime of focusable particle sizes is shifted towards lower sizes in this device. We bring to mind the two assumptions of the radiation forces,  $\lambda_f \gg a > \delta_{\text{visc}}$ . In this device, the acoustic wavelength of water is  $\lambda_f = 16 \mu\text{m}$ . This sets an upper limit to the validity of the calculation radiation force below the size of red ( $a \approx 6 \mu\text{m}$ ) and white ( $a \approx 5 - 15 \mu\text{m}$ ) blood cells that make up the majority of the cell constituents in blood.

In D2 the radiation force focuses most particles in their nearest node, while some particles are pushed to the radiation-inactive region as in D1. Unlike in D1 though, particles that are dragged down along the streaming force are also pulled in by the radiation force at the lower node, which causes a slightly higher concentration of particles here. This is even more pronounced when including that significant sedimentation of particles takes place in the experiments before the ultrasound is turned on.

Experimentally, the predictions regarding the lateral positions of the large particles are verified with particles in D1 focusing on the sides of electrodes and those in D2 in the center of electrode fingers. Vertically, the predicted final position of particles in D1 at the top and bottom of the channel is reproduced experimentally, however the distribution between the two is not. For D2 both the predicted position and distribution are found to be in good agreement with the experimentally observed one, especially when taking the sedimentation into account.

Note that the acoustophoretic motion described here is observed in each unit cell of the fluid domain over the IDT. Moving away from the IDTs the fields decrease in magnitude and change their topology.

### 6.3.5 3D acoustophoresis

Having studied the device in the simple 2D model, we conclude with a brief study on the acoustophoretic fields in the scaled-down 3D-model shown in Fig. 6.8(a).

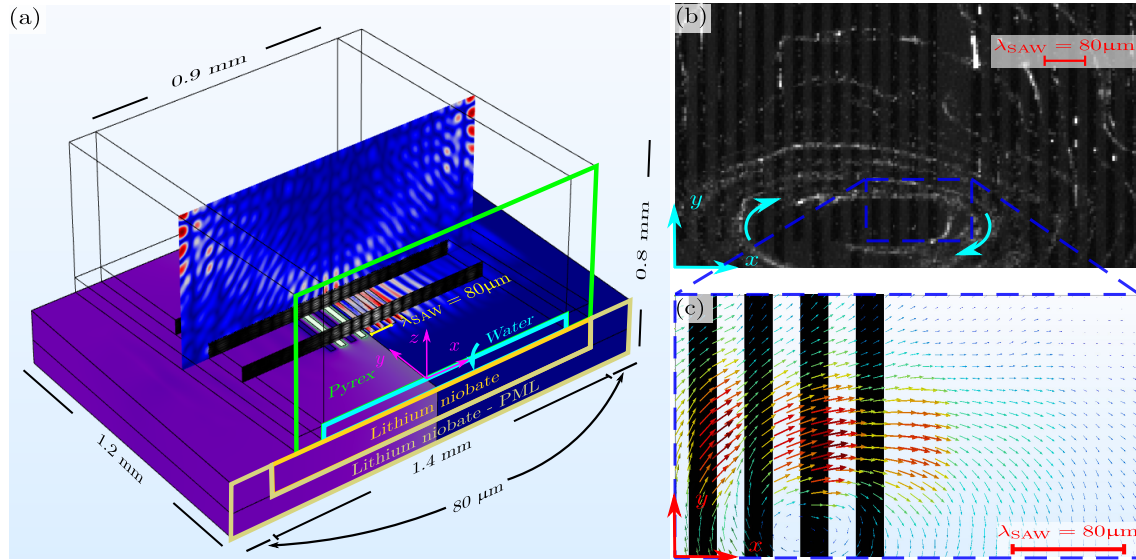


**Figure 6.8:** The used 3D model and 3D acoustophoretic results at  $f = 49.94$  MHz and  $V_0 = 1$  V. (a) Color slice plot of the solid displacement magnitude  $|u_1|$  in the Pyrex, gray-scale slice plots of the acoustic radiation force magnitude  $F^{\text{rad}}$  in the fluid. Also plotted are surface plots on the lithium niobate of the electric potential  $\phi_1$  on the left side and the solid displacement magnitude  $|u_1|$  on the right side. The black frame shows the contours of the entire model and the colored frames show the domain bounds in the front cross-section. (b) Image of the microchannel over one corner of the IDT. The white streaks are closely packed particles following streaming vortices, and the cyan arrows indicate the direction of particle motion. (c) Arrow plot of the numerically calculated streaming velocity field  $v_2$  from 0 (blue) to  $66 \mu\text{m/s}$  (red) in the corner of the IDT shown with magenta in (a). The color and size of arrows showing the magnitude  $|v_2|$ , and black lines show electrode positions. Adapted from [3]

We see in Fig. 6.8(a) that the radiation force field in the 3D model is similar to that found in the 2D simulations in Fig. 6.7(f), despite the inclusion of the IDT angle relative to the microchannel wall in the 3D model. While the intensity varies along the depth of the electrode in the  $y$ -direction, the structures remain the same. As in the 2D simulations, the 3-node pattern is strongest over the IDTs and decreases in magnitude away from them.

In (b) we see that at the edges of the IDT streaming rolls in the horizontal plane appear. These lateral rolls are much larger in size than those we find in the vertical direction near the center of the IDT, spanning over several unit cells.

Using our numeric model we observe the same streaming pattern in (c) - albeit with a lower streaming velocity - although the model is scaled down to just 4 pairs and no reflectors, whereas the physical device has 24 pairs and 8 reflector strips on both sides. We also have a reasonable

quantitative match between the largest measured ( $\sim 210 \mu\text{m s}^{-1}$ ) and calculated ( $v_2 \sim 66 \mu\text{m s}^{-1}$ ) streaming velocities, when scaling with the ratio of electrode pairs (6)  $v_2^{\text{scaled}} \sim 240 \mu\text{m s}^{-1}$ . Our experimental values are based on manually tracking a few recognizable features and measuring the distance they travel in between frames of a known interval in a movie taken through the microscope.

## 6.4 Concluding remarks

We have reshaped our numeric model to represent a SAW device in both 2D and 3D. While doing so we added symmetry conditions, a method to numerically estimate the impedance of the device, and the possibility of modeling materials of any orientation. We computed the 2D models on a regular workstation but for the 3D model high performance cluster computations were necessary.

As a first verification of the model we compared the numerically calculated and physically measured electric response of the device and saw a good qualitative agreement, and a reasonable quantitative one particularly considering we used our 2D model.

We study the system acoustically and find Pyrex to work better as a resonator particularly with a fluid domain of height  $H_{\text{fl}} = 50\mu\text{m}$  in our 2D model, as this matches the SAW resonance with the  $f_{0,0,3}$  fluid eigenfrequency. Accordingly we revised the design from Ref. [44].

With the new design we predict the acoustophoresis to be stronger and find the radiation force to be stronger relative to the streaming drag force. We find that the new design focuses particles vertically as well as laterally, which is advantageous to avoid particles being trapped at the top or bottom of the microchannel.

One element we did not capture well was the ratio of particles settling at the floor and ceiling of the fluid channel in the PDMS device D1. The observed particle clustering was estimated to be larger at the ceiling rather than the floor of the microchannel. For the Pyrex-lid device, however, we saw good agreement between the predicted and the observed particle settling positions when using the sedimented initial distribution. The sedimented distribution was used because there was a marked delay in experiments between loading the suspension was loaded into the channel and turning on the ultrasound to achieve a quiescent background flow  $v_0$ .

In acoustofluidics a distinction is often made between devices driven by bulk and surface acoustic waves in the piezoelectric element due to the acoustic fields they usually contain. In D2 the fields are very similar to those in classical BAW devices with a acoustic resonance building up in the fluid due to the partial reflections at the Pyrex-water and piezo-water interfaces. Hence, the distinction here seems inadequate as it is the walls surrounding the fluid determining the resonance behavior, rather than the waves actuated in the piezoelectric element.

Using the 3D model we observed a streaming motion parallel to the piezoelectric transducer that did not appear in 2D simulations. As in Chapter 5 the streaming was driven by the energy dissipating into the fluid. In this design, however, it is caused by the SAWs in the substrate with wavefronts parallel to the electrodes. As they travel along the surface energy is transferred into the fluid and drives the streaming. As waves are not emitted in all directions, the resulting flow circulates away from the IDT normal to the electrodes.

As a final application of the numeric model we use its predictive power in a device design process to test a number of different design ideas.

*Three-Dimensional Numerical Modeling of Surface Acoustic Wave Devices: Acoustophoresis of Microparticles including Streaming*

**Authors:** N.R. Skov, P. Sehgal, B. J. Kirby and H. Bruus.

**Journal:** Phys. Rev. Applied **submitted**, 26 June (2019).

# Three-Dimensional Numerical Modeling of Surface Acoustic Wave Devices: Acoustophoresis of Micro- and Nanoparticles including Streaming

Nils R. Skov,<sup>1,\*</sup> Prateek Sehgal,<sup>2,†</sup> Brian J. Kirby,<sup>2,3,‡</sup> and Henrik Bruus<sup>1,§</sup>

<sup>1</sup>*Department of Physics, Technical University of Denmark, DTU Physics Building 309, DK-2800 Kongens Lyngby, Denmark*

<sup>2</sup>*Sibley School of Mechanical and Aerospace Engineering, Cornell University, Ithaca, New York 14853, USA*

<sup>3</sup>*Department of Medicine, Division of Hematology and Medical Oncology, Weill-Cornell Medicine, New York, New York 10021, USA*

(Dated: 25 June 2019)

Surface acoustic wave (SAW) devices form an important class of acoustofluidic devices, in which the acoustic waves are generated and propagate along the surface of a piezoelectric substrate. Despite their wide-spread use, only a few fully three-dimensional (3D) numerical simulations have been presented in the literature. In this paper, we present a 3D numerical simulation taking into account the electromechanical fields of the piezoelectric SAW device, the acoustic displacement field in the attached elastic material, in which the liquid-filled microchannel is embedded, the acoustic fields inside the microchannel, as well as the resulting acoustic radiation force and streaming-induced drag force acting on micro- and nanoparticles suspended in the microchannel. A specific device design is presented, for which the numerical predictions of the acoustic resonances and the acoustophoretic response of suspended microparticles in 3D are successfully compared with experimental observations. The simulation provides a physical explanation of the observed qualitative difference between devices with an acoustically soft and hard lid in terms of traveling and standing waves, respectively. The simulations also correctly predict the existence and position of the observed in-plane streaming flow rolls. The presented simulation model may be useful in the development of SAW devices optimized for various acoustofluidic tasks.

## I. INTRODUCTION

During the past decade, surface acoustic wave (SAW) devices have been developed for a multitude of different types of acoustofluidic handling of micrometer-sized particles inside closed microchannels. Examples include acoustic mixing [1], continuous particle or droplet focusing [2, 3] and separation [4, 5], single-particle handling [6, 7], acoustic tweezing [8–10], two-dimensional single patterning [11, 12], on-chip studies of microbial organisms [13, 14], and non-trivial electrode shapes to generate chirped, focused, and rotating acoustic waves [10, 15–17].

The development of effective handling of submicrometer-sized particles has been less successful. It remains a challenge to handle this in biotechnology highly important class of particles including small bacteria, exosomes, and viruses. Could these particles be handled in a controlled way, it would be of particular interest for developing new and more efficient diagnostics [18]. The first steps towards acoustofluidics handling of nanometer-sized particles have been taken relying on acoustic streaming effects with both bulk acoustic waves (BAW) [19] and SAW [20], or using seed particles to enhance acoustic trapping in BAW devices [21].

However, these methods have a low selectivity. However, recently SAW devices have been developed to focusing nanoparticles [22] and separation of nanoparticles [23, 24]. In particular Sehgal and Kirby [23] demonstrated separation between 100- and 300-nm-diameter particles on the proof-of-concept stage. To fully utilize the potential of this and similar devices, further development is necessary to increase the efficiency and sorting flow rates. Here, numerical simulations may play a crucial role, both in improving the understanding of the underlying physical acoustofluidic processes, and to ease the cumbersome development cycle consisting of an iterative series of creating, fabricating, and testing device designs.

An increasing amount of numerical studies include piezoelectric dynamics in two-dimensional (2D) models [25–28], but mostly the piezoelectric transducers are introduced in numeric models in the form of analytic approximations [29–34], and designs are often based on a priori knowledge of the piezoelectric effect in the unloaded substrates typically applied in telecommunication. In acoustofluidic devices, the acoustic impedance of the contacting fluid is much closer to that of the substrate causing waves to behave much differently from those in telecommunications devices. It is thus prudent to include the piezoelectric effect and the coupling between the fluid and substrate in numeric models to accurately describe the device behavior. Additionally, three-dimensional (3D) simulations in the literature are scarce, but they are essential for making full-device acoustophoresis predictions as many actual acoustofluidic devices do exhibit

\* nilsre@fysik.dtu.dk

† ps824@cornell.edu

‡ kirby@cornell.edu

§ bruus@fysik.dtu.dk

non-trivial features in 3D due to asymmetric and intricate shapes of electrodes and channels.

In this paper, we present 3D numerical simulations taking into account the electromechanical fields of the piezoelectric SAW device, the acoustic displacement field in the attached elastic material, in which the liquid-filled microchannel is embedded, the acoustic fields inside the microchannel, as well as the resulting acoustic radiation force and streaming-induced drag force acting on microparticles suspended in the microchannel. The model is validated experimentally with devices based on the SAW device described by Sehgal and Kirby [23]. In Section II we describe the physical model system representing the SAW device and state the governing equations, and in Section III we treat the implementation of the model system in a weak-form, finite-element model. The results of the model in reduced 2D and in full 3D are presented in Sections V and VI, and finally in Sections VII and VIII we discuss our findings and summarize our conclusions.

## II. THE MODEL SAW SYSTEM AND THE GOVERNING EQUATIONS

The model SAW system is shown in Fig. 1a. Essentially, it consists of a piezoelectric lithium niobate substrate with a specific interdigitated transducer (IDT) metal-electrode configuration on the surface. On top of the substrate a microfluidic channel is defined in an elastic material, either the acoustically soft rubber polydimethylsiloxane polymer (PDMS) or the acoustically hard borosilicate glass (Pyrex).

We follow Sehgal and Kirby [23] and place the IDT electrodes directly underneath the microchannel and choose the periodicity of the electrode pattern to result in a SAW wavelength  $\lambda_{\text{SAW}} = 80 \mu\text{m}$  and a (unloaded) resonance frequency  $f_{\text{SAW}} = c_{\text{SAW}}/\lambda_{\text{SAW}} = (3995 \text{ m/s})/(80 \mu\text{m}) = 49.9 \text{ MHz}$ . The driving electrodes are flanked by Bragg-reflector electrodes to (partially) reflect the outgoing SAWs traveling along the surface from the driving electrodes. As described in more detail in Appendix A, the lattice coordinate system  $X, Y, Z$  of the  $128^\circ$  YX-cut lithium niobate wafer is rotated the usual  $38^\circ = 128^\circ - 90^\circ$  about the  $x$ -axis to obtain an optimal SAW configuration.

To facilitate separation of nanoparticles, the axis of the microchannel is tilted  $10^\circ$  angle relative to the IDT electrodes. At both ends, the microchannel branches out in a number of side channels with vertical openings for inlet and outlet tubing. In the numerical model, this inlet/outlet structure is represented by ideally absorbing boundary conditions.

The SAW device is actuated by a time-harmonic voltage difference at frequency  $f$  applied to the IDT electrodes. The corresponding angular frequency is  $\omega = 2\pi f$ .

The following formulation of the governing equations, is a further development of our previous work presented in Refs. [32, 35, 36] to take into account SAW in 3D

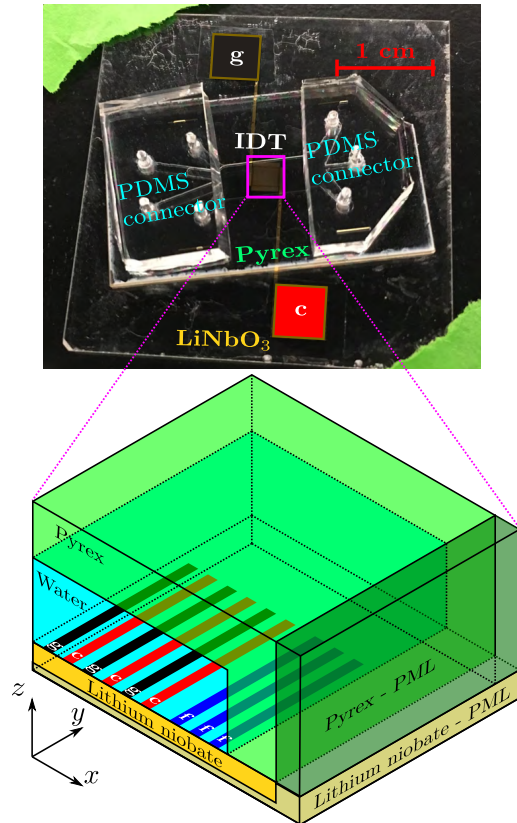


FIG. 1. Experimental and numeric testing devices. (a) A testing device, similar to that of Ref. [23]. A wide lithium niobate base with a 24-pair interdigitated surface metal electrode (IDT) and contact pads (grounded g or ge, charged c or ce) supporting a borosilicate glass (Pyrex) slab containing an etched microchannel above the IDT. (b) 3D sketch of the numerical model containing only a 3-pair electrode (grounded g or ge: black, charged c or ce: red), and three floating electrodes (f or fe, blue).

models of lithium-niobate-driven ultrasound acoustics in liquid-filled microchannels.

### A. The Voigt notation for elastic solids

In linear elastodynamics with the elasticity tensor  $C_{iklm}$ , the stress  $\sigma_{ik}$  and strain  $\epsilon_{ik}$  tensors with  $i, k = 1, 2, 3$  (or  $x, y, z$ ) are defined in index notation as

$$\epsilon_{ik} = \frac{1}{2}(\partial_i u_k + \partial_k u_i), \quad (1a)$$

$$\sigma_{ik} = C_{iklm}\epsilon_{lm} \quad (1b)$$

In the Voigt notation (subscript V) [37], the symmetric stress and strain double-index tensor components  $\sigma_{ik} = \sigma_{ki}$  and  $\epsilon_{ik} = \epsilon_{ki}$  are organized in single-index vectors  $\sigma_\alpha$



and  $\epsilon_\alpha$  with  $\alpha = 1, 2, \dots, 6$ , as,

$$\boldsymbol{\epsilon}_V = \begin{pmatrix} \epsilon_1 \\ \epsilon_2 \\ \epsilon_3 \\ \epsilon_4 \\ \epsilon_5 \\ \epsilon_6 \end{pmatrix} = \begin{pmatrix} \epsilon_{11} \\ \epsilon_{22} \\ \epsilon_{33} \\ 2\epsilon_{23} \\ 2\epsilon_{13} \\ 2\epsilon_{12} \end{pmatrix}, \quad \boldsymbol{\sigma}_V = \begin{pmatrix} \sigma_1 \\ \sigma_2 \\ \sigma_3 \\ \sigma_4 \\ \sigma_5 \\ \sigma_6 \end{pmatrix} = \begin{pmatrix} \sigma_{11} \\ \sigma_{22} \\ \sigma_{33} \\ \sigma_{23} \\ \sigma_{13} \\ \sigma_{12} \end{pmatrix}, \quad (2a)$$

and the stress-strain relation is written,

$$\sigma_\alpha = C_{\alpha\beta} \epsilon_\beta, \quad (3)$$

where  $C_{\alpha\beta}$  is the  $6 \times 6$  Voigt elasticity matrix. We also introduce the  $3 \times 6$  Voigt matrix gradient operator  $\nabla_V$ ,

$$\nabla_V = \begin{pmatrix} \partial_x & 0 & 0 & 0 & \partial_z & \partial_y \\ 0 & \partial_y & 0 & \partial_z & 0 & \partial_x \\ 0 & 0 & \partial_z & \partial_y & \partial_x & 0 \end{pmatrix}. \quad (4)$$

The equations governing the device are divided into three sets. One set is the first-order time-harmonic equations for the acoustic fields, the second set contains the steady time-averaged second-order fields, and the third set are the time-dependent equations describing the acoustophoretic motion of suspended particles.

### B. The time-harmonic first-order fields

By construction, all first-order fields are proportional to the time-harmonic electric potential actuating the SAW device at angular frequency  $\omega$ . Consequently, all first-order fields are time-harmonic acoustic fields of the form  $\hat{g}(\mathbf{r}, t) = g(\mathbf{r}) e^{-i\omega t}$ , where  $g(\mathbf{r})$  is the complex-valued field amplitude. The corresponding physical field is the real part  $\text{Re}[\hat{g}(\mathbf{r}, t)]$ . All terms thus have the same explicit time dependence  $e^{-i\omega t}$ , so this factor is divided out, leaving us with the governing equations for the amplitude  $g$ , where we for brevity suppress the spatial argument  $\mathbf{r}$ .

In a linear piezoelectric material with a mass density  $\rho_{\text{sl}}$  and no free charges, the solid displacement field  $\mathbf{u}$  and the electric potential  $\phi$  are governed by the Cauchy equation and Gauss's law,

$$\nabla_V \cdot \boldsymbol{\sigma}_V = -\rho_{\text{sl}} \omega^2 \mathbf{u}, \quad (5a)$$

$$\nabla \cdot \mathbf{D} = 0. \quad (5b)$$

This equation system is closed by the constitutive equations relating the stress  $\boldsymbol{\sigma}_V$  and the electrical displacement  $\mathbf{D}$  to the strain  $\boldsymbol{\epsilon}_V$  and the electric field  $\mathbf{E}$ , through the elasticity matrix  $\mathbf{C}$ , the relative dielectric tensor  $\boldsymbol{\epsilon}_r$ , and the piezoelectric coupling matrix  $\mathbf{e}$ ,

$$\boldsymbol{\sigma}_V = \mathbf{C} \boldsymbol{\epsilon}_V - \mathbf{e}^T \mathbf{E}, \quad \text{with } \mathbf{E} = -\nabla \phi, \quad (5c)$$

$$\mathbf{D} = \epsilon_0 \boldsymbol{\epsilon}_r \mathbf{E} + \mathbf{e} \boldsymbol{\epsilon}_V. \quad (5d)$$

Here,  $\epsilon_0$  is the vacuum permittivity,  $\boldsymbol{\epsilon}_r$  is the relative permittivity tensor of the material, and superscript "T" denotes the transpose of a matrix, see Table I.

TABLE I. Elasticity constants  $C_{\alpha\beta}$ , mass density  $\rho_{\text{sl}}$ , piezoelectric coupling constants  $e_{i\alpha}$  and relative dielectric constants  $\epsilon_{ik}$  of materials used in this work.  $128^\circ$  YX-cut lithium niobate values are defined in the global system  $x, y, z$ , for derivations see Appendix A. Note that  $C_{12} = C_{11} - 2C_{44}$  for isotropic materials (Pyrex and PDMS).

Parameter	Value	Parameter	Value
<i>128° YX-cut lithium niobate</i> [38]			
$C_{11}$	202.89 GPa	$C_{12}$	72.33 GPa
$C_{13}$	60.17 GPa	$C_{14}$	10.74 GPa
$C_{22}$	194.23 GPa	$C_{23}$	90.59 GPa
$C_{24}$	8.97 GPa	$C_{33}$	220.29 GPa
$C_{34}$	8.14 GPa	$C_{44}$	74.89 GPa
$C_{55}$	72.79 GPa	$C_{56}$	-8.51 GPa
$\rho_{\text{sl}}$	4628 kg m <sup>-3</sup>	$C_{66}$	59.51 GPa
$e_{15}$	1.56 C m <sup>-2</sup>	$e_{16}$	-4.23 C m <sup>-2</sup>
$e_{21}$	-1.73 C m <sup>-2</sup>	$e_{22}$	4.48 C m <sup>-2</sup>
$e_{23}$	-1.67 C m <sup>-2</sup>	$e_{24}$	0.14 C m <sup>-2</sup>
$e_{31}$	1.64 C m <sup>-2</sup>	$e_{32}$	-2.69 C m <sup>-2</sup>
$e_{33}$	2.44 C m <sup>-2</sup>	$e_{34}$	0.55 C m <sup>-2</sup>
$\epsilon_{11}$	44.30	$\epsilon_{22}$	38.08
$\epsilon_{23}$	-7.96	$\epsilon_{33}$	34.12
<i>Pyrex</i> [39]			
$C_{11}$	69.73 GPa	$C_{12}$	17.45 GPa
$\rho_{\text{sl}}$	2230 kg m <sup>-3</sup>	$C_{44}$	26.14 GPa
$\epsilon$	4.6	$\Gamma_{\text{sl}}$	0.0002
<i>PDMS</i> [40–42]			
$C_{11}$	1.13 GPa	$C_{12}$	1.11 GPa
$\rho_{\text{sl}}$	1070 kg m <sup>-3</sup>	$C_{44}$	0.011 GPa
$\epsilon$	2.5	$\Gamma_{\text{sl}}$	0.0213

For anisotropic lithium niobate, Eqs. (5a) and (5b) are turned into equations for  $\mathbf{u}$  and  $\phi$  by using the explicit form of Eqs. (5c) and (5d) written as the coupling-matrix,

$$\begin{pmatrix} \sigma_1 \\ \sigma_2 \\ \sigma_3 \\ \sigma_4 \\ \sigma_5 \\ \sigma_6 \\ D_x \\ D_y \\ D_z \end{pmatrix} = \begin{pmatrix} C_{11} & C_{12} & C_{13} & C_{14} & 0 & 0 & 0 & -e_{21}-e_{31} \\ C_{12} & C_{22} & C_{23} & C_{24} & 0 & 0 & 0 & -e_{22}-e_{32} \\ C_{13} & C_{23} & C_{33} & C_{34} & 0 & 0 & 0 & -e_{23}-e_{33} \\ C_{14} & C_{24} & C_{34} & C_{44} & 0 & 0 & 0 & -e_{24}-e_{34} \\ 0 & 0 & 0 & 0 & C_{55} & C_{56} & -e_{15} & 0 & 0 \\ 0 & 0 & 0 & 0 & C_{56} & C_{66} & -e_{16} & 0 & 0 \\ 0 & 0 & 0 & 0 & e_{15} & e_{16} & \epsilon_{11} & 0 & 0 \\ e_{21} & e_{22} & e_{23} & e_{24} & 0 & 0 & 0 & \epsilon_{22} & \epsilon_{23} \\ e_{31} & e_{32} & e_{33} & e_{34} & 0 & 0 & 0 & \epsilon_{23} & \epsilon_{33} \end{pmatrix} \begin{pmatrix} \epsilon_1 \\ \epsilon_2 \\ \epsilon_3 \\ \epsilon_4 \\ \epsilon_5 \\ \epsilon_6 \\ E_x \\ E_y \\ E_z \end{pmatrix}, \quad (6a)$$

For isotropic elastic solids with no charges and no piezoelectric coupling  $\mathbf{e} = \mathbf{0}$ , only Eq. (5a) is relevant, and it becomes an equation for  $\mathbf{u}$ , as Eq. (5c) reduces to

$$\begin{pmatrix} \sigma_1 \\ \sigma_2 \\ \sigma_3 \\ \sigma_4 \\ \sigma_5 \\ \sigma_6 \end{pmatrix} = \begin{pmatrix} C_{11} & C_{12} & C_{12} & 0 & 0 & 0 \\ C_{12} & C_{11} & C_{12} & 0 & 0 & 0 \\ C_{12} & C_{12} & C_{11} & 0 & 0 & 0 \\ 0 & 0 & 0 & C_{44} & 0 & 0 \\ 0 & 0 & 0 & 0 & C_{44} & 0 \\ 0 & 0 & 0 & 0 & 0 & C_{44} \end{pmatrix} \begin{pmatrix} \epsilon_1 \\ \epsilon_2 \\ \epsilon_3 \\ \epsilon_4 \\ \epsilon_5 \\ \epsilon_6 \end{pmatrix}, \quad (6b)$$

TABLE II. Material parameters of water from Ref. [44].

Parameter	Symbol	Value
Speed of sound	$c_{\text{fl}}$	$1497 \text{ m s}^{-1}$
Mass density	$\rho_{\text{fl}}$	$997 \text{ kg m}^{-3}$
Dynamic viscosity	$\eta_{\text{fl}}$	$0.89 \text{ mPa s}$
Bulk viscosity	$\eta_{\text{fl}}^{\text{b}}$	$2.485 \text{ mPa s}$
Compressibility	$\kappa_{\text{fl}}$	$452 \text{ TPa}^{-1}$

with only two independent elastic constants,  $C_{11}$  and  $C_{44}$ , because  $C_{12} = C_{11} - 2C_{44}$  for isotropic material.

In a fluid with speed of sound  $c_{\text{fl}}$ , mass density  $\rho_{\text{fl}}$ , dynamic viscosity  $\eta_{\text{fl}}$ , viscous boundary layer thickness  $\delta = \sqrt{\frac{2\eta_{\text{fl}}}{\rho_{\text{fl}}\omega}}$ , viscosity ratio  $\beta = \frac{\eta_{\text{fl}}^{\text{b}}}{\eta_{\text{fl}}} + \frac{1}{3}$ , and effective damping coefficient  $\Gamma_{\text{fl}} = \frac{1+\beta}{2}(k_0\delta)^2$ , the first-order pressure field  $p_1$  is governed by the Helmholtz equation, and the acoustic velocity field  $\mathbf{v}_1$  is given by the pressure gradient,

$$\nabla \cdot (\nabla p_1) = -k_c^2 p_1, \quad \text{with } k_c = \frac{\omega}{c_{\text{fl}}} \left(1 + i \frac{\Gamma_{\text{fl}}}{2}\right), \quad (7a)$$

$$\mathbf{v}_1 = \frac{-i}{\omega \rho_{\text{fl}}} (1 - i\Gamma_{\text{fl}}) \nabla p_1, \quad (7b)$$

where  $k_c$  is the weakly damped compressional wavenumber [43]. See Table II for parameter values.

Turning to the boundary conditions, we introduce  $\mathbf{n}$  as the normal vector for a given surface. The SAW device in Fig. 1 is actuated by a time-harmonic potential of amplitude  $V_0$  on the surfaces of the charged electrodes (ce) and 0 V on the grounded electrodes (ge), respectively,

$$\phi_{\text{ce}} = V_0 e^{-i\omega t}, \quad \phi_{\text{ge}} = 0, \quad (8a)$$

A given floating electrode (fe) is modeled as an ideal equipotential domain with a vanishing tangential electrical field on its surface,

$$(\mathbf{I} - \mathbf{nn}) \cdot \nabla \phi_{\text{fe}} = \mathbf{0}, \quad (8b)$$

where  $\mathbf{I}$  is the unit tensor, and  $(\mathbf{I} - \mathbf{nn})$  is the usual tangent projection tensor. Note that this condition is automatically enforced on any surface with a spatially invariant Dirichlet condition applied along it. Note also that the value of the potential on each floating electrode is a priori unknown and must be determined self-consistently from the governing equations and boundary conditions.

At a given fluid-solid interface we impose the usual continuity conditions [32] with the recently developed boundary-layer corrections included [43]: the solid stress  $\boldsymbol{\sigma}_{\text{sl}}$  is given by the acoustic pressure  $p_1$  with the addition of the boundary-layer stress, and the fluid velocity  $\mathbf{v}_1$  is given by the solid-wall velocity  $\mathbf{v}_{\text{sl}} = -i\omega \mathbf{u}$  with the

addition of the boundary-layer velocity  $\mathbf{v}_{\text{sl}} - \mathbf{v}_1$ ,

$$\boldsymbol{\sigma}_{\text{sl}} \cdot \mathbf{n} = -p_1 \mathbf{n} + ik_s \eta_{\text{fl}} (\mathbf{v}_{\text{sl}} - \mathbf{v}_1), \quad (9a)$$

$$\mathbf{n} \cdot \mathbf{v}_1 = \mathbf{n} \cdot \mathbf{v}_{\text{sl}} + \frac{i}{k_s} \nabla_{\parallel} \cdot (\mathbf{v}_{\text{sl}} - \mathbf{v}_1), \quad (9b)$$

$$\text{with shear wavenumber } k_s = \frac{1+i}{\delta}. \quad (9c)$$

The terms containing the shear wavenumber  $k_s$  represent the corrections arising from taking the 400-nm wide, viscous boundary layer into account analytically [43].

All exterior solid surfaces facing the air have a stress-free boundary condition prescribed,

$$\boldsymbol{\sigma} \cdot \mathbf{n} = \mathbf{0}. \quad (10)$$

This is a good approximation because the surrounding air has an acoustic impedance 3 to 4 orders of magnitude lower than that of the solids causing 99.99 % of incident acoustic waves from the solid to be reflected. Moreover the shear stress from the air is negligible.

### C. The time-averaged second-order fields

The slow timescale or steady fields in the fluid are the time-averaged second-order velocity  $\mathbf{v}_2$  and pressure  $p_2$  field. These are governed by the time-averaged momentum and mass-conservation equations,

$$\nabla \cdot \boldsymbol{\sigma}_2 - \rho_0 \nabla \cdot \langle \mathbf{v}_1 \mathbf{v}_1 \rangle = \mathbf{0}, \quad (11a)$$

$$\nabla \cdot (\rho_0 \mathbf{v}_2 + \langle \rho_1 \mathbf{v}_1 \rangle) = 0, \quad (11b)$$

where  $\boldsymbol{\sigma}_2$  is the second-order stress tensor of the fluid

$$\boldsymbol{\sigma}_2 = -p_2 \mathbf{I} + \eta [\nabla \mathbf{v}_2 + (\nabla \mathbf{v}_2)^{\text{T}}] + (\beta - 1) \eta (\nabla \cdot \mathbf{v}_2) \mathbf{I}. \quad (11c)$$

Along a fluid-solid interface with tangential vectors  $\mathbf{e}_{\xi}$  and  $\mathbf{e}_{\eta}$  and the normal vector  $\mathbf{e}_{\zeta} = \mathbf{n}$ , we use for  $\mathbf{v}_2$  the effective boundary condition derived in Ref. [43]. Here, the viscous boundary layer is taken into account analytically by introducing the boundary-layer velocity field  $\mathbf{v}^{\delta 0} = \mathbf{v}_{\text{sl}} - \mathbf{v}_1$  in the fluid along the fluid-solid interface,

$$\mathbf{v}_2 = (\mathbf{A} \cdot \mathbf{e}_{\xi}) \mathbf{e}_{\xi} + (\mathbf{A} \cdot \mathbf{e}_{\eta}) \mathbf{e}_{\eta} + (\mathbf{B} \cdot \mathbf{e}_{\zeta}) \mathbf{e}_{\zeta}, \quad (12a)$$

$$\mathbf{A} = -\frac{1}{2\omega} \text{Re} \left\{ \mathbf{v}_1^{\delta 0*} \cdot \nabla \left( \frac{1}{2} \mathbf{v}_1^{\delta 0} - i \mathbf{v}_{\text{sl}} \right) - i \mathbf{v}_{\text{sl}}^* \cdot \nabla \mathbf{v}_1 \right. \\ \left. + \left[ \frac{2-i}{2} \nabla \cdot \mathbf{v}_1^{\delta 0*} + i \left( \nabla \cdot \mathbf{v}_{\text{sl}}^* - \partial_{\zeta} v_{1\zeta}^* \right) \right] \mathbf{v}_1^{\delta 0} \right\}, \quad (12b)$$

$$\mathbf{B} = \frac{1}{2\omega} \text{Re} \left\{ i \mathbf{v}_1^* \cdot \nabla \mathbf{v}_1 \right\}, \quad (12c)$$

where the asterisk denotes complex conjugation.

### D. Acoustophoresis of suspended particles

To predict the acoustophoretic motion of a dilute suspension of spherical micro- and submicrometer-sized particles in the fluid of density  $\rho_{\text{fl}}$ , compressibility  $\kappa_{\text{fl}}$ , and



viscosity  $\eta_{\text{fl}}$ , we implement a particle tracing routine in the model. We consider Newton's second law for a single spherical particle of radius  $a_{\text{pt}}$  and density  $\rho_{\text{pt}}$  moving with velocity  $\mathbf{v}_{\text{pt}}$  under the influence of gravity  $\mathbf{g}$ , the acoustic radiation force  $\mathbf{F}^{\text{rad}}$  [45], and the Stokes drag force  $\mathbf{F}^{\text{drag}}$  [46] induced by acoustic streaming of the fluid,

$$\frac{4\pi}{3} a_{\text{pt}}^3 \rho_{\text{pt}} \frac{d\mathbf{v}_{\text{pt}}}{dt} = \rho_{\text{pt}} \mathbf{g} + \mathbf{F}^{\text{rad}} + \mathbf{F}^{\text{drag}}, \quad (13a)$$

$$\mathbf{F}^{\text{rad}} = -\frac{4}{3} \pi a^3 \left[ \kappa_{\text{fl}} \langle (f_0 p_1) \nabla p_1 \rangle - \frac{3}{2} \rho_{\text{fl}} \langle (f_1 \mathbf{v}_1) \cdot \nabla \mathbf{v}_1 \rangle \right], \quad (13b)$$

$$\mathbf{F}^{\text{drag}} = 6\pi a \eta_{\text{fl}} (\mathbf{v}_2 - \mathbf{v}_{\text{pt}}). \quad (13c)$$

Here,  $f_0 = 0.444$  and  $f_1 = 0.034$  are the monopole and dipole scattering coefficients of the suspended particles at 50 MHz, where the values are for polystyrene micro- and nanoparticles in water [47]. When studying different particle sizes it is convenient to introduce the radiation force density  $\mathbf{f}^{\text{rad}}$  as

$$\mathbf{f}^{\text{rad}} = \frac{3}{4\pi a^3} \mathbf{F}^{\text{rad}}. \quad (13d)$$

By direct time integration of Eq. (13a) applied to a set of particles initially placed on a square grid, the acoustophoretic motion of the particles can be predicted and compared to the experimentally observed one. We note that gravity effects are negligible as  $\rho_{\text{pt}} \mathbf{g} \ll \kappa_{\text{fl}} \langle (f_0 p_1) \nabla p_1 \rangle$ .

### III. NUMERICAL IMPLEMENTATION

Inspired by our previous experimental work, Sehgal and Kirby [23], we study the SAW test system shown

TABLE III. Dimensions of the numeric 2D and 3D models.

Parameter	Symbol	2D	3D	Unit
Device depth ( $y$ )	$L_{\text{sl}}$	-	1200	$\mu\text{m}$
Solid height ( $z$ )	$H_{\text{sl}}$	40-1000	500	$\mu\text{m}$
Solid width ( $x$ )	$W_{\text{sl}}$	200	80	$\mu\text{m}$
Channel height	$H_{\text{fl}}$	50-200	50	$\mu\text{m}$
Channel width	$W_{\text{fl}}$	3500	900	$\mu\text{m}$
Piezo height	$H_{\text{pz}}$	100-500	300	$\mu\text{m}$
PML length	$L_{\text{PML}}$	80	80	$\mu\text{m}$
Electrode depth ( $y$ )	$L_{\text{el}}$	-	400	$\mu\text{m}$
Electrode height ( $z$ )	$H_{\text{el}}$	0.4	0.4	$\mu\text{m}$
Electrode width ( $x$ )	$W_{\text{el}}$	20	20	$\mu\text{m}$
Electrode gap	$G_{\text{el}}$	20	20	$\mu\text{m}$
SAW wavelength	$\lambda_{\text{SAW}}$	80	80	$\mu\text{m}$
No. of electrode pairs	$n_{\text{el}}$	24	4	-
No. of reflectors	$n_{\text{rf}}$	0-6	0	-
Actuation frequency	$f_0$	30-60	50	MHz
Driving voltage	$V_0$	1	1	V
Degrees of freedom	$n_{\text{DOF}}$	$\mathcal{O}(10^5)$	$\mathcal{O}(10^6)$	-
Memory requirements	$R$	$\mathcal{O}(10)$	$\mathcal{O}(10^3)$	GB

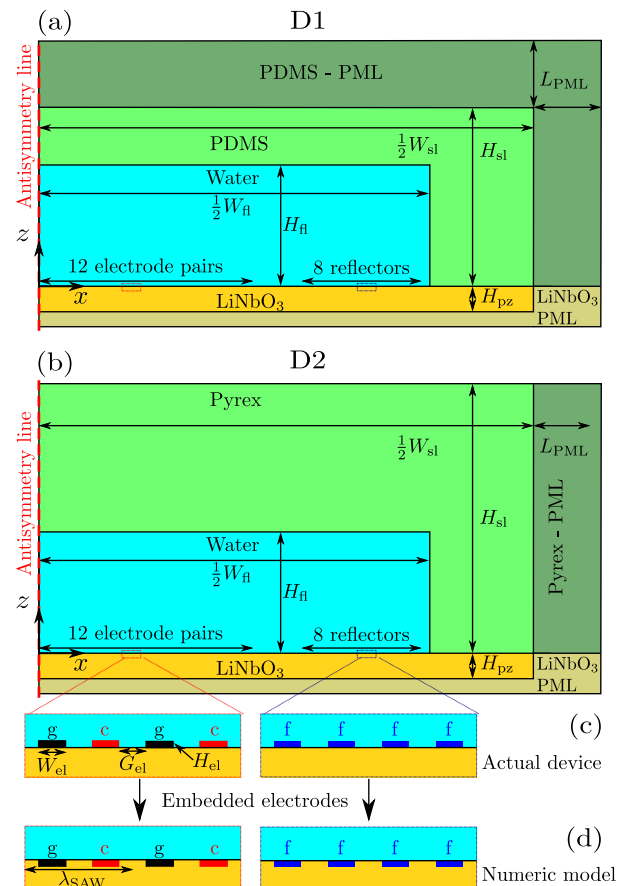


FIG. 2. The vertical 2D cross section of the numeric model and illustration of the embedded electrodes used in simulations, with (a) a highly attenuating, low-reflection polymer PDMS lid as used in Ref. [23], and (b) a stiff, acoustically reflecting Pyrex glass lid. (c) The twelve pairs of grounded (g, black) and charged (c, red) electrodes, as well as the floating (f, blue) electrodes, are all included in their entire height, but (d) lowered into the lithium niobate (yellow) to level with the substrate. Note that  $\lambda_{\text{SAW}} = 2(W_{\text{el}} + G_{\text{el}})$ .

in Fig. 1 with actuating electrodes and Bragg-reflector electrodes placed directly underneath the microchannel. The parameter values used in the numerical simulation are listed in Table III, and a sketch of the vertical cross section of the test system is shown in Fig. 2. Note that the SAW wavelength  $\lambda_{\text{SAW}}$  is set by the IDT electrode geometry as  $\lambda_{\text{SAW}} = 2(W_{\text{el}} + G_{\text{el}})$ . We study microcavities defined in either acoustically soft PDMS, see Fig. 2(a), or the acoustically hard borosilicate glass (Pyrex), see Fig. 2(b), and we perform numerical simulation in both 2D and 3D.

Following the procedure of our previous numerical simulations [32, 36], the coupled governing equations from Sections II B-II D are implemented in the finite-element-method software COMSOL Multiphysics 5.3a [48], using the weak-form partial differential equation interface “PDE Weak Form” in the mathematics module. For

a given driving voltage  $V_0$ , actuation frequency  $f$ , and angular frequency  $\omega = 2\pi f$  specified in the actuation boundary condition (8a), the numeric model is solved in three sequential steps: (1) the first-order equations (5) and (7a) presented in Section II B for the pressure  $p_1$ , displacement  $\mathbf{u}$ , and electric potential  $\phi$ , together with the corresponding boundary conditions (8)-(10); (2) the steady second-order streaming velocity  $\mathbf{v}_2$  in Section II C governed by (11) and (12), where time-averaged products of the first-order fields appear as source terms; and (3) the acoustophoretic motion of suspended test particles in Section II D found by time integration of Eq. (13). As in previous works [32], we have performed convergence analyses of the model to verify that the model converges towards a single solution as the mesh size decreases.

Simulations of the full 3D model are time and computer-memory consuming. Therefore, part of the analysis has been performed on 2D models to study the resonance behavior of the device and the acoustic radiation force in the vertical  $y$ - $z$  plane normal to the electrodes in the horizontal  $x$ - $y$  plane. In these simulations, presented in Section V, it is possible to model a cross-section of the device to scale. To investigate effects that have non-trivial behavior in full 3D, such as the acoustic streaming and the acoustophoretic motion of suspended particles presented in Section V, we must perform full 3D modeling. However, in this case, the extended computer memory requirements has necessitated a scale down of the model. The parameters for the 2D and 3D simulations are listed in Table III.

### A. Perfectly matched layers

We reduce the numeric footprint of the model by implementing perfectly matched layers (PMLs) in the model as described by Ley and Bruus [32]: Large passive domains surrounding the acoustically active region are replaced by much smaller domains, in which PMLs act as ideal absorbers of out-going acoustic waves thus completely removing reflections. In contrast to Ref. [32], the PMLs in the present model are functions of all three spatial coordinates.

In the small surrounding domains, the PMLs are implemented in the weak-form governing equations by a complex-valued coordinate transformation of the spatial derivatives  $\partial x_i$  and integral measures  $dx_i$  appearing,

$$\partial x_i \rightarrow \partial \tilde{x}_i = \frac{1}{1 + i s(\mathbf{r})} \partial x_i, \quad (14a)$$

$$dx_i \rightarrow d\tilde{x}_i = [1 + i s(\mathbf{r})] dx_i, \quad (14b)$$

$$s(\mathbf{r}) = k_{\text{PML}} \sum_{i=x,y,z} \frac{(x_i - x_{0i})^2}{L_{\text{PML},i}^2} \Theta(x_i - x_{0i}), \quad (14c)$$

where  $s(\mathbf{r})$  is a real-valued function of position. Here,  $s(\mathbf{r})$  is given for the specific case shown in Fig. 2 with a

PML of width  $L_{\text{PML},i}$  in the three coordinate directions  $i = x, y, z$  placed outside the region  $x < x_0$ ,  $y < y_0$ , and  $z < z_0$ ,  $\Theta(x)$  is the Heaviside step function ( $= 1$  for  $x > 0$ , and 0 otherwise), and  $k_{\text{PML}}$  is an adjustable parameter for the strength of the PML absorption. The bottom PML in the niobate substrate is used because SAWs decay exponentially in the depth on the scale of the wavelength, whereas the top and side PMLs are used to mimic attenuating in respective materials over large distances.

### B. Symmetry planes

As in previous numeric works [32, 49], we use an antisymmetry line to reduce the numerical cost of our 2D models. The antisymmetry line is realized by boundary conditions on the solid displacement, the electric potential, and the fluid pressure along the line,

$$\partial_x u_x = 0 \quad (15a)$$

$$u_z = 0 \quad (15b)$$

$$\phi = \frac{1}{2} V_0 \quad (15c)$$

$$p_1 = 0 \quad (15d)$$

We check these conditions against the values along the device centerline in a 2D simulation for a fully symmetric device and observe that they are in good agreement.

In 3D we cannot use symmetry planes, as the device is manifestly asymmetric due to the  $10^\circ$  angle between the IDT and the walls of the microchannel.

### C. Embedded electrodes

In the actual device, the 400-nm thick electrodes protrude into the fluid domain. In our numeric model we simplify the device by submerging them into the substrate to form a planar solid-fluid interface as shown in Fig. 2. Thereby the fluid-solid interface has no sharp corners, at which singularities appear in the numeric gradients. Furthermore, the planar interface mitigates the need for an enormous number of mesh elements ranging from nm to  $\mu\text{m}$  in the fluid domain, which would either lower the element quality greatly or add massive computational costs. This reduction in model complexity is justified by the height of the electrodes being less than 1 % of the channel height and having no influence on the pressure acoustics of the system. On the other hand, we cannot completely neglect the electrodes, because jumps in acoustic impedance between the metal electrodes and the niobate substrate cause partial reflections of SAWs running along the substrate. Thus we choose to keep but submerge the electrodes.

TABLE IV. The devices D1 and D2, used in the experimental validation of the numerical model, differs by the choice of lid. The other parameters of D1 and D2 are listed in Table III.

Device	Lid material	Lid thickness
D1	PDMS	15 mm
D2, see Fig. 1(a)	Pyrex	0.45 mm

#### IV. EXPERIMENTAL METHODS

To validate the numerical models, we have performed experiments on two type of devices listed in table IV, namely microchannels defined in slabs of either PDMS (D1) or Pyrex (D2) bonded on top of the lithium niobate substrate equipped with the IDT and Bragg reflectors. The PDMS device (D1) is fabricated by standard photolithography techniques listed in our previous work [23]. The Pyrex device (D2) is fabricated by glass microfabrication techniques, briefly described in the following. A microchannel of desired dimensions is wet-etched in a borosilicate glass wafer by 49% hydrofluoric (HF) acid using a multilayered mask of chrome, gold, and SPR220 photoresist. The input and output ports of the microchannel are obtained from the laser cutting of glass. The bonding between glass microchannel and lithium niobate substrate is achieved by coating a 5  $\mu\text{m}$  layer of SU-8 epoxy on the surface of lithium niobate. The microchannel is gently placed on the uncured SU-8 and the epoxy is baked following standard steps. The SU-8 outside the microchannel region is selectively crosslinked to achieve bonding and the SU-8 inside the microchannel region is dissolved away with a developer, thus obtaining a Pyrex lid microchannel on top of the lithium niobate substrate (D2). The devices are tested with 1.7- $\mu\text{m}$ -diameter fluorescent polystyrene particles (Polysciences, Inc.) that are suspended in de-ionized water (18.2  $\text{M}\Omega/\text{cm}$ , Labconco WaterPro PS) containing 0.7% (w/v) Pluronic F-127 to prevent particle aggregation. The particle solution is injected into the microchannel after priming the devices with 70% ethanol solution to avoid the formation of air bubbles. An ultrasound field is set up in the devices by applying an RF signal at desired frequency to the IDT with a HP 8643A signal generator and an ENI 350L RF power amplifier. The acoustophoretic motion of the tracer particles are visualized on a fixed-stage, upright fluorescent microscope (Olympus BX51WI) with a digital CCD camera (Retiga 1300, Q Imaging). The images are acquired with Q-Capture Pro 7 software and post processed in ImageJ. The electrical impedance of the devices is measured directly from an impedance analyzer (Agilent 4395A).

#### V. RESULTS OF THE 2D MODELING

In the following, we compare the results of the 2D modeling in the vertical  $x$ - $z$  with experiments carried out on the two devices D1 and D2 listed in Table IV. Such a comparison is reasonable because the low channel height of 50  $\mu\text{m}$  implies an approximate translation invariance along the  $y$ -axis spanning the length (aperture) 2400  $\mu\text{m}$  of the IDT electrodes, as seen in the 3D geometry of Fig. 1. Also the variation along the  $x$  axis given by the width 20  $\mu\text{m}$  of the individual electrodes, and the periodicity  $\lambda_{\text{SAW}} = 80 \mu\text{m}$  the IDT, are much smaller than IDT aperture along  $y$  axis. We can therefore obtain a reasonable estimate of the electrical and acoustical response of the device, by just considering the 2D domain in the vertical  $x$ - $z$  plane shown in Fig. 2.

##### A. Electrical response

As a first validation of the model, we study the electrical impedance

$$Z^{\text{el}} = |Z^{\text{el}}| e^{-i\psi} = \frac{V_0}{I}, \quad (16)$$

in terms of the driving voltage  $V_0$  and the complex-valued current  $I$  through the device, because this quantity is relatively easy to obtain both in simulation and in experiment. We compare model predictions of the magnitude

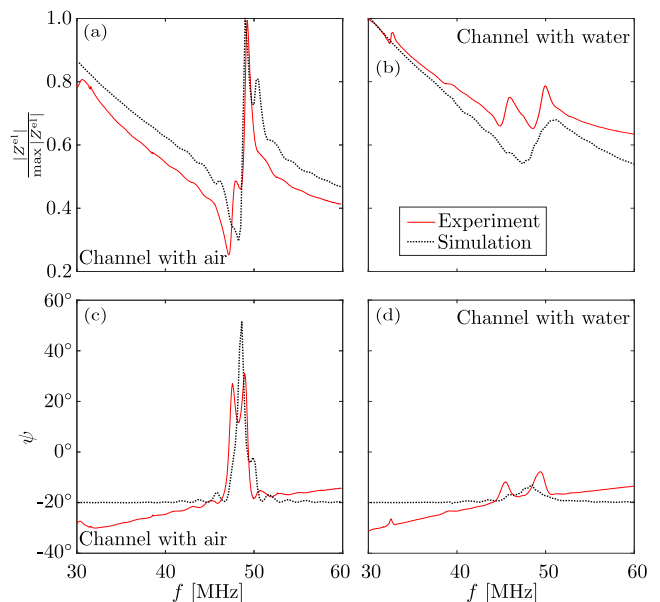


FIG. 3. Line plots of the normalized magnitude  $|Z^{\text{el}}|$  and phase  $\psi$  of the electrical impedance  $Z^{\text{el}}$ , as functions of frequency determined by experiment (full red line) and by numerical simulation (dotted black line). The measurements and simulations are carried out for a microchannel containing either vacuum or deionized water.

TABLE V. Measured and simulated values of the frequencies  $f$  near the ideal (unloaded) frequency  $f_{\text{SAW}} = 49.9$  MHz, where  $|Z^{\text{el}}(f)|$  and  $\psi(f)$  have local minima and maxima in Pyrex device D2.

Extremum	$f_{\text{exp}}$ [GHz]	$f_{\text{num}}$ [GHz]	Relative error [%]
A	47.35	48.25	1.9
B	48.05	49.00	2.0
C	49.40	50.25	1.7
D	48.65	47.50	1.7
E	50.00	50.75	1.7
F	47.70	48.75	2.2
G	49.10	50.00	1.8
H	45.50	46.00	1.1
I	49.40	48.50	1.8

$|Z^{\text{el}}|$  and phase  $\psi$  of the impedance with the experimentally measured counterparts.

In the model, we compute  $Z^{\text{el}}$  from the time-harmonic dielectric polarization density  $\mathbf{P}$  and the corresponding polarization current  $\mathbf{J}_{\text{pol}}$  in the lithium niobate substrate, which we treat as an ideal dielectric without free charges,

$$\mathbf{P} = \mathbf{D} - \varepsilon_0 \mathbf{E}, \quad (17a)$$

$$\mathbf{J}_{\text{pol}} = -i\omega \mathbf{P}. \quad (17b)$$

The total current  $I$  through the device is given by the surface integral of  $\mathbf{J}_{\text{pol}}$ , over one of the charged electrodes with potential  $\phi_{\text{ce}} = V_0$  and surface  $\partial\Omega_{\text{ce}}$ ,

$$I = \int_{\partial\Omega_{\text{ce}}} \mathbf{J}_{\text{pol}} \cdot \mathbf{n} \, dA. \quad (17c)$$

The modulus  $|Z^{\text{el}}|$  and phase angle  $\psi = \arg(Z^{\text{el}})$  are thus

$$|Z^{\text{el}}| = \left| \frac{V_0}{I} \right|, \quad \psi = \arg\left( \frac{V_0}{I} \right). \quad (17d)$$

In Fig. 3(a) and (b), we compare the values of  $|Z^{\text{el}}|$  computed by Eq. (17d) for our 2D model with those measured on Pyrex device D2 of Fig. 1(a) and Table IV for microchannels with air or with DI water. The numerical simulation predicts correctly the value of the resonance observed near 48 MHz in the experiments. As shown in Table V, the relative difference between computed and measured values of the frequencies  $f$ , where  $|Z^{\text{el}}(f)|$  and  $\psi(f)$  have local minima or maxima, is about 2 % or less. We also see that simulation also predicts the monotonically decreasing background signal for  $|Z^{\text{el}}(f)|$  before and after the resonance relatively well for both an air- and water-filled microchannel. However, the simulation fails to predict the correct ratio of the resonance peak heights.

For the phase  $\psi$  shown in Fig. 3(c) and (d), the simulation predicts the resonance frequencies correctly, but fails to predict the monotonically increasing background

signal. By adding external stray impedances to our 2D model to simulate the surrounding 3D system, it is however possible to generate a slant in the phase curves by fitting the values of these stray impedances. We do not show these results as they are descriptive and not predictive in nature.

## B. Wall material: hard pyrex versus soft PDMS

Our previous device [23] features a soft PDMS polymer lid, as is commonly used due to the ease of fabrication and handling. However, the acoustic properties of PDMS are far from ideal: its impedance is nearly equal to that of water (20 % lower) and the attenuation is about two orders of magnitude larger than that of the boundary layer in water. In the following, we therefore simulate the acoustic properties of the device D1 with a PDMS lid and contrast them with those of device D2 with a much stiffer Pyrex lid, using the two models shown in Fig. 2 and Table IV. Compared to water, the acoustic impedance of Pyrex is 8.3 times larger and its attenuation 10 times smaller.

We study by numerical simulation the acoustic fields of device D1 and D2 near the ideal (unloaded) frequency  $f_{\text{SAW}} = 49.9$  MHz. By locating the maximum of the average acoustic energy in the water-filled channel plotted versus the actuation frequency  $f$  (not shown), we determine the (loaded) resonance frequency  $f_{\text{res}}$  of the two devices to be  $f_{\text{res}}^{\text{D1}} = 47.75$  MHz and  $f_{\text{res}}^{\text{D2}} = 46.50$  MHz, respectively. In Fig. 4 we show line plots along the height ( $z$  direction) and across the width ( $x$  direction) of numerically simulated acoustic fields for these two devices.

In Fig. 4(a) and (b) is shown the magnitude  $|u_z|$  of the  $z$  component of the acoustic displacement  $\mathbf{u}$ , which in water is defined through acoustic velocity Eq. (7b) as  $\mathbf{v}_1 = -i\omega \mathbf{u}$ , along a vertical cut-line through the entire device. In D1,  $|u_z|$  has the characteristics of a traveling wave emitted from the SAW substrate (maximum amplitude), traversing the water with little reflection (a small oscillation amplitude), and being absorbed in the PDMS lid (decaying amplitude). In contrast,  $|u_z|$  in D2 has the characteristics of a standing wave localized in the water channel with reflections from the surrounding solids: huge oscillations in the water domain with minima close to zero and an amplitude exceeding that in the emitting substrate and the receiving lid. We also notice that in the stiff Pyrex the attenuation is weak, and that the wave is reminiscent of a standing wave between the water interface below the lid and the air interface above. The corresponding acoustic energy flux density  $\mathbf{S}_{\text{ac}} = \langle p_1 \mathbf{v}_1 \rangle$  in both systems is non-zero and predominantly vertical, but with a much larger amplitude in D1 compared to D2.

In Fig. 4(c) is shown the the magnitude  $|\mathbf{u}|$  of the acoustic displacement  $\mathbf{u}$  along horizontal cut-lines following the top ( $z = H_{\text{fl}}$ ) and the bottom ( $z = 0$ ) of the water channel across the region containing the IDT. In both devices the periodicity of the IDT electrodes is



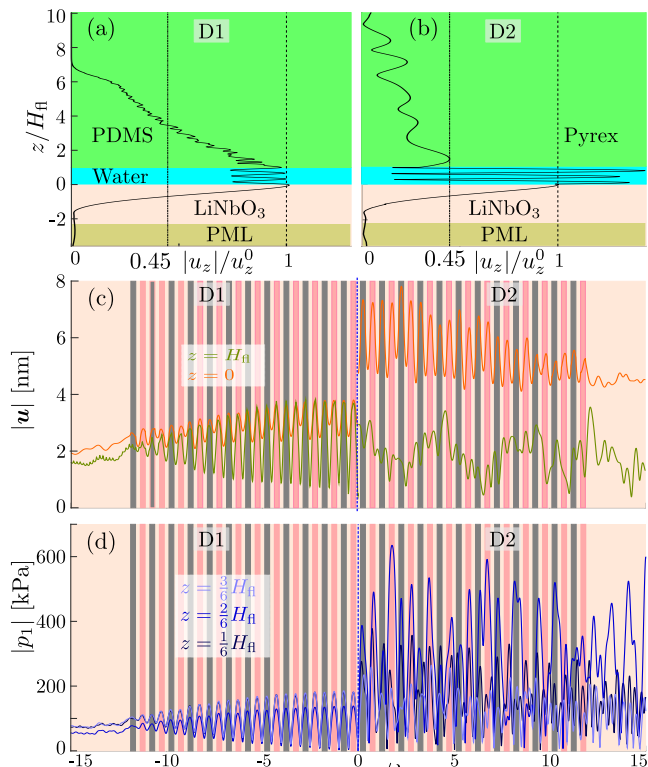


FIG. 4. The amplitude of the displacement  $|u|$  and the pressure amplitude  $|p_1|$  in the PDMS-lid device D1 and in the Pyrex-lid device D2 at their respective resonance frequencies  $f_{\text{res}}^{\text{D1}} = 47.75$  MHz and  $f_{\text{res}}^{\text{D2}} = 46.50$  MHz at  $V_0 = 1$  V. (a) Line plot of the  $z$  component  $|u_z|$  along the vertical line  $x = W_{\text{el}}$  (the center of the middle electrode) from the bottom of the substrate (beige), through the water (blue), to the top of the PDMS lid (green). (b) As in (a), but for the Pyrex-lid device D2. (c) Line plot of  $|u|$  along the top ( $z = H_{\text{fl}}$ ) and the bottom ( $z = 0$ ) of the channel in D1 ( $x < 0$ ) and D2 ( $x > 0$ ). The dark gray and pink rectangles for  $-12 < \frac{x}{\lambda_{\text{SAW}}} < 12$  represent the IDT electrodes. (d) As in panel (c), but for  $|p_1|$  along the horizontal lines at  $z/H_{\text{fl}} = \frac{3}{6}, \frac{2}{6}, \frac{1}{6}$  inside the channel.

clearly seen, but the amplitude in the nearly-standing wave case of D2 is 2-3 times larger than in the traveling wave case of D1. Moreover, it is seen that the acoustic waves dies out faster in D1 than in D2 away from the IDT region. The tiny oscillations in the PDMS lid (green curve) for  $x < -12\lambda_{\text{SAW}}$  stems from the minute transverse wavelength  $\sim 11 \mu\text{m} = 0.13 \lambda_{\text{SAW}}$  in PDMS.

In Fig. 4(d) is shown the the magnitude  $|p_1|$  of the acoustic pressure  $p_1$  in the water along the horizontal cut-lines  $z/H_{\text{fl}} = \frac{1}{6}, \frac{2}{6}, \frac{3}{6}$ . Here the traveling versus standing wave nature of the two devices mentioned above, is prominent: In D1,  $|p_1|$  is nearly independent of the height, and its envelope amplitude is steadily decaying from 90 to 55 kPa from the center to the edge of the IDT region. In contrast,  $|p_1|$  has large amplitude fluctuations as a function of the horizontal position  $x$  and for the three vertical  $z$  positions. Moreover,  $|p_1|$  does not decay

away from the the IDT. Clear,  $p_1$  in the water channel of D2 is dominated by reflections between the solid-water interfaces. This observation can be quantified by the the standing wave ratio,  $\text{SWR} = \max(|p_1|)/\min(|p_1|)$  that describes the ratio of standing to traveling waves in a given field. In an ideal resonator and an ideally transmitting system,  $\text{SWR} = \infty$  and 1, respectively. Here, we find  $\text{SWR}(\text{D2}) = 12.7$  and  $\text{SWR}(\text{D1}) = 1.3$ . These numbers underlines the good acoustic properties of the water-Pyrex systems compared to the bad one of the PDMS system. The ratio of the SWR numbers is 9.8, almost equal to the impedance ratio 10.5, which emphasizes the nearly perfect vertical energy flux density  $\mathcal{S}_{\text{ac}}$  discussed above, as the impedance extracted from the properties of a plane wave with a vertical incident on a planar surface.

### C. Acoustophoresis

Whereas we have not made experimental validation of the above simulation results for the acoustic fields  $p_1$  and  $\mathbf{u}$ , we compare in the following the experimentally observed acoustophoretic motion at the SAW resonance frequency  $f_{\text{SAW}}$  of microparticle suspensions in the water-filled microchannel, with that obtained by numerical simulation in our 2D model. The central experimental and numerical results are shown in Fig. 5, in the left column for the PDMS-lid device D1 and in the right column for the Pyrex-lid device D2. In the Supplemental Material [50] are shown four animations of the acoustophoresis in Fig. 5(c) and (g) of 0.1- and 1.7- $\mu\text{m}$ -diameter particles in device D1 and D2.

In Fig. 5(a) and (e) we observe that the suspended 1.7- $\mu\text{m}$ -diameter particles in D1 focus on the edges of the electrodes, whereas in D2 they mainly focus along the center line of each electrode. This difference in acoustophoretic focusing is caused solely by choice of lid material and its thickness. Already in Fig. 4, we saw how the change from the PDMS lid to the Pyrex lid led to a change from a predominantly traveling wave, to a nearly standing wave in the  $z$  direction. As a consequence, both the pressure and its gradients in device D1 are smaller than those in D2, and from Eq. (13b) follows that the acoustic radiation force  $\mathbf{F}^{\text{rad}}$  changes significantly.

This change in  $\mathbf{F}^{\text{rad}}$  per particle volume, named  $\mathbf{f}^{\text{rad}}$  in Eq. (13d), is shown as the vector and gray-scale plots for device D1 and D2 in the right half of Fig. 5(b) and (f), respectively. Compared to D2 having  $|\mathbf{f}^{\text{rad}}| = 7.4 \text{ pN}/\mu\text{m}^3$ , the magnitude  $|\mathbf{f}^{\text{rad}}| = 0.4 \text{ pN}/\mu\text{m}^3$  is 18 times smaller in D1, and  $|\mathbf{f}^{\text{rad}}|$  is more smeared out (even smaller gradients). Both force fields have a three-period structure along the vertical  $z$  axis, reflecting that  $H_{\text{fl}} \approx \frac{3}{2}c_{\text{fl}}/f_{\text{SAW}}$ . In D1, the center of the force-field structure is displayed relative to the center of the electrode, whereas in D2 it is above the electrode center. Moreover, whereas  $\mathbf{f}^{\text{rad}}$  has four less-marked, unstable nodal planes in D1 at  $z/H_{\text{fl}} = 0, \frac{1}{3}, \frac{2}{3}, 1$ , it has three well-defined, stable ones in

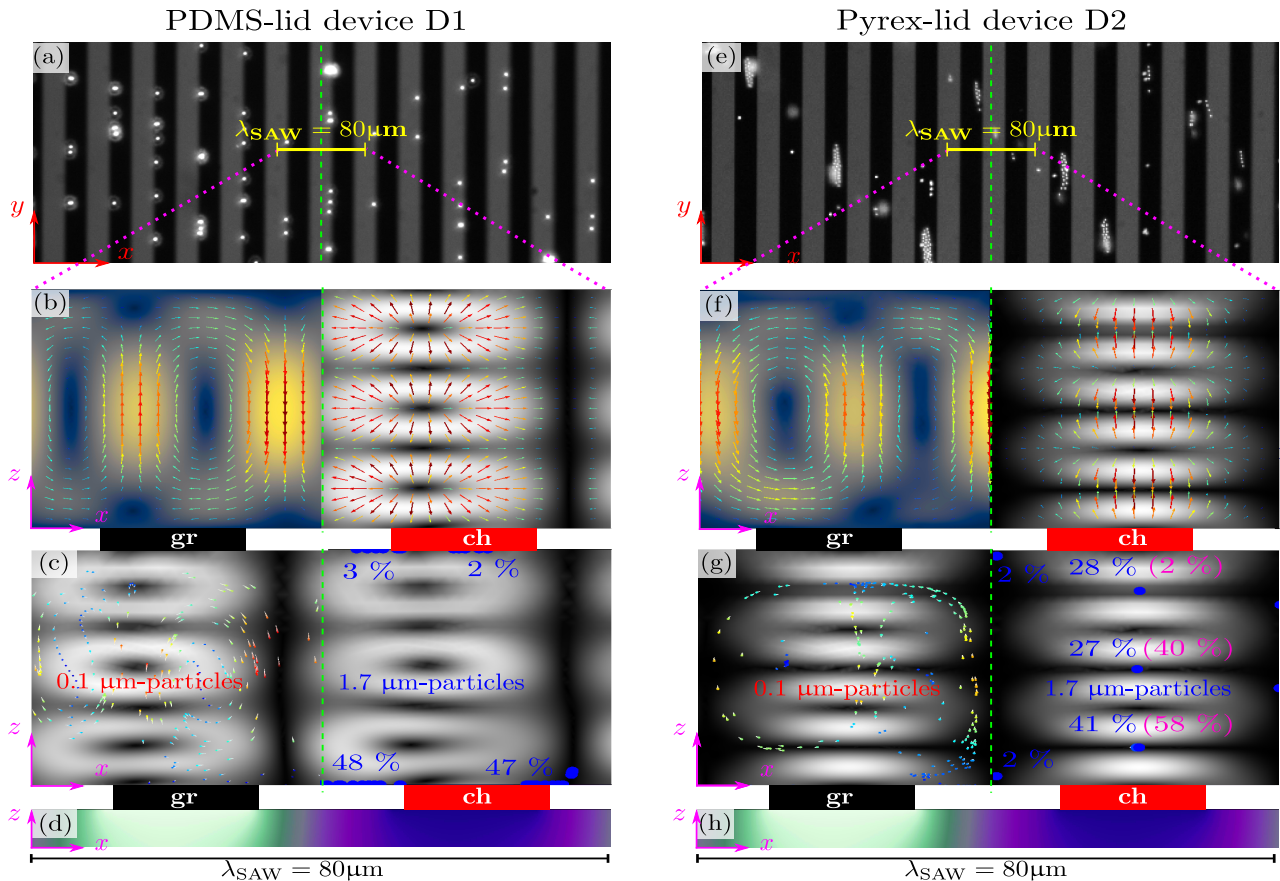


FIG. 5. Microparticle acoustophoresis in experiments and in simulations for actuation frequency  $f_{\text{SAW}} = 49.9$  MHz and driving voltage  $V_0 = 4.35$  V, rescaling the simulation from 1 to 4.35 V. (a) Top-view photograph ( $x$ - $y$  plane) of the center region of the IDT array in device D1, where suspended 1.7- $\mu\text{m}$ -diameter fluorescent polystyrene particles (white) are focused above the edge of each metal electrode (black). (b) Numerical simulations in the vertical  $x$ - $z$  plane over a single electrode pair ( $6\lambda_{\text{SAW}} < x < 7\lambda_{\text{SAW}}$ , the yellow line in panel (a)) in the fluid domain of device D1 with (to the left) a color plot of the magnitude  $|\mathbf{v}_2|$  [from 0 (blue) to  $66 \mu\text{m/s}$  (yellow)] of the streaming velocity  $\mathbf{v}_2$ , and (to the right) a gray-scale plot of  $|\mathbf{f}^{\text{rad}}|$  [from 0 (black) to  $0.4 \text{ pN}/\mu\text{m}^3$  (white)] of the acoustic radiation force density  $\mathbf{f}^{\text{rad}}$ . Superimposed are colored vector plots of  $\mathbf{v}_2$  [from 0 (blue) to  $66 \mu\text{m/s}$  (red)] and of  $\mathbf{f}^{\text{rad}}$  [from 0 (blue) to  $0.4 \text{ pN}/\mu\text{m}^3$  (red)]. (c) Color-comet-tail plot of the simulated acoustophoretic motion of 247 0.1- $\mu\text{m}$ -diameter spherical polystyrene particles (to the left), superimposed on the gray-scale plot of  $|\mathbf{f}^{\text{rad}}|$  from panel (b), 0.5 s after being released from initial positions in a regular  $13 \times 19$  grid to the left of the green-dashed centerline. Similarly for 1.7- $\mu\text{m}$ -diameter particles to the right. The comet tail indicates the direction of the velocity with length and color from 0 (dark blue) to  $66 \mu\text{m/s}$  (orange) representing the speed. The percentages indicate the portion of particles accumulating in these final positions: the blue set for a homogeneous initial particle distribution, and the purple set for an inhomogeneous initial particle distribution created by 3 min of sedimentation. (d) Color plot in the vertical  $x$ - $z$  plane below a single electrode pair  $5\lambda_{\text{SAW}} < x < 6\lambda_{\text{SAW}}$  of the numerically simulated electric potential  $V$  from  $-4.35$  (light cyan) to  $4.35$  V (purple) in the lithium niobate substrate. The width and  $x$ -position of the grounded and charged electrodes in the IDT-pair are represented by the black (ge) and red (ce) rectangles, respectively. (e-h) Same as in (a-d) but for Pyrex-lid device D2, and in (f) the gray-scale for  $|\mathbf{v}_2|$  is from 0 (blue) to  $76 \mu\text{m/s}$  (yellow) and  $|\mathbf{f}^{\text{rad}}|$  from 0 (black) to  $7.4 \text{ pN}/\mu\text{m}^3$  (white).

D2 at  $z/H_{\text{fl}} = \frac{1}{6}, \frac{3}{6}, \frac{3}{6}$ .

The corresponding streaming velocity field  $\mathbf{v}_2$  in D1 and D2 is shown as the vector and color plots in the left half of Fig. 5(b) and (f). The streaming appears strikingly equal both in magnitude ( $66 \mu\text{m/s}$  for D1 and  $76 \mu\text{m/s}$  for D2), shape and topology, but again with the center of the pattern in D1 shifted slightly away from the electrode center. The reason for this resemblance in  $\mathbf{v}_2$  stems from the energy flux density  $\mathcal{S}_{\text{ac}}$ , which in both de-

vices points (nearly) vertically up along the  $z$  axis above the electrodes, and is weak in between. As the (Eckart) streaming is proportional to  $\mathcal{S}_{\text{ac}}$  [51], even in microcavities [36], the streaming moves upward due to  $\mathcal{S}_{\text{ac}}$  above the electrodes and downward by recirculation between the electrodes.  $\mathcal{S}_{\text{ac}}$  has nearly the same amplitude in D1 and D2 because, although the acoustic field in D2 is much larger than in D1, it is mostly a standing wave with zero energy flux density, and the little part that is a travel-

ing wave in D2 that carries the energy flux density, is nearly of the same magnitude as the traveling wave that constitutes the main part of the weaker acoustic field in D1.

According to Newton's second law (13), the above-mentioned properties of the acoustic radiation force density  $\mathbf{f}^{\text{rad}}$  and streaming velocity field  $\mathbf{v}_2$  governs the observable acoustophoretic motion of suspended particles. In Fig. 5(c) and (g), as well as in the Supplemental Material [50], is shown the results of simulating such motion for 0.1- and 1.7- $\mu\text{m}$ -diameter polystyrene beads in both D1 and D2, 0.5 s after starting from an initial homogeneous distribution (blue points and percentage numbers). The motion of the large particles is dominated by the radiation force [52], so the different focusing of these particles seen in the right half of Fig. 5(c) and (g) is explained in terms of  $\mathbf{f}^{\text{rad}}$ : Because  $\mathbf{f}^{\text{rad}}$  has no stable nodal planes in D1, all particles accumulate the floor or the ceiling of the channel, and most of them (98 %) are pushed to the regions above the electrode gaps as indicated by the vector plot in the right half of Fig. 5(c). In contrast, the stable nodal planes of  $\mathbf{f}^{\text{rad}}$  in D2, Fig. 5(g) right half, guides 96 % of the particles into the three stable points above the electrode center, with 41 %, 27 %, and 28 % at  $z/H_{\text{fl}} = \frac{1}{6} = 0.17$ ,  $\frac{3}{6} = 0.50$ , and  $\frac{5}{6} = 0.83$ , respectively. If we instead, as in the experiments described below, allow for a sedimentation time of 3 min before turning on the acoustics, the distribution of the focused particles changes to 58 %, 40 %, and 2 % at  $z/H_{\text{fl}} = \frac{1}{6} = 0.17$ ,  $\frac{3}{6} = 0.50$ , and  $\frac{5}{6} = 0.83$ , respectively.

The acoustophoretic motion of the small 0.1- $\mu\text{m}$ -diameter particles are dominated by the Stokes drag from the streaming field  $\mathbf{v}_2$ , see the left side of Fig. 5(c) and (g) and the videos in the Supplemental Material [50]. The simulation shows that the particles do not settle in fixed positions but follow oblong paths in the vertical plane similar in shape to the large streaming rolls spanning the entire height of the channel with an upwards motion over the electrodes and downwards in between electrodes, see Fig. 5(b) and (f). In D1,  $\mathbf{F}^{\text{rad}}$  is so small that it plays essentially no role. In D2, however,  $\mathbf{F}^{\text{rad}}$  is stronger and superposes with  $\mathbf{F}^{\text{drag}}$  to govern the acoustophoretic motion. This superposition of forces is similar to the analysis presented by Antfolk *et al.* [19], but whereas in their system the nanoparticles spirals towards the point at the center of a single flow roll, the nanoparticles above a single electrode in D2 are focused into the center line of each of the two flow rolls shown in Fig. 5(f). The location of these center lines are defined by the vertical and horizontal nodal lines of  $\mathbf{f}^{\text{rad}}$  represented by the black regions at the electrode gaps  $x/\lambda_{\text{SAW}} = \frac{n}{2}$  and at the stable nodal planes  $z/H_{\text{fl}} = \frac{1}{6}, \frac{5}{6}$ , respectively, in the gray-scale plot of Fig. 5(f) and (g).

Most of these theoretical predictions are validated by experiments. After loading the particle suspension in to the device, it takes about 3 min for the fluid to come to rest, during which time the 1.7- $\mu\text{m}$ -diameter particles

sediment slowly. This partial sedimentation shifts the homogeneous particle distribution downwards, so that the particle distribution is inhomogeneous when the acoustic field is turned on. In the experiments on PDMS-lid device D1, the large 1.7- $\mu\text{m}$ -diameter particles are observed to accumulate at the floor and the ceiling in the regions between the electrodes, and the small 0.1- $\mu\text{m}$ -diameter particles are observed to circulate in broad streaming rolls. In contrast, in the experiments on the Pyrex-lid device D2, the large particle are seen to accumulate above the center of the electrodes near two planes, 36 % of them at  $z = (15 \pm 5) \mu\text{m} = (0.3 \pm 0.1)H_{\text{fl}}$  and 64 % of them at  $z = (30 \pm 5) \mu\text{m} = (0.6 \pm 0.1)H_{\text{fl}}$ . Here, the uncertainty is estimated from the optical focal depth in the setup. These numbers are in fair agreement with the simulation results mentioned above and shown in Fig. 5(g) (purple numbers). Finally, the observed acoustophoretic focusing time of 0.1 s matches the theoretical predictions.

## VI. RESULTS OF THE 3D MODELING

In this section we address the more realistic, but also more cumbersome simulations in 3D for the Pyrex-lid device D2. Even given our access to the High Performance Computing clusters at the DTU Computing Center (HPC-DTU) [53], we cannot simulate the entire chip shown in Fig. 1(a). Whereas we keep the correct dimensions in the height, we scale down the width and length to both be around 1 mm. The 3D model geometry is shown in Fig. 6 with the detailed parameter values listed in Table III. In this reduced geometry, the IDT contains only 4 electrode pairs and no Bragg reflectors. Although the model is down-sized in two of the three dimensions, it still contains all the main components of a acoustofluidic SAW device: A first step, in which the piezo-electric device, the IDT electrodes, the elastic lid, and the microchannel with the fluid and its viscous boundary layer, are combined in the calculation of the electrically induced acoustic fields. A second step, in which the acoustic radiation force and the acoustic streaming velocity are computed, and used in the governing equation predict the acoustophoretic motion of suspended spherical particles.

### A. The acoustic fields and radiation force

The 3D model shown in Fig. 6 contains 4.6 million degrees of freedom. The calculation was distributed across 80 nodes on the HPC-DTU cluster and took 14 hours to compute. The first result is that the computed pressure and displacement fields  $p_1$  and  $\mathbf{u}$  in 3D are both qualitatively and quantitatively similar to the ones computed in the 2D model. For vertical slice planes parallel to the  $x$ - $z$  plane and place near the center of the IDT at  $y = \frac{1}{2}L_{\text{sl}}$ , the agreement is of course better than for those near the edge of the IDT near  $y = \frac{1}{2}(L_{\text{sl}} \pm L_{\text{el}})$ , but in all cases we find the period-3 structure of  $|p_1|$  along the  $z$  direction



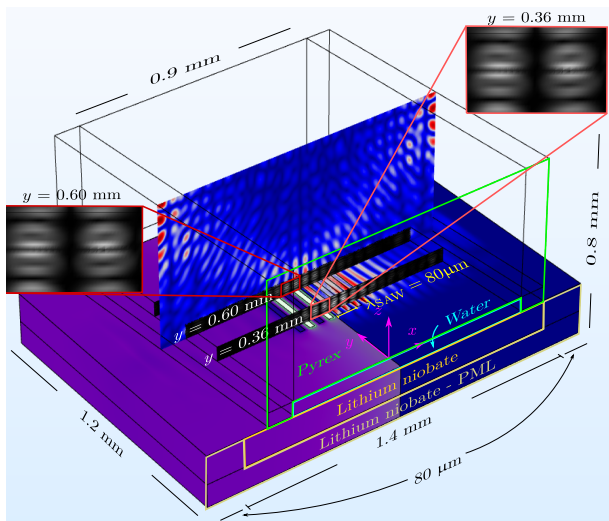


FIG. 6. A 4.4 MDOF simulation of a mm-sized Pyrex-lid device D2 in 3D actuated at  $f_{\text{SAW}} = 50$  MHz. A surface plot of the electric potential  $V$  [from  $-4.35$  (purple) to  $4.35$  V (light cyan), rescaled from  $V_0 = 1$  V] in the piezoelectric substrate, combined with a slice plot at  $y = \frac{1}{2}L_{\text{sl}}$  of the acoustic pressure magnitude  $|p_1|$  [from 0 (black) to  $566$  kPa (yellow)] in the channel and the magnitude of the displacement  $|u|$  [from 0 (blue) to  $0.05$  nm (red)] in the surrounding Pyrex.

seen in Fig. 4(b). Likewise, for the acoustic radiation force density, we recover the period-3 structure in  $|f^{\text{rad}}|$  seen in Fig. 5(f) and for the particle focusing points in Fig. 5(g). The experimental observation of this vertical focusing is thus validating this point in our 3D model.

### B. The acoustic streaming rolls

The streaming-dominated, in-plane acoustophoretic motion of  $0.75\text{-}\mu\text{m}$ -diameter particles suspended in the device is used in Fig. 7 to compare our model predictions to observed particle motion. As shown in Fig. 7(a), the experimentally observed particle motion in Pyrex-lid device D2 at the edges of the IDT electrodes is dominated by streaming rolls in the horizontal  $x$ - $y$  plane. We compare this motion with the streaming velocity field  $\mathbf{v}_2$  calculated using the 3D model and shown in Fig. 7(b). Although the model only includes a mm-sized sub-region of the experimental device, the same streaming pattern is evident in both the model device and in the experimental device. The agreement in terms of direction, position, and magnitude is good, albeit with small differences. In both the simulation and in the experiment, the centers of the streaming rolls are located at the edges of the electrodes, with clockwise-circulating flows. Similar to the 2D streaming pattern in Fig. 5, the observed horizontal streaming rolls are a combination of a recirculating flow and an energy flux density, here perpendicular to and away from the IDT array. The streaming velocity in D2

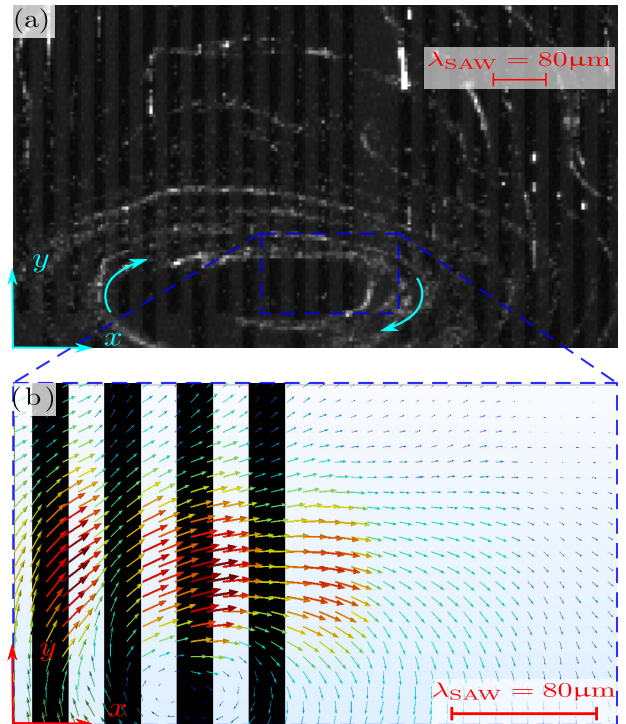


FIG. 7. Acoustic streaming in the horizontal  $x$ - $y$  plane of Pyrex-lid device D2. (a) Experimental top view of device D2 containing suspended  $0.75\text{-}\mu\text{m}$ -diameter polystyrene particles (white), actuated at  $50$  MHz with  $V_0 = 4.35$  V. Arrows (cyan) indicate the flow direction, and the blue dashed rectangle indicates the area shown in (b). (b) Colored arrow plot of the simulated streaming velocity field  $\mathbf{v}_2$  [from 0 (blue) to  $66\text{ }\mu\text{m/s}$  (red)] in the 3D model actuated as in panel (a). The black stripes represent the electrodes.

near the right edge of the blue rectangular region shown in Fig. 7(a) and (b) is measured in the 24-electrode-pair device to be  $\sim 200\text{ }\mu\text{m/s}$  and in the simulated 4-electrode-pair device to be  $\sim 20\text{ }\mu\text{m/s}$ , or  $\sim 120\text{ }\mu\text{m/s}$  if multiplied by the ratio of the number of electrode pairs,  $24/4$ .

## VII. DISCUSSION

By comparing our model simulations to measurable quantities, we find that the model can predict the overall electrical and acoustophoretic behavior of the two types of SAW-devices D1 (PDMS lid) and D2 (Pyrex lid) fairly well. For the electrical response of the device we see a good agreement between the trends near resonance of the predicted and measured values of the electrical impedance, although the predicted values are obtained in an ideal 2D model neglecting stray impedances. The predicted acoustophoretic focusing of the  $1.7\text{-}\mu\text{m}$ -diameter polystyrene particles at the ceiling and floor above the edges of the electrodes in D1, and at  $1/6$  and  $3/6$  of the channel height above the center of the electrodes in D2, agrees well with experimental observations.



An interesting feature of the model is the three half-wave resonance excited vertically in the Pyrex-lid device D2. It highlights the importance of careful consideration of the material selection for acoustofluidic devices, to fit with the desired purpose of the device. Because a PDMS lid is an acoustically soft material with an acoustic impedance  $Z^{\text{ac}}$  similar to that of water ( $Z_{\text{PDMS}}^{\text{ac}} = 1.19 \text{ MRayl}$ ,  $Z_{\text{H}_2\text{O}}^{\text{ac}} = 1.49 \text{ MRayl}$ ), most of the energy in an acoustic wave in water impinging on the water-PDMS interface is transmitted into the PDMS, where it dissipates into heat. Only a small fraction of the energy is reflected back into the fluid. As illustrated in Fig. 4, by replacing the PDMS lid of the device in Ref. [23] with an acoustically hard ( $Z_{\text{Py}}^{\text{ac}} = 12.47 \text{ MRayl}$ ) Pyrex lid, 78.6% of the wave energy is theoretically reflected back into the fluid domain at the channel lid, compared to the 10.9% in a PDMS lid. The resonance build-up in the microchannel is further enhanced, as the height of the channel sustains three half-waves at the resonant frequency of the IDT,  $f_{\text{res}} = \frac{c_{\text{SAW}}}{\lambda_{\text{SAW}}} = \frac{c_{\text{fl}}}{3\lambda_{\text{Wa}}}$ . This resonance behavior is very similar to the integer-half-wave resonances common in BAW devices, whereas the beneficial energy localization at the surface of the SAW is still retained. Thus, the energy loss and heat generation occurring in the piezoelectric substrate in BAW devices is mitigated in this device whereas strong microchannel resonances can be achieved, when using a Pyrex lid in an IDT-inside SAW design. Considering this the terms 'BAW' and 'SAW' seem inadequate when describing acoustofluidic devices, as the actuation scheme of the piezo-electric transducer alone does not suffice to describe the resonance behavior of a device. A more descriptive feature of a device is the nature of the wave field in the fluid, because we show the main factor determining acoustophoresis in the SAW is the difference between traveling and standing wave fields in the fluid.

In acoustofluidic focusing devices, a strong streaming flow is often detrimental to the desired application, as they tend to counteract the radiation force by pulling small particles away from the nodes. In the Pyrex-lid device, however, the vertical part of the streaming enhances particle focusing, as it pulls particles from areas with weak radiation force into the lower node of the acoustic radiation force, increasing the focusing efficiency.

### VIII. CONCLUSION

We have presented a 3D model, and implemented it in the finite-element software COMSOL Multiphysics, for numerical simulation of SAW-devices taking into account the piezo-electric substrate, the IDT metal electrodes, the elastic solid defining the microchannel, the water in the microchannel as the viscous boundary layer of the water. With such simulations, we are able to decrease the gap between the systems that we can model and those used in actual experiments. This work thus brings us closer to the point, where numerical simulation can guide

rational design of acoustofluidic devices.

To push acoustofluidic devices closer to medical application, the development of novel device designs beyond the proof-of-concept stage is vital. We have presented a close-to-scale numeric model of an acoustofluidic SAW device by expanding on previous model experiences [32, 36] and the recently developed effective-boundary-layer theory [43]. With this we have captured the inner workings of a non-trivial device. The model includes the linear elasticity of the defining material, the scalar pressure field of the microchannel fluid and the piezoelectricity of the lithium niobate substrate.

Using the numeric model, we illustrate the impact that the material selection in acoustofluidic chips has on acoustophoretic performance. Based on the numerically predicted acoustic fields, we propose design improvements over the previous design [23], consisting primarily of substituting the original PMDS lid with a Pyrex lid. According to our model, the new lid leads to higher energy densities and more uniform particle focusing. This causes the chip to build up strong resonances in a standing wave field, similar to those in a BAW device. Furthermore, we have used our model to predict the electrical response of the a 2D model of the system, the acoustophoretic focusing of particles suspended over the IDT area of the device, and the streaming motion within devices. For each of these comparison parameters we have found an agreement between predictions and experiments.

Despite our focus on a specific device design in this manuscript, the model can handle a much wider class of acoustofluidic devices. We have developed a model that can be reshaped to simulate any BAW or SAW device design of well-characterized piezoelectric transducers, Newtonian fluids, and isotropic and anisotropic linear solids.

In future work it would be prudent to improve the model accuracy by including the temperature field to account for the thermal dependence of material parameters, particularly the fluid bulk and dynamic viscosities. To implement the temperature field one must account for the various sources of thermal generation in terms of mechanical losses and viscous dissipation described in [54], which requires a good knowledge of the damping properties of each component of the device.

### IX. ACKNOWLEDGEMENTS

This work is partially supported by NSF CBET-1605574, NSF CBET-1804963, and NIH PSOC-1U54CA210184-01. The device fabrication is performed in part at the Cornell Nanoscale Facility (CNF), which is supported by the National Science Foundation (Grant ECCS-1542081).

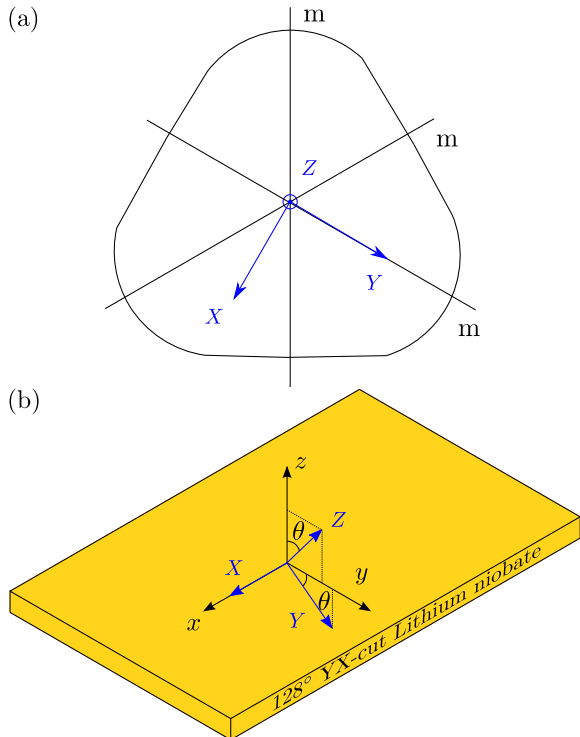


FIG. 8. (a) Top-view sketch of the material coordinate system  $X, Y, Z$  in mono-crystalline, hexagonal lithium niobate with three mirror planes  $m$ . (b)  $128^\circ$  YX-cut lithium niobate chip showing the global coordinate system  $x, y, z$  rotated counter-clockwise  $\theta = 128^\circ - 90^\circ = 38^\circ$  around the  $X$ -axis relative to the material coordinate system  $X, Y, Z$ .

### Appendix A: Bond and rotation matrices

The elasticity, coupling and permittivity properties of mono-crystalline lithium niobate are listed in Ref. [38] for a Cartesian material coordinate system  $X, Y, Z$  defined as shown in Fig. 8(a). The  $Z$ -axis is oriented in the growth direction, the  $X$ -axis is the normal to one of the three mirror planes, and the  $Y$ -axis follows from the right-hand rule, placing it within the mirror plane the  $X$ -axis is normal to. The device in this manuscript, however, is manufactured on a wafer of the more commonly used  $128^\circ$  YX-cut lithium niobate. These are wafers of lithium niobate cut from a single crystal so that the positive surface normal forms a  $128^\circ$  angle with the material  $Y$ -axis. In our model, we define a coordinate system  $x, y, z$  with the  $x$ -axis coinciding with the material  $X$ -axis, the  $z$ -axis normal to the wafer surface and the  $y$ -axis determined by the right-hand rule. This global coordinate system coincides with the material coordinate system rotated an angle  $\theta = 128^\circ - 90^\circ = 38^\circ$  counter-clockwise around the  $X$ -axis, as shown in Fig. 8(b).

In the following, we define the matrix operations necessary to determine the material parameters in the global system  $x, y, z$  from the values known in  $X, Y, Z$ .

In the usual Cartesian notation exists a matrix  $\mathbf{R}$  transforming a  $3 \times 1$  vector  $\mathbf{P}^{\text{mt}}$  expressed in material coordinates  $X, Y, Z$  to the vector  $\mathbf{P}^{\text{gl}}$  expressed in terms of a global coordinate system  $x, y, z$ .

$$\mathbf{P}^{\text{gl}} = \mathbf{R}\mathbf{P}^{\text{mt}}, \quad (\text{A1})$$

whereas  $3 \times 3$  matrices are transformed as

$$\boldsymbol{\epsilon}_r^{\text{gl}} = \mathbf{R}\boldsymbol{\epsilon}_r^{\text{mt}}\mathbf{R}^{-1}. \quad (\text{A2})$$

For  $6 \times 1$  vectors in Voigt notation similar matrices called Bond matrices  $\mathbf{M}_s$  transform stress vectors  $\boldsymbol{\sigma}_V^{\text{mt}}$  expressed in material coordinates into the same stress in terms of the global coordinate system  $\boldsymbol{\sigma}_V^{\text{gl}}$

$$\boldsymbol{\sigma}_V^{\text{gl}} = \mathbf{M}_s\boldsymbol{\sigma}_V^{\text{mt}}, \quad (\text{A3})$$

and similarly to Eq. (A2)  $6 \times 6$  matrices are transformed as

$$\mathbf{c}_r^{\text{gl}} = \mathbf{M}_s\mathbf{c}_r^{\text{mt}}\mathbf{M}_s^T \quad (\text{A4})$$

It is important to note that Voigt notation stress and strain vectors do not transform alike and two transformation matrices exist in Voigt notation  $\mathbf{M}_\sigma \neq \mathbf{M}_\epsilon$ . Hence, the transformation rules deviate slightly from those in  $3 \times 3$  matrices.

Finally,  $3 \times 6$  matrices such as the coupling tensor,  $\mathbf{e}$  can be transformed using a rotation matrix and Bond matrix.

$$\mathbf{e}_r^{\text{gl}} = \mathbf{R}\mathbf{e}_r^{\text{mt}}\mathbf{M}_\sigma^T \quad (\text{A5})$$

Mathematically, a positive rotation  $\theta$  degrees about the material  $X$ -axis is obtained by the rotation  $\mathbf{R}_x(\theta)$  and Bond  $\mathbf{M}_{\sigma,x}(\theta)$  matrices

$$\mathbf{R}_x(\theta) = \begin{pmatrix} 1 & 0 & 0 \\ 0 & \mathcal{C} & \mathcal{S} \\ 0 & -\mathcal{S} & \mathcal{C} \end{pmatrix}, \quad (\text{A6})$$

$$\mathbf{M}_{\sigma,x}(\theta) = \begin{pmatrix} 1 & 0 & 0 & 0 & 0 & 0 \\ 0 & \mathcal{C}^2 & \mathcal{S}^2 & 2\mathcal{C}\mathcal{S} & 0 & 0 \\ 0 & \mathcal{S}^2 & \mathcal{C}^2 & -2\mathcal{C}\mathcal{S} & 0 & 0 \\ 0 & -\mathcal{C}\mathcal{S} & \mathcal{C}\mathcal{S} & \mathcal{C}^2 - \mathcal{S}^2 & 0 & 0 \\ 0 & 0 & 0 & 0 & \mathcal{C} & \mathcal{S} \\ 0 & 0 & 0 & 0 & -\mathcal{S} & \mathcal{C} \end{pmatrix}, \quad (\text{A7})$$

using  $\mathcal{C}$  and  $\mathcal{S}$  as shorthand for  $\cos(\theta)$  and  $\sin(\theta)$  respectively.

- 
- [1] K. Sritharan, C. Strobl, M. Schneider, A. Wixforth, and Z. Guttenberg, Acoustic mixing at low reynold's numbers, *Appl Phys Lett* **88**, 054102 (2006).
- [2] J. Shi, X. Mao, D. Ahmed, A. Colletti, and T. J. Huang, Focusing microparticles in a microfluidic channel with standing surface acoustic waves (SSAW), *Lab Chip* **8**, 221 (2008).
- [3] T. Franke, A. R. Abate, D. A. Weitz, and A. Wixforth, Surface acoustic wave (SAW) directed droplet flow in microfluidics for pdms devices, *Lab Chip* **9**, 2625 (2009).
- [4] M. K. Tan, R. Tjeung, H. Ervin, L. Y. Yeo, and J. Friend, Double aperture focusing transducer for controlling microparticle motions in trapezoidal microchannels with surface acoustic waves, *Appl Phys Lett* **95**, 134101 (2009).
- [5] J. Shi, H. Huang, Z. Stratton, Y. Huang, and T. J. Huang, Continuous particle separation in a microfluidic channel via standing surface acoustic waves (SSAW), *Lab Chip* **9**, 3354 (2009).
- [6] X. Ding, S.-C. S. Lin, B. Kiraly, H. Yue, S. Li, I.-K. Chiang, J. Shi, S. J. Benkovic, and T. J. Huang, On-chip manipulation of single microparticles, cells, and organisms using surface acoustic waves, *PNAS* **109**, 11105 (2012).
- [7] S. B. Q. Tran, P. Marmottant, and P. Thibault, Fast acoustic tweezers for the two-dimensional manipulation of individual particles in microfluidic channels, *Appl. Phys. Lett.* **101**, 114103 (2012).
- [8] J. Shi, D. Ahmed, X. Mao, S.-C. S. Lin, A. Lawit, and T. J. Huang, Acoustic tweezers: patterning cells and microparticles using standing surface acoustic waves (SSAW), *Lab Chip* **9**, 2890 (2009).
- [9] D. J. Collins, C. Devendran, Z. Ma, J. W. Ng, A. Neild, and Y. Ai, Acoustic tweezers via sub-time-of-flight regime surface acoustic waves, *Science Advances* **2**, e1600089 (2016).
- [10] A. Riaud, M. Baudoin, O. Bou Matar, L. Becerra, and J.-L. Thomas, Selective manipulation of microscopic particles with precursor swirling rayleigh waves, *Phys. Rev. Applied* **7**, 024007 (2017).
- [11] D. J. Collins, B. Morahan, J. Garcia-Bustos, C. Doerig, M. Plebanski, and A. Neild, Two-dimensional single-cell patterning with one cell per well driven by surface acoustic waves, *Nat. Commun.* **6**, 8686 (2015).
- [12] D. J. Collins, R. O'Rorke, C. Devendran, Z. Ma, J. Han, A. Neild, and Y. Ai, Self-aligned acoustofluidic particle focusing and patterning in microfluidic channels from channel-based acoustic waveguides, *Phys. Rev. Lett.* **120**, 074502 (2018).
- [13] W. Zhou, J. Wang, K. Wang, B. Huang, L. Niu, F. Li, F. Cai, Y. Chen, X. Liu, X. Zhang, H. Cheng, L. Kang, L. Meng, and H. Zheng, Ultrasound neuro-modulation chip: activation of sensory neurons in caenorhabditis elegans by surface acoustic waves, *Lab Chip* **17**, 1725 (2017).
- [14] J. Zhang, S. Yang, C. Chen, J. H. Hartman, P.-H. Huang, L. Wang, Z. Tian, P. Zhang, D. Faulkenberry, J. N. Meyer, and T. J. Huang, Surface acoustic waves enable rotational manipulation of caenorhabditis elegans, *Lab Chip* **19**, 984 (2019).
- [15] X. Ding, S.-C. S. Lin, M. I. Lapsley, S. Li, X. Guo, C. Y. Chan, I.-K. Chiang, L. Wang, J. P. McCoy, and T. J. Huang, Standing surface acoustic wave (ssaw) based multichannel cell sorting, *Lab Chip* **12**, 4228 (2012).
- [16] A. Riaud, J.-L. Thomas, E. Charron, A. Bussonnière, O. Bou Matar, and M. Baudoin, Anisotropic swirling surface acoustic waves from inverse filtering for on-chip generation of acoustic vortices, *Phys. Rev. Applied* **4**, 034004 (2015).
- [17] D. J. Collins, A. Neild, and Y. Ai, Highly focused high-frequency travelling surface acoustic waves (saw) for rapid single-particle sorting, *Lab Chip* **16**, 471 (2016).
- [18] A. Liga, A. D. B. Vliegenthart, W. Oosthuyzen, J. W. Dear, and M. Kersaudy-Kerhoas, Exosome isolation: a microfluidic road-map, *Lab Chip* **15**, 2388 (2015).
- [19] M. Antfolk, P. B. Muller, P. Augustsson, H. Bruus, and T. Laurell, Focusing of sub-micrometer particles and bacteria enabled by two-dimensional acoustophoresis, *Lab Chip* **14**, 2791 (2014).
- [20] Z. Mao, P. Li, M. Wu, H. Bachman, N. Mesyngier, X. Guo, S. Liu, F. Costanzo, and T. J. Huang, Enriching nanoparticles via acoustofluidics, *ACS Nano* **11**, 603 (2017).
- [21] B. Hammarström, T. Laurell, and J. Nilsson, Seed particle enabled acoustic trapping of bacteria and nanoparticles in continuous flow systems, *Lab Chip* **12**, 4296 (2012).
- [22] D. J. Collins, Z. Ma, J. Han, and Y. Ai, Continuous micro-vortex-based nanoparticle manipulation via focused surface acoustic waves, *Lab Chip* **17**, 91 (2017).
- [23] P. Sehgal and B. J. Kirby, Separation of 300 and 100 nm particles in fabry-perot acoustofluidic resonators, *Anal. Chem.* **89**, 12192 (2017).
- [24] M. Wu, Z. Mao, K. Chen, H. Bachman, Y. Chen, J. Rufo, L. Ren, P. Li, L. Wang, and T. J. Huang, Acoustic separation of nanoparticles in continuous flow, *Advanced Functional Materials* **27**, 1606039 (2017).
- [25] L. Johansson, J. Enlund, S. Johansson, I. Katardjiev, and V. Yantchev, Surface acoustic wave induced particle manipulation in a pdms channel – principle concepts for continuous flow applications, *Biomed Microdevices* **14**, 279 (2012).
- [26] F. Garofalo, T. Laurell, and H. Bruus, Performance Study of Acoustophoretic Microfluidic Silicon-Glass Devices by Characterization of Material- and Geometry-Dependent Frequency Spectra, *Phys. Rev. Applied* **7**, 054026 (2017).
- [27] A. N. Darinskii, M. Weihnacht, and H. Schmidt, Computation of the pressure field generated by surface acoustic waves in microchannels, *Lab Chip* **16**, 2701 (2016).
- [28] M. K. Tan, J. R. Friend, O. K. Matar, and L. Y. Yeo, Capillary wave motion excited by high frequency surface acoustic waves, *Phys Fluids* **97**, 234106 (2010).
- [29] D. Köster, Numerical simulation of acoustic streaming on surface acoustic wave-driven biochips, *SIAM J. Sci. Comput.* **29**, 2352 (2007).
- [30] H. Zhang, Z. Tang, Z. Wang, S. Pan, Z. Han, C. Sun, M. Zhang, X. Duan, and W. Pang, Acoustic streaming and microparticle enrichment within a microliter droplet using a lamb-wave resonator array, *Phys Rev. Applied* **9**, 064011 (2018).
- [31] J. Lei, P. Glynne-Jones, and M. Hill, Acoustic streaming

- in the transducer plane in ultrasonic particle manipulation devices, *Lab Chip* **13**, 2133 (2013).
- [32] M. W. H. Ley and H. Bruus, Three-dimensional numerical modeling of acoustic trapping in glass capillaries, *Phys. Rev. Applied* **8**, 024020 (2017).
- [33] N. Nama, R. Barnkob, Z. Mao, C. J. Kähler, F. Costanzo, and T. J. Huang, Numerical study of acoustophoretic motion of particles in a pdms microchannel driven by surface acoustic waves, *Lab Chip* **15**, 2700 (2015).
- [34] J. Vanneste and O. Bühler, Streaming by leaky surface acoustic waves, *Proc. R. Soc. A* **467**, 1779 (2011).
- [35] N. R. Skov and H. Bruus, Modeling of Microdevices for SAW-Based Acoustophoresis - A Study of Boundary Conditions, *Micromachines* **7**, 182 (2016).
- [36] N. R. Skov, J. S. Bach, B. G. Winkelmann, and H. Bruus, 3D modeling of acoustofluidics in a liquid-filled cavity including streaming, viscous boundary layers, surrounding solids, and a piezoelectric transducer, *AIMS Mathematics* **4**, 99 (2019).
- [37] B. A. Auld, *Acoustic fields and waves in solids, Vol. 1* (R.E. Krieger, 1990).
- [38] R. Weis and T. Gaylord, Lithium niobate: summary of physical properties and crystal structure, *Applied Physics A* **37**, 191 (1985).
- [39] R. H. D. Narottam P. Bansal, N. P. Bansal, *Handbook of Glass Properties* (Elsevier LTD, 1986).
- [40] E. L. Madsen, Ultrasonic shear wave properties of soft tissues and tissuelike materials, *The Journal of the Acoustical Society of America* **74**, 1346 (1983).
- [41] K. Zell, J. I. Sperl, M. W. Vogel, R. Niessner, and C. Haisch, Acoustical properties of selected tissue phantom materials for ultrasound imaging, *Phys Med Biol* **52**, N475 (2007).
- [42] *Material Property Database*, MIT, 77 Massachusetts Avenue, Cambridge, MA, USA, <http://www.mit.edu/~6.777/matprops/pdms.htm>, accessed 21 August 2018.
- [43] J. S. Bach and H. Bruus, Theory of pressure acoustics with viscous boundary layers and streaming in curved elastic cavities, *J. Acoust. Soc. Am.* **144**, 766 (2018).
- [44] P. B. Muller and H. Bruus, Numerical study of thermoviscous effects in ultrasound-induced acoustic streaming in microchannels, *Phys. Rev. E* **90**, 043016 (2014).
- [45] M. Settne and H. Bruus, Forces acting on a small particle in an acoustical field in a viscous fluid, *Phys. Rev. E* **85**, 016327 (2012).
- [46] H. Bruus, Acoustofluidics 1: Governing equations in microfluidics, *Lab Chip* **11**, 3742 (2011).
- [47] J. T. Karlsen and H. Bruus, Forces acting on a small particle in an acoustical field in a thermoviscous fluid, *Phys. Rev. E* **92**, 043010 (2015).
- [48] COMSOL Multiphysics 5.3a, <http://www.comsol.com> (2017).
- [49] P. B. Muller and H. Bruus, Theoretical study of time-dependent, ultrasound-induced acoustic streaming in microchannels, *Phys. Rev. E* **92**, 063018 (2015).
- [50] The Supplemental Material at [URL] contains four animations of the numerically simulated acoustophoresis of 0.1- and 1.7- $\mu\text{m}$ -diameter particles in device D1 and D2, respectively, corresponding to Fig. 5(c) and (g).
- [51] C. Eckart, Vortices and streams caused by sound waves, *Phys. Rev.* **73**, 68 (1948).
- [52] P. B. Muller, R. Barnkob, M. J. H. Jensen, and H. Bruus, A numerical study of microparticle acoustophoresis driven by acoustic radiation forces and streaming-induced drag forces, *Lab Chip* **12**, 4617 (2012).
- [53] High Performance Computing, Technical University of Denmark, <https://www.hpc.dtu.dk/> (2019).
- [54] P. Hahn and J. Dual, A numerically efficient damping model for acoustic resonances in microfluidic cavities, *Physics of Fluids* **27**, 062005 (2015).

## Chapter 7

# A wall-free multiwell system

In this chapter we introduce an ongoing numerical and experimental research project carried out in collaboration with Postdoc Björn Hammarström from KTH Stockholm, who conducts the experimental part of the work. We use the numeric model developed over the last few chapters to create a new device design for biological studies, and verify its predictions experimentally. Unlike Chapters 5 and 6 we do not add new functionalities to the numeric model in this chapter, but merely reshape it in search of new device designs. Enclosed in full in the appendix is an abstract submitted for the Acoustofluidics 2019 conference presenting the state of this research project by this thesis's submission.

### 7.1 Motivation

Biological cell-cell studies are often performed on an average basis, although the study of individual cells can provide valuable insight for instance regarding immunology studies [137]. At KTH Stockholm the  $10 \times 10$  multi-well chip defined in Ref. [41] has been used extensively in biological studies [138, 139, 140]. The configuration of this chip allows for studying 100 simultaneous cell-cell interactions, but its closed nature hamper loading and unloading of cells and cell media. Additionally the static wells are defined in silicon and must be deep reactive-ion etched in a clean room. To supplement the studies performed by this chip we create a new design that can dynamically alter its focusing and is open for flow-through.

A device meeting some of these demands was presented by Neild *et al.*[141] in a silicon-glass-piezo device which had two strip electrodes on the piezo that could be turned on independently of each other giving two distinct particle patterns. However, in their paper they do not discuss if additional modes can be excited or whether the resonance is caused by the piezoelectric substrate or the fluid cavity dimensions.

The device by Lilliehorn *et al.*[142] also showed potential in dynamic focusing as various focusing patterns could be achieved by changing the frequency, which they attributed to a near field effect between particles. We have, however, found that the particle patterns they observed is attributed to the piezoelectric ceramic's motion directly transferring to the fluid. Based on this insight, we study the motion of free, unloaded piezoelectric transducers of various designs that can all be achieved through micro-milling a standard slab.

### 7.1.1 Array patterns in piezoelectric transducers

We study the of motion piezoelectric transducers of various designs that can all be achieved using a standard slab of Pz26 and a micromiller. We discovered that a piezoelectric transducer with a regular planar configuration of electrodes on the top and bottom give rise to a number of resonance modes in close proximity in the frequency domain akin to the Chladni figures observed by Hooke over three centuries ago in elastic plates. Typically, the patterns reflect the structure defining them similar to the wave-guides shown by Bian *et al.*[45]. For rectangular plates we find a number of modes having a diamond pattern similar to the desired arrays of the multi-well.

We find that by removing part of the electrode similar to Neild *et al.*[141], these patterns can be altered and in some cases even localized on the surface opposite the removal. Through trial-and-error we discover that a design featuring a quadratic protrusion leads to particularly useful focusing patterns, which we show in Section 7.3.2.

Lei [143] carried out an analysis of the acoustophoretic motion of particles suspended in a fluid in direct contact with a Chladni-disk that bears some similarities to this work. However, his work involved a linearly elastic material and used analytical Bessel functions to model the displacement of the disk, while we use a piezoelectric material and model the piezoelectric element completely.

## 7.2 Model system

The device shown in Fig. 7.1 consists of a  $22 \times 15 \text{ mm}^2$  slab of the piezoelectric ceramic PZ26 poled in the  $z$ -direction with two electrodes initially covering the entirety of each of the  $z$ -facing surfaces.

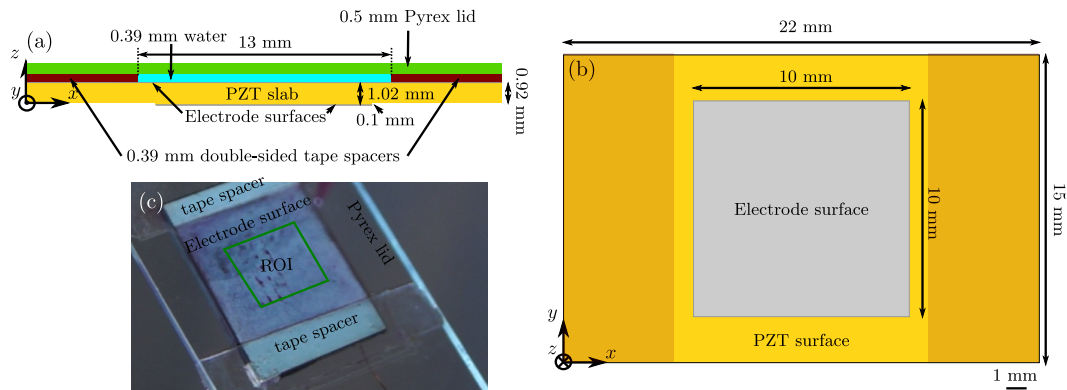


**Figure 7.1:** Physical device and numeric model. (a) Sketch of the devices as seen from one of the open-ended side of the fluid domain. A fluid domain is defined by a Pz26 slab below, double-sided tape on two sides and a microscope slide on top. The Pz26 slab is milled to leave a protrusion of electroded surface on the bottom. (b) The numeric model seen from below. The dark regions show the positions of tape on the top surface. We denote the portion of the top surface directly opposite the electrode the region of interest (ROI). This is the most acoustically active part of the top surface. (c) The physical device being filled with red particles in suspension by pipette. Image courtesy of B. Hammarström.



The majority of the bottom surface is micromilled away to leave a  $10 \times 10 \text{ mm}^2$  electroded surface protruding 0.1 mm from the remaining milled Pz26 surface, while the top surface is left intact. Stacks of double-sided tape are adhered on both ends of the 22 mm-long side to define the side walls of an  $15 \times 13 \times 0.39 \text{ mm}^3$  open-ended channel and a Pyrex glass microscope slide placed on top of the tape defines the upper perimeter of the microchannel. Note that the width and length of the channel are of little consequence as long as it is wider than 10 mm. Fluid is fed to the channel through either of the open ends using a pipette and fills through capillary forces.

The top electrode is grounded while the bottom one is charged and an ac potential of  $V_0$  is applied across the device with a frequency of  $f$  in the range 1.74-1.84 MHz. This is slightly lower than the half-wavelength resonance in the height of the device of  $f_{0,0,1} = 1.91 \text{ MHz}$ , but close enough that a standing half-wave is present in the fluid across all frequencies. Accordingly, the lateral focusing shown in Fig. 7.3 is always combined with a vertical focusing in the middle of the fluid domain.

**Table 7.1:** Dimensions of the final device design.

Domain	Length ( $x$ ) [mm]	Width ( $y$ ) [mm]	Height ( $z$ ) [mm]
Pz26 slab	22	15	0.92
Pz26 protrusion	10	10	0.1
Electrode top surface	22	15	0.001
Electrode bottom protrusion	10	10	0.001
Fluid domain	13	15	0.39
Tape spacers	2	15	0.39
Pyrex lid	75	26	0.5

### 7.2.1 Full numeric model

We set up a full one-to-one numeric model containing each of the elements of the actual device. In want of its exact material parameters the acrylic double-sided tape is modeled as polymethyl-methacrylate (PMMA). The device contains a PML layer in the fluid at the open ends of the channel and in the Pyrex lid beyond the glue tape pieces. The numeric model consists of roughly 1.6 million degrees of freedom, so finding resonance peaks is a quite cumbersome process a single frequency calculation takes 48 minutes.

### 7.2.2 Reduced model

Based on the results shown in Section 7.3.1 we create a reduced model consisting solely of the milled Pz26 slab. The reduced model has only 0.7 million degrees of freedom, which reduces the calculation time for a single frequency to 43 seconds allowing for large calculation sweeps in frequency.

## 7.3 Key results and observations

We here go through the results discovered so far in this research project. We first present a reasoning for using the reduced model rather than the full one in Fig. 7.2. We then present some of

the acoustophoretic predictions and results obtained thus far in Fig. 7.3 and in Fig. 7.4 show that the focusing is largely independent of the cavity dimensions. Lastly, in Fig. 7.5 we investigate whether a similar effect can be observed in the lead-free piezoelectric ceramic aluminum nitride (AlN).

### 7.3.1 Correlation between displacement and radiation potential

In Fig. 7.2 we present the similarity between; (i) the calculated vertical displacement magnitude  $|u_{1,z}|$  for an unloaded Pz26 slab, (ii) ditto for a piezo loaded with water and a Pyrex lid, and (iii) the acoustic radiation potential  $U^{\text{rad}}$  in the vertical center of the fluid domain loaded on a piezo.

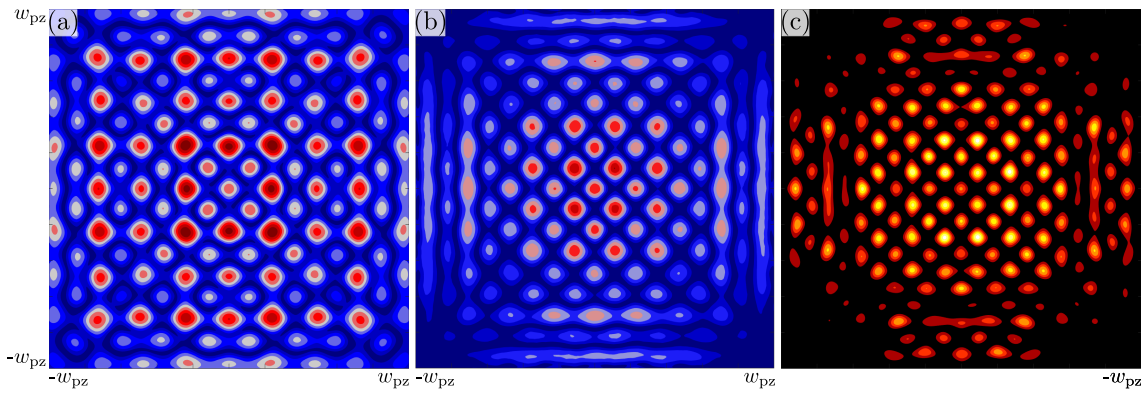


**Figure 7.2:** (a) Color plot of the vertical displacement magnitude  $|u_{1,z}|$  from 0 (blue) to 3.1 nm (red) in a  $15 \times 15 \times 1.02 \text{ mm}^3$  slab of Pz26 with electrodes on the entirety of the top and bottom surfaces, at the resonance frequency  $f = 1.81 \text{ MHz}$  and  $V_0 = 1 \text{ V}$ . (b) As in (a) but where the slab is loaded with a 0.39 mm layer of water and a 0.5 mm layer of Pyrex. The resonance frequency is shifted to  $f = 1.80 \text{ MHz}$ , and the magnitudes are 0 (blue) to 1.6 nm (red). (c) Color plot of the radiation potential  $U^{\text{rad}}$  from 0 (black) to 0.6 fJ (orange) in the fluid layer from (b) in the horizontal plane containing the vertical center  $z/h = \frac{1}{2}$  of the fluid domain. Adapted from [4]

In Fig. 7.2(a) we see that the predicted displacement magnitude field of the free Pz26 slab at this frequency is a pattern of dozens of distinct antinodes. In the inner region spanning  $\sim 80\%$  of the width and length of the surface, the antinodes all have the approximately same displacement magnitude and are spaced by primarily straight nodal lines making a  $45^\circ$  with the edges of the surface.

In Fig. 7.2(b) we see the same pattern in the inner region, albeit with slightly more compact antinodes and unlike in (a) the magnitude of the antinodes decreases with distance from the surface centers. We also note that adding the water and Pyrex domains only shifts the calculated resonance frequency by 0.6% while halving the overall displacement magnitude. The small shift in frequency is important as the modes estimated numerically with the reduced model are still similar to the experimentally found ones.

Similarly, we see that in Fig. 7.2(c) the same pattern appears, but again the antinodes with the largest radiation potential is not observed at the antinodes with the highest displacement magnitude. As particles settle in regions of low potential, however, it is the position of nodes, not the



magnitude of antinodes that is of interest when studying the acoustophoretic behavior of a device.

Accordingly, the good agreement between the antinode positions in Figs. 7.2(a), (b), and (c) show that the possible settling positions of particles in this device design with reasonable certainty can be approximated from the regions of low vertical displacement magnitude of an unloaded Pz26 slab. We thus use the reduced model to estimate acoustophoretic motion in the following.

### 7.3.2 Acoustophoresis comparisons

In Fig. 7.3 we compare experimentally observed particle focusing patterns with normalized vertical displacement magnitudes  $|u_{1,z}|/\max(|u_{1,z}|)$  calculated using the reduced model.

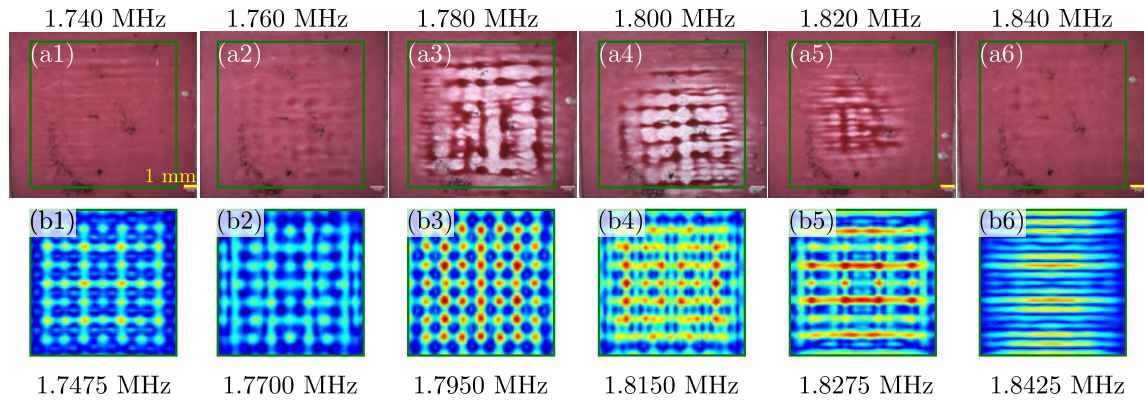


**Figure 7.3:** Particle position observations and predictions. (top row) Images of observed positions of 3- $\mu\text{m}$ -diameter polystyrene beads (red) 180 s after turning ultrasound on in a device with initially homogeneous distributed particles for a series of frequencies  $f_{\text{exp}}$  with fixed voltage  $V_0 = 2.3 V_{\text{pp}}$ . The green outline shows the region of interest, which is the area directly opposite the electrode protrusion on the bottom of the Pz26 slab. (bottom row) Color plots of the calculated normalized vertical displacement magnitude fields  $|u_{1,z}|/\max(|u_{1,z}|)$  from 0 (blue) to 1 (red) at the numerical local maxima  $f_{\text{num}}$  closest in value to the experimentally observed frequencies. The surfaces correspond to the Pz26 surface within the green insets in the top row. From [4].

We see in the top row in Fig. 7.3 that the strongest particle focusing is at  $f_{\text{exp}} = 1.800$  MHz, where the beads agglomerate in clusters that are connected in the  $x$ -direction through thinner bands of particles. Meanwhile, at the adjacent frequency of  $f_{\text{exp}} = 1.780$  MHz the clusters are connected in bands in the  $y$ -direction. At  $f_{\text{exp}} = 1.760$  MHz a weak cluster-and-band focusing can be observed, while the particles form thin lines with no clusters at  $f_{\text{exp}} = 1.820$  MHz.

In the bottom row the blue color shows regions of low magnitude and thus expected agglomeration of particles. At  $f_{\text{num}} = 1.8150$  MHz the blue regions show the same cluster-and-connector structure observed for particles at  $f_{\text{exp}} = 1.800$  MHz. Likewise, the cluster-and-band structure of particles at  $f_{\text{exp}} = 1.780$  MHz is to some degree mirrored by the field of  $f_{\text{num}} = 1.7950$  MHz.

However, as one would expect considering the simplicity of the reduced model there are some discrepancies between the observed particle focusing and the numerical predictions. For instance the line structure of  $f_{\text{exp}} = 1.820$  MHz is more better replicated by the field of  $f_{\text{num}} = 1.8425$  MHz than that at the closest resonance  $f_{\text{num}} = 1.8275$  MHz.

### 7.3.3 Focusing robustness to cavity dimensions

In Fig. 7.4 we show particles focusing under two conditions to illustrate the decoupling between the fluid cavity dimensions and the focusing patterns.

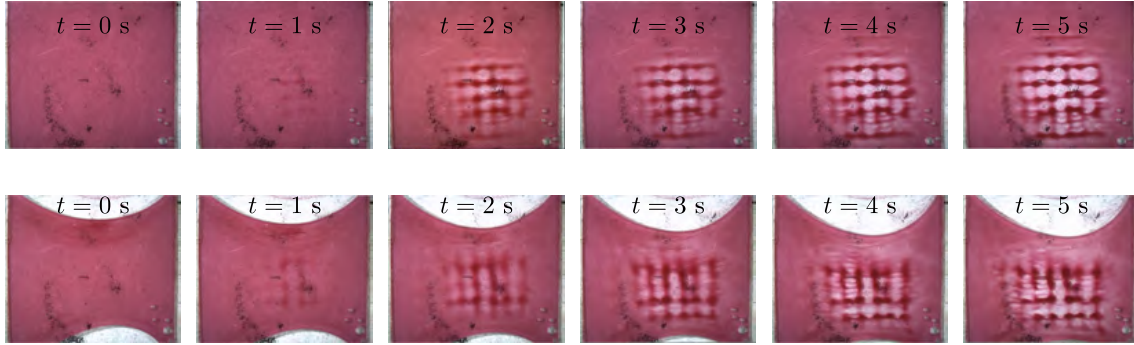


**Figure 7.4:** Time-evolution images of particles focusing at  $f_{\text{exp}} = 1.800$  MHz and  $V_0 = 2.33 V_{\text{pp}}$ . (top row) The particle agglomeration due the first 5 seconds after turning on the ultrasound in a no-flow situation. (bottom row) The particle agglomeration due the first 5 seconds after turning on the ultrasound when part of the liquid in the channel is gradually displaced by air. Images courtesy of B. Hammarström

In the top row of Fig. 7.4 we see that the majority of particles focusing at  $f_{\text{exp}} = 1.800$  MHz in Fig. 7.3 are settled after just  $\sim 5$  s at  $V_0 = 2.33V_{\text{pp}}$ . Note that the presence of bubbles does not affect the pattern as the focusing structures near the bubbles is identical to the structure furthest from the bubbles. This is in stark contrast to the presence of bubbles in classical BAW devices relying on cavity resonances. In such devices air-fluid interfaces and changes in acoustic impedance completely alter the acoustic landscape and cause devices to behave unpredictably.

We further illustrate the robustness of the system with regards to the exact dimensions of the fluid cavity in the bottom row of Fig. 7.4. Here a large portion of the fluid is purposefully displaced by an air meniscus pushed in by a pipette starting when ultrasound as turned on. The focusing patterns here are only affected by the advancing meniscus, due to the flow it induces in the water, and even so the pattern is largely unchanged. This further cements that the focusing is due to the motion of the Pz26 slab, and that only the height of the fluid cavity influences the focusing.

### 7.3.4 Reproducibility in lead-free piezoelectric ceramics

There is an increasing interest in moving away from PZTs in ultrasonics towards lead-free transducers due to the EU directive 2015/863 [144] prohibiting "the use of lead [...] in electrical and electronic equipment placed on the Union market."

A lead-free alternative to PZTs is the piezoelectric material aluminum nitride (AlN). It has the same isotropy in the plane normal to the poling direction, although it is slightly less dense but stiffer and has markedly lower coupling coefficients and far lower dielectric constants. The two will likely interact similarly with water, however, because the specific acoustic impedances of the Pz26 and AlN are very similar, at 15.0 MRayl and 18.9 MRayl respectively.

We do a preliminary study to see if we can reproduce patterns similar to those in Fig. 7.3 in AlN. In Fig. 7.5 we show a comparison between the reduced model described in Section 7.2.2, and a similar one with the PZT replaced by AlN. We choose to study a large band of frequencies, as the fluid domain height can easily be changed in discrete steps, and the eigenmodes shown in Fig. 7.3, may not necessarily be the best ones.

We have chosen to use AlN as a lead-free alternative as it had material parameters that were readily available and because it is an other commonly used transducer material in BAW. Typically it is made in thin films, however. Therefore, we have chosen to study two pieces of AlN with the same surface area as the Pz26 slab; a 3-mm-thick bulk slab of AlN that may not physically be realizable and a 200- $\mu\text{m}$ -thick film pushing the limits of the report maximum film thicknesses. The protrusion heights in the two designs are 100  $\mu\text{m}$  and 10  $\mu\text{m}$ , respectively.

In Fig. 7.3(a) we see that the spectra of the three designs all have many narrow peaks. The position of peaks do not generally coincide, however. The displacement magnitudes in AlN are all an order of magnitude lower for the same applied voltage, but this is easily alleviated by increasing the applied potential.

The strongest modes shown for PZT in Fig. 7.3(b) to (e) and AlN in (f) to (m), are also quite dissimilar. This is due to the patterns being functions of all the material parameters, and their relative magnitudes in AlN is markedly different from that in PZT. To generalize, the modes found for Pz26 have more complex structures, whereas the most powerful modes in AlN are patterns of lines parallel to either the  $x$  or the  $y$  axis. This may yet prove useful, as a superposition of an  $x$ -aligned mode and an  $y$ -aligned mode will give a regular array and alternating the actuation frequency is trivial in most modern function generators.

## 7.4 Concluding remarks

We have presented an on-going project in which we have used our numeric model to create a design for a new device for biological studies through an iterative trial-and-error process. We have tested the design experimentally and found its acoustophoretic properties to be as expected. The computer-aided design process was enabled by the discovery that the vertical displacement magnitude served in a reduced computational model served as a good predictor of the acoustic radiation potential in the full model.

The new device is very easy to make and requires no clean room to fabricate as the only non-assembly process is micromilling a single surface. Additionally, it is made of components that are commonplace in acoustofluidics labs. The device has a high efficiency, and has been used to focus and grow organic tissue at an input power of 80 milliwatts with no external cooling. By comparison the multiwell device we mention is run at decades of watts and requires external cooling. Furthermore, the device has the added advantage of having a focusing that can dynamically be altered by changing the frequency.

The downside of the current stage of device is the contents of lead in the transducer. However, with some clever control of the function generator the PZT transducer may possibly be replaced by aluminum nitride, by combining multiple modes into a single useful pattern. A further study of alternative materials is necessary.

By comparison between the observed particle focusing in the newly designed device and the

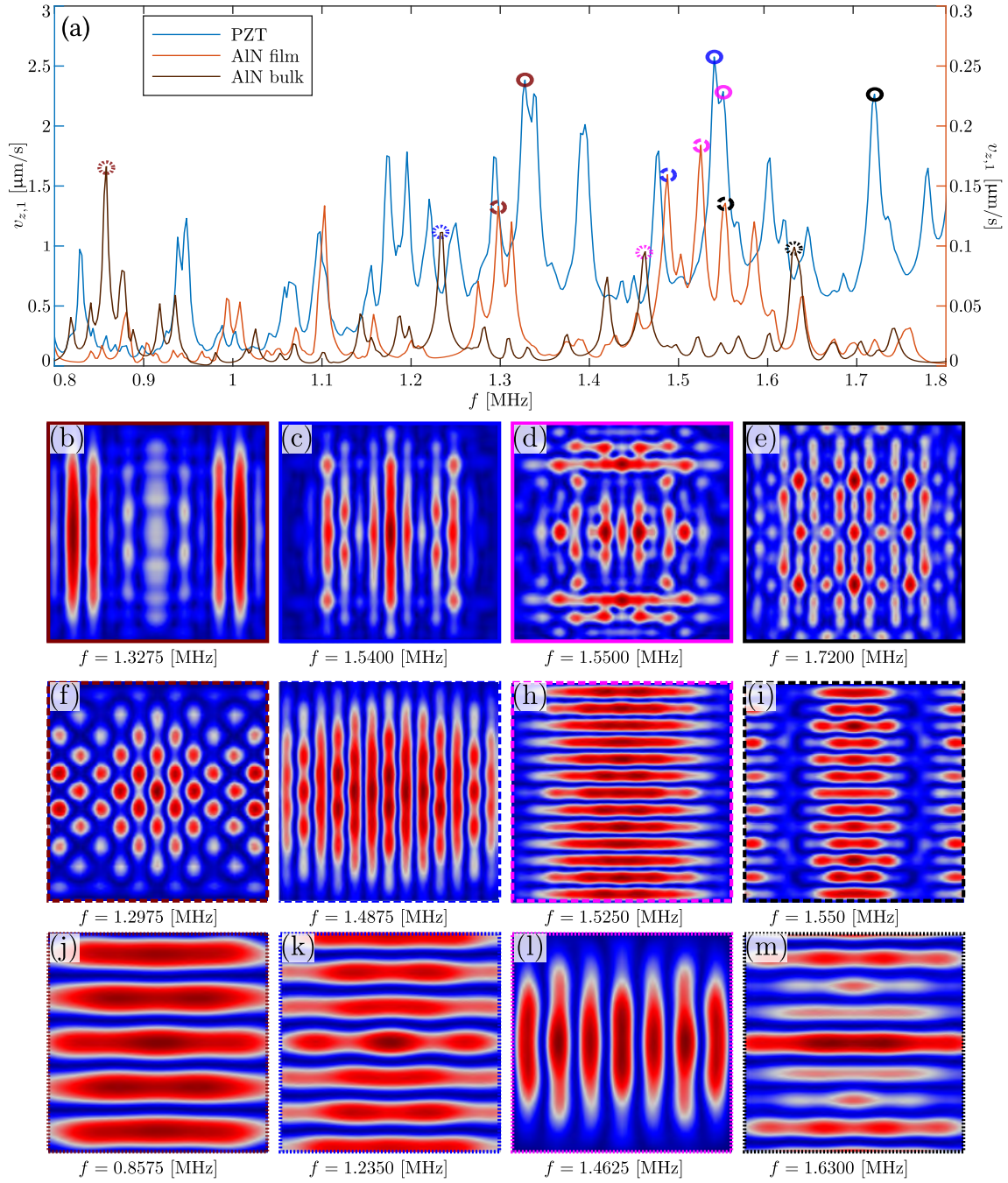


**Figure 7.5:** Lead zirconium titanate and aluminum nitride comparison. (a) Line plots of the average vertical displacement magnitude  $|v_{z,1}|$  of the  $10 \times 10$  region of interest as functions of the actuation frequency,  $f$  for Pz26 and aluminum nitride. The circles show the positions of the color plots of (b) to (i) on the spectra. (b) to (e) Color plots of the normalized vertical displacement magnitude  $|v_{z,1}| / \max(|v_{z,1}|)$  in the region of interest for the four highest peaks in the spectrum of Pz26. (f) to (i) As in (b) to (i) but for a 200  $\mu\text{m}$  aluminum nitride film. (j) to (m) as in (f) to (i) in a 3 mm thick slab of aluminum nitride.

---

qualitative predictions made using the reduced model, particularly for the strongest focusing frequency at  $f_{\text{exp}} = 1.800$  MHz, we have shown the reduced model to be a reasonable predictor of the acoustophoretic performance of the device.





## Chapter 8

# Conclusion and Outlook

We here sum up the work carried out with our numeric model and the most important discoveries made using the model. Finally we provide an outlook describing possible numeric and experimental elements that can be added to the research project described in Chapter 7, and possible future addition to the numeric model.

### 8.1 Conclusion

This thesis serves as an introduction to a versatile numerical model that encompasses the primary aspects involved in acoustophoresis and can be reshaped to represent any isothermal device consisting of a fluid microchannel defined by linear elastic materials and driven by a piezoelectric transducer.

We have described each step of the gradual improvement and outlined the verification of the device through comparison with analytical solutions and experimental data. Most importantly, we used the model to study complex systems where numerics is the only recourse and gained insights into the experimentally 'invisible' acoustic fields of devices.

The four primary research topics of the thesis are; *(i)* A study of the validity of boundary conditions that are widely used in the literature. *(ii)* A full-scale numerical study of a bulk acoustic wave device with emphasis on the atypical acoustophoretic motion of particles within. *(iii)* A near-scale numerical and experimental study of a surface acoustic wave device with the intent to further improve the acoustophoretic capabilities of the device. *(iv)* A numerical and experimental design process resulting in a new device showing promise for biotechnological research.

First, we generate two sets of two-dimensional models of a fluid bounded by a linear elastic to calculate the acoustic first-order fields in an idealized surface acoustic wave device. The models are used to determine whether the hard wall and lossy wall boundary conditions approximate the calculated motion of a borosilicate glass wall and a polydimethylsiloxane rubber wall under such actuation conditions for a number of material thicknesses.

We find that while there are instances where the hard wall condition does give roughly the same acoustic fields in the fluid, neither of the two conditions approximate the wall motion well under any circumstances.

Secondly, we expand on the numeric model to three dimensions while adding more com-

plex materials, a cost-effective means of calculating the fluid acoustic fields and the physics of piezoelectric materials. Using the model we study an acoustofluidic device with a nearly quadratic fluid cavity to verify our numeric model and provide an explanation of the acoustophoretic motion observed within.

In the cavity the degeneration of acoustic modes gives rise to atypical radiation- and streaming-induced motion. Particularly the streaming is of interest as we, surprisingly for its small size, find it to be driven by bulk forces and not by the viscous boundary layer at the edges of the cavity.

Thirdly, we study a promising surface acoustic wave to explain its inner workings and improve upon the design. In this study the numerical model is a scaled-down version of the real device requiring a high performance cluster to compute. Still the model captures the interesting streaming patterns parallel to the piezoelectric substrate.

We find that the device performance can be altered markedly by replacing the polydimethylsiloxane rubber lid with a borosilicate glass one. The higher acoustic impedance in the glass causes the device to act akin to bulk acoustic waves, by building up pressure nodes in the vertical direction and keeping particles levitated in the fluid, while the rubber lid caused particles to stick to the bottom or top of the channel.

Fourthly, we move on to using the numeric model as a design tool to test out a multitude of device designs including a piezoelectric transducer, a fluid microchannel and a borosilicate glass casing. We find that it is not necessary to include the fluid domain and glass lid when modeling this particular device, as the radiation field building up in the fluid can be estimated solely by the displacement field of the piezoelectric transducer's fluid-contacting surface even without including the fluid in the simulations.

The new design functions as numerically predicted at resonance, and shows promise in tissue engineering due to its easy fabrication, inexpensive components, good scalability and dynamic nature.

## 8.2 Outlook

### Temperature field in the numeric model

Regardless of the application areas the most imminent improvement for the numeric model is the implementation of thermal effects induced by losses as described by Hahn and Dual [59]. This is difficult, however, as it requires knowledge of the temperature-dependence of all relevant material parameters. It also adds markedly to the computational cost of a model by adding a temperature field to be solved for in all nodes of the model. Accordingly it should only be implemented when thermal effects are known to be an issue, which has not been the case in the research projects presented in this thesis.

### Chladni-figure motion control

Thus far the experimental localized BAW device of Chapter 7 has primarily been run at a single frequency or swept through a consecutive span of frequencies. Zhou *et al.*[145] described a method of independently controlling single objects resting on a Chladni-plate. They achieve this by characterizing a number of displacement modes in terms of the spatial distribution of induced



motion of particles resting on the plate. Through a feedback loop a piece of software then makes several particles follow predetermined reference paths independent of each other by actuating an appropriate sequence of modes. The modes need not be resonant and so the applied actuation magnitude must be scaled according to the 'transfer function' of the actuation frequency.

A similar cataloging and programming for the modes observed in Chapter 7 could be of interest to create a tool for independently manipulating single cells in a fluid chamber. The focusing of particles in the device is very similar that on a Chladni plate and the method just might be realizable for this very reason. This would require a suitable optical setup, a programmable function generator and an immense amount of work programming and cataloging the modes, but is nonetheless feasible.

Ideally, one would want the largest possible library of modes for the method above to be versatile. For the method described above clearly the accuracy of the method increases with the number of cataloged modes. Wang *et al.* [146] found that by applying a dc bias in addition to an ac potential over a thin plate of PZT the elastic and dielectric properties of the material changes noticeably. By applying this to the device from Chapter 7 the topologies and shapes of the observed modes may change as the shapes are dependent on the relative elasticity to permittivity.

The ideas here can be tested out both numerically and experimentally, but do require quite the amount of both time and effort. If the independent particle can be realized, however, it will be well worth the investment.

### 8.2.1 Capacitive micromachined ultrasonic transducer

Typically the ultrasonic displacements in acoustofluidics are generated by an ac potential applied to a piezoelectric material. While some beneficial motion may be found as in Chapter 7 exact control of piezoelectric transducers can not be obtained.

As an interesting perspective capacitive micromachined ultrasonic transducers (cMUTs) have been emerging since the 1990's, enabled by advances in microfabrication techniques. Rather than the piezoelectric effect cMUTs rely on a the electrostatic force in a capacitor with a thin membrane allowing for deflections. By applying an ac potential across the capacitor the thin membrane vibrates harmonically with the frequency of the potential, similarly to a piezoelectric element.

cMUTs can be collected in arrays of multiple unit cells that can be separately controlled, providing excellent control of the exact motion of the cMUT surface. To my knowledge this this has only been used in a acoustofluidic experiment twice, [147, 148] but may likely prove to replace piezoelectric materials. Implementing of cMUTs in the numeric model along with verification experiments could prove very interesting, particularly for devices with direct contact between the fluid and transducer as in Chapter 7.



## Appendix A

# Abstract submitted for Acoustofluidics 2019

*A wall-free acoustic multi-well system for particle trapping*

**Authors:** N.R. Skov, B. Hammarström, M. Wiklund and H. Bruus.

**Conference:** Acoustofluidics 2019, 26-28 August, Enschede, Netherlands.

# A wall-free acoustic multi-well system for particle trapping

Nils Refstrup Skov<sup>1</sup>, Björn Hammarström<sup>2</sup>, Martin Wiklund<sup>2</sup>, and Henrik Bruus<sup>1</sup>

<sup>1</sup>Department of Physics, Technical University of Denmark, Kongens Lyngby, Denmark  
E-mail: bruus@fysik.dtu.dk, URL: <http://www.fysik.dtu.dk/microfluidics>

<sup>2</sup>Department of Applied Physics, KTH Royal Institute of Technology, Stockholm, Sweden

## Introduction

We study experimentally and numerically a wall-free acoustic multi-well system based on the Chladni-plate-like motion of a piezoelectric lead-zirconium-titanate (PZT) slab. This system is similar to the multi-well systems with acoustic particle levitation used extensively for biological research and in biotechnology for nearly a decade [1,2]. However, the wall-free multi-well system is much simpler to fabricate, and it can be changed dynamically *in situ*, because the multi-well trapping is defined solely by the applied acoustic field and not by solid walls. The idea derives from the particle patterns observed by Lilliehorn *et al.* [3], which they attributed to near-field particle effects, but we can confirm that they instead correlate with the piezoelectric resonance modes of the PZT slab. Our study also bears resemblance to the numerical study of particle handling driven by a classical, clamped, isotropic, elastic Chladni disk by Lei [4], however, we study piezoelectric slabs and how their resonance modes drive particle trapping.

## Device design

The wall-free acoustic multi-well system consists of a PZT slab, on which double-sided tape is attached to define the height and the outer perimeter of the water domain. The water domain is capped by a lid in the form of a standard microscope slide attached to the top-side of the tape. Sketches of the system are shown in Fig. 1. The original dimension of the PZT slab is  $22 \times 15 \times 1.02 \text{ mm}^3$ , and it is covered by metal electrodes on the top and bottom surfaces perpendicular to the polarization axes. On its bottom surface, a protrusion of size  $10 \times 10 \times 0.1 \text{ mm}^3$  is created in the center by milling away the surrounding material to a depth of 0.1 mm. On the top surface of the PZT in the  $x$ - $y$  plane, two parallel pieces of double-sided tape constitute the side walls in the definition of an open-ended microchannel of length  $L = 15 \text{ mm}$  (along  $y$ ), width  $W = 13 \text{ mm}$  (along  $x$ ), and height  $H = 0.39 \text{ mm}$  (the thickness of the tape). A 0.5-mm-thick Pyrex microscope slide is adhered to the tape and forms the lid. Thus, the floor of the microchannel is the electrode surface, its walls are the double-sided tape, and its ceiling is the Pyrex slide. The acoustic trapping of suspended particles in the microchannel is determined by the displacement field at the top surface of the resonating PZT slab pushing directly on the water in a near-field effect, and not by acoustic resonances in the water as in conventional bulk-acoustic-wave devices.

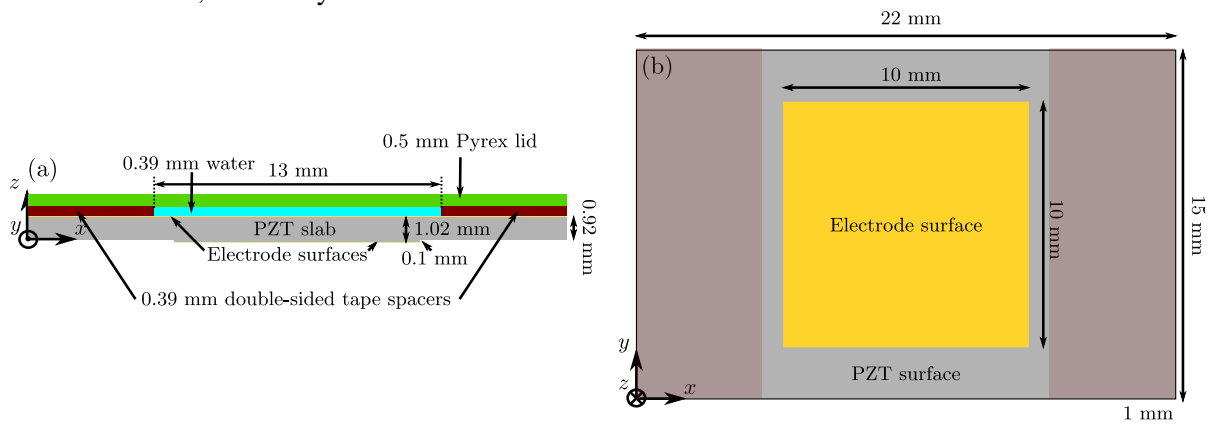


**Figure 1:** Sketches of the device design: (a) Side view with the PZT slab (gray) and its metal electrodes (yellow), the water-filled microchannel (blue), the tape spacer (brown), and the Pyrex lid (green). (b) Bottom view showing the  $10 \times 10 \text{ mm}^2$  electrode (yellow) on the 0.1-mm-high protrusion in the center. The shaded rectangles to the left and right indicate the position of the tape spacers on the top surface. The device consists of inexpensive components commonly found in acoustofluidics laboratories, and it requires no clean room to manufacture. Besides assembling the device, the only fabrication step is to make the protrusion on the bottom-surface of the PZT slab by milling.

## Numerical simulations of the acoustofluidic system in 3D

Using the COMSOL Multiphysics implementation presented in Ref. [5], we set up a three-dimensional numerical model that includes the piezoelectricity of the PZT slab, the solid mechanics of the tape and the glass lid, the acoustics in the water including the viscous boundary layer, and the acoustic potential  $U_{ac}$  in the water for trapping of suspended microparticles. In Fig. 2(a) is shown the vertical component  $u_z^{\text{top}}$  of the displacement at the top surface of an  $15 \times 15 \times 1.02 \text{ mm}^3$  unloaded PZT slab, and similarly in Fig. 2(b), but now for the full

acoustofluidic system consisting of the same slab with water, tape, and lid mounted on top. In Fig. 2(c) is shown  $U_{ac}$  inside the water, a pattern clearly correlated to that of  $u_z^{top}$  in Fig. 2(b). Due to the small added mass and low impedance of water,  $U_{ac}$  even correlates to  $u_z^{top}$  in the unloaded PZT slab of Fig. 2(a). The computational cost reduces significantly going from the full system to the unloaded PZT slab, by going from 1.3 to 0.3 million degrees of freedom, or 78 %. In the following we therefore make qualitative predictions of the acoustic trapping of microparticles from the less costly unloaded-PZT simulations.

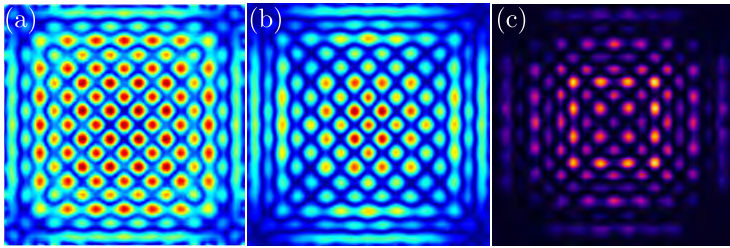


**Figure 2:** Numerical simulations of (a) the vertical displacement field  $u_z^{top}$  (from 0 to 3.1 nm) at the top surface of a free PZT slab at the 1.81-MHz resonance, (b)  $u_z^{top}$  (from 0 to 1.6 nm) in a full acoustofluidic system (slab, water and lid) at the 1.80 MHz resonance, and (c) the acoustic radiation potential  $U_{rad}$  (from 0 to 0.6 fJ) of 3  $\mu\text{m}$  polystyrene beads in the vertical center plane of the fluid domain of the full system driven at 1 V peak-to-peak.

### Experimental and numerical results for microparticle trapping in a wall-free acoustic multi-well

In Fig. 3 top row, the experimentally observed trapping positions of suspended 10- $\mu\text{m}$  polystyrene beads (dark red) are shown at six different resonance modes of the PZT slab. In the bottom row are shown the corresponding numerically simulated displacement patterns at the top surface of the unloaded PZT slab run at resonance frequencies determined from resonance peaks in a series of simulations sweeping from 1.74 to 1.84 MHz in steps of 2.5 kHz. The zero-displacement nodal areas are colored dark blue, and it is expected that suspended particles should agglomerate there. We note a fair agreement between (a3) and (b3), and between (a4) and (b4), and we note that the aggregation lines of (a5) also appear to some extent in (b5). The relative error between corresponding experimental and numerical resonance frequencies is less than 0.8 %.

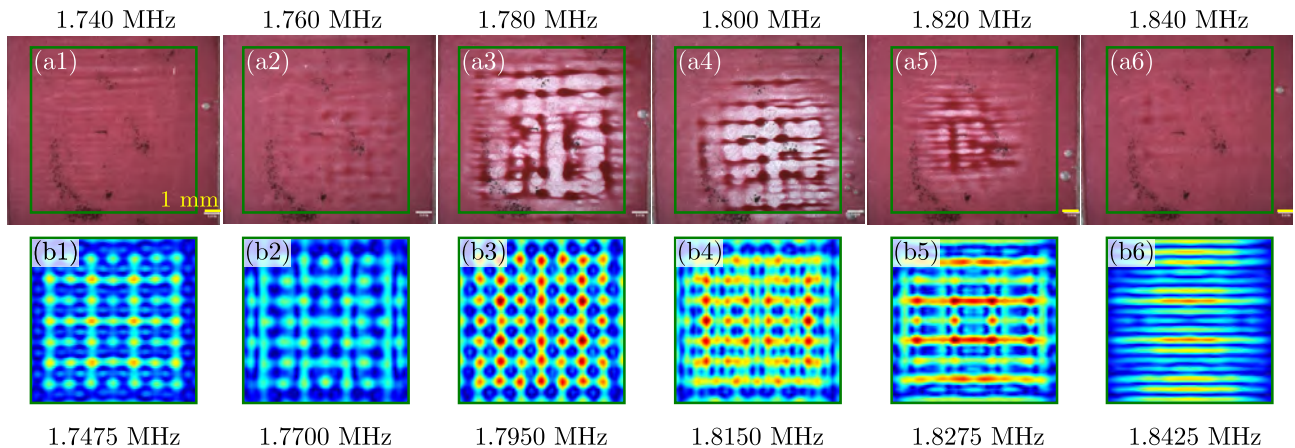


**Figure 3:** Experimentally observed positions of trapped particles and numerical predictions of the displacement field in the PZT slab at corresponding resonance frequencies. (a1)-(a6) Images, each obtained at a given single frequency, of the agglomeration of suspended 3- $\mu\text{m}$ -diameter polystyrene beads loaded in the water-filled microchannel above the PZT slab. The green outline indicates the  $10 \times 10 \text{ mm}^2$  protrusion on the bottom of the PZT slab. (b1)-(b6) Color plots of the numerically predicted vertical displacement field on the top surface of an unloaded PZT slab with electrode patterning, from low (blue) to high (red) field magnitude. The scale bar applies for both rows.

### Conclusion

We have presented a combined experimental and numerical study of a device design based on Chladni-plate-like motion of box-shaped PZT slabs driven at resonance. We have shown that this motion when coupled to a water-fill microchannel may lead to the appearance of a wall-free acoustic multi-well that can trap suspended microparticles. The specific multi-well configuration can be changed dynamically simply by changing from one resonance mode of the PZT slab to another. This dynamically defined, wall-free acoustic multi-well system is potentially useful in biotech applications such as; tissue engineering, formation of cellular organoids, and drug screening applications, while consisting only of inexpensive components available in most acoustofluidics laboratories.

### References

- [1] B Vanherberghen *et al.*, *Lab Chip* **10**, 2727-2732 (2010).
- [2] K Olofsson, B Hammarström and M Wiklund, *Micromachines* **9**, 594 1-19 (2018).
- [3] T Lilliehorn, U Simu, M Nilsson, M Almqvist, T Stepinski, T Laurell, J Nilsson, S Johansson *Ultrasonics* **43**, 293 (2005).
- [4] J Lei, *Microfluid Nanofluid* **21**, 50 1-15 (2017).
- [5] NR Skov, JS Bach, BG Winckelmann, and H Bruus, *AIMS Mathematics* **4**, 99-111 (2019).



## Appendix B

# Notes on the governing equations and notation

### Symmetries in the general elasticity tensor

Using the definitions of strain energy density  $U_m$  and stress in a linear elastic we find

$$U_m = \sigma_{ik}\epsilon_{ik} = C_{iklm}\epsilon_{lm}\epsilon_{ik} \quad (\text{B.1a})$$

From this we can derive the following expressions for the elasticity

$$C_{iklm} = \frac{\partial U}{\partial \epsilon_{ik} \partial \epsilon_{lm}}, \quad C_{lmik} = \frac{\partial U}{\partial \epsilon_{lm} \partial \epsilon_{ik}} \quad (\text{B.1b})$$

As the order of derivatives is inconsequential, we see that the  $C_{iklm} = C_{lmik}$  adding to the degree of symmetry in the elasticity tensor.

$$C_{iklm} = C_{kilm} = C_{ikml} = C_{kiml} = C_{mlik} = C_{lmik} = C_{mlki} = C_{lmki} \quad (\text{B.1c})$$

### Basis for the factor 2 in Voigt shear element

The strain energy density  $U_m = \frac{1}{2}\sigma_{ik}\epsilon_{ik}$  is invariant of notation. In roman letter indices we find

$$U_m = \frac{1}{2}(\sigma_{11}\epsilon_{11} + \sigma_{12}\epsilon_{12} + \sigma_{13}\epsilon_{13} + \sigma_{12}\epsilon_{12} + \sigma_{22}\epsilon_{22} + \sigma_{23}\epsilon_{23} + \sigma_{31}\epsilon_{31} + \sigma_{32}\epsilon_{32} + \sigma_{33}\epsilon_{33}), \quad (\text{B.2a})$$

whereas it in Voigt components is

$$U_m = \frac{1}{2}(\sigma_1\epsilon_1 + \sigma_2\epsilon_2 + \sigma_3\epsilon_3 + \sigma_4\epsilon_4 + \sigma_5\epsilon_5 + \sigma_6\epsilon_6). \quad (\text{B.2b})$$

Equating the two expression and employing the symmetry of the stress,  $\sigma_{ik} = \sigma_{ki}$ , and strain,  $\epsilon_{ik} = \epsilon_{ki}$ , tensors we find

$$\sigma_4\epsilon_4 + \sigma_5\epsilon_5 + \sigma_6\epsilon_6 = 2(\sigma_{23}\epsilon_{23} + \sigma_{13}\epsilon_{13} + \sigma_{21}\epsilon_{12}). \quad (\text{B.2c})$$

Thus, the shear elements of either stress or strain in Voigt notation must be twice that in roman indices. By convention the factor is added to the shear elements, to keep Eq. (2.8) consistent with Eq. (2.3a)

$$\epsilon_4 = 2\epsilon_{23}, \quad \epsilon_5 = 2\epsilon_{31}, \quad \epsilon_6 = 2\epsilon_{12} \quad (\text{B.2d})$$

## Voigt transformation derivations

Rotations using Bond matrices  $M_\epsilon$  and  $M_\sigma$  must be isometric, *i.e.* the elastic energy must be invariant of rotations.

$$\begin{aligned} U_m &= U'_m & (\text{B.3a}) \\ \frac{1}{2} \sigma_V^T \epsilon_V &= \frac{1}{2} \sigma_V'^T \epsilon_V', \\ \sigma_V^T \epsilon_V &= \sigma_V^T M_\sigma^T M_\epsilon \epsilon_V, \\ M_\sigma^T M_\epsilon &= I \Leftrightarrow M_\sigma = (M_\epsilon^{-1})^{-T} \Leftrightarrow M_\epsilon = (M_\sigma^T)^{-1}. \end{aligned}$$

We use the stress definition  $\sigma_V = C \epsilon_V$  to determine the transformation laws for the elasticity matrix  $C$ ,

$$\begin{aligned} \sigma_V' &= C' \epsilon_V', & (\text{B.3b}) \\ M_\sigma \sigma_V &= C' M_\epsilon \epsilon_V, \\ \sigma_V &= M_\sigma^{-1} C' M_\epsilon \epsilon_V, \\ C &= M_\sigma^{-1} C' (M_\sigma^{-T})^{-1} \Leftrightarrow C' = M_\sigma C M_\sigma^{-T}. \end{aligned}$$

Similarly, we use the definition for the mechanically induced polarization density  $P^m$  to determine the transformation of the piezoelectric coupling tensor  $e$ ,

$$\begin{aligned} P^m &= e' \epsilon_V', & (\text{B.3c}) \\ R P^m &= e' (M_\sigma^T)^{-1} \epsilon_V, \\ P^m &= R^{-1} e' (M_\sigma^T)^{-1} \epsilon_V, \\ e &= R^{-1} e' (M_\sigma^T)^{-1} \Leftrightarrow e' = R e M_\sigma^T. \end{aligned}$$

The transformation of the permittivity tensor is trivial but we include it for good measure.

$$\begin{aligned} D' &= \epsilon' E', & (\text{B.3d}) \\ R D &= \epsilon' R E, \\ D &= R^{-1} \epsilon' R E, \\ \epsilon &= R^{-1} \epsilon' R \Leftrightarrow \epsilon' = R \epsilon R^{-1}. \end{aligned}$$



## Appendix C

### Material parameters for $128^\circ$ Y-X cut $\text{LiNbO}_3$

$$\begin{pmatrix} 202.89 & 72.33 & 60.17 & 10.74 & 0 & 0 & 0 & 1.73 & -1.64 \\ & 194.23 & 90.59 & 8.97 & 0 & 0 & 0 & -4.48 & 2.69 \\ & & 220.29 & 8.14 & 0 & 0 & 0 & 1.67 & -2.44 \\ & & & 74.89 & 0 & 0 & 0 & -0.14 & -0.55 \\ & & & & 72.79 & 8.51 & -0.10 & 0 & 0 \\ & & & & & 59.51 & 6.09 & 0 & 0 \\ & & \textit{Symmetric} & & & & 44.3 & 0 & 0 \\ & & & & & & & 38.08 & -7.96 \\ & & & & & & & & 34.12 \end{pmatrix} \quad (\text{C.1})$$



# Bibliography

- [1] N. R. Skov and H. Bruus, *Modeling of Microdevices for SAW-Based Acoustophoresis - A Study of Boundary Conditions*. *Micromachines* **7**(10), 182 (2016).
- [2] N. R. Skov, J. S. Bach, B. G. Winkelmann, and H. Bruus, *3D modeling of acoustofluidics in a liquid-filled cavity including streaming, viscous boundary layers, surrounding solids, and a piezoelectric transducer*. *AIMS Mathematics* **4**, 99–111 (2019).
- [3] N. R. Skov, P. Sehgal, B. J. Kirby, and H. Bruus, *Three-dimensional numerical modeling of surface acoustic wave devices: Acoustophoresis of microparticles including streaming*. *Phys. Rev. Applied Submitted* (2019).
- [4] N. R. Skov, B. Hammarström, and M. W. H. Bruus, *A wall-free acoustic multi-well system for particle trapping*. In *Proceedings of Acoustofluidics 2019, Aug 26-28, Enschede, Netherlands* (2019).
- [5] R. D. Pedde, B. Mirani, A. Navaei, T. Styan, S. Wong, M. Mehrali, A. Thakur, N. K. Mohtaram, A. Bayati, A. Dolatshahi-Pirouz, M. Nikkhah, S. M. Willerth, and M. Akbari, *Emerging biofabrication strategies for engineering complex tissue constructs*. *Advanced Materials* **29**(19), 1606061 (2017).
- [6] C. W. Shields, C. D. Reyes, and G. P. López, *Microfluidic cell sorting: A review of the advances in the separation of cells from debulking to rare cell isolation*. *Lab Chip* **15**, 1230–1249 (2015).
- [7] M. Karabacak, P. Spuhler, F. Fachin, E. J. Lim, V. Pai, E. Ozkumur, J. Martel-Foley, N. Kojic, K. Smith, P.-i. Chen, J. Yang, H. Hwang, B. Morgan, J. Trautwein, T. A. Barber, S. Stott, S. Maheswaran, R. Kapur, D. A. Haber, and M. Toner, *Microfluidic, marker-free isolation of circulating tumor cells from blood samples*. *Nature protocols* **9**, 694–710 (2014).
- [8] Y. Chen, P. Li, P.-H. Huang, Y. Xie, J. Mai, L. Wang, N.-T. Nguyen, and T. Jun Huang, *Rare cell isolation and analysis in microfluidics*. *Lab on a chip* **14**, 626–645 (2014).
- [9] A. Lenshof, A. Ahmad-Tajudin, K. Jaras, A.-M. Sward-Nilsson, L. Aberg, G. Marko-Varga, J. Malm, H. Lilja, and T. Laurell, *Acoustic whole blood plasmapheresis chip for prostate specific antigen microarray diagnostics*. *Anal. Chem.* **81**(15), 6030–6037 (2009).

- [10] P. Ohlsson, M. Evander, K. Petersson, L. Mellhammar, A. Lehmusvuori, U. Karhunen, M. Soikkeli, T. Seppa, E. Tuunainen, A. Spangar, P. von Lode, K. Rantakokko-Jalava, G. Otto, S. Scheduling, T. Soukka, S. Wittfooth, and T. Laurell, *Integrated acoustic separation, enrichment, and microchip polymerase chain reaction detection of bacteria from blood for rapid sepsis diagnostics*. *Analytical Chemistry* **88**(19), 9403–9411 (2016).
- [11] M. Madou, L. Lee, S. Daunert, S. Lai, and C.-H. Shih, *Design and fabrication of cd-like microfluidic platforms for diagnostics: Microfluidic functions*. *Biomedical Microdevices* **3**, 245–254 (2001).
- [12] D. Sugiyama, Y. Teshima, K. Yamanaka, M. P. Briones-Nagata, M. Maeki, K. Yamashita, M. Takahashi, and M. Miyazaki, *Simple density-based particle separation in a microfluidic chip*. *Anal. Methods* **6**(1), 308–311 (2014).
- [13] D. Dicarolo, *Inertial microfluidics*. *Lab Chip* **9**, 3038–46 (2009).
- [14] J. Zhang, S. Yan, D. Yuan, G. Alici, N.-T. Nguyen, M. E. Warkiani, and W. Li, *Fundamentals and applications of inertial microfluidics: a review*. *Lab Chip* **16**(1), 10–34 (2016).
- [15] H. Chen, *A triplet parallelizing spiral microfluidic chip for continuous separation of tumor cells*. *Scientific Reports* **8** (2018).
- [16] H. Nilsson, M. Wiklund, T. Johansson, H. Hertz, and S. Nilsson, *Microparticles for selective protein determination in capillary electrophoresis*. *Electrophoresis* **22**(12), 2384–2390 (2001).
- [17] J. N. Mehrishi and J. Bauer, *Electrophoresis of cells and the biological relevance of surface charge*. *ELECTROPHORESIS* **23**(13), 1984–1994 (2002).
- [18] P. R. C. Gascoyne, J. Noshari, T. J. Anderson, and F. F. Becker, *Isolation of rare cells from cell mixtures by dielectrophoresis*. *Electrophoresis* **30**(8), 1388–1398 (2009).
- [19] J. Voldman, *Electrical forces for microscale cell manipulation*. *Annual Review of Biomedical Engineering* **8**(1), 425–454 (2006).
- [20] N. Pamme and C. Wilhelm, *Continuous sorting of magnetic cells via on-chip free-flow magnetophoresis*. *Lab on a Chip* **6**(8), 974 (2006).
- [21] H. Zhang, E. Tu, N. D Hagen, C. Schnabel, M. J Paliotti, W. Soo Hoo, P. Nguyen, J. R Kohrumel, W. F Butler, M. Chachisvilis, and P. Marchand, *Time-of-flight optophoresis analysis of live whole cells in microfluidic channels*. *Biomedical microdevices* **6**, 11–21 (2004).
- [22] P. Geelhoed, R. Lindken, and J. Westerweel, *Thermophoretic separation in microfluidics*. *Chemical Engineering Research and Design* **84**(5), 370 – 373 (2006).
- [23] J. Hultström, O. Manneberg, K. Dopf, H. M. Hertz, H. Brismar, and M. Wiklund, *Proliferation and viability of adherent cells manipulated by standing-wave ultrasound in a microfluidic chip*. *Ultrasound Med Biol* **33**(1), 145–151 (2007).

- [24] D. N. Ankrett, D. Carugo, J. Lei, P. Glynne-Jones, P. A. Townsend, X. Zhang, and M. Hill, *The effect of ultrasound-related stimuli on cell viability in microfluidic channels*. *Journal of Nanobiotechnology* **11**(1), 20 (2013).
- [25] J. T. Karlsen, W. Qiu, P. Augustsson, and H. Bruus, *Acoustic streaming and its suppression in inhomogeneous fluids*. *Phys. Rev. Lett.* **120**(5), 054501 (2018).
- [26] L. V. King, *On the acoustic radiation pressure on spheres*. *Proc. R. Soc. London, Ser. A* **147**(861), 212–240 (1934).
- [27] P. B. Muller and H. Bruus, *Theoretical study of time-dependent, ultrasound-induced acoustic streaming in microchannels*. *Phys. Rev. E* **92**, 063018 (2015).
- [28] Lord Rayleigh (John William Strutt), *On the circulation of air observed in Kundt's tubes, and on some allied acoustical problems*. *Philos. Trans. R. Soc. London* **175**, 1–21 (1884).
- [29] C. Eckart, *Vortices and streams caused by sound waves*. *Phys. Rev.* **73**, 68–76 (1948).
- [30] P. B. Muller, R. Barnkob, M. J. H. Jensen, and H. Bruus, *A numerical study of microparticle acoustophoresis driven by acoustic radiation forces and streaming-induced drag forces*. *Lab Chip* **12**, 4617–4627 (2012).
- [31] S. Liu, Y. Yang, Z. Ni, X. Guo, L. Luo, J. Tu, D. Zhang, and J. Zhang, *Investigation into the effect of acoustic radiation force and acoustic streaming on particle patterning in acoustic standing wave fields*. *Sensors* **17**, 1664 (2017).
- [32] K. Sritharan, C. Strobl, M. Schneider, A. Wixforth, and Z. Guttenberg, *Acoustic mixing at low reynold's numbers*. *Appl Phys Lett* **88**(5), 054102 (2006).
- [33] H. Zhang, Z. Tang, Z. Wang, S. Pan, Z. Han, C. Sun, M. Zhang, X. Duan, and W. Pang, *Acoustic streaming and microparticle enrichment within a microliter droplet using a lamb-wave resonator array*. *Phys Rev. Applied* **9**, 064011 (2018).
- [34] R. Moiseyenko and H. Bruus, *Whole-system ultrasound resonances as the basis for acoustophoresis in all-polymer microfluidic devices*. *Phys. Rev. Appl.* **11**, 014014 (2019).
- [35] D. Morgan, *Surface acoustic wave devices and applications*. *Ultrasonics* **11**, 121–131 (1973).
- [36] F. Petersson, L. Åberg, A. M. Swärd-Nilsson, and T. Laurell, *Free flow acoustophoresis: microfluidic-based mode of particle and cell separation*. *Anal. Chem.* **79**(14), 5117–23 (2007).
- [37] J. Shi, S. Yazdi, S.-C. S. Lin, X. Ding, I.-K. Chiang, K. Sharp, and T. J. Huang, *Three-dimensional continuous particle focusing in a microfluidic channel via standing surface acoustic waves (SSAW)*. *Lab Chip* **11**(14), 2319–2324 (2011).
- [38] B. Hammarström, T. Laurell, and J. Nilsson, *Seed particle enabled acoustic trapping of bacteria and nanoparticles in continuous flow systems*. *Lab Chip* **12**, 4296–4304 (2012).

- [39] P. Mishra, M. Hill, and P. Glynne-Jones, *Deformation of red blood cells using acoustic radiation forces*. *Biomicrofluidics* **8**(3), 034109 (2014).
- [40] I. Gralinski, S. Raymond, T. Alan, and A. Neild, *Continuous flow ultrasonic particle trapping in a glass capillary*. *Journal of Applied Physics* **115**(5), 054505 (2014).
- [41] B. Vanherberghen, O. Manneberg, A. Christakou, T. Frisk, M. Ohlin, H. M. Hertz, B. Önfelt, and M. Wiklund, *Ultrasound-controlled cell aggregation in a multi-well chip*. *Lab Chip* **10**(20), 2727–2732 (2010).
- [42] A. Riaud, M. Baudoin, O. Bou Matar, L. Becerra, and J.-L. Thomas, *Selective manipulation of microscopic particles with precursor swirling rayleigh waves*. *Phys. Rev. Applied* **7**, 024007 (2017).
- [43] I. Leibacher, P. Hahn, and J. Dual, *Acoustophoretic cell and particle trapping on microfluidic sharp edges*. *Microfluid Nanofluid* **19**(4), 923–933 (2015).
- [44] P. Sehgal and B. J. Kirby, *Separation of 300 and 100 nm particles in fabry-perot acoustofluidic resonators*. *Anal. Chem.* **89**(22), 12192–12200 (2017).
- [45] Y. Bian, F. Guo, S. Yang, Z. Mao, H. Bachman, S.-Y. Tang, L. Ren, B. Zhang, J. Gong, X. Guo, and T. J. Huang, *Acoustofluidic waveguides for localized control of acoustic wavefront in microfluidics*. *Microfluidics and Nanofluidics* **21**(8), 132 (2017).
- [46] P. B. Muller, M. Rossi, A. G. Marin, R. Barnkob, P. Augustsson, T. Laurell, C. J. Kähler, and H. Bruus, *Ultrasound-induced acoustophoretic motion of microparticles in three dimensions*. *Phys. Rev. E* **88**(2), 023006 (2013).
- [47] M. Hill, Y. Shen, and J. J. Hawkes, *Modelling of layered resonators for ultrasonic separation*. *Ultrasonics* **40**(1-8), 385–392 (2002).
- [48] N. Nama, R. Barnkob, Z. Mao, C. J. Kähler, F. Costanzo, and T. J. Huang, *Numerical study of acoustophoretic motion of particles in a pdms microchannel driven by surface acoustic waves*. *Lab Chip* **15**, 2700 (2015).
- [49] C. Devendran, T. Albrecht, J. Brenker, T. Alan, and A. Neild, *The importance of travelling wave components in standing surface acoustic wave (SSAW) systems*. *Lab Chip* **16**, 3756–3766 (2016).
- [50] J. T. Karlsen and H. Bruus, *Acoustic tweezing and patterning of concentration fields in microfluidics*. *Phys. Rev. Applied* **7**, 034017 (2017).
- [51] D. J. Collins, R. O’Rorke, C. Devendran, Z. Ma, J. Han, A. Neild, and Y. Ai, *Self-aligned acoustofluidic particle focusing and patterning in microfluidic channels from channel-based acoustic waveguides*. *Phys. Rev. Lett.* **120**(7), 074502 (2018).
- [52] J. Lei, P. Glynne-Jones, and M. Hill, *Acoustic streaming in the transducer plane in ultrasonic particle manipulation devices*. *Lab Chip* **13**(11), 2133–2143 (2013).

- [53] J. Lei, M. Hill, and P. Glynne-Jones, *Numerical simulation of 3d boundary-driven acoustic streaming in microfluidic devices*. *Lab Chip* **14**(3), 532–541 (2014).
- [54] S. M. Hagsäter, T. G. Jensen, H. Bruus, and J. P. Kutter, *Acoustic resonances in microfluidic chips: full-image micro-PIV experiments and numerical simulations*. *Lab Chip* **7**(10), 1336–1344 (2007).
- [55] S. M. Hagsäter, A. Lenshof, P. Skafte-Pedersen, J. P. Kutter, T. Laurell, and H. Bruus, *Acoustic resonances in straight micro channels: Beyond the 1D-approximation*. *Lab Chip* **8**(7), 1178–1184 (2008).
- [56] A. Neild, S. Oberti, and J. Dual, *Design, modeling and characterization of microfluidic devices for ultrasonic manipulation*. *Sensors and Actuators B: Chemical* **121**(2), 452 – 461 (2007).
- [57] F. Garofalo, T. Laurell, and H. Bruus, *Performance Study of Acoustophoretic Microfluidic Silicon-Glass Devices by Characterization of Material- and Geometry-Dependent Frequency Spectra*. *Phys. Rev. Applied* **7**, 054026 (2017).
- [58] M. W. H. Ley and H. Bruus, *Three-dimensional numerical modeling of acoustic trapping in glass capillaries*. *Phys. Rev. Applied* **8**, 024020 (2017).
- [59] P. Hahn and J. Dual, *A numerically efficient damping model for acoustic resonances in microfluidic cavities*. *Physics of Fluids* **27**, 062005 (2015).
- [60] P. Hahn, O. Schwab, and J. Dual, *Modeling and optimization of acoustofluidic micro-devices*. *Lab Chip* **14**, 3937–3948 (2014).
- [61] J. S. Bach and H. Bruus, *Theory of pressure acoustics with viscous boundary layers and streaming in curved elastic cavities*. *J. Acoust. Soc. Am.* **144**, 766–784 (2018).
- [62] D. Köster, *Numerical simulation of acoustic streaming on surface acoustic wave-driven biochips*. *SIAM J. Sci. Comput.* **29**(6), 2352–2380 (2007).
- [63] M. Settnes and H. Bruus, *Forces acting on a small particle in an acoustical field in a viscous fluid*. *Phys. Rev. E* **85**, 016327 (2012).
- [64] J. T. Karlsen and H. Bruus, *Forces acting on a small particle in an acoustical field in a thermoviscous fluid*. *Phys. Rev. E* **92**, 043010 (2015).
- [65] H. Bruus, *Acoustofluidics 2: Perturbation theory and ultrasound resonance modes*. *Lab Chip* **12**, 20–28 (2012).
- [66] <https://www.hpc.dtu.dk/> (2019).
- [67] I. Leibacher, S. Schatzer, and J. Dual, *Impedance matched channel walls in acoustofluidic systems*. *Lab Chip* **14**(3), 463–470 (2014).

- [68] F. Guo, Z. Mao, Y. Chen, Z. Xie, J. P. Lata, P. Li, L. Ren, J. Liu, J. Yang, M. Dao, S. Suresh, and T. J. Huang, *Three-dimensional manipulation of single cells using surface acoustic waves*. PNAS **113**(6), 1522–1527 (2016).
- [69] Z. Mao, Y. Xie, F. Guo, L. Ren, P.-H. Huang, Y. Chen, J. Rufo, F. Costanzo, and T. J. Huang, *Experimental and numerical studies on standing surface acoustic wave microfluidics*. Lab Chip **16**(3), 515–524 (2016).
- [70] I. D. Johnston, D. K. McCluskey, C. K. L. Tan, and M. C. Tracey, *Mechanical characterization of bulk sylgard 184 for microfluidics and microengineering*. J. Micromech. Microeng. **24**(3), 035017 (2014).
- [71] M. F. Ashby, *Materials and the environment* (Elsevier LTD) (2013).
- [72] P. B. Muller and H. Bruus, *Numerical study of thermoviscous effects in ultrasound-induced acoustic streaming in microchannels*. Phys. Rev. E **90**(4), 043016 (2014).
- [73] H. Amini, W. Lee, and D. Di Carlo, *Inertial microfluidic physics*. Lab Chip **14**, 2739–2761 (2014).
- [74] J. Shi, H. Huang, Z. Stratton, Y. Huang, and T. J. Huang, *Continuous particle separation in a microfluidic channel via standing surface acoustic waves (SSAW)*. Lab Chip **9**(23), 3354–3359 (2009).
- [75] Y. Chen, A. A. Nawaz, Y. Zhao, P.-H. Huang, J. P. McCoy, S. J. Levine, L. Wang, and T. J. Huang, *Standing surface acoustic wave (SSAW)-based microfluidic cytometer*. Lab on a Chip **14**(5), 916 (2014).
- [76] K. Lee, H. Shao, R. Weissleder, and H. Lee, *Acoustic purification of extracellular microvesicles*. ACS Nano **9**(3), 2321–2327 (2015).
- [77] A. Liga, A. D. B. Vliegthart, W. Oosthuyzen, J. W. Dear, and M. Kersaudy-Kerhoas, *Exosome isolation: a microfluidic road-map*. Lab Chip **15**(11), 2388–2394 (2015).
- [78] N. Pamme, *Continuous flow separations in microfluidic devices*. Lab on a Chip **7**(12), 1644 (2007).
- [79] P. Sethu, A. Sin, and M. Toner, *Microfluidic diffusive filter for apheresis (leukapheresis)*. Lab Chip **6**(1), 83–89 (2006).
- [80] D. Huh, J. H. Bahng, Y. Ling, H.-H. Wei, O. D. Kripfgans, J. B. Fowlkes, J. B. Grotberg, and S. Takayama, *Gravity-driven microfluidic particle sorting device with hydrodynamic separation amplification*. Analytical Chemistry **79**(4), 1369–1376 (2007).
- [81] R. Guldiken, M. C. Jo, N. D. Gallant, U. Demirci, and J. Zhe, *Sheathless size-based acoustic particle separation*. Sensors **12**(12), 905–922 (2012).
- [82] M. Travagliati, R. Shilton, F. Beltram, and M. Cecchini, *Fabrication, operation and flow visualization in surface-acoustic-wave-driven acoustic-counterflow microfluidics*. J. Vis. Exp. **78**, e50524 (2013).



- [83] H. Bruus, J. Dual, J. Hawkes, M. Hill, T. Laurell, J. Nilsson, S. Radel, S. Sadhal, and M. Wiklund, *Forthcoming lab on a chip tutorial series on acoustofluidics: Acoustofluidics-exploiting ultrasonic standing wave forces and acoustic streaming in microfluidic systems for cell and particle manipulation*. *Lab Chip* **11**(21), 3579–3580 (2011).
- [84] M. Evander, O. Gidlof, B. Olde, D. Erlinge, and T. Laurell, *Non-contact acoustic capture of microparticles from small plasma volumes*. *Lab Chip* **15**, 2588–2596 (2015).
- [85] M. Wiklund, *Acoustofluidics 12: Biocompatibility and cell viability in microfluidic acoustic resonators*. *Lab Chip* **12**, 2018–28 (2012).
- [86] D. J. Collins, B. Morahan, J. Garcia-Bustos, C. Doerig, M. Plebanski, and A. Neild, *Two-dimensional single-cell patterning with one cell per well driven by surface acoustic waves*. *Nat. Commun.* **6**, 8686 (2015).
- [87] D. Ahmed, A. Ozcelik, N. Bojanala, N. Nama, A. Upadhyay, Y. Chen, W. Hanna-Rose, and T. J. Huang, *Rotational manipulation of single cells and organisms using acoustic waves*. *Nat. Commun.* **7**, 11085 (2016).
- [88] P. Augustsson, J. T. Karlsen, H.-W. Su, H. Bruus, and J. Voldman, *Iso-acoustic focusing of cells for size-insensitive acousto-mechanical phenotyping*. *Nat. Commun.* **7**, 11556 (2016).
- [89] D. Carugo, T. Octon, W. Messaoudi, A. L. Fisher, M. Carboni, N. R. Harris, M. Hill, and P. Glynne-Jones, *A thin-reflector microfluidic resonator for continuous-flow concentration of microorganisms: a new approach to water quality analysis using acoustofluidics*. *Lab Chip* **14**(19), 3830–3842 (2014).
- [90] G. Sitters, D. Kamsma, G. Thalhammer, M. Ritsch-Marte, E. J. G. Peterman, and G. J. L. Wuite, *Acoustic force spectroscopy*. *Nat. Meth.* **12**(1), 47–50 (2015).
- [91] P. Augustsson, C. Magnusson, M. Nordin, H. Lilja, and T. Laurell, *Microfluidic, label-free enrichment of prostate cancer cells in blood based on acoustophoresis*. *Anal. Chem.* **84**(18), 7954–7962 (2012).
- [92] P. Li, Z. Mao, Z. Peng, L. Zhou, Y. Chen, P.-H. Huang, C. I. Truica, J. J. Drabick, W. S. El-Deiry, M. Dao, S. Suresh, and T. J. Huang, *Acoustic separation of circulating tumor cells*. *PNAS* **112**(16), 4970–4975 (2015).
- [93] B. Hammarström, B. Nilson, T. Laurell, J. Nilsson, and S. Ekström, *Acoustic trapping for bacteria identification in positive blood cultures with maldi-tof ms*. *Anal. Chem.* **86**(21), 10560–10567 (2014).
- [94] E. M. Arruda and M. C. Boyce, *A three-dimensional constitutive model for the large stretch behavior of rubber elastic materials*. *Journal of the Mechanics and Physics of Solids* **41**(2), 389–412 (1993).
- [95] Y.-S. Yu and Y.-P. Zhao, *Deformation of PDMS membrane and microcantilever by a water droplet: Comparison between mooney–rivlin and linear elastic constitutive models*. *Journal of Colloid and Interface Science* **332**(2), 467–476 (2009).

- [96] H. Bourbaba, C. B. achaiba, and B. Mohamed, *Mechanical behavior of polymeric membrane: Comparison between PDMS and PMMA for micro fluidic application*. Energy Procedia **36**, 231–237 (2013).
- [97] A. N. Darinskii, M. Weihnacht, and H. Schmidt, *Computation of the pressure field generated by surface acoustic waves in microchannels*. Lab Chip **16**(14), 2701–2709 (2016).
- [98] R. Weis and T. Gaylord, *Lithium niobate: summary of physical properties and crystal structure*. Applied Physics A **37**(4), 191–203 (1985).
- [99] R. H. D. Narottam P. Bansal, N. P. Bansal, *Handbook of Glass Properties* (Elsevier LTD) (1986).
- [100] E. L. Madsen, *Ultrasonic shear wave properties of soft tissues and tissuelike materials*. The Journal of the Acoustical Society of America **74**(5), 1346 (1983).
- [101] K. Zell, J. I. Sperl, M. W. Vogel, R. Niessner, and C. Haisch, *Acoustical properties of selected tissue phantom materials for ultrasound imaging*. Phys Med Biol **52**(20), N475 (2007).
- [102] D.-H. Kim, J. Song, W. M. Choi, H.-S. Kim, R.-H. Kim, Z. Liu, Y. Y. Huang, K.-C. Hwang, Y. w. Zhang, and J. A. Rogers, *Materials and noncoplanar mesh designs for integrated circuits with linear elastic responses to extreme mechanical deformations*. Proceedings of the National Academy of Sciences **105**(48), 18675–18680 (2008).
- [103] F. Schneider, T. Fellner, J. Wilde, and U. Wallrabe, *Mechanical properties of silicones for MEMS*. J. Micromech. Microeng. **18**(6), 065008 (2008).
- [104] D. N. Hohne, J. G. Younger, and M. J. Solomon, *Flexible microfluidic device for mechanical property characterization of soft viscoelastic solids such as bacterial biofilms*. Langmuir **25**(13), 7743–7751 (2009).
- [105] T. Still, M. Oudich, G. K. Auerhammer, D. Vlassopoulos, B. Djafari-Rouhani, G. Fytas, and P. Sheng, *Soft silicone rubber in phononic structures: Correct elastic moduli*. Phys. Rev. B **88**(9), 094102 (2013).
- [106] I.-K. Lin, K.-S. Ou, Y.-M. Liao, Y. Liu, K.-S. Chen, and X. Zhang, *Viscoelastic characterization and modeling of polymer transducers for biological applications*. Journal of Microelectromechanical Systems **18**(5), 1087–1099 (2009).
- [107] COMSOL Multiphysics 5.2. [www.comsol.com](http://www.comsol.com) (2015).
- [108] B. H. Ha, K. S. Lee, G. Destgeer, J. Park, J. S. Choung, J. H. Jung, J. H. Shin, and H. J. Sung, *Acoustothermal heating of polydimethylsiloxane microfluidic system*. Sci. Rep. **5**, 11851 (2015).
- [109] J. S. Bach, *Theory and simulation of microscale acoustic streaming in 3 dimensions: a study in effective modelling*. MSc thesis (2017).

- [110] E. B. Christoffel, *Ueber die Fortpflanzung von Stößen durch elastische feste Körper*. *Annali di Matematica Pura ed Applicata* **8**, 193–243 (1877).
- [111] T. Huang and C.-X. Deng, *Current progresses of exosomes as cancer diagnostic and prognostic biomarkers*. *Int J Biol Sci.* **15**(1), 1–11 (2017).
- [112] M. Antfolk, P. B. Muller, P. Augustsson, H. Bruus, and T. Laurell, *Focusing of sub-micrometer particles and bacteria enabled by two-dimensional acoustophoresis*. *Lab Chip* **14**, 2791–2799 (2014).
- [113] Z. Mao, P. Li, M. Wu, H. Bachman, N. Mesyngier, X. Guo, S. Liu, F. Costanzo, and T. J. Huang, *Enriching nanoparticles via acoustofluidics*. *ACS Nano* **11**(1), 603–612 (2017).
- [114] D. J. Collins, Z. Ma, J. Han, and Y. Ai, *Continuous micro-vortex-based nanoparticle manipulation via focused surface acoustic waves*. *Lab Chip* **17**, 91–103 (2017).
- [115] K. Shibayama, K. Yamanouchi, S. Hiroaki, and T. Meguro, *Optimum cut for rotated y-cut linbo3 crystal used as the substrate of acoustic-surface-wave filters*. *Proceedings of the IEEE* **64**(5), 595–597 (1976).
- [116] M. K. Tan, L. Y. Yeo, and J. R. Friend, *Unique flow transitions and particle collection switching phenomena in a microchannel induced by surface acoustic waves*. *Appl Phys Lett* **97**(23), 234106 (2010).
- [117] K.-y. Hashimoto, *Surface acoustic wave devices in telecommunications. Modelling and simulation* (Springer) (2000).
- [118] J. Shi, X. Mao, D. Ahmed, A. Colletti, and T. J. Huang, *Focusing microparticles in a microfluidic channel with standing surface acoustic waves (SSAW)*. *Lab Chip* **8**(2), 221–223 (2008).
- [119] T. Franke, A. R. Abate, D. A. Weitz, and A. Wixforth, *Surface acoustic wave (SAW) directed droplet flow in microfluidics for pdms devices*. *Lab Chip* **9**(18), 2625–2627 (2009).
- [120] M. K. Tan, R. Tjeung, H. Ervin, L. Y. Yeo, and J. Friend, *Double aperture focusing transducer for controlling microparticle motions in trapezoidal microchannels with surface acoustic waves*. *Appl Phys Lett* **95**(13), 134101 (2009).
- [121] X. Ding, S.-C. S. Lin, B. Kiraly, H. Yue, S. Li, I.-K. Chiang, J. Shi, S. J. Benkovic, and T. J. Huang, *On-chip manipulation of single microparticles, cells, and organisms using surface acoustic waves*. *PNAS* **109**(28), 11105–11109 (2012).
- [122] S. B. Q. Tran, P. Marmottant, and P. Thibault, *Fast acoustic tweezers for the two-dimensional manipulation of individual particles in microfluidic channels*. *Appl. Phys. Lett.* **101**(11), 114103 (2012).
- [123] J. Shi, D. Ahmed, X. Mao, S.-C. S. Lin, A. Lawit, and T. J. Huang, *Acoustic tweezers: patterning cells and microparticles using standing surface acoustic waves (SSAW)*. *Lab Chip* **9**(20), 2890–2895 (2009).

- [124] D. J. Collins, C. Devendran, Z. Ma, J. W. Ng, A. Neild, and Y. Ai, *Acoustic tweezers via sub-time-of-flight regime surface acoustic waves*. *Science Advances* **2**(7), e1600089 (2016).
- [125] W. Zhou, J. Wang, K. Wang, B. Huang, L. Niu, F. Li, F. Cai, Y. Chen, X. Liu, X. Zhang, H. Cheng, L. Kang, L. Meng, and H. Zheng, *Ultrasound neuro-modulation chip: activation of sensory neurons in caenorhabditis elegans by surface acoustic waves*. *Lab Chip* **17**(10), 1725–1731 (2017).
- [126] J. Zhang, S. Yang, C. Chen, J. H. Hartman, P.-H. Huang, L. Wang, Z. Tian, P. Zhang, D. Faulkenberry, J. N. Meyer, and T. J. Huang, *Surface acoustic waves enable rotational manipulation of caenorhabditis elegans*. *Lab Chip* **19**, 984–992 (2019).
- [127] X. Ding, S.-C. S. Lin, M. I. Lapsley, S. Li, X. Guo, C. Y. Chan, I.-K. Chiang, L. Wang, J. P. McCoy, and T. J. Huang, *Standing surface acoustic wave (ssaw) based multichannel cell sorting*. *Lab Chip* **12**, 4228–4231 (2012).
- [128] A. Riaud, J.-L. Thomas, E. Charron, A. Bussonnière, O. Bou Matar, and M. Baudoin, *Anisotropic swirling surface acoustic waves from inverse filtering for on-chip generation of acoustic vortices*. *Phys. Rev. Applied* **4**, 034004 (2015).
- [129] D. J. Collins, A. Neild, and Y. Ai, *Highly focused high-frequency travelling surface acoustic waves (saw) for rapid single-particle sorting*. *Lab Chip* **16**, 471–479 (2016).
- [130] M. Wu, Z. Mao, K. Chen, H. Bachman, Y. Chen, J. Rufo, L. Ren, P. Li, L. Wang, and T. J. Huang, *Acoustic separation of nanoparticles in continuous flow*. *Advanced Functional Materials* **27**(14), 1606039 (2017).
- [131] L. Johansson, J. Enlund, S. Johansson, I. Katardjiev, and V. Yantchev, *Surface acoustic wave induced particle manipulation in a pdms channel – principle concepts for continuous flow applications*. *Biomed Microdevices* **14**, 279–89 (2012).
- [132] M. K. Tan, J. R. Friend, O. K. Matar, and L. Y. Yeo, *Capillary wave motion excited by high frequency surface acoustic waves*. *Phys Fluids* **97**(23), 234106 (2010).
- [133] J. Vanneste and O. Bühler, *Streaming by leaky surface acoustic waves*. *Proc. R. Soc. A* **467**(2130), 1779–1800 (2011).
- [134] B. A. Auld, *Acoustic fields and waves in solids, Vol. 1* (R.E. Krieger,) (1990).
- [135] MIT, 77 Massachusetts Avenue, Cambridge, MA, USA, *Material Property Database*. <http://www.mit.edu/~6.777/matprops/pdms.htm>, accessed 21 August 2018.
- [136] H. Bruus, *Acoustofluidics I: Governing equations in microfluidics*. *Lab Chip* **11**, 3742 – 3751 (2011).
- [137] M. Wiklund, A. E. Christakou, M. Ohlin, I. Iranmanesh, T. Frisk, B. Vanherberghen, and B. Önfelt, *Ultrasound-induced cell-cell interaction studies in a multi-well microplate*. *Micromachines* **5**(1), 27 (2014).

- [138] M. Ohlin, A. Christakou, T. Frisk, B. Önfelt, and M. Wiklund, *Controlling acoustic streaming in a multi-well microplate for improving live cell assays*. In J. Landers, A. Herr, D. Juncker, N. Pamme, and J. Bienvenue (eds.), *Proc. 15th MicroTAS, 2 - 6 October 2011, Seattle (WA), USA*, 1612–1614 (CBMS) (2011).
- [139] M. Ohlin, A. E. Christakou, T. Frisk, B. Önfelt, and M. Wiklund, *Influence of acoustic streaming on ultrasonic particle manipulation in a 100-well ring-transducer microplate*. *J. Micromech. Microeng.* **23**(3), 035008 (2013).
- [140] K. Olofsson, B. Hammarström, and M. Wiklund, *Ultrasonic based tissue modelling and engineering*. *Micromachines* **9**(11) (2018).
- [141] A. Neild, S. Oberti, G. Radziwill, and J. Dual, *Simultaneous positioning of cells into two-dimensional arrays using ultrasound*. *Biotechnology and Bioengineering* **97**(5), 1335–1339 (2007).
- [142] T. Lilliehorn, U. Simu, M. Nilsson, M. Almqvist, T. Stepinski, T. Laurell, J. Nilsson, and S. Johansson, *Trapping of microparticles in the near field of an ultrasonic transducer*. *Ultrasonics* **43**(5), 293–303 (2005).
- [143] J. Lei, P. Glynne-Jones, and M. Hill, *Comparing methods for the modelling of boundary-driven streaming in acoustofluidic devices*. *Microfluidics and Nanofluidics* **21**(2), 23 (2017).
- [144] The European Commission, *2015/863 On the restriction of the use of certain hazardous substances in electrical and electronic equipment* (2015).
- [145] Q. Zhou, V. Sariola, K. Latifi, and V. Liimatainen, *Controlling the motion of multiple objects on a chladni plate*. *Nature Comm.* **7**, 12764 (2016).
- [146] Q.-M. Wang, T. Zhang, Q. Chen, and X.-H. Du, *Effect of dc bias field on the complex materials coefficients of piezoelectric resonators*. *Sensors and Actuators A: Physical* **109**(1), 149 – 155 (2003).
- [147] S. P. Mao, K. Zhong, V. Rochus, S. Severi, B. Nauwelaers, H. A. C. Tilmans, and X. Rottenberg, *Capacitive micromachined ultrasonic transducers for acoustic manipulation*. In *2015 Transducers - 2015 18th International Conference on Solid-State Sensors, Actuators and Microsystems (TRANSDUCERS)*, 662–665 (2015).
- [148] C. Samarasekera, J. G.W. Sun, Z. Zheng, and J. T.W. Yeow, *Trapping, separating, and palpating microbead clusters in droplets and flows using capacitive micromachined ultrasonic transducers (cmuts)*. *Sensors and Actuators B: Chemical* **276**, 481–488 (2018).